

**UCLA**

**UCLA Electronic Theses and Dissertations**

**Title**

Metal-Organic Frameworks-Based Electrolytes for Lithium Rechargeable Batteries

**Permalink**

<https://escholarship.org/uc/item/6cd132n0>

**Author**

Shen, Li

**Publication Date**

2018

Peer reviewed|Thesis/dissertation

UNIVERSITY OF CALIFORNIA

Los Angeles

**Metal–organic Frameworks-Based Electrolytes for Lithium Rechargeable Batteries**

A dissertation submitted in partial satisfaction of the  
requirements for the degree Doctor of Philosophy  
in Chemical Engineering

by

Li Shen

2018

© Copyright by

Li Shen

2018

## ABSTRACT OF DISSERTATION

Metal–organic Frameworks-Based Electrolytes for Lithium Rechargeable Batteries

by

Li Shen

Doctor of Philosophy in Chemical Engineering

University of California, Los Angeles, 2018

Professor Yunfeng Lu, Chair

The extensive utilization of fossil fuels since 2<sup>nd</sup> industry revolution bears a major responsibility for climate change. The raising awareness towards sustainable and renewable energy supply calls for game-changing research and progress in field of electrochemical energy storage, among which lithium-ion batteries (LIBs) is of particular interest. The developments of LIBs, in conjunction with the revolutions in the area of semiconductor and information technologies, have triggered the rapid growth of portable electronics and electric vehicles. Particularly, the transition of gasoline-powered automobiles to electrification ones requires better LIBs with higher energy density, faster charging rate, cheaper cost and longer-lasting lifetime.

To achieve the goals, it is essential to rethink and closely examine the fundamental electrochemistry beneath the conversion between electricity and chemical reactions. The operation of batteries relies on the separation of electrons and ions in electrodes, and their

subsequent respective translocation through the electronic pathways and the electrolytes. The electronic conductivity of electrodes has been improved by rational architecture design and incorporation of conductive agents. While optimizing ionic transport is more challenging since the electrode-electrolyte interface is dynamic during cycling. Variation of electrolytes would not only impact the electrochemical reactions in electrodes, but also the ohmic and concentration polarizations throughout the devices. Therefore, advances in electrolyte are vital for driving innovations in battery technologies.

Commercial liquid electrolytes, which are based on ion diffusion in fluidic medium, have merit in ionic conductivity. However, its suitability for next-generation LIBs is under dispute. Firstly, the  $\text{Li}^+$  transference number, defined as the ratio of conductivity carried by  $\text{Li}^+$  versus by  $\text{Li}^+$  and counter anions, is typically as low as 0.3, indicating an inferior transport efficiency. Such scenario is responsible for severe polarization and deterioration of the cycling life, particularly, during fast charging/discharging process. Second, liquid electrolytes are not compatible with high energy electrodes (e.g. Li anode, high voltage cathode, etc.) viewed from the aspects of electrochemical voltage window and safety. To address these issues, solid electrolytes and polymer electrolytes have been extensively explored due to their high  $\text{Li}^+$  transference number and superior safety. Yet their implementation to commercial LIBs still encounters considerable challenges from the aspects of low ionic conductivity and manufactural difficulties.

In this dissertation, a novel class of ionic conductors with biomimetic ionic channels have been developed to overcome the aforementioned limitations in liquid electrolytes. By thermal activation, porous metal-organic frameworks (MOFs) yield unsaturated metal centers which could be complexed with liquid electrolytes. The anions in liquid electrolytes can spontaneously bind with the unsaturated metal centers, forming ionic channels mimicking those of in the biologic

systems and allowing effective transport of  $\text{Li}^+$ . The ionic conductors built upon MOFs outperform liquid electrolytes in terms of high ionic conductivity, high transference number, broad electrochemical window and improved safety.

The dissertation research could be outlined briefly with following two parts:

1. Development of MOFs-based electrolytes with high ionic conductivity and high  $\text{Li}^+$  transfer number. This part of work firstly demonstrated the concept of biomimetic ionic channels within MOFs. Second, optimization of MOF pore structures according to infiltrated liquid electrolyte affords the synthesis of suitable MOF-based electrolytes with high  $\text{Li}^+$  ionic conductivity and low cost.

2. Integration of MOFs-based electrolytes into batteries. Three strategies were explored in this part to integrate the MOFs-based ionic conductors as following components: 1) separator; 2) electrolyte additive; 3) electrode additive.

Overall, this dissertation research has developed a new class of fast lithium ion conductors based on MOFs and commercially available liquid electrolytes, a variety of architecture designs for incorporating these fast  $\text{Li}^+$  conductors into battery device could be implemented in a cost-effective manner. By taking advantage of unsaturated metal sites in MOFs, immobilized anions and fast  $\text{Li}^+$  mobility enable superior device performances with prolonged cycling performance, especially at fast charging rate. Based on these works, one can expect the advances in electrolytes will impact the markets of lithium rechargeable batteries in the near future.

The dissertation of Li Shen is approved.

Harold G. Monbouquette

Dante A. Simonetti

Suneel Kodambaka

Yunfeng Lu, Committee Chair

University of California, Los Angeles

2018

## Table of Contents

|   |    |
|---|----|
| <i>Chapter 1 Background and Introduction</i> .....  | 1  |
| 1.1 Overview of Energy Storage Supplies .....   | 1  |
| 1.2 Operation of Batteries and Thermodynamics.....  | 5  |
| 1.3 Considerations of battery parameters.....   | 7  |
| 1.4 Kinetics and Interface.....   | 9  |
| 1.5 Critical Needs for Next-Generation Batteries .....  | 14 |
| 1.6 Reported Electrolytes with High Li <sup>+</sup> Transport Efficiency .....                                      | 23 |
| 1.7 Dissertation Objectives and Scope.....  | 24 |
| 1.8 References .....  | 25 |
| <i>Chapter 2 Creating Solid-State Electrolytes with Biomimetic Ionic Channels in Metal–organic Frameworks</i> ..... | 30 |
| 2.1 Introduction .....  | 31 |
| 2.2 Results and Discussions .....   | 35 |
| 2.2.1 Synthesis of Solid-State Electrolytes with High Ionic Conductivity .....                                      | 35 |
| 2.2.2 Spectroscopic Studies of Activated and Modified Ionic Channels .....  | 50 |
| 2.2.3 Electrochemical Performance of the Electrolytes .....   | 58 |
| 2.3 Conclusion .....  | 65 |
| 2.4 Experimental Section.....   | 66 |
| 2.5 References .....  | 71 |



|  |     |
|--|-----|
| <i>Chapter 3 Metal–organic Frameworks Enabled Tethered Anion Separator for Durable Lithium Rechargeable Batteries</i> .....    | 79  |
| <b>3.1 Introduction</b> .....  | 80  |
| <b>3.2 Result and Discussion</b> .....   | 83  |
| <b>3.3 Conclusion</b> .....  | 91  |
| <b>3.4 Experimental Section</b> .....  | 92  |
| <b>3.5 References</b> .....  | 94  |
| <br><i>Chapter 4 Improving Li<sup>+</sup> Transference Number of Liquid Electrolyte by Metal–organic Frameworks</i> .....      | 97  |
| <b>4.1 Introduction</b> .....  | 98  |
| <b>4.2 Results and Discussions</b> .....   | 100 |
| <b>4.3 Conclusion</b> .....  | 110 |
| <b>4.4 Experimental Section</b> .....  | 111 |
| <b>4.5 References</b> .....  | 114 |
| <br><i>Chapter 5 Nanofluidic Electrolyte with Versatile Electrolyte Modulator for High-Performance Lithium Batteries</i> ..... | 118 |
| <b>5.1 Introduction</b> .....  | 119 |
| <b>5.2 Results and Discussions</b> .....   | 122 |
| <b>5.2.1 MOF Structure and Electrolyte Properties of Nanofluidic Electrolyte</b> .....   | 122 |
| <b>5.2.2 Ion Dynamic Behavior Confined within MOF</b> .....  | 128 |

|   |            |
|---|------------|
| 5.2.3 Electrochemical Performance of the Electrolytes .....   | 134        |
| 5.2.4 Mechanism Insights on Interface between Nanofluidic Electrolyte and Electrodes<br>.....                         | 139        |
| 5.3 Conclusions.....  | 150        |
| 5.4 Experimental Section.....   | 151        |
| 5.5 References .....  | 156        |
| <i>Chapter 6 Metal–organic Frameworks as Electrode additives for High-Performance Lithium<br/>Ion Batteries .....</i> | <i>160</i> |
| 6.1 Introduction .....  | 161        |
| 6.2 Result and Discussion .....   | 162        |
| <i>Chapter 7: Summary and Perspectives .....</i>  | <i>171</i> |

## List of Figures

|   |    |
|---|----|
| <b>Figure 1-1</b> (a) Comparison of the operational characteristics of energy storage and conversion devices. (b) Comparison of the different battery technologies in terms of volumetric and gravimetric energy density.....   | 1  |
| <b>Figure 1-2</b> Bar chart showing the practical specific energy (pink) and energy densities (blue) of petrol (gasoline) and typical Li batteries including the state-of-the-art Li-ion battery, the Li metal/LMO cell, Li-S and Li-air cells.....   | 4  |
| <b>Figure 1-3</b> Schematic illustration of the lithium-ion battery (LiCoO <sub>2</sub>  electrolyte graphite).....   | 5  |
| <b>Figure 1-4</b> (a) Schematic illustration of potential phases and interfaces in lithium-ion battery (LiCoO <sub>2</sub>  electrolyte graphite). (b) Scheme of multistep of electrochemical process in electrode reaction.....  | 9  |
| <b>Figure 1-5</b> Scheme for ionic and electronic pathways in an electrode.....   | 10 |
| <b>Figure 1-6</b> Cost of lithium ion cell pack in electric vehicles.....   | 14 |
| <b>Figure 1-7</b> Standard capacity fade curves at various charging rates for 2400 mA h lithium-ion polymer battery from one of the leading manufacturers.....  | 15 |
| <b>Figure 1-8</b> Crystal structures and discharge profiles of representative intercalation cathodes: structure of (a) layered (LiCoO <sub>2</sub> ), (b) spinel (LiMn <sub>2</sub> O <sub>4</sub> ), (c) olivine (LiFePO <sub>4</sub> ), (d) tavorite (LiFeSO <sub>4</sub> F), and (e) typical discharge profiles of intercalation cathodes..... | 16 |
| <b>Figure 1-9</b> Schematic showing the formation of dendritic Li during Li stripping/plating process.....  | 17 |
| <b>Figure 1-10</b> Energy density of commercialized cathode coupled with anodes (graphite, Li) as a function of areal density (loading of active materials).....  | 17 |

**Figure 1-11** Schematic showing transport of solvated  $\text{Li}^+$  in a lithium ion cell during discharge process ..... 18

**Figure 1-12** Schematic showing the energy diagram of an aqueous electrolyte..... 19

**Figure 1-13** Space charge model-based diagram: showing ion concentration (C), electric field (E), and potential (V) as a function of distance to the Li electrode ..... 21

**Figure 1-14** Schematic of a modeled  $\text{Li}^+$  concentration distribution as a function of varied  $\text{Li}^+$  transference number throughout a lithium ion cell comprising  $\text{LiCoO}_2$  cathode and graphite anode ..... 22

**Figure 1-15** (a) Temperature dependent ionic conductivity of lithium solid electrolyte, polymer electrolyte, ionic liquid and organic liquid electrolyte; (b) Chemical structure of single-ion polymer electrolyte..... 23

**Figure 2-1** Schematic illustrations of the biomimetic ionic channels in MOFs. (a) A  $\text{Na}^+$ -ions channel in biological systems with negatively charged glutamate ions.<sup>16</sup> (b) Structure of HKUST-1 made from copper nodes (blue) and BTC ligands (black) with pore channels of  $\sim 1.1$  nm. (c) A schematic showing the formation of biomimetic ionic channels in HKUST-1 with  $\text{ClO}_4^-$  anions bound to the OMSs and solvated  $\text{Li}^+$  ions in the channels with high conductivity (copper: blue; carbon: black; oxygen: red). (d) Schematic of biomimetic ionic channels in a MOF scaffold (dark gray) with bound  $\text{ClO}_4^-$  ions (cyan dots), enabling fast transport of solvated  $\text{Li}^+$  ions (purple dots). ..... 33

**Figure 2-2** Structure characterizations and lithium ion conductivity of LPC@MOFs electrolytes. (a) A SEM image of HKUST-1 particles (insets: photographs of pristine HKUST-1, activated HKUST-1, and LPC@HKUST-1 electrolyte). (b) XRD patterns of pristine HKUST-1, activated HKUST-1, and LPC@HKUST-1 electrolyte. (c) Nyquist plots of various LPC@MOFs

electrolytes at ambient temperature. ☆: LPC@MIL-100-Al, ○: LPC@MIL-100-Fe, ▽: LPC@UiO-67, □: LPC@HKUST-1, ◇: LPC@MIL-100-Cr, Δ: LPC@UiO-66. (d) Arrhenius plots of various LPC@MOFs electrolytes and their calculated activation energies for lithium-ion conduction. (e) Arrhenius plots of LPC@MIL-100-Al (pink), LPC@MIL-100-Fe (dark yellow), and LPC@UiO-67 (cyan) in comparison with representative 1) ceramic electrolytes (Li<sub>10</sub>GeP<sub>2</sub>S<sub>12</sub>, garnet Li<sub>7</sub>La<sub>3</sub>Zr<sub>2</sub>O<sub>12</sub>, and LiPON Li<sub>3.5</sub>PO<sub>3</sub>N<sub>0.5</sub>), 2) polymeric electrolytes (LiClO<sub>4</sub>/PEO with TiO<sub>2</sub> additive,<sup>15</sup> LiTFSI-PC in crosslinked SiO<sub>2</sub>-PEO composites, and single ion polymer P(STFSILi)-PEO-P(STFSILi)), and 3) liquid-in-solid lithium-ion conductors, including liquid electrolyte@mesoporous silica, LiPF<sub>6</sub>-EC/DMC/DEC@SiO<sub>2</sub>,<sup>27</sup> LPC@organic porous solids, CB[6]·0.4LiClO<sub>4</sub>·3.4PC,<sup>28</sup> Li alkoxide@MOFs, Mg<sub>2</sub>(dobdc)·0.35LiO<sup>i</sup>Pr·0.25LiBF<sub>4</sub>·EC·DEC,<sup>21</sup> Li halide-PC@MOFs, Li<sub>0.8</sub>[Cu<sub>2</sub>Cl<sub>2</sub>Br<sub>0.8</sub>BTDD]·10(PC),<sup>23</sup> and ionic liquid@MOFs, (EMI<sub>0.8</sub>Li<sub>0.2</sub>)TFSA@ZIF-67;<sup>29</sup> and 4) liquid electrolyte, 1 M LiClO<sub>4</sub> in PC (LPC)..... 35

**Figure 2-3** N<sub>2</sub> adsorption/desorption isotherms of HKUST-1 and LPC@HKUST-1 electrolyte. HKUST-1 shows a type I isotherm characteristic of microporous solids with a BET surface area of 1150 cm<sup>2</sup> g<sup>-1</sup> and microporous volume of 0.5 cm<sup>3</sup> g<sup>-1</sup>..... 37

**Figure 2-4** Enlarged XRD patterns of as-prepared HKUST-1 (black), activated HKUST-1 (blue), and LPC@HKUST-1 (red). The coordination status of guest molecules on Cu<sup>II</sup> metal sites is indicated by the 2-theta peak at 5.8°..... 38

**Figure 2-5** TGA curve of LPC@HKUST-1 electrolyte in air..... 39

**Figure 2-6** SEM image of a pressed LPC@HKUST-1 pellet used for the conductivity studies (inset of 6a: a photograph of an electrolyte pellet). ..... 40

**Figure 2-7** (a) Nyquist plots of LPC@HKUST-1 as a function of temperature. (b) N<sub>2</sub> adsorption/desorption isotherms of pyridine@HKUST-1. (c) Arrhenius plot of

LPC@pyridine@HKUST-1 (inset: Nyquist plot of LPC-pyridine@HKUST-1 at room temperature). ..... 41

**Figure 2-8** Structures and characterizations of MIL-100 serial MOFs: (a) Structure representation of two types of mesoporous cages in MIL-100 serial MOFs. (b) Illustration of OMS evolution in a metal trimer unit of MIL-100 serial MOFs (orange atoms Al/Cr/Fe, red atoms O, grey atoms C, green atoms anionic ligands). Characterizations of synthesized MIL-100 serial MOFs. (c) XRD patterns. (d) N<sub>2</sub> adsorption/desorption isotherms. The analogous isotherms confirm the similar porous structure of the MIL-100 serial MOFs. There is a large non-negligible N<sub>2</sub> adsorption at relative high pressure for MIL-100-Cr, which corresponds to large interparticular porosity and is expected to be eliminated during preparation of electrolyte pellet. (d) FT-IR spectra. The FT-IR spectra together with the XRD patterns confirm the successful synthesis of isostructural MIL-100 materials. SEM images of (f) MIL-100-Al, (g) MIL-100-Cr, and (h) MIL-100-Fe. .... 44

**Figure 2-9** Structures and characterizations of UiO-(66/67) serial MOFs: (a) Topology structure of UiO-(66/67) serial MOFs, the purple polyhedra represent inorganic Zr<sub>6</sub>O<sub>4</sub>(OH)<sub>4</sub> clusters, the grey sticks manifest organic linkers (BDC and BPDC for UiO-66 and UiO-67, respectively). (b) Schematic illustration for activation of UiO-(66/67) serial MOFs (purple: Zr, red: O, blue: H). OMSs are created by dehydration of Zr<sub>6</sub>O<sub>4</sub>(OH)<sub>4</sub> units. Characterizations of synthesized (c-e) UiO-66 and (f-h) UiO-67. (c, f) XRD patterns. Insets show the crystal structures of the corresponding MOFs. (d, g) N<sub>2</sub> adsorption/desorption measurements. The curve of UiO-66 exhibit a typical microporous isotherm with a BET surface area of 1376 cm<sup>2</sup> g<sup>-1</sup> and a microporous volume of 0.55 cm<sup>3</sup> g<sup>-1</sup>. The isotherm of UiO-67 show an adsorption/desorption step at ca. 0.1 P/P<sub>0</sub> due to presence of two types of pores (see supplementary Table 1). The calculated BET surface area is 2000 cm<sup>2</sup> g<sup>-1</sup> and microporous volume is 0.7 cm<sup>3</sup> g<sup>-1</sup>. (e, h) SEM images..... 45

|  |    |
|--|----|
| <b>Figure 2-10</b> FT-IR spectra of (a) pristine UiO-66, activated UiO-66 and LPC@UiO-66, (b) pristine UiO-67, activated UiO-67 and LPC@UiO-67.....  | 47 |
| <b>Figure 2-11</b> Arrhenius plot of LPC liquid electrolyte and calculated activation energy for ionic conduction.....   | 49 |
| <b>Figure 2-12</b> Spectroscopic investigation of LPC@MOFs electrolytes. (a) Raman spectra of PC, LPC, PC@HKUST-1, and LPC@HKUST-1. (b) FT-IR spectra of PC, LPC, PC@HKUST-1, and LPC@HKUST-1. (c) Raman spectra of PC@MOF-5 and LPC@MOF-5. (d) Comparison of the activation energies of four LPC@MOFs electrolytes (LPC@HKUST-1, LPC@UiO-66, LPC@UiO-67, and LPC@MOF-5) and two liquid-in-solid conductors ((LPC@CB[6]) <sup>28</sup> and LPC@MCM-48) vs. their pore sizes, indicating the effect of pore size and OMS on their activation energy. The pore size of LPC@UiO-66 and LPC@UiO-67 are averaged based the pore diameter of their bi-continuous pore channels.....  | 50 |
| <b>Figure 2-13</b> FT-IR spectra of (a) PC and 1M LPC, (b) PC@HKUST-1 and LPC@HKUST-1..  | 53 |
| <b>Figure 2-14</b> FT-IR spectra of Cu(ClO <sub>4</sub> ) <sub>2</sub> ·6H <sub>2</sub> O and Cu(ClO <sub>4</sub> ) <sub>2</sub> ·xH <sub>2</sub> O, where 2<x<4.....  | 54 |
| <b>Figure 2-15</b> (a) Cubic structure of MOF-5 (Zn <sub>4</sub> O(BDC) <sub>3</sub> ) in a ball-and-stick model (purple: Zn, red: oxygen, black: carbon), in which oxo-centered (μ <sub>4</sub> -O) Zn <sub>4</sub> tetrahedra are interconnected through BDC to yield a highly porous framework with pore aperture of 8 Å and pore diameter of 12 Å. <sup>59, 60</sup> (b) N <sub>2</sub> adsorption/desorption isotherms of MOF-5. The pristine MOF-5 exhibits higher BET surface area of 1810 m <sup>2</sup> g <sup>-1</sup> and pore volume of 0.75 cm <sup>3</sup> g <sup>-1</sup> compared with HKUST-1. (c) SEM image of MOF-5. (d) XRD patterns of simulated, pristine, activated, and LPC infiltrated MOF-5. The major crystal structure is unaltered, except for the change of a few peak intensities due to the presence of guest molecules. <sup>61</sup> ..... | 55 |

**Figure 2-16** Arrhenius plots of LPC@CB[6],<sup>28</sup> LPC@MOF-5, and LPC@MCM-48. The plot of LPC@CB[6] is linearly fitted based on conductivity data reported in the reference, resulting in an activation energy different from the reported value. .... 56

**Figure 2-17** Synthesized MCM-48 mesoporous silica (a) N<sub>2</sub> adsorption/desorption isotherms (BET surface area: 1301 cm<sup>2</sup> g<sup>-1</sup>, total pore volume: 0.85 cm<sup>3</sup> g<sup>-1</sup>). (b) BJH pore size distribution. MCM-48 was prepared according to a method reported in the literature.<sup>62</sup> ..... 57

**Figure 2-18** Electrochemical performance of LPC@MOF electrolyte and prototype lithium-based batteries. (a) Cyclic voltammetry (CV) comparison between LPC@UiO-67 pellet and LPC electrolytes. (b) Flammability test of a LPC@UiO-67 electrolyte pellet. (c) Photograph of a LPC@UiO-67/PTFE membrane (LPC@UM) next to a coin cell (inset shows a bent LPC@UM). (d) SEM images of LPC@UM (top-left: cross-sectional view). (e) Current-time profile for Li|LPC@UM|Li cell at 20 mV of polarization (inset: impedance spectra at initial and steady states). (f) Li symmetric cell test comparison between LPC@UM and LPC at a current density of 0.125 mA cm<sup>-2</sup> (0.25 mAh cm<sup>-2</sup>). (g) Galvanostatic long-cycle stability tests at 1 C (1 C=170 mA g<sup>-1</sup>, initially cycled at 0.2, 0.5, 1, and 2 C for five cycles each) of prototype LiFePO<sub>4</sub>|Li batteries with LPC@UM electrolyte and LPC liquid electrolyte. (h) Long-term cycling stability of prototype LiFePO<sub>4</sub>|Li<sub>4</sub>Ti<sub>5</sub>O<sub>12</sub> batteries with LPC@UM electrolyte and LPC liquid electrolyte at 5 C (first two cycles at 1 C). .... 59

**Figure 2-19** Cyclic voltammetry of stainless steel|electrolyte|Li with (a) LPC@HKUST-1, (b) LPC@UiO-66, (c) LPC@UiO-67, (d) LPC@MIL-100-Al, (e) LPC@MIL-100-Cr and (f) LPC@MIL-100-Fe at 0.5 mV s<sup>-1</sup> between -0.2 to 5 V vs. Li/Li<sup>+</sup>..... 60

**Figure 2-20** Flammability test for PP separator saturated with LPC..... 61

**Figure 2-21** DC miropolarization of Li|LPC@UM|Li cell from 2.5 to 50 uA cm<sup>-2</sup>..... 62



**Figure 2-22** Li symmetric cell using LPC@UM electrolyte at (a-c) 0.25 mAh cm<sup>-2</sup> (0.125 mA cm<sup>-2</sup>), (d) 0.5 mAh cm<sup>-2</sup> (0.25 mA cm<sup>-2</sup>) and (e) 1 mAh cm<sup>-2</sup> (0.5 mA cm<sup>-2</sup>) ..... 62

**Figure 2-23** Typical voltage-capacity curves of LPC@UM electrolyte in LiFePO<sub>4</sub>|Li cells at various rates. .... 64

**Figure 3-1** Schematic drawing and photograph showing *in-situ* growth of MOF on bare glass fiber separator..... 83

**Figure 3-2** SEM images of (a) glass fiber (GF, inset shows the pictures of white GF and yellowish MOF/GF) and (b) MOF/GF composite separator (MOG). (c) XRD patterns of MOF, GF and MOG (bottom of the figure: simulated pattern for MOF). (d) FT-IR spectra of MOF, GF and MOG.. 85

**Figure 3-3** N<sub>2</sub> adsorption/desorption isotherms (insets: pore size distribution curves) of (a) MOG and (b) GF. .... 85

**Figure 3-4** Measurement of Li<sup>+</sup> transference number by potentiostatic polarizations of Li|Li symmetric cells using GF and MOG, where the insets show the EIS before and after polarization. (b) Temperature dependent conductivities of electrolyte saturated GF and MOG, the activation energies were obtained from linear fittings of Arrhenius equation. CV curves of stainless steel|Li cells using (c) GF and (d) MOG. The tests were performed between -0.2 to 5 V (vs. Li/Li<sup>+</sup>) at sweep rate of 1 mV s<sup>-1</sup>. .... 86

**Figure 3-5** Li<sup>+</sup> transference number of liquid electrolyte in GF separator..... 87

**Figure 3-6** (a) Polarization characterization of Li stripping and plating tests in Li|Li cells using GF and MOG (3 mA h cm<sup>-2</sup> for each cycle at 1.5 mA cm<sup>-2</sup>). (b) Coulombic efficiency evaluation of Li stripping and plating process in Cu|Li cells (2 mA h cm<sup>-2</sup> for each discharge at 1 mA cm<sup>-2</sup>). (c) Galvanostatic cycling of LiFePO<sub>4</sub>|Li cells using GF and MOG at current density of 1C (2.5 mA

cm<sup>-2</sup>). (d) Long-term cycling of LiFePO<sub>4</sub>|Li<sub>4</sub>Ti<sub>5</sub>O<sub>12</sub> full cells using GF and MOG at current density of 0.5C (4 mA cm<sup>-2</sup>) ..... 88

**Figure 3-7** Typical voltage-capacity plots of LiFePO<sub>4</sub>|Li<sub>4</sub>Ti<sub>5</sub>O<sub>12</sub> full cells using GF and MOG at 0.5C (4 mA cm<sup>-2</sup>)..... 89

**Figure 4-1** (a) Representative topology structure of UiO-66-NH<sub>2</sub> (MOF) constructed from organic linkers (grey sticks) bridged metal clusters (purple polyhedron). (b) Illustration showing creation of unsaturated metal sites by dehydration (thermal activation) of capped hydroxyl on Zr<sup>4+</sup> centers. (c) Schematic drawing of hybrid electrolyte containing MOF and liquid electrolyte (LE) in electrochemical device..... 100

**Figure 4-2** (a) SEM image of as-synthesized MOF. (b) As-synthesized and simulated XRD patterns of MOF. (c) N<sub>2</sub> adsorption/desorption isotherms of MOF (inset: pore size distribution derived from DFT model). (d) Photograph: the vial in the left of is activated MOF, the vial in the right is 0.2MOF@LE prepared by blending MOF with LE..... 101

**Figure 4-3** Temperature dependent conductivities of LE (LPC and LPF) and 0.2MOF@LE (0.2MOF@LPC and 0.2MOF@LPF)..... 101

**Figure 4-4** Measurements on Li<sup>+</sup> transference number of LE and 0.2MOF@LE using potentiostatic polarization (insets: EIS curves of Li symmetric cells before and after polarization) ..... 103

Figure 4-5 (a) Li<sup>+</sup> transference number, ionic conductivity and thermal activation energy of LE and 0.2MOF@LE. Comparison of CV curves at sweep rate of 1 mV s<sup>-1</sup> between -0.2 to 5 V vs. Li/Li<sup>+</sup>: (b) LPC and 0.2MOF@LPC, (c) LPF and 0.2MOF@LPF. (d) FT-IR spectra of as-synthesized MOF, activated MOF, LPC@MOF and LPF@MOF..... 104

|   |     |
|---|-----|
| <b>Figure 4-6</b> FT–IR spectra of as-synthesized MOF, activated MOF, LPC@MOF and LPF@MOF in wavenumber between 900 to 2000 $\text{cm}^{-1}$ .....  | 105 |
| <b>Figure 4-7</b> Li Li symmetric cells in (a) LPC and 0.2MOF@LPC, and (b) LPF and 0.2MOF@LPF for Li stripping and plating tests at 0.25 $\text{mA cm}^{-2}$ (time interval: 1 h). (c) LFP Li cells using LPC and 0.2MOF@LPC at current density of 5C (1.5 $\text{mA cm}^{-2}$ ). (d) NCM Li cells using LPF and 0.2MOF@LPF at current density of 2C (2 $\text{mA cm}^{-2}$ ) .....   | 106 |
| <b>Figure 4-8</b> Long term Li stripping and plating tests under 0.25 $\text{mA cm}^{-2}$ using LPF and 0.2MOF@LPF .....  | 107 |
| <b>Figure 4-9</b> XPS analysis of Li collected from Li Li cells after cycling at 0.25 $\text{mA cm}^{-2}$ for 100 h. (a) C1s, (b) Li1s, (c) Zr3d, (d) Cl2p .....  | 109 |
| <b>Figure 5-1</b> (a) Structure representation of two types of mesoporous cages in MIL-100(Al) and Illustration of OMS evolution in a metal trimer unit of MIL-100(Al) serial MOFs (orange atoms Al, red atoms O, grey atoms C, green atoms anionic ligands). (b) Schematic showing ion distribution in bare liquid electrolyte and in liquid electrolyte with MOF. (c) SEM image of as-synthesized MOF. (d) $\text{N}_2$ adsorption/desorption isotherms (inset: pore size distribution diagram). (e) Basic electrolyte properties (conductivity and activation energy) of baseline electrolyte and nanofluidic electrolyte. (f) Two-electrode CV tests comparing the $\text{Li}^+$ stripping/plating kinetics | 122 |
| <b>Figure 5-2</b> XRD pattern of as-synthesized, activated and LP40 complexed MIL-100(Al).....  | 123 |
| <b>Figure 5-3</b> Arrhenius plots (temperature dependent conductivity) of LP40 and nanofluidic electrolyte.....   | 125 |
| <b>Figure 5-4</b> Potentiostatic polarizations of LP40 and nanofluidic electrolyte in symmetric Li-Li cell configuration (insets: EIS measurements before and after polarizations) .....  | 125 |
| <b>Figure 5-5</b> $\text{Li}^+$ transference number of LP40 and nanofluidic electrolyte.....  | 125 |

|  |     |
|--|-----|
| <b>Figure 5-6</b> Two-electrode CV evolutions of first 5 cycles for (a, b) LP40, (c, d) 0.125Al@LP40, (e, f) 0.25Al@LP40.....  | 126 |
| <b>Figure 5-7</b> Three-electrode CV comparison between LP40 and 0.125Al@LP40.....   | 127 |
| <b>Figure 5-8</b> (a) Weight percentages of MOF, LiPF <sub>6</sub> and solvents (EC/DEC) for nanofluidic electrolyte (0.125Al@LP40) and LP40@MOF. (b) TGA curves of LP40 and LP40@MOF....  | 128 |
| <b>Figure 5-9</b> LP40 and NE comparison in (a) FT-IR. (b) Static <sup>7</sup> Li and (c) <sup>19</sup> F NMR spectra. (d) Evaluation of diffusion polarization by rate performance of double layer capacitors. (e) Evaluation of reaction kinetics by exchange current density derived from stepped D.C. micropolarization (Li-Li symmetric cells).....   | 129 |
| <b>Figure 5-10</b> FT-IR spectra of pristine and activated MIL-100(Al).....  | 131 |
| <b>Figure 5-11</b> Voltage-time curves of double layer capacitors using LP40 and nanofluidic electrolyte at different rates.....   | 133 |
| <b>Figure 5-12</b> Stepped D.C. micropolarization of Li-Li symmetric cells using LP40 and nanofluidic electrolyte.....   | 133 |
| <b>Figure 5-13</b> LP40 and NE device performances in (a) Li Li symmetric cells at 0.5 mAh cm <sup>-2</sup> . (b) Li Cu asymmetric cells at 0.25 mAh cm <sup>-2</sup> . (c) NCM Li cells at 0.3C (1C=160 mA g <sup>-1</sup> ) with upper voltage of 4.3V. (d) Rate performance of NCM Li cells (4.3 V). (e) NCM Li cells at 0.3C (1C=250 mA g <sup>-1</sup> ) with upper voltage of 4.8V. (f) NCM graphite full cells at 0.3C with upper voltage of 4.7 V..... | 134 |
| <b>Figure 5-14</b> Rate performances of NCM-Li cells using LP40 and nanofluidic electrolyte at upper voltage of (a, b) 4.3V and (c, d) 4.8V.....   | 136 |
| <b>Figure 5-15</b> Post-cycle evaluations of Li-Li cells using LP40 and NE after 300 hours' operation at 0.5 mAh cm <sup>-2</sup> : (a) SEM images, (b) Electrochemical impedance spectroscopy of cycled cells,  |     |

and (c) XPS analysis of cycled Li. (d) Activation energy of charge transfer resistance derived from NCM-Li cells employing LE and NE..... 139

**Figure 5-16** SEM images of Li harvested from NCM-Li cells using (a, b) LP40 and (c, d) nanofluidic electrolyte (0.125Al@LP40) after 50 cycles at 0.3C and 4.3V..... 140

**Figure 5-17** SEM images of Li harvested from NCM-Li cells using (a, b) LP40 and (c, d) nanofluidic electrolyte (0.125Al@LP40) after 50 cycles at 0.3C and 4.8V..... 141

**Figure 5-18** SEM of pristine NCM electrode..... 143

**Figure 5-19** XRD patterns of pristine NCM electrode and NCM electrodes harvested from cycled NCM-Li cells using LP40 and nanofluidic electrolyte (50 cycles at 0.3C and 4.3V)..... 143

**Figure 5-20** (a) SEM and (b-d) EDS mappings of NCM electrode collected from NCM-Li cell using nanofluidic electrolyte. MOF distribution was confirmed by SEM equipped with EDS. Microspherical NCM composed by secondary nanoparticles could be identified by Ni mapping. Moreover, MIL-100(Al) spreading on NCM is confirmed by Al signals. .... 144

**Figure 5-21** SEM images of NCM cathode electrodes collected from NCM-Li cells using (a, b) LP40 and (c, d) 0.125Al@LP40 after 50 cycles at 0.3C and 4.3V. MOF containing organic component could be recognized by low contrast under electron beam irradiation under vacuum. .... 144

**Figure 5-22** SEM images of NCM cathode electrodes collected from NCM-Li cells using (a, b) LP40 and (c, d) 0.125Al@LP40 after 50 cycles at 0.3C and 4.3V. .... 145

**Figure 5-23** HRTEM and SEAD images of NCM electrodes harvested from cycled NCM-Li cells using (a, b) LP40 and (c, d) nanofluidic electrolyte (50 cycles at 0.3C and 4.3V)..... 146

|   |     |
|---|-----|
| <b>Figure 5-24</b> XPS signals from cycled NCM electrodes (50 cycles at 0.3C) harvested from NCM-Li cells using LP40 and nanofluidic electrolyte (0.125Al@LP40): F1s at (a) 4.3V, (b) 4.8V; Ni2p at (c) 4.3V, (d) 4.8V.....   | 147 |
| <b>Figure 5-25</b> Schematic drawings depicting solvated Li <sup>+</sup> travel from bulk electrolyte to electrode at (a) liquid electrolyte (LE), and (b) nanofluidic electrolyte (NE). .....  | 147 |
| <b>Figure 5-26</b> Temperature dependent EIS curves of NCM-Li cells using LP40 and nanofluidic electrolyte.....   | 148 |
| <b>Figure 6-1</b> Illustrative configuration of electrode structure and components. ....  | 162 |
| <b>Figure 6-2</b> The cyclic voltammetry of (a) NCM cathode (LiNi <sub>0.33</sub> Co <sub>0.33</sub> Mn <sub>0.33</sub> O <sub>2</sub> , reference electrode, denoted as REF) and (b) NCM cathode with MOF additive (high-performance electrode, abbreviated as HPE) at a variety of sweep rate, where metallic Li were used as both reference and counter electrodes. .... | 162 |
| <b>Figure 6-3</b> Long-term cycling performance comparison between REF and HPE using NCM-NCM symmetric cell configurations. ....  | 164 |
| <b>Figure 6-4</b> Evolution comparison of electrochemical impedance spectroscopy (EIS) between REF and HPE. ....  | 165 |
| <b>Figure 6-5</b> (a) Cycling performance comparison between REF and HPE using graphite-graphite (C-C) symmetric cell configurations. (b) Cycling performance comparison between REF and HPE using Li <sub>4</sub> Ti <sub>5</sub> O <sub>12</sub> - Li <sub>4</sub> Ti <sub>5</sub> O <sub>12</sub> symmetric cell configurations. ....                                    | 166 |
| <b>Figure 6-6</b> Evolution comparison of electrochemical impedance spectroscopy (EIS) between REF and HPE for graphite anodes.....   | 167 |
| <b>Figure 6-7</b> Evolution comparison of electrochemical impedance spectroscopy (EIS) between REF and HPE for LTO anodes.....  | 167 |

**Figure 6-8** The cyclic voltammetry of (a) graphite anode and (b) graphite anode with MOF additive at a variety of sweep rate, where metallic Li were used as both reference and counter electrodes. .... 168

**Figure 6-9** The cyclic voltammetry of (a) LTO anode and (b) LTO anode with MOF additive at a variety of sweep rate, where metallic Li were used as both reference and counter electrodes... 168

**Figure 6-10** Cycling performance comparisons between REF and HPE using NCM-C full cell configurations at different rates..... 169

**Figure 6-11** Cycling performance comparisons between REF and HPE using NCM-C pouch cell. .... 170

## List of Tables

|   |     |
|---|-----|
| <b>Table 1-1</b> Theoretical (Th.) and approximate practical (Pr.) specific (Sp.) energies of rechargeable batteries (theoretical values based on the masses of active electrode–electrolyte materials only; practical values based on mass of battery pack) <sup>4</sup> ..... | 2   |
| <b>Table 1-2</b> Comparison of the theoretical specific capacity, charge density, volume change and onset potential of various anode materials.....   | 3   |
| <b>Table 2-1</b> MOFs selected to synthesize electrolytes with biomimetic ionic channels. ....  | 41  |
| <b>Table 2-2</b> Ambient conductivities and activation energies of various LPC@MOF electrolytes. 46   |     |
| <b>Table 2-3</b> Major peak assignments for pristine/activated UiO-(66/67) and LPC@UiO-(66/67) electrolytes. ....   | 47  |
| <b>Table 2-4</b> Detailed peak assignments for Raman spectra of PC, LPC, activated HKUST-1, <sup>44</sup> PC@HKUST-1, and LPC@HKUST-1. <sup>a</sup> .....   | 51  |
| <b>Table 2-5</b> Vibration of ClO <sub>4</sub> group as a function of symmetry. <sup>48, 49a</sup> .....  | 52  |
| <b>Table 5-1</b> Summary of weight contribution and estimated formula for nanofluidic electrolyte (0.125Al@LP40) and LP40@MOF. ....   | 129 |
| <b>Table 5-2</b> Diffusion coefficients of electrolyte components from NMR DOSY .....   | 132 |
| <b>Table 5-3</b> Evolution of capacity fading rate for NCM-Li cells using LP40 and nanofluidic electrolyte, liquid electrolyte was replenished for all cells after 50 cycles at 0.3C. ....  | 138 |
| <b>Table 5-4</b> Ohmic resistance and interfacial resistance (SEI resistance plus charge transfer resistance) of Li-Li fresh cells and cycled cells using LP40 and nanofluidic electrolyte. ....  | 142 |
| <b>Table 6-1</b> Performance improvements of electrodes using MOF additives.....  | 168 |



## ACKNOWLEDEMENTS

This is a truly tough yet enjoyable journey, I have reached a special moment in my life and here at UCLA I prepared myself for being an independent researcher. I'm indebted to numerous people who provide supports and accompanies along the way. It's impossible to accomplish the dissertation without them.

First and foremost, I would like to express my sincere gratitude to my advisor, Prof. Yunfeng Lu, for offering the incredible research opportunities. He is such an amazing mentor that I could clearly recall those memorable moments we spent together. His passion, imagination, rigorousness and thoughtfulness sharpen my professional skills; His encouragements help me get through those experimental roadblocks; He teaches me learn to be a humble man before pursuing knowledge; He enlightens me the importance of leadership and teamwork; He drives me to think fundamentally and critically; He presents me the grand picture for being a scientist with strong sense of responsibility to the society. Too much thanks beyond words to express my appreciations.

I would also like to thank the valuable help and discussions on my dissertation works from my Ph.D. committee: Prof. Harold Monbouquette, Prof. Dante Simonetti and Prof. Suneel Kodambaka. Additional thanks to my formal committee members, Prof. Robert Hicks and Prof. Qibing Pei, for their guidance at early stage of my doctoral works. I'm grateful to our collaborators Prof. Jeffrey Zink and his Ph.D. student Jonathan Brosmer, who made significant contribution to the understanding of my research works. Moreover, I would like to thank Prof. Bruce Dunn for guiding me in the area of electrochemistry and his valuable suggestions on my doctoral works.

Many thanks to my dear group members at UCLA. Thank you, Yanhua, for introducing me to the group. Thank you, Fang, for helping me patiently on familiarizing the labs. Thank you, Prof. Hao Bin Wu, for those insightful advices and guidance on technical writing. Prof. Jian Zhu,

Huihui, Zhe, Jing, Gen, Lu, Runwei, Chaoyong, Haiping, Jianqiang, Zaiyuan, Xinru, Shuning, Fei, Xu, Xiaomin, Zheng, Addis, Gurong, Xiaoyan, Zhuang, Duo, Di, Jie, Xianyang, Ping, Yilong, you guys mean a lot to me. I also would like to thank the supports from our junior graduate students, especially Chen, Shengxiang, and Wenye. I would also like to thank those who guided my basic academic trainings at Central South University, especially Prof. Zhixing Wang, Prof. Huajun Guo, Dr. Jiexi Wang and Dr. Bing Huang.

Finally, special thanks to my family, I'm the blessed and lucky one who was born in this wonderful family. My parents and elder sister are always being extremely supportive. Especially, my dad, your attitude towards challenges and the sacrifices you have made for the family continuously drive me forward.

Mom and Dad, I love you!

## VITA

### Education:

2009-2013      B. S., Metallurgical Engineering, Central South University, China

### Publications:

1. **L. Shen**, F. Liu, G. Chen, H. Zhou, Z. Le, H. B. Wu\*, G. Wang, Y. Lu\*. Encapsulation of SnO<sub>2</sub> nanocrystals into hierarchically porous carbon by melt infiltration for high-performance lithium storage. *Journal of Materials Chemistry A*, 2016, 4.48: 18706-18710.
2. F. Liu, Q. Xiao, H. B. Wu, F. Sun, X. Liu, F. Li, Z. Le, **L. Shen**, G. Wang, C. Mei, Y. Lu\*. Regenerative Polysulfide-Scavenging Layers Enabling Lithium–Sulfur Batteries with High Energy Density and Prolonged Cycling Life. *ACS nano*, 2017, 11.3: 2697-2705.
3. F. Liu, Q. Xiao, H. B. Wu, **L. Shen**, D. Xu, M. Cai, Y. Lu\*. Fabrication of Hybrid Silicate Coatings by a Simple Vapor Deposition Method for Lithium Metal Anodes. *Advanced Energy Materials*, 2017.
4. **L. Shen**, H. B. Wu, F. Liu, J. L. Brosmer, G. Shen, X. Wang, J. I. Zink, Q. Xiao, M. Cai, G. Wang\*, Y. Lu\*, B. Dunn\*. Creating Lithium-Ion Electrolytes with Biomimetic Ionic Channels in Metal–organic Frameworks. *Advanced Materials*, 2018. (in press)
5. **L. Shen**, Y. Lu\* *et al.* Metal–organic Frameworks Enabled Tethered Anion Separator for Durable Lithium Rechargeable Batteries. (ready for submission)
6. **L. Shen**, Y. Lu\* *et al.* Improving Li<sup>+</sup> Transference Number of Liquid Electrolyte by Metal–organic Frameworks. (ready for submission)
7. **L. Shen**, Y. Lu\* *et al.* Nanofluidic Electrolyte with Versatile Electrolyte Modulator for High-Performance Lithium Batteries. (ready for submission)

8. **L. Shen**, Y. Lu\* *et al.* Metal–organic Frameworks as Electrode additives for High-Performance Lithium Ion Batteries. (in preparation)

**Patent:**

M. Cai, Y. Lu, L. Yang, F. Dai, J. Shen, A. Fuhr, **L. Shen**. Electrolyte structure for metal batteries. U.S. Patent Application No. 15/055,306.

# Chapter 1 Background and Introduction

## 1.1 Overview of Energy Storage Supplies

The second industrial revolution triggered by electricity and internal combustion engine has a profound impact on advancement of human civilization. Life's comforts over the past two centuries have been largely derived from the discovery and exploitation of fossil fuel. With the burgeoning growth of global population and rising demand of energy supply, it could be speculated that the ultimate depletion of natural non-renewable energy sources would take place within the next several hundreds of years. As a primary power source for transportation, the state vulnerability on fossil fuel imports and the warming climate result from CO<sub>2</sub> emission have driven the politicians and scientists to harness a viable alternative energy supply for sustainable development.<sup>1</sup> Renewable energy sources from solar, wind, nuclear, hydropower, *etc.* are under meticulous consideration and intense investigations. The regenerative electric power has long been regarded as a feasible displacement for conventional carbon-laden fuels.

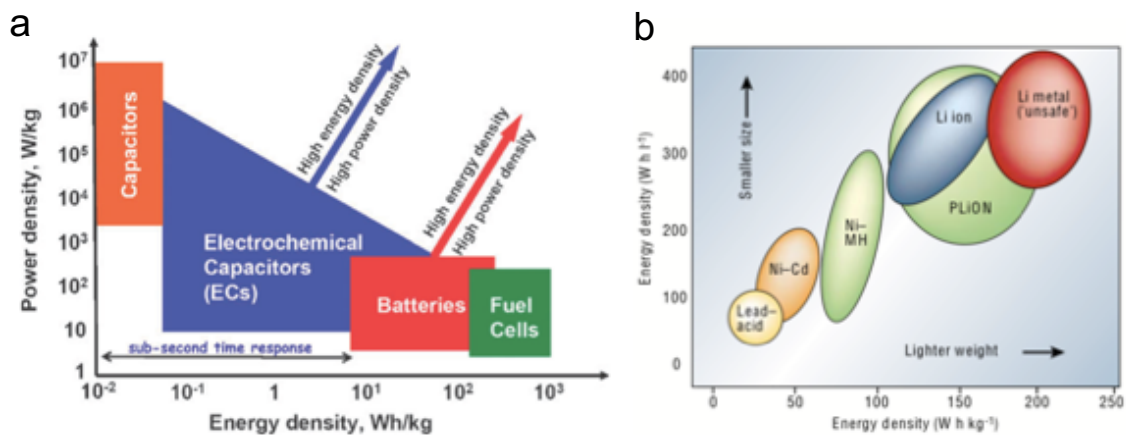


**Figure 1-1** (a) Comparison of the operational characteristics of energy storage and conversion devices. (b) Comparison of the different battery technologies in terms of volumetric and gravimetric energy density

Therefore, the development and advancement of energy storage and conversion materials are of interest and significance. One promising technology is electrochemical devices. As compared in **Figure 1-1a**, from the prospective of energy density, fuel cell is regarded as one of the ultimate energy storage candidates.<sup>2</sup> Since the fuel cells that convert fuel into electricity with oxidizing agent possess so far the highest energy density. Yet it's hindered by lacking of breakthroughs in the fuel storage materials and by high cost for further development and commercialization.<sup>3</sup> By comparison, there are notable improvements of simultaneously energy density and power density in electrochemical capacitors and batteries, especially in battery technologies.

**Figure 1-1b** depicts the energy density comparison of different battery technologies.<sup>5</sup> The lithium batteries have remarkable advantages over conventional batteries in terms of energy density. As a high performance and environmental benign battery, lithium rechargeable batteries have been widely used and dramatically transformed today's life. Portable battery power used in cell phones, laptops, digital cameras, etc., stationary rechargeable batteries employed as back up electricity storage in smart grid and hybrid electric vehicles (HEV). However, the state-of-the-art lithium ion batteries, with a specific energy density of  $150 \text{ W h kg}^{-1}$  (pack-level), do not yet have sufficient energy density to compete the gasoline-powered automobiles with long driving range between rapid and convenient fuel refills.<sup>4</sup>

**Table 1-1** Theoretical (Th.) and approximate practical (Pr.) specific (Sp.) energies of rechargeable batteries (theoretical values based on the masses of active electrode–electrolyte materials only; practical values based on mass of battery pack)<sup>4</sup>

| System                      | Anode                          | Cathode   | OCV (V)   | Th. Sp. Cap. (Ah kg <sup>-1</sup> ) | Th. Sp. En (Wh kg <sup>-1</sup> ) | Pr. Sp. En (Wh kg <sup>-1</sup> ) |
|-----------------------------|--------------------------------|---|-----------|-------------------------------------|-----------------------------------|-----------------------------------|
| Lead-acid                   | Pb                             | PbO <sub>2</sub>  | 2.1       | 83                                  | 171                               | 20-40                             |
| Ni-Cd                       | Cd                             | NiOOH   | 1.35      | 162                                 | 219                               | 20-40                             |
| Ni-MH                       | MH                             | NiOOH   | 1.35      | ~178                                | ~240                              | 50-70                             |
| Na-S (350°C)                | Na                             | S   | 2.1-1.78  | 377                                 | 754                               | ~120                              |
| Na-MCl <sub>2</sub> (300°C) | Na                             | NiCl <sub>2</sub>   | 2.58      | 305                                 | 787                               | ~90                               |
| Li-ion (1)                  | Li <sub>x</sub> C <sub>6</sub> | Li <sub>1-x</sub> CoO <sub>2</sub> (layered)  | 4.2-3.0   | 158                                 | 584                               | 100-150                           |
| Li-ion (2)                  | Li <sub>x</sub> C <sub>6</sub> | Li <sub>1-x</sub> Mn <sub>2</sub> O <sub>4</sub> (spinel)                               | 4.2-3.0   | 104                                 | 424                               | 80-100                            |
| Li-ion (3)                  | Li <sub>x</sub> C <sub>6</sub> | Li <sub>1-x</sub> FePO <sub>4</sub> (olivine)   | 3.4 (3.4) | 117                                 | 398                               | 80-100                            |
| Li-ion (4)                  | LTO                            | Li <sub>1-x</sub> Mn <sub>2</sub> O <sub>4</sub> (spinel)                               | 2.5 (2.5) | 80<br>(x=1.0)                       | 200                               | 50-70                             |
| Li-ion (5)                  | Li <sub>x</sub> C <sub>6</sub> | Advanced spinel<br>Li <sub>1-x</sub> Mn <sub>1.5</sub> Ni <sub>0.5</sub> O <sub>4</sub> | 4.7       | 104<br>(x=1.0)                      | 690                               | Lab                               |
| Li-ion (6)                  | Li <sub>x</sub> C <sub>6</sub> | Advanced layered<br>Li <sub>1-x</sub> MO <sub>2</sub>                                   | 3.7       | 160<br>(x=1.0)                      | 592                               | Lab                               |
| Li-ion (7)                  | Li <sub>y</sub> Si             | Advanced layered<br>Li <sub>1-x</sub> MO <sub>2</sub>                                   | 3.2       | 263<br>(x=1.0)                      | 843                               | Lab                               |

**Table 1-2** Comparison of the theoretical specific capacity, charge density, volume change and onset potential of various anode materials

| Materials  | Li   | C                | Li <sub>4</sub> Ti <sub>5</sub> O <sub>12</sub> | Si                   | Sn                   |
|--|------|------------------|---|----------------------|----------------------|
| Density (g cm <sup>-3</sup> )  | 0.53 | 2.25             | 3.5   | 2.33                 | 7.29                 |
| Lithiated phase  | Li   | LiC <sub>6</sub> | Li <sub>7</sub> Ti <sub>5</sub> O <sub>12</sub> | Li <sub>4.4</sub> Si | Li <sub>4.4</sub> Sn |
| Theoretical gravimetric capacity (mA h g <sup>-1</sup> )                   | 3862 | 372              | 175   | 4200                 | 994                  |
| Theoretical volumetric density (unlithiated state, mA h cm <sup>-3</sup> ) | 2047 | 837              | 613   | 9786                 | 7246                 |
| Volume change (%)  | 100  | 12               | 1   | 320                  | 260                  |
| Potential vs. Li (~V)  | 0    | 0.05             | 1.6   | 0.4                  | 0.6                  |

Advances in anodes and cathodes are anticipated, so far, to double the current state-of-the-art energy density ( $300 \text{ W h kg}^{-1}$ ), as can be seen from **Table 1-1**, current advanced layered or spinal cathode with higher operating voltage or affordable specific capacity, like  $\text{Li}_{1-x}\text{Mn}_{1.5}\text{Ni}_{0.5}\text{O}_4$  and  $\text{Li}_{1-x}\text{MO}_2$ , delivering theoretical energy density around  $600 \sim 850 \text{ W h kg}^{-1}$ . **Table 1-2** shows some representatives from each type of anodes for comparison.<sup>6</sup> The displacement of commercialized graphite with high-energy silicon or metallic Li anode materials is considered as an alternative strategy to boost the overall energy density. For instance, doubling the graphite capacity would give rise to 20% improvement in the whole capacity.<sup>7</sup> Metallic anode based battery systems theoretically doubles the energy density of lithium-ion batteries as shown in **Figure 1-2**.<sup>8</sup>

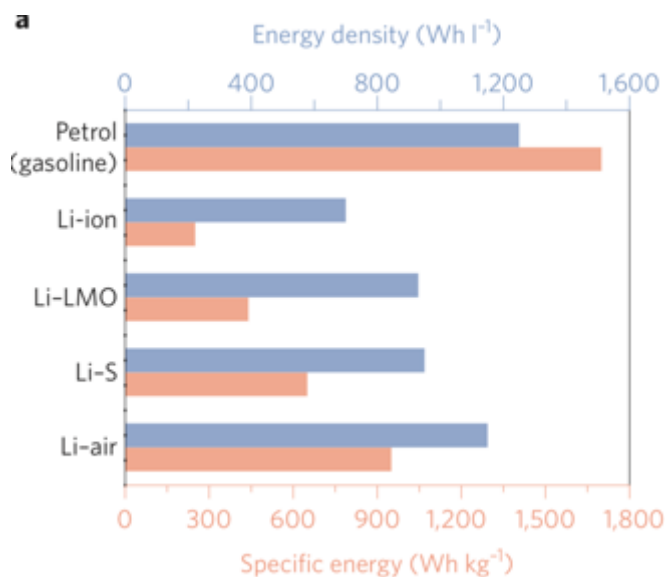


**Figure 1-2** Bar chart showing the practical specific energy (pink) and energy densities (blue) of petrol (gasoline) and typical Li batteries including the state-of-the-art Li-ion battery, the Li metal/LMO cell, Li-S and Li-air cells.



## 1.2 Operation of Batteries and Thermodynamics

**Figure 1-3** represents the illustrative scheme for the first commercialized lithium ion battery by Yoshino in 1990.<sup>9</sup> In principle, the cathode (oxidant) and anode (reductant) are working electrodes that are immersed in a liquid electrolyte, separated by an electronic isolating and ionic conductive membrane. On discharge state, the occurrences of chemical reactions are accompanied by transfer of lithium ion inside the cell and electron outside for charge compensation. The output on discharge is an external circuit current  $I$  at a voltage  $V$  for a time  $t$ .<sup>1, 10</sup> The charge process is opposite way for rechargeable lithium-ion batteries.

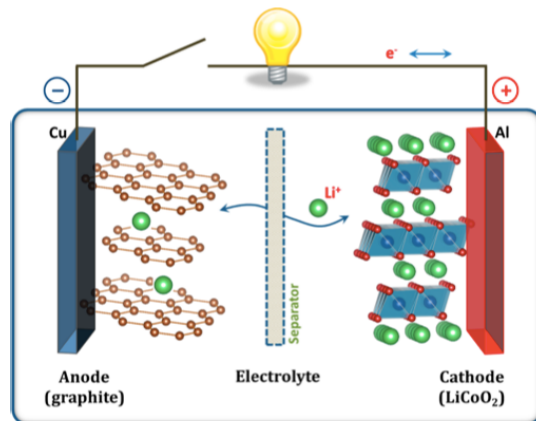
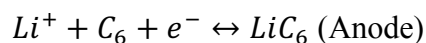
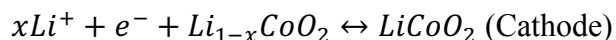


**Figure 1-3** Schematic illustration of the lithium-ion battery (LiCoO<sub>2</sub>|electrolyte|graphite)

This electrochemical energy conversion can be explicated from a fundamental thermodynamic viewpoint. Taking above battery as an example, the following chemical reaction would take place during charge and discharge process:



An ideal rechargeable or fully reversible battery should satisfy following conditions based on the thermodynamic concept of a “reversible process”<sup>11</sup>:

- 1) The chemical reactions must be reversible;
- 2) Energy conversion is reversible, suggesting that under extreme small current and steady state, the chemical reactions are under ideal equilibrium.

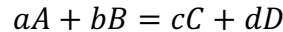
Using Gibbs free energy depicting the chemical energy difference for reactions, if the difference between the products Gibbs free energy with reactants Gibbs free energy is negative under standard state, thermodynamically we can deduce that this reaction can automatically take place.<sup>11</sup>

$$\Delta_r G = \sum r_i \Delta_f G_i$$

Overall, as indicated by thermodynamic principle, under constant temperature and pressure, if the battery chemical reactions are reversible, the reduction of Gibbs free energy is equal to the maximum output as electrical work:

$$\Delta_r G_{T,P} = -nEF$$

If we have reversible reaction:



$$\Delta_r G_m = \Delta_r G_m^\ominus + RT \ln \left( \frac{x_C^c x_D^d}{x_B^b x_A^a} \right)$$

$$E = E^\ominus - \frac{RT}{nF} \ln \left( \frac{x_C^c x_D^d}{x_B^b x_A^a} \right) \text{ (Nerst equation)}$$

$$E^\ominus = -\frac{\Delta_r G_m^\ominus}{nF} = \frac{RT}{nF} \ln k_x^\ominus$$

n: charge amount (molar, mol);

E: battery potential (volt, V);

F: Farady constant ( $9.65 \times 10^4$  C/mol)

$E^\ominus$ : Standard potential,  $k_x^\ominus$ : standard equilibrium constant;

### 1.3 Considerations of battery parameters

#### 1) Theoretical specific capacity

For a given redox electrode reaction, the theoretical specific gravimetric capacity can be calculated based on the following equations<sup>12, 13, 14</sup>:

$$nZF = It \text{ (Farady's law)}$$

$$Q_{theoretical} = \frac{zF}{3.6M} \text{ (mAh g}^{-1}\text{)}$$

z: amount of electron involved per molar active material;

F: Farady constant ( $9.65 \times 10^4$  C/mol, A·s/mol);

M: molar mas of active material (g/mol);

#### 2) Energy density and power density

The merits of a rechargeable cell are energy density and calendar life aside from cost and safety. The energy density can be obtained by measuring the time  $\Delta t_{discharge}$  for its complete discharge under constant current  $I_{dis} = dQ/dt$ :

$$E = \int_0^t V I dt = \int_0^q V dQ \text{ (Wh kg}^{-1}\text{)}$$

the specific power density  $W h L^{-1}$  can be calculated by  $E \cdot \rho$ , where  $\rho$  is the tap density or packing density for electrode materials.

#### 3) Coulombic efficiency

$$E = \frac{Q_{discharge}}{Q_{charge}} \text{ (\%)}$$

The Coulombic efficiency is primarily induced by irreversible process due to parasitic reactions, like electrolyte decomposition and SEI formations. Unstable SEI layer with electrolyte-permeable defects or cracks would result in continuous consumption of electrolyte and

deterioration of battery calendar life. For instance, lithium titanate ( $\text{Li}_4\text{Ti}_5\text{O}_{12}$ , LTO) with inferior gravimetric capacity yet high lithiation/delithiation potential (around 0.8-1 V) could achieve remarkable cyclicality and rate capability since substantial SEI formation would occur under 0.8 V vs Li/Li<sup>+</sup>. In comparison, for graphite anode, the SEI formation during first few cycles would lead to irreversible capacity loss (CE: 90-95 %), afterwards it would maintain high CE at around 99.5 % for subsequent cycles.

#### 4) Mass loading and electrode thickness

The electrode prepared from mixing the active materials, polymeric binder and conductive additive are fabricated via a slurry casting and drying technique. Mass loading typically indicates the average mass of active materials per area ( $\text{mg cm}^{-2}$ ) instead of whole electrode mass. The mass loading or electrode thickness would dramatically impact high-energy materials because high polarizations would be induced by poor ionic/electronic conductivity and lithium-plug SEI layer arises from mechanical instability once the thickness gets higher.<sup>15</sup> That explains why the thinner electrode and low mass loading might exhibit higher performance since the kinetics limitations are hindered by the electrode parameters.

## 1.4 Kinetics and Interface

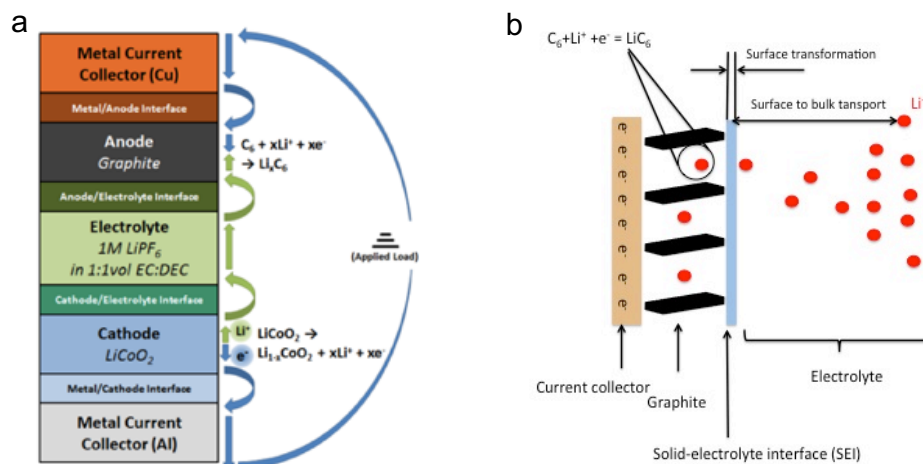
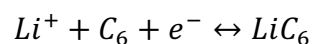


**Figure 1-4** (a) Schematic illustration of potential phases and interfaces in lithium-ion battery (LiCoO<sub>2</sub>|electrolyte|graphite). (b) Scheme of multistep of electrochemical process in electrode reaction

As illustrated **Figure 1-4a**, the general battery configuration consists of five components (two current collectors, two electrodes, one electrolyte), corresponding four interfaces, and more importantly two charge transfer resistance (electrons, lithium ions). **Figure 1-4b** and **Figure 5** reveals the series steps involved in an electrode reaction.<sup>11, 16</sup> Typically, (1) ion transport from bulk electrolyte to active material surface; (2) surface transformation from surface into bulk material; (3) redox reaction; (4) surface transformation from surface into electrolyte; (5) diffusion back to bulk electrolyte.

The key challenge for kinetics is to determine the control step and thereby manipulating the overall reaction rate. For instance,



When the lithium ions intercalate and deintercalate with the graphite under equilibrium, the reaction rate and corresponding current density (exchange current density) for intercalation and deintercalation are the same, suggesting the overall current is approaching to zero (ultra-small current density assumption). However, the real battery operation departs from the ideal equilibrium steady state. When applied a current to the electrode, the real reaction potential would also deviate from the equilibrium potential. The difference is called over potential and this phenomenon is known as polarization.

The degree of polarization is largely correlated with the current density. During charge and discharge, the difference between output/input voltages with open-circuit voltage is ascribed from polarization.

$$V_{discharge} = V_{oc} - \eta (q, I_{discharge})$$

$$V_{charge} = V_{oc} + \eta (q, I_{charge})$$

There are three types of polarizations<sup>16</sup>: (1) The resistance polarization, which can be attributable to the poorly conductive materials in battery system ( $\eta_r = IR$ ); (2) concentration polarization, which is induced by concentration difference due to a diffusion-limited step; (3) electrochemical polarization: the sluggish redox reaction rate or poor electronic conductivity caused inefficient as well as obstructed electron pathways.

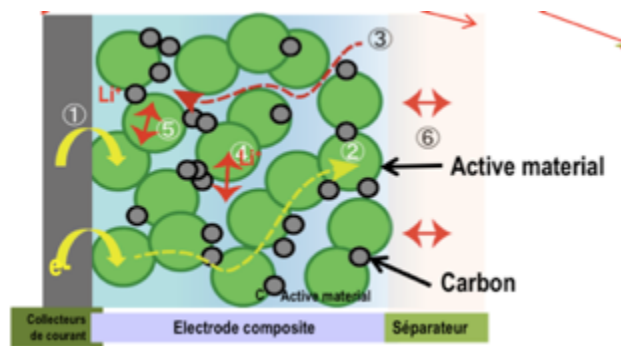


**Figure 1-5** Scheme for ionic and electronic pathways in an electrode

The polarization study is critical for high rate capability of electrode. In order to achieve high power output, the following kinetics should be optimized and improved: 1) ion transport in electrolyte; 2) ion transport in electrode; 3) electrochemical reaction in electrode; 4) electron conduction in the electrode and current collector.

As for ion transport, the battery system is configured in a layer-by-layer structure (**Figure 1-4a**). Assuming the solid electrolyte-electrode interface is not diffusion controlled and both electrode and separator are porous layers, the polarization associated with mass transport can be calculated by following equations<sup>17, 18</sup>:

$$T = \left(\frac{P\rho_m}{\rho_b}\right)^{1/2}, \sigma = \frac{1}{\rho_b}$$

$$\Delta E_{i,R} = i \frac{\rho_m l}{A}$$

$$\Delta E_{i,R} = \frac{i l T^2}{\sigma P A}$$

$l$ : Layer thickness;

$A$ : Area (transport face);

$i$ : Current;

$P$ : Volume fraction occupied by electrolyte in porous layer;

$\rho_m, \rho_b$ : the resistance of electrolyte through a porous layer and bulk electrolyte, respectively;

$\sigma$  is the electrolyte conductivity

$T$ : Tortuosity

$P$ : Porosity

Therefore, the polarization induced by diffusion can be alleviated by reducing the layer thickness, tortuosity, and increasing the electrolyte conductivity, porosity and facing area.

Generally, the reduction of thickness and increase of porosity are viable approaches for manipulative convenience.

Based on the assumption that negligible mass transfer in electrolyte due to the presence of excess supporting electrolyte, the rate of charge transfer on the surface of electrode can be described by Butler-Volmer equation:

$$i = i_0 [e^{a_0 f \eta} - e^{-a_R f \eta}]$$

$i_0$ : exchange current, zero net current at equilibrium with Faradaic activity,

$a_0$  and  $a_R$ : transfer coefficient of oxidation and reduction reactions

$f$ :  $f=F/RT$  (F: Faraday constant)

$\eta$ : overpotential,  $\eta=E-E_{eq}$

Ionic charge flux in an electrolyte can be described by

$$J_{Li^+} = Z_i F u_i C_i \frac{d\Phi}{dx}$$

$Z_i$ : charge of lithium ion

F: Faraday constant

$u_i$ : mobility of lithium ion,  $F \times u_i$  is the ionic conductivity

$C_i$ : concentration of lithium ion

$d\Phi/dx$ : potential difference

The kinetics of surface charge transfer follows Bulter-Volmer equation and it also follows the diffusion migration theory:

$$i = nFAm_i C_i$$

A: surface area

$m_i$ : mass transfer coefficient

$C_i$ : ionic concentration on the surface



As for ion transport in the bulk active materials, the characteristic time constant for diffusion<sup>19, 20</sup>:

$$t \approx L^2/D$$

t: characteristic constant time

L: diffusion length

D: diffusion coefficient

The reduction of diffusion length L is more efficient than diffusion coefficient D in mitigating ion transport polarization, thus nanosizing the active material could significantly promote the ion transport.

As for electronic conductivity, since most active materials are semiconductors,<sup>21</sup>

$$\sigma = \sum_i Qu_i \mu_i$$

$\sigma$  : Electrical conductivity, S cm<sup>-1</sup>;

Q: Charge in Coulombs;

$\mu_i$ : Mobility, cm<sup>2</sup> s<sup>-1</sup> V<sup>-1</sup>;

[i]: Concentration of defects, ions, *etc* (in cm<sup>-3</sup>)

## 1.5 Critical Needs for Next-Generation Batteries

The material chemistry of current state-of-the-art lithium ion batteries has slightly changed in comparison with the first commercialized cell by SONY in 1991. The optimization/engineering of battery structure, development of sophisticated battery management system<sup>22</sup> and continuing reduction in battery cost (**Figure 1-6**)<sup>23</sup> enable the overall energy density of battery package reaching  $150 \text{ Wh kg}^{-1}$  and gradual adaptation of electric vehicles.

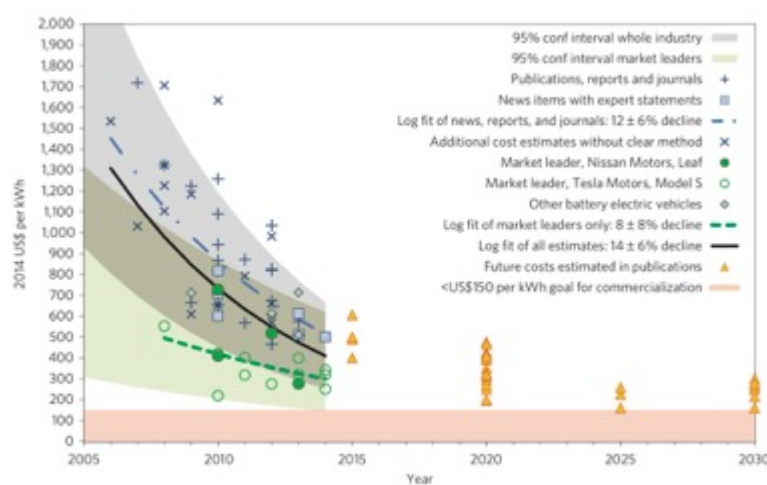


**Figure 1-6** Cost of lithium ion cell pack in electric vehicles

Taking Tesla model S as an example (data from tesla.com), one of the most advanced and popular electric vehicles, battery package of  $\sim 100 \text{ kWh}$  could afford driving range of  $\sim 400$  miles per full charge, which is competitive to vehicles powered by combustion engines. However, the full charge at Tesla deployed supercharging stations even take longer than  $\sim 5$  hours. Moreover, compared with the slow charging at domestic socket, the fast charging leads to catastrophic cycle life decay (**Figure 1-7**). Therefore, the bottlenecks existing in the cutting-edge of battery technologies for electric vehicles are insufficient driving range and fast-charging ability, namely, the poor energy density and power capability.

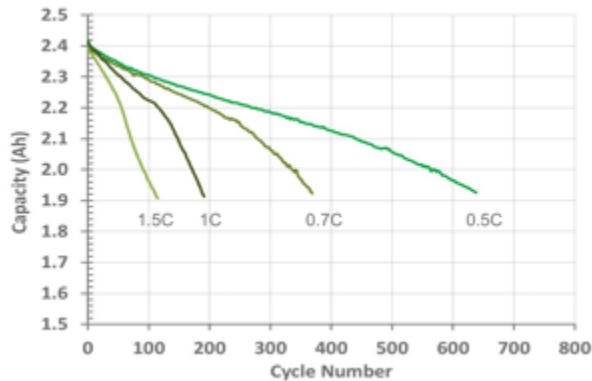


**Figure 1-7** Standard capacity fade curves at various charging rates for 2400 mA h lithium-ion polymer battery from one of the leading manufacturers.

To improve the energy density, utilization of high-capacity electrodes and wider electrochemical window have been extensively researched. For instance, enhancing the operational voltage and deliverable capacity of cathodes is a well-established direction for developing high energy batteries as shown in **Figure 1-8**.<sup>24</sup> For the anode sides, the reviving of lithium metal anode has been a hot research topic recently benefiting from its high theoretical capacity of 3860 mA h g<sup>-1</sup> and low operating voltage (0 V vs. Li/Li<sup>+</sup>). Nevertheless, the poor Coulombic efficiency of Li stripping and plating process and formation of dendritic Li remain challenging (**Figure 1-9**).<sup>8</sup> From engineering standpoints, as shown in **Figure 1-10**, further increasing the loading of active material (commercialized level: 15-20 mg cm<sup>-2</sup>) potentially offers higher theoretical volumetric capacity, while thicker electrodes have limited applications since the corresponding rate performances are substantially compromised due to severe polarization of ion transport within the electrodes.

The operation of lithium rechargeable batteries relies on separation of electrons and ions in the electrodes, and their subsequent translocation respectively through the external circuits and the electrolytes. The power density in electrochemical devices is essentially determined by the

mobility of charge carriers (electrons and ions) and kinetics of electrochemical reactions. The electronic conductivity of electrodes typically could be improved by incorporation of conductive matrix and rational architecture design.<sup>25, 26</sup> The elevated rates of ion diffusion within the active materials have been reported through reduced diffusion length<sup>27</sup>, minimized diffusion tortuosity<sup>28, 29</sup> and tuned phase composition<sup>30</sup>. Surprisingly, less efforts have been dedicated on the efficiency of ion transport throughout the electrochemical device. Indeed, the initiation of Li dendrites, limited electrode thickness and poor power capability could all be attributable to the laggard Li<sup>+</sup> transport under high current operation.

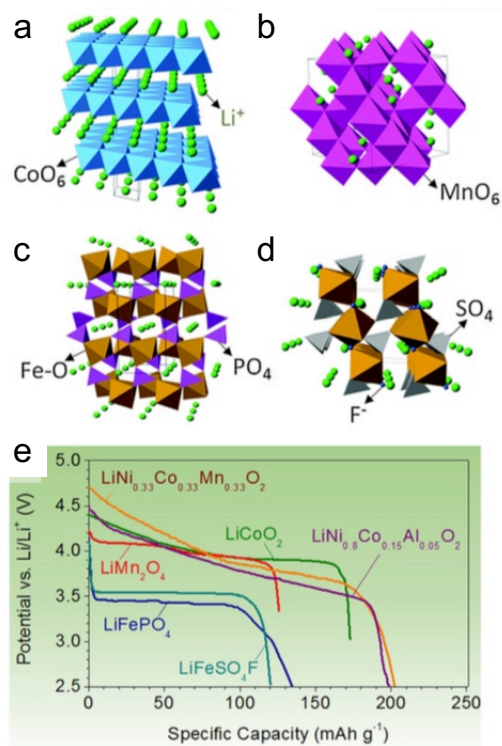


**Figure 1-8** Crystal structures and discharge profiles of representative intercalation cathodes: structure of (a) layered (LiCoO<sub>2</sub>), (b) spinel (LiMn<sub>2</sub>O<sub>4</sub>), (c) olivine (LiFePO<sub>4</sub>), (d) tavorite (LiFeSO<sub>4</sub>F), and (e) typical discharge profiles of intercalation cathodes

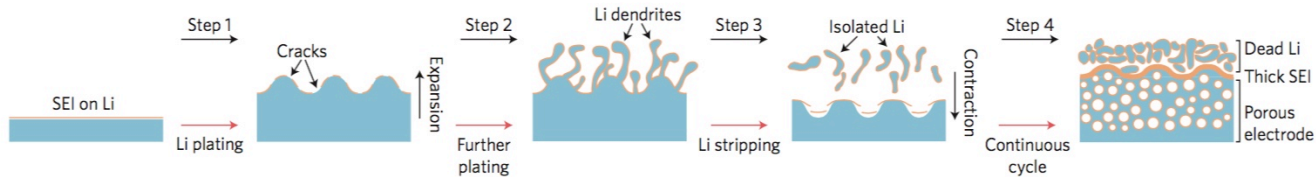


**Figure 1-9** Schematic showing the formation of dendritic Li during Li stripping/plating process

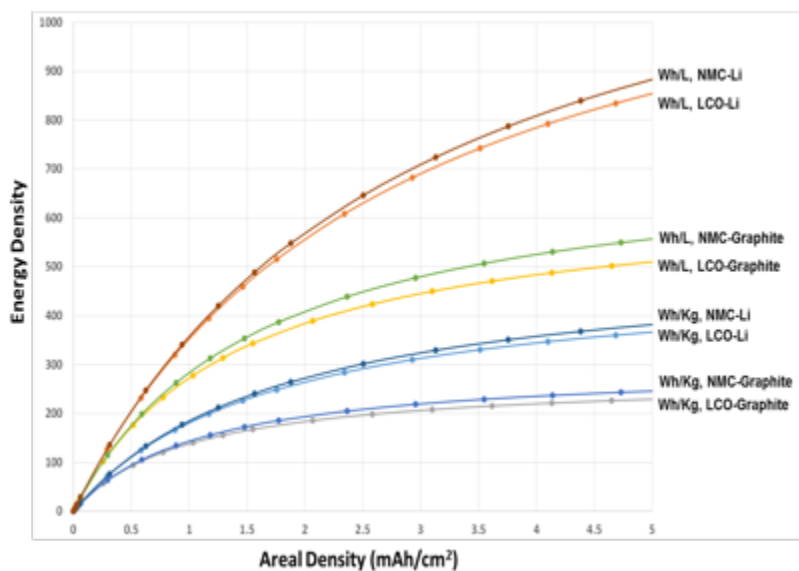


**Figure 1-10** Energy density of commercialized cathode coupled with anodes (graphite, Li) as a function of areal density (loading of active materials)

The ion transportation behavior is commonly existing in biological systems, photovoltaics, gas sensors, and electrochemical devices, *etc.*<sup>31</sup> The mechanisms of ion conduction could be categorized into ion hopping type in like solid state structure and ion diffusion type in solvating medium. The universal parameters influencing the ionic conductivity is described by the following equation:

$$\sigma_i = nC_i\mu_i$$

$\sigma_i$ : Electrical conductivity, S cm<sup>-1</sup>;

n : Valence state of ion carriers;

$C_i$ : Concentration, mol L<sup>-1</sup>;

$\mu_i$ : Mobility, cm<sup>2</sup> s<sup>-1</sup>;

Besides above significant parameters, spatial distribution and working temperature are also closely related to the conductivity. The activation energy depicts the energy barriers that needs to be overcame for ions hopping between structural sites and diffusional dynamics. The activation energy ( $E_a$ ) of temperature (T) dependent conductivity that exhibits Arrhenius behavior could be derived from equation below:

$$\sigma = A \exp\left(\frac{-E_a}{RT}\right)$$

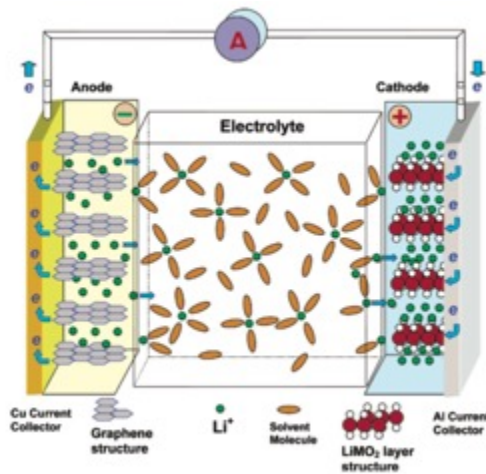


**Figure 1-11** Schematic showing transport of solvated Li<sup>+</sup> in a lithium ion cell during discharge process

As shown in **Figure 1-11**, The ion transport in commercial lithium ion batteries is realized by non-aqueous liquid electrolyte, where lithium salts are dissolved in polar solvents and solvated

ions migrate in liquid medium.<sup>32, 33</sup> Extensively selected Li-salts (LiClO<sub>4</sub>, LiAsF<sub>6</sub>, LiPF<sub>6</sub>, LiBF<sub>4</sub>, LiTFSI, *etc*) and solvent mixtures (carbonates, esters, ethers, *etc.*) afford high ionic conductivity up to ~ 12 mS cm<sup>-1</sup> at room temperature.<sup>34</sup> In addition, non-aqueous liquid electrolyte provides wide electrochemical stability window defined by the lowest unoccupied molecular orbital (LUMO) and the highest occupied molecular orbital (HOMO) (see **Figure 1-12**).<sup>35</sup> For example, 1M LiPF<sub>6</sub> in ethylene carbonate:diethyl carbonate (EC:DEC) is thermodynamically stable between 1.2 to 4.5 V (*vs.* Li/Li<sup>+</sup>). For electrochemical potential beyond the window, for instance, graphite (0.2 V *vs.* Li/Li<sup>+</sup>), electrolyte would be reduced to create a passivation layer (solid electrolyte interphase, SEI) to block the electron transfer from graphite to electrolyte, rendering a kinetically stable interphase.

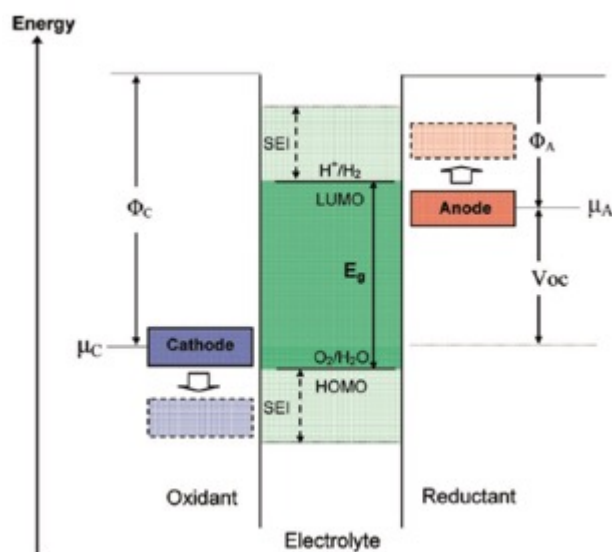


**Figure 1-12** Schematic showing the energy diagram of an aqueous electrolyte

However, the drawbacks of commercial liquid electrolyte are evident. Based on Stokes-Einstein equation, the Stokes radius of ions in electrolyte could be calculated by:

$$r = \frac{k_B T}{6\pi\eta D}$$

Where  $k_B$ ,  $\eta$  and  $D$  refer to Boltzman constant, dynamic viscosity and diffusion coefficient, respectively

Meanwhile, from Einstein relation (kinetic theory)

$$D = \mu k_B T$$

Therefore, the ion mobility is proportional to the dynamic radius of ions

$$\mu = 1/6 \pi \eta r$$

Unfortunately, the  $\text{Li}^+$  mobility is typically inferior than the anion mobility due to the larger solvation shell of  $\text{Li}^+$  compared with anions. The stronger dipole interaction (coordination) between  $\text{Li}^+$  and polar solvents and mobile anions render only a small fraction of overall conductivity contributing to the effective  $\text{Li}^+$  conductivity. A quantitative parameter evaluating the corresponding  $\text{Li}^+$  transport efficiency is defined as  $\text{Li}^+$  transference number:

$$t_{\text{Li}^+} = \frac{\sigma_{\text{Li}^+}}{\sigma_{\text{Li}^+} + \sigma_{\text{anion}}} = \frac{\mu_{\text{Li}^+}}{\mu_{\text{Li}^+} + \mu_{\text{anion}}} = \frac{D_{\text{Li}^+}}{D_{\text{Li}^+} + D_{\text{anion}}}$$

From experimental results, the average  $\text{Li}^+$  transference number ( $t_{\text{Li}^+}$ ) for commercial liquid electrolyte (e.g. 1M  $\text{LiPF}_6$  in EC:DEC) is as low as  $\sim 0.3$ .<sup>36</sup> Such disadvantage is blurred by claimed high overall conductivity and the potential for improving transport efficiency of current electrolytes is not fully exploited. Mainstream theories explaining Li dendrites formation and limited charging rate borrow the concept of  $\text{Li}^+$  transference number, which highlight the importance of the electrolyte properties. In a space charge model justifying ramified Li, limiting current density ( $J^*$ ) and Sand's time ( $\tau$ ) were proposed as characteristic parameters depicting the initiation of dendritic growth.<sup>37-41</sup>

$$\frac{dC}{dx} = -\frac{J(1 - t_{\text{Li}^+})}{FD}$$



$$J^* = \frac{2FC_0D}{(1 - t_{Li^+})L}$$

$$\tau = \pi D \left( \frac{FC_0}{2J(1 - t_{Li^+})} \right)^2$$

where F and L refer to Faraday's constant and distance between electrodes.

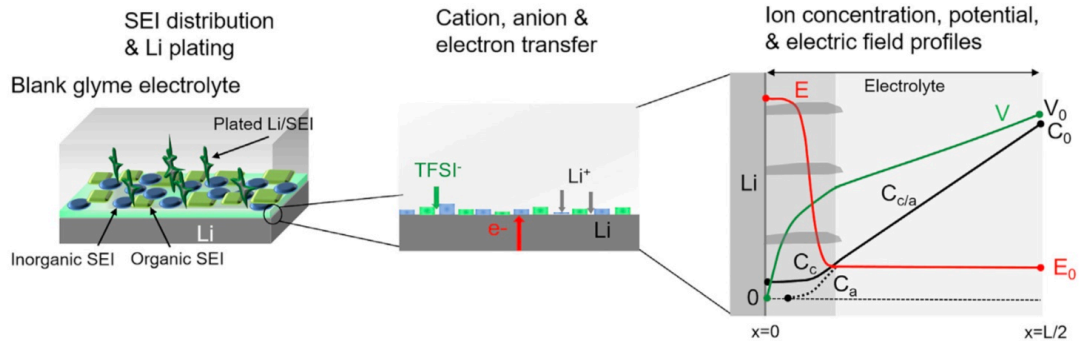


**Figure 1-13** Space charge model-based diagram: showing ion concentration (C), electric field (E), and potential (V) as a function of distance to the Li electrode

In the space charge model, as illustrated in **Figure 1-13**, where Li electrodes exhibit anions blocking characteristics.<sup>41</sup> Upon polarization, the  $Li^+$  are reduced at negatively charged electrode, leading to diffusion and migration of  $Li^+$  from the positive electrode. Correspondingly, the mobile anions migrate from negative electrode to the positive side, resulting in anion depletion on negative side and anion piling up on positive side. Such circumstances (generation of an opposite overpotential) bring about the neutralization regime near the positive electrode and acceleration of  $Li^+$  electrodeposition at negative electrode, giving rise to filament electrodeposition (dendritic Li).

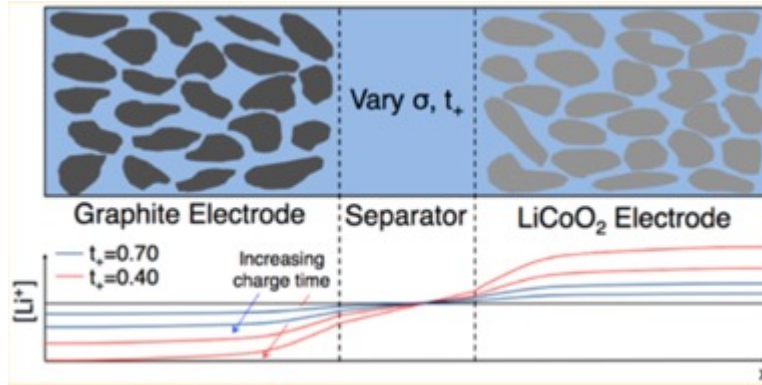


**Figure 1-14** Schematic of a modeled  $\text{Li}^+$  concentration distribution as a function of varied  $\text{Li}^+$  transference number throughout a lithium ion cell comprising  $\text{LiCoO}_2$  cathode and graphite anode

Besides the deleterious effect of mobile anions in producing ramified Li, the anion conductivity should also be responsible for the limited powder output and electrode thickness. Simulated results from classical lithium ion cell model show that electrolyte depletion and corresponding concentration polarization account for the poor rate performance of electrode with high areal loading.<sup>42</sup> In addition, it has been demonstrated that improving  $\text{Li}^+$  transference number mitigate concentration polarization and enhance the power capability.<sup>43</sup> Therefore, studies on improving  $\text{Li}^+$  transport efficiency and immobilizing anion movements are of particular significance on boosting energy density and enhancing power density of lithium rechargeable batteries.

## 1.6 Reported Electrolytes with High Li<sup>+</sup> Transport Efficiency

As a well-established category of electrolytes, solid-state electrolytes hold great potential for next generation battery systems utilizing metallic Li due to their unity Li<sup>+</sup> transference number, mechanical robustness and inflammability. Recent advancements in area of solid electrolyte are encouraging, for instance, the ionic conductivity of sulfide-based electrolyte was improved by tuning phase structure, which surpass the values of liquid electrolytes (**Figure 1-15a**).<sup>44, 45</sup> Moreover, formidable interfacial resistance between solid electrolyte (garnet-type, LLZO) was substantially alleviated by a surface coating using chemical vapor deposition (CVD), affording decent electrochemical device performance in solid state configuration.<sup>46</sup>

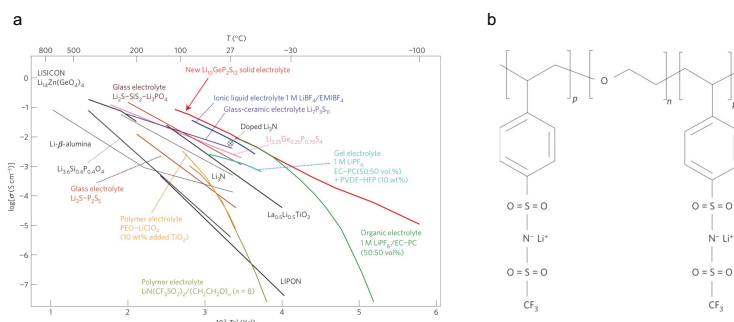


**Figure 1-15** (a) Temperature dependent ionic conductivity of lithium solid electrolyte, polymer electrolyte, ionic liquid and organic liquid electrolyte; (b) Chemical structure of single-ion polymer electrolyte

Unlike crystalline framework in solid electrolyte, single-ion polymer electrolytes achieve high Li<sup>+</sup> transference number by covalently grafting anions on polymer backbones (**Figure 1-15b**).<sup>47</sup> Such design eliminates the polarization carried out by anion movements, while scarce studies reported sufficient Li<sup>+</sup> conductivity accompanied with improved transference number.

## 1.7 Dissertation Objectives and Scope

A comprehensive survey of literature reveals the absence of appropriate ionic conductor simultaneously possessing high  $\text{Li}^+$  transport efficiency ( $\text{Li}^+$  transference number) and superionic conductivity. Such dilemma substantially hampers the progresses in batteries technologies seeking high energy density and high rate performances in that the concentration polarization induced by the low transport efficiency restrict the employment of metallic Li anode, high current operation and thick electrodes.

In this dissertation, a novel type fast  $\text{Li}^+$  conductor built upon functional porous scaffold (metal–organic framework) and liquid electrolyte was proposed, which not only possesses the characteristics of solid electrolyte in terms of high efficiency but also has superionic conductivity close to commercial electrolyte. The studies of the developed  $\text{Li}^+$  conductors center around the conduction mechanisms from scientific prospective and their applications on lithium ion cells from engineering standpoint.

To integrate these fast  $\text{Li}^+$  conductors into lithium rechargeable batteries, the road map of dissertation objective was outlined in four directions: (a) solid-state electrolyte; (b) functional battery separator; (c) electrolyte additive; (d) electrode additive. Incorporation of this fast  $\text{Li}^+$  conductor into battery components demonstrated substantially improved electrochemical performances of batteries. Compared with the plain  $\text{Li}^+$  conduction of commercial electrolyte, the novel fast  $\text{Li}^+$  conductor exhibits multiple superiorities, including high-rate, high voltage (high energy), cycle longevity at faster charging and improved safety aspects, which are encouraging results especially for electric vehicle applications. Such findings are expected to transform the fundamental material chemistry of battery and significantly impact the energy storage markets.

## 1.8 References

1. Goodenough, J.B. & Park, K.S. The Li-ion rechargeable battery: a perspective. *Journal of the American Chemical Society* **135**, 1167-1176 (2013).
2. Rolison, D.R. et al. Multifunctional 3D nanoarchitectures for energy storage and conversion. *Chemical Society reviews* **38**, 226-252 (2009).
3. Ormerod, R.M. Solid oxide fuel cells. *Chemical Society reviews* **32**, 17-28 (2003).
4. Thackeray, M.M., Wolverton, C. & Isaacs, E.D. Electrical energy storage for transportation—approaching the limits of, and going beyond, lithium-ion batteries. *Energy & Environmental Science* **5**, 7854 (2012).
5. J.-M. Tarascon, M.A. Issues and challenges facing rechargeable lithium batteries. *Nature* **414**, 359-367 (2001).
6. Zhang, W.-J. A review of the electrochemical performance of alloy anodes for lithium-ion batteries. *Journal of Power Sources* **196**, 13-24 (2011).
7. Peng, J., Zu, C. & Li, H. Fundamental scientific aspects of lithium batteries- Thermodynamic calculations of theoretical energy densities of chemical energy storage systems. *Energy storage science and technology* **2**, 55-63 (2013).
8. Lin, D., Liu, Y. & Cui, Y. Reviving the lithium metal anode for high-energy batteries. *Nature Nanotechnology* **12**, 194 (2017).
9. Yoshino, A., Sanekika, K. & Nakajima, T. (1985).
10. Goodenough, J.B. Electrochemical energy storage in a sustainable modern society. *Energy & Environmental Science* **7**, 14 (2014).
11. Glasstone, S. Textbook of physical chemistry, Edn. 2nd ed. (London : Macmillan, 1951. - 1320 p., 1951).

12. Linden, D. & Reddy, T.B. Hand book of batteries. (1995).
13. Wakihara, M. & Yamamoto, O. Lithium ion batteries: fundamentals and performance. (John Wiley & Sons, 2008).
14. Nazri, Gholam-Abbas & Pistoia, G. Lithium batteries: science and technology. (Springer Science & Business, 2008).
15. Nitta, N. & Yushin, G. High-Capacity Anode Materials for Lithium-Ion Batteries: Choice of Elements and Structures for Active Particles. *Particle & Particle Systems Characterization* **31**, 317-336 (2014).
16. Bard, A.J. & Faulkner, L.R. Electrochemical methods: fundamentals and applications, Vol. 2. (Wiley, New York; 1980).
17. Sakamoto, J.S. & Dunn, B. Hierarchical battery electrodes based on inverted opal structures. *Journal of Materials Chemistry* **12**, 2859-2861 (2002).
18. Abraham, K.M., Pasquariello, D.M. & Willstaedt, E.M. Discharge Rate Capability of the LiCoO<sub>2</sub> Electrode. *Journal of The Electrochemical Society* **145**, 482-486 (1998).
19. Welty, J.R., Wicks, C.E., Wilson, R.E. & Rorrer, G.L. Fundamentals of momentum, heat, and mass transfer. (John Wiley & Sons, 2009).
20. Bird, R.B., Stewart, W.E. & Lightfoot, E.N. Transport phenomena. (John Wiley & Sons, 2007).
21. Cardona, M. & Peter, Y.Y. Fundamentals of semiconductors. (Springer-Verlag Berlin Heidelberg, 2005).
22. Hannan, M.A., Lipu, M.S.H., Hussain, A. & Mohamed, A. A review of lithium-ion battery state of charge estimation and management system in electric vehicle applications:

- Challenges and recommendations. *Renewable and Sustainable Energy Reviews* **78**, 834-854 (2017).
23. Nykvist, B. & Nilsson, M. Rapidly falling costs of battery packs for electric vehicles. *Nature Climate Change* **5**, 329 (2015).
  24. Nitta, N., Wu, F., Lee, J.T. & Yushin, G. Li-ion battery materials: present and future. *Materials Today* **18**, 252-264 (2015).
  25. Shen, L. et al. Encapsulation of SnO<sub>2</sub> nanocrystals into hierarchically porous carbon by melt infiltration for high-performance lithium storage. *Journal of Materials Chemistry A* **4**, 18706-18710 (2016).
  26. Le, Z. et al. Pseudocapacitive Sodium Storage in Mesoporous Single-Crystal-like TiO<sub>2</sub>-Graphene Nanocomposite Enables High-Performance Sodium-Ion Capacitors. *ACS Nano* **11**, 2952-2960 (2017).
  27. Sun, Y.-K. et al. Nanostructured high-energy cathode materials for advanced lithium batteries. *Nature Materials* **11**, 942 (2012).
  28. Sander, J.S., Erb, R.M., Li, L., Gurijala, A. & Chiang, Y.M. High-performance battery electrodes via magnetic templating. *Nature Energy* **1**, 16099 (2016).
  29. Billaud, J., Bouville, F., Magrini, T., Villevieille, C. & Studart, A.R. Magnetically aligned graphite electrodes for high-rate performance Li-ion batteries. *Nature Energy* **1**, 16097 (2016).
  30. Kang, B. & Ceder, G. Battery materials for ultrafast charging and discharging. *Nature* **458**, 190 (2009).

31. Horike, S., Umeyama, D. & Kitagawa, S. Ion Conductivity and Transport by Porous Coordination Polymers and Metal–Organic Frameworks. *Accounts of Chemical Research* **46**, 2376-2384 (2013).
32. Xu, K. Nonaqueous Liquid Electrolytes for Lithium-Based Rechargeable Batteries. *Chemical Reviews* **104**, 4303-4418 (2004).
33. Xu, K. Electrolytes and Interphases in Li-Ion Batteries and Beyond. *Chemical Reviews* **114**, 11503-11618 (2014).
34. Younesi, R., Veith, G.M., Johansson, P., Edstrom, K. & Vegge, T. Lithium salts for advanced lithium batteries: Li-metal, Li-O<sub>2</sub>, and Li-S. *Energy & Environmental Science* **8**, 1905-1922 (2015).
35. Goodenough, J.B. & Kim, Y. Challenges for Rechargeable Li Batteries. *Chemistry of Materials* **22**, 587-603 (2010).
36. Zugmann, S. et al. Measurement of transference numbers for lithium ion electrolytes via four different methods, a comparative study. *Electrochimica Acta* **56**, 3926-3933 (2011).
37. Chazalviel, J.N. Electrochemical aspects of the generation of ramified metallic electrodeposits. *Physical Review A* **42**, 7355-7367 (1990).
38. Brissot, C., Rosso, M., Chazalviel, J.N. & Lascaud, S. Dendritic growth mechanisms in lithium/polymer cells. *Journal of Power Sources* **81-82**, 925-929 (1999).
39. Sand, H.J.S. III. On the concentration at the electrodes in a solution, with special reference to the liberation of hydrogen by electrolysis of a mixture of copper sulphate and sulphuric acid. *The London, Edinburgh, and Dublin Philosophical Magazine and Journal of Science* **1**, 45-79 (1901).



40. Bai, P., Li, J., Brushett, F.R. & Bazant, M.Z. Transition of lithium growth mechanisms in liquid electrolytes. *Energy & Environmental Science* **9**, 3221-3229 (2016).
41. Pang, Q., Liang, X., Shyamsunder, A. & Nazar, L.F. An In Vivo Formed Solid Electrolyte Surface Layer Enables Stable Plating of Li Metal. *Joule* **1**, 871-886 (2017).
42. Du, Z., Wood, D.L., Daniel, C., Kalnaus, S. & Li, J. Understanding limiting factors in thick electrode performance as applied to high energy density Li-ion batteries. *Journal of Applied Electrochemistry* **47**, 405-415 (2017).
43. Diederichsen, K.M., McShane, E.J. & McCloskey, B.D. Promising Routes to a High Li<sup>+</sup> Transference Number Electrolyte for Lithium Ion Batteries. *ACS Energy Letters* **2**, 2563-2575 (2017).
44. Kamaya, N. et al. A lithium superionic conductor. *Nature Materials* **10**, 682 (2011).
45. Kato, Y. et al. High-power all-solid-state batteries using sulfide superionic conductors. *Nature Energy* **1**, 16030 (2016).
46. Han, X. et al. Negating interfacial impedance in garnet-based solid-state Li metal batteries. *Nature Materials* **16**, 572 (2016).
47. Bouchet, R. et al. Single-ion BAB triblock copolymers as highly efficient electrolytes for lithium-metal batteries. *Nature Materials* **12**, 452 (2013).

## **Chapter 2 Creating Solid-State Electrolytes with Biomimetic Ionic Channels**

### **in Metal–organic Frameworks**

Solid-state electrolytes are the key to the development of lithium-based batteries with dramatically improved energy density and safety. Inspired by ionic channels in biological systems, we report herein a novel class of solid-state electrolytes with biomimetic ionic channels. This is achieved by complexing the anions of an electrolyte to the open metal sites (OMSs) of metal–organic frameworks (MOFs), which transforms the MOF scaffolds into ionic-channel analogs with lithium-ion conduction and low activation energy. This work suggests the emergence of a new class of solid-state lithium-ion conducting electrolytes.

## 2.1 Introduction

In lithium-ion battery operation, nonaqueous liquid electrolytes enable ion transport between redox active electrodes.<sup>1</sup> The electrolyte chemistry involved here requires that polar solvents dissociate/dissolve the lithium salt which then allows facile ion transport *via* the fluidic medium.<sup>2</sup> There are, however, certain limitations with current electrolyte systems. The thermal instability of organic solvents poses formidable concerns about safety, particularly for large-scale applications and Li metal-based secondary batteries.<sup>3</sup> Moreover, the bulky size of solvated Li<sup>+</sup> cations results in lower mobility relative to the anions. Consequently, during battery operation the effective current carried by the cations is mitigated by anion movement, leading to concentration polarization, battery life decay and inferior power output.<sup>4</sup> Solid-state electrolytes overcome some of these deficiencies and are considered to be a promising direction for developing next-generation batteries due to improved safety and transport properties.

Solid-state electrolytes are most commonly categorized as being either ceramic or polymeric. Ionic conductivity of ceramic electrolytes exceeding  $10^{-4}$  S cm<sup>-1</sup> has been achieved with several electrolyte systems such as garnet Li<sub>7</sub>La<sub>3</sub>Zr<sub>2</sub>O<sub>12</sub>, Li<sub>7</sub>P<sub>3</sub>S<sub>11</sub> in the Li<sub>2</sub>S-P<sub>2</sub>S<sub>5</sub> family, and thio-LISICON Li<sub>10</sub>GeP<sub>2</sub>S<sub>12</sub>.<sup>5,6</sup> However, their implementation has encountered critical challenges, such as unsatisfactory electrochemical stability, sensitivity to moisture and oxygen, poor interfacial contact with electrodes, and high grain boundary resistance.<sup>7-11</sup> Despite recent advances in reducing interfacial resistance,<sup>12</sup> scalable adaptation of ceramic electrolytes remains challenging. Dry polymer electrolytes complexed with lithium salts usually exhibit ionic conductivity on the order of  $10^{-7}$  S cm<sup>-1</sup> at room temperature.<sup>13</sup> Enhancing the ionic conductivity by introducing liquid plasticizers results in gel polymer electrolytes with decreased mechanical strength and the inability to block dendrite growth.<sup>14</sup> Alternatively, nano-sized ceramic fillers were

demonstrated to promote ionic mobility by modulating reorganization of polymer chains,<sup>15</sup> whereas elevated temperature (e.g., 50 °C) is still required for an operational conductivity ( $10^{-4}$  S  $\text{cm}^{-1}$ ).

Herein, we report a novel class of solid-state electrolytes with biomimetic ionic channels. Ionic channels commonly exist in cell membranes and organelles, allowing selective permittivity of cations (e.g.,  $\text{H}^+$ ,  $\text{Na}^+$ , and  $\text{K}^+$ ) with little metabolic energy input.<sup>16</sup> **Figure 2-1a** depicts a typical structure of  $\text{Na}^+$ -ion channels, of which the key components are the  $\alpha$ -helix domains folded from glutamic-acid-rich peptide chains.<sup>17</sup> The carboxylic residues are deprotonated under the physiological environment (pH 7.4), forming negatively charged glutamate ions ( $-\text{CH}_2\text{CH}_2\text{COO}^-$ ) along the channels, which exclude anions (e.g.,  $\text{Cl}^-$ ) but allow effective transport of cations.<sup>16</sup>

We envision that novel solid-state electrolytes with biomimetic ionic channels could be constructed using metal–organic frameworks (MOFs) as scaffolds. This was first demonstrated using HKUST-1, one of the well investigated MOFs constructed from Cu (II) paddle wheels and benzene-1,3,5-tricarboxylate (BTC) ligands (linkers).<sup>18</sup> As illustrated in **Figure 2-1b**, HKUST-1 possesses three-dimensional pore channels with a pore diameter of  $\sim 1.1$  nm. Similar to many other MOFs, HKUST-1 contains coordinated solvent molecules (e.g., water) along the channels. Removing the coordinated molecules results in nanoporous HKUST-1 with unsaturated metal centers (i.e., open metal sites, OMSs).<sup>19</sup> In the presence of  $\text{LiClO}_4$  in propylene carbonate (PC),  $\text{ClO}_4^-$  ions spontaneously bind to the OMSs, forming  $\text{ClO}_4^-$ -decorated MOF channels (**Figure 2-1c**). Similar to the glutamate-like ionic channels, such negatively charged MOF channels enable transport of  $\text{Li}^+$  ions with low activation energy (**Figure 2-1d**).

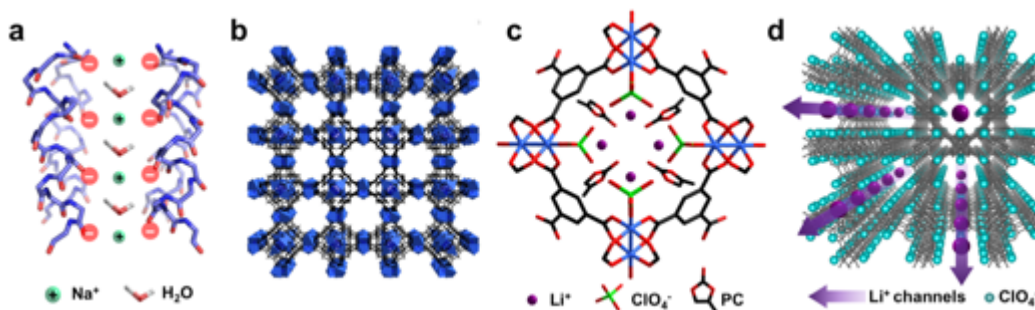


**Figure 2-1** Schematic illustrations of the biomimetic ionic channels in MOFs. (a) A Na<sup>+</sup>-ions channel in biological systems with negatively charged glutamate ions.<sup>16</sup> (b) Structure of HKUST-1 made from copper nodes (blue) and BTC ligands (black) with pore channels of ~1.1 nm. (c) A schematic showing the formation of biomimetic ionic channels in HKUST-1 with ClO<sub>4</sub><sup>-</sup> anions bound to the OMSs and solvated Li<sup>+</sup> ions in the channels with high conductivity (copper: blue; carbon: black; oxygen: red). (d) Schematic of biomimetic ionic channels in a MOF scaffold (dark gray) with bound ClO<sub>4</sub><sup>-</sup> ions (cyan dots), enabling fast transport of solvated Li<sup>+</sup> ions (purple dots).

The development of MOFs as ionic conductors has been reported previously. Proton conducting electrolytes in particular have received considerable attention as MOFs were loaded with protonic inorganic (e.g., H<sub>2</sub>O, H<sub>2</sub>SO<sub>4</sub>) or organic (e.g., imidazole, 1,2,4-triazole) molecules.<sup>20</sup> Lithium electrolytes were also synthesized from a MOF, Mg<sub>2</sub>(dobdc), where dobdc is 1,4-dioxido-2,5-benzenedicarboxylate. By reacting Mg<sub>2</sub>(dobdc) with lithium isopropoxide and subsequent infiltration with LiBF<sub>4</sub> in ethylene carbonate (EC) and diethyl carbonate (DEC), a lithium-ion conductivity of ~10<sup>-4</sup> S cm<sup>-1</sup> was reported.<sup>21, 22</sup> Similarly, upon reaction with stoichiometric amounts of halide followed by soaking with LiBF<sub>4</sub> in PC, a Cu(II)-azolate MOF could afford ionic conductivity of ~10<sup>-4</sup> S cm<sup>-1</sup>.<sup>23</sup> In another approach,<sup>24</sup> MOF particles were mixed with an acrylate monomer to form composite membranes after polymerization, providing a lithium-ion conductivity below 10<sup>-5</sup> S cm<sup>-1</sup>. MOF was also incorporated into poly(ethylene oxide)-based

polymer electrolyte,<sup>25,26</sup> where it functions as a conventional solid filler. In these previous studies, there was no indication of whether ionic channels were involved in Li<sup>+</sup> transport nor was there an indication that these MOF-related materials with ionic channels were able to serve as electrolytes in electrochemical devices.

## 2.2 Results and Discussions

### 2.2.1 Synthesis of Solid-State Electrolytes with High Ionic Conductivity

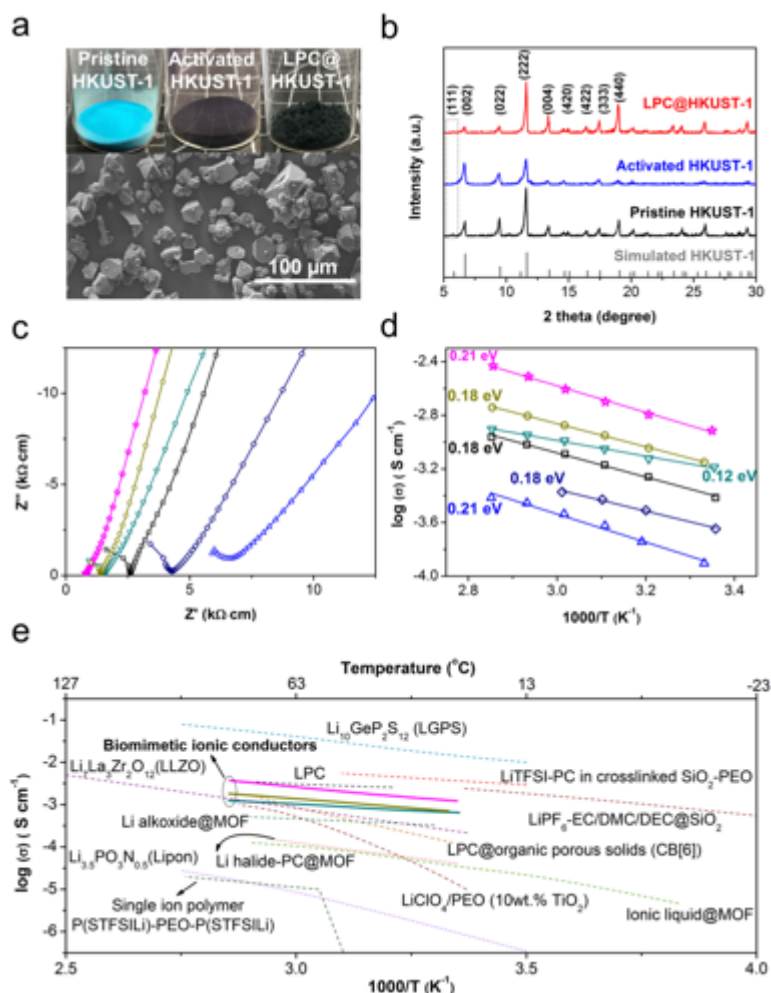


**Figure 2-2** Structure characterizations and lithium ion conductivity of LPC@MOFs electrolytes.

(a) A SEM image of HKUST-1 particles (insets: photographs of pristine HKUST-1, activated HKUST-1, and LPC@HKUST-1 electrolyte). (b) XRD patterns of pristine HKUST-1, activated HKUST-1, and LPC@HKUST-1 electrolyte. (c) Nyquist plots of various LPC@MOFs electrolytes at ambient temperature. ☆: LPC@MIL-100-Al, ○: LPC@MIL-100-Fe, ∇: LPC@UiO-67, □: LPC@HKUST-1, ◇: LPC@MIL-100-Cr, Δ: LPC@UiO-66. (d) Arrhenius

plots of various LPC@MOFs electrolytes and their calculated activation energies for lithium-ion conduction. (e) Arrhenius plots of LPC@MIL-100-Al (pink), LPC@MIL-100-Fe (dark yellow), and LPC@UiO-67 (cyan) in comparison with representative 1) ceramic electrolytes ( $\text{Li}_{10}\text{GeP}_2\text{S}_{12}$ , garnet  $\text{Li}_7\text{La}_3\text{Zr}_2\text{O}_{12}$ , and LiPON  $\text{Li}_{3.5}\text{PO}_3\text{N}_{0.5}$ ), 2) polymeric electrolytes ( $\text{LiClO}_4/\text{PEO}$  with  $\text{TiO}_2$  additive,<sup>15</sup> LiTFSI-PC in crosslinked  $\text{SiO}_2$ -PEO composites, and single ion polymer P(STFSILi)-PEO-P(STFSILi)), and 3) liquid-in-solid lithium-ion conductors, including liquid electrolyte@mesoporous silica,  $\text{LiPF}_6\text{-EC/DMC/DEC@SiO}_2$ ,<sup>27</sup> LPC@organic porous solids,  $\text{CB}[6]\cdot 0.4\text{LiClO}_4\cdot 3.4\text{PC}$ ,<sup>28</sup> Li alkoxide@MOFs,  $\text{Mg}_2(\text{dobdc})\cdot 0.35\text{LiO}^i\text{Pr}\cdot 0.25\text{LiBF}_4\cdot \text{EC}\cdot \text{DEC}$ ,<sup>21</sup> Li halide-PC@MOFs,  $\text{Li}_{0.8}[\text{Cu}_2\text{Cl}_2\text{Br}_{0.8}\text{BTDD}]\cdot 10(\text{PC})$ ,<sup>23</sup> and ionic liquid@MOFs,  $(\text{EMI}_{0.8}\text{Li}_{0.2})\text{TFSA@ZIF-67}$ ,<sup>29</sup> and 4) liquid electrolyte, 1 M  $\text{LiClO}_4$  in PC (LPC).

**Figure 2-2a** presents a scanning electron microscope (SEM) image of the as-synthesized HKUST-1, which shows an average particle size of tens of micrometers (see Supporting Information for synthetic details). The light blue color is due to its water-coordinated copper centers. Removing the coordinated water (activation process) turns the color to dark purple, which then becomes dark cyan after soaking with a  $\text{LiClO}_4$ -PC solution (LPC), implying the emergence of unsaturated sites and re-coordination of the unsaturated sites with  $\text{ClO}_4^-$  ions, respectively (insets of **Figure 2-2a**). The LPC-soaked HKUST-1 (denoted as LPC@HKUST-1) was collected after filtration and removal of any excessive solvent, showing a free-flowing powder form.

HKUST-1 exhibits a typical microporous structure with a surface area of  $1150\text{ cm}^2\text{ g}^{-1}$  and a pore volume of  $0.5\text{ cm}^3\text{ g}^{-1}$ . Both of these features decrease to near zero in LPC@HKUST-1, suggesting incorporation of  $\text{LiClO}_4$  into the pore channels (**Figure 2-3**). The crystalline structure of the HKUST-1 is well retained after the activation process and soaking with LPC as confirmed



by the x-ray diffraction (XRD) patterns shown in **Figure 2-2b**. The (111) peak disappears after the activation process and reappears after incorporating with LPC. These characteristics are consistent with removal of the coordinated water molecules (**Figure 2-4**)<sup>30</sup> and binding of the OMSs with  $\text{ClO}_4^-$  ions, respectively.

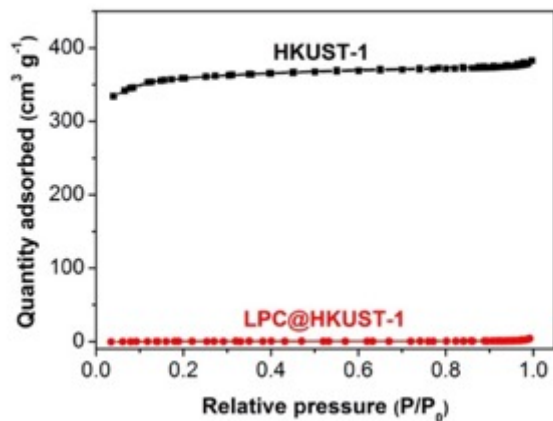


**Figure 2-3** N<sub>2</sub> adsorption/desorption isotherms of HKUST-1 and LPC@HKUST-1 electrolyte. HKUST-1 shows a type I isotherm characteristic of microporous solids with a BET surface area of 1150 cm<sup>2</sup> g<sup>-1</sup> and microporous volume of 0.5 cm<sup>3</sup> g<sup>-1</sup>.

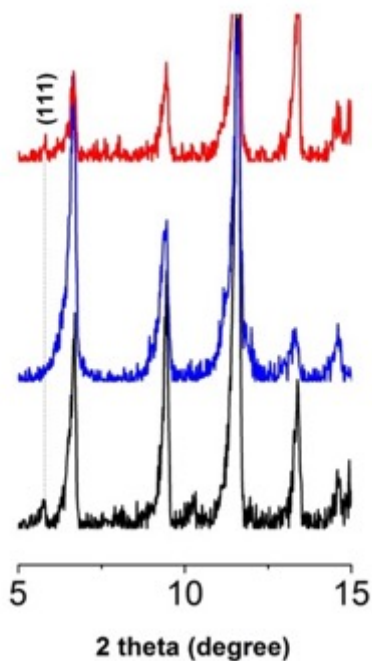


**Figure 2-4** Enlarged XRD patterns of as-prepared HKUST-1 (black), activated HKUST-1 (blue), and LPC@HKUST-1 (red). The coordination status of guest molecules on Cu<sup>II</sup> metal sites is indicated by the 2-theta peak at 5.8°.

The composition of LPC@HKUST-1 was estimated using coupled plasma atomic emission spectroscopy (ICP-AES) and thermogravimetric analysis (TGA). ICP-AES gives a Li/Cu molar ratio of 0.94, which is consistent with our hypothesis that each ClO<sub>4</sub><sup>-</sup> ion binds to an OMS (Cu center). Compared with the reported electrolyte based on Mg<sub>2</sub>(dobdc), which possesses a Li/Mg molar ratio of 0.3,<sup>21</sup> the concentration of Li<sup>+</sup> ions in LPC@HKUST-1 is three-fold higher, which is important for providing high ionic conductivity. The content of PC within LPC@HKUST-1 is estimated by TGA, which gives a formula of LPC@HKUST-1 as Cu<sub>3</sub>(BTC)<sub>2</sub>(LiClO<sub>4</sub>)<sub>2.8</sub>(PC)<sub>4.6</sub> (see details in **Figure 2-5**). The low PC/Li molar ratio (~ 1.6) suggests that each Li<sup>+</sup> ion is solvated

by less than two PC molecules, in sharp contrast to a much larger PC/Li ratio in LPC of approximately four PC molecules per Li<sup>+</sup> ion.<sup>31</sup>

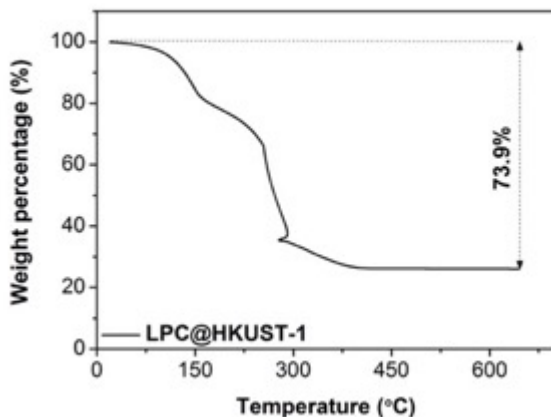


**Figure 2-5** TGA curve of LPC@HKUST-1 electrolyte in air.

Based on the result of ICP-AES, the formula of LPC@HKUST-1 is determined as  $\text{Cu}_3(\text{BTC})_2(\text{LiClO}_4)_{2.8}(\text{PC})_x$ . In the TGA measurement, the initial two-step weight loss (in total of ~ 33%) up to 250 °C is attributed to the decomposition and oxidation of PC, respectively.<sup>32</sup> The subsequent weight drop originates from disintegration of MOF structure (leaves copper oxide) and decomposition of lithium salts. The remaining weight (26.1%) corresponds to a mixture of CuO and LiCl, and the value of  $x$  can be deduced from the following equation:

$$26.1\% / (3 \times M(\text{CuO}) + 2.8 \times M(\text{LiCl})) = 100\% / M(\text{Cu}_3(\text{BTC})_2(\text{LiClO}_4)_{2.8}(\text{PC})_x),$$

where  $M(\text{CuO})$ ,  $M(\text{LiCl})$ , and  $M(\text{Cu}_3(\text{BTC})_2(\text{LiClO}_4)_{2.8}(\text{PC})_x)$  are the molecular weights of CuO, LiCl and the LPC@HKUST-1, respectively. Based on the calculated molecular weight of LPC@HKUST-1, the nominal formula is determined as  $\text{Cu}_3(\text{BTC})_2(\text{LiClO}_4)_{2.8}(\text{PC})_{4.6}$ .

LPC@HKUST-1 powder was pressed into dense pellets (inset of **Figure 2-6**) and sandwiched between two stainless steel plates in coin cells to measure the ionic conductivity. The pellets are free of notable cracks or interparticle voids as examined by SEM (**Figure 2-6**). The ionic conductivity of LPC@HKUST-1 was determined using electrochemical impedance

spectroscopy (EIS). **Figure 2-7a** shows the Nyquist plots of the LPC@HKUST-1 pellets at various temperatures. The ionic resistance of the electrolytes was taken at the intersection between the high frequency semi-circle and the low frequency tail. The conductivity of LPC@HKUST-1 at room temperature is determined as  $0.38 \text{ mS cm}^{-1}$ , which is approximately one order of magnitude lower than that of liquid LPC, yet sufficiently high for device applications.

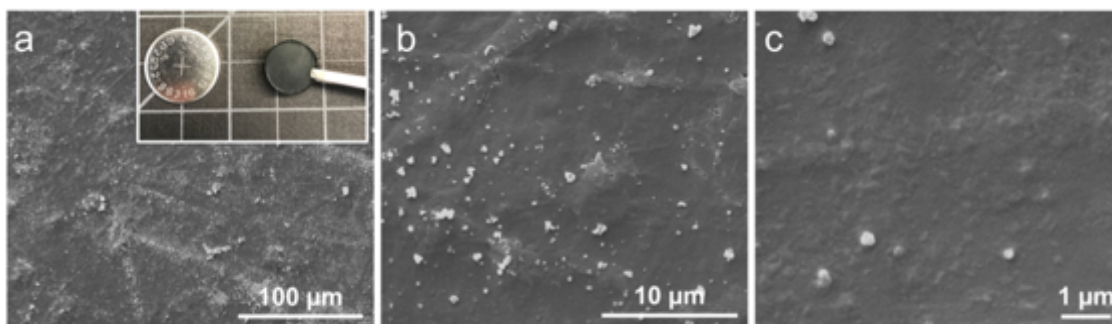


**Figure 2-6** SEM image of a pressed LPC@HKUST-1 pellet used for the conductivity studies (inset of 6a: a photograph of an electrolyte pellet).

To address a possible concern that the as-measured ionic conductivity is mainly contributed by the LPC trapped within the interparticle voids rather than by the ionic channels, we pre-soaked activated HKUST-1 with pyridine, a complexing agent that strongly binds to the OMSs. After removing any excess pyridine, the pore volume determined for pyridine-treated HKUST-1 (pyridine@HKUST-1) was determined to be  $\sim 0.05 \text{ cm}^3 \text{ g}^{-1}$  (**Figure 2-7b**). This value is ten times less than that measured for LPC@HKUST-1. The pyridine@HKUST-1 was then infiltrated with LPC, and pressed into pellets (LPC@ pyridine@HKUST-1) using the same ionic conductivity measurement procedure. Because of the pyridine binding, the conduction of lithium ions through the ionic channels is inhibited while that through the interparticle LPC is retained. As expected, the ionic conductivity for LPC@ pyridine@HKUST-1 exhibited 100X lower conductivity than LPC@HKUST-1 at room temperature and a significantly higher activation energy of 0.62 eV

(Figure 2-7c). This experiment is consistent with the hypothesis that the conductivity of LPC@HKUST-1 is mainly due to transport through the MOF channels.

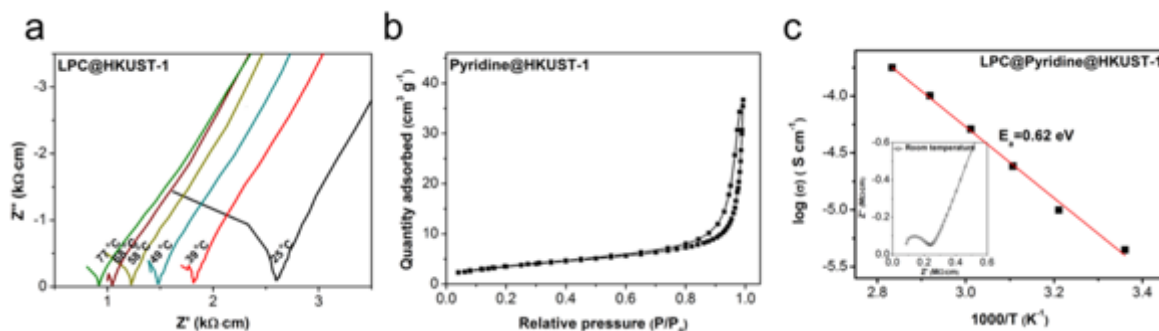


**Figure 2-7** (a) Nyquist plots of LPC@HKUST-1 as a function of temperature. (b) N<sub>2</sub> adsorption/desorption isotherms of pyridine@HKUST-1. (c) Arrhenius plot of LPC@pyridine@HKUST-1 (inset: Nyquist plot of LPC-pyridine@HKUST-1 at room temperature).

**Table 2-1** MOFs selected to synthesize electrolytes with biomimetic ionic channels.

|            | Formula  | Ligand structure                        | Pore size (nm)                  |
|------------|--|---|---------------------------------|
| HKUST-1    | Cu <sub>3</sub> (BTC) <sub>2</sub>                                   | BTC<br>benzene-1,3,5-tricarboxylic acid | 1.1                             |
| MIL-100-Al | Al <sub>3</sub> O(OH)(BTC) <sub>2</sub>                              |   | 2.5, 2.9<br>(windows: 0.6, 0.9) |
| MIL-100-Cr | Cr <sub>3</sub> O(OH)(BTC) <sub>2</sub>                              |   |                                 |
| MIL-100-Fe | Fe <sub>3</sub> O(OH)(BTC) <sub>2</sub>                              |   |                                 |
| UiO-66     | Zr <sub>6</sub> O <sub>4</sub> (OH) <sub>4</sub> (BDC) <sub>6</sub>  | BDC<br>benzene-1,4-dicarboxylic acid    | 0.75, 1.2                       |
| UiO-67     | Zr <sub>6</sub> O <sub>4</sub> (OH) <sub>4</sub> (BPDC) <sub>6</sub> | BPDC<br>Biphenyl-4,4'-dicarboxylic acid | 1.2, 2.3                        |

Notes:

- (1) MIL-100 serial MOFs ( $M_3O(BTC)_2OH \cdot (H_2O)_2$ ) are built from  $M^{3+}$  ( $M=Al, Cr, Fe$ ) octahedra trimer sharing a common  $\mu_3-O$ . Each  $M^{3+}$  is bonded to four oxygen atoms of bidendate dicarboxylate (BTC), and their linkage generates a hierarchical structure with mesoporous cages (25 and 29 Å) that are accessible through microporous windows (6 and 9 Å). The corresponding terminals in octahedra are generally occupied by removable guest molecules.
- (2) UiO-66 is obtained by bridging  $Zr_6O_4(OH)_4$  inorganic clusters with BDC linkers (BDC=1,4-dicarboxylate). The  $Zr_6$ -octahedrons are alternatively coordinated by  $\mu_3-O$ ,  $\mu_3-OH$  and O atoms from BDC, where  $\mu_3-OH$  could undergo dehydration to form a distorted  $Zr_6O_6$  node (seven-coordinated Zr) upon thermal activation. UiO-67 has the same topology as UiO-66 with expanded pore channels due to the larger linker size of BPDC (BPDC=biphenyl-4,4'-dicarboxylate). Both UiO-66 and UiO-67 contain two types of pore size, small tetrahedral pore and large octahedral pore.

The approach taken with LPC@HKUST-1 can be generalized to synthesize a family of solid-state electrolytes using MOFs with different metal centers, organic linkers, and crystalline structures (see **Table 2-1** for a list of selected MOFs), which are denoted as LPC@MOFs hereinafter. The Nyquist plots of the LPC@MOFs electrolytes at ambient temperature are displayed in **Figure 2-2c**, and their conductivities are summarized in **Table 2-2**. In this work, two series of isostructural MOFs were selected to study the effect of OMS and pore size on ionic conductivity. MIL-100 MOFs ( $M_3O(BTC)_2OH \cdot (H_2O)_2$ ,  $M = Al, Cr, Fe$ ) are built from  $M^{3+}$  octahedra trinuclear units interconnected by BTC ligands, which exhibit an identical pore structure

but with different OMSs (**Figure 2-8**).<sup>33</sup> The electrolyte based on MIL-100-Al (LPC@MIL-100-Al) exhibits the highest ionic conductivity of the LPC@MOF materials we characterized. The value of over 1 mS cm<sup>-1</sup> at room temperature is in the same order of magnitude as commercial gel electrolytes.<sup>34</sup> The conductivities of two other electrolytes, LPC@UiO-67 and LPC@MIL-100-Fe, also exhibit conductivity values over 0.5 mS cm<sup>-1</sup>. We found that the order of ionic conductivity of LPC@MIL-100-(Al/Cr/Fe) electrolytes is in line with the well-established Lewis acidity of OMS in the isostructural MIL-100-(Al/Cr/Fe) MOFs (Al > Fe > Cr).<sup>35</sup> This result suggests that the stronger acidity of OMS leads to greater dissociation of ion pairings and enhances ion transport.

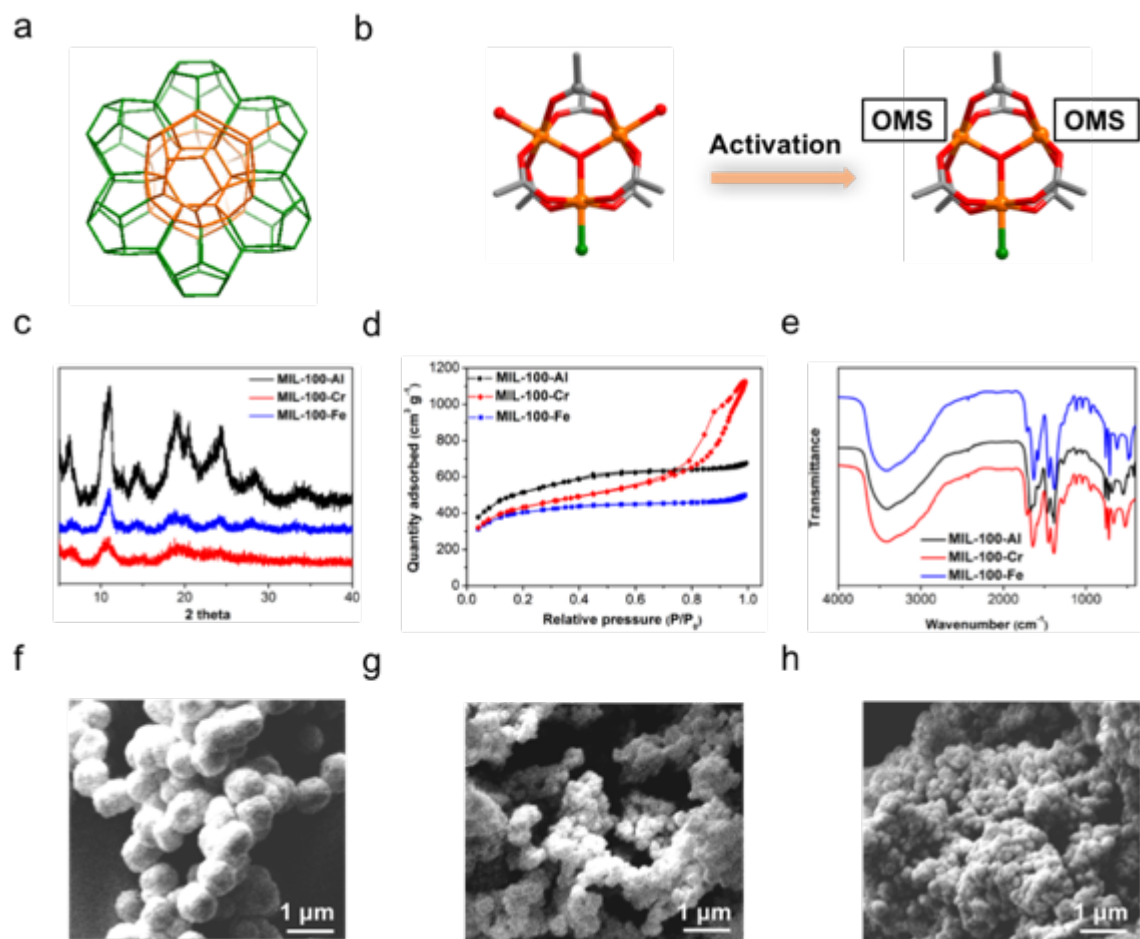


**Figure 2-8** Structures and characterizations of MIL-100 serial MOFs: (a) Structure representation of two types of mesoporous cages in MIL-100 serial MOFs. (b) Illustration of OMS evolution in a metal trimer unit of MIL-100 serial MOFs (orange atoms Al/Cr/Fe, red atoms O, grey atoms C, green atoms anionic ligands). Characterizations of synthesized MIL-100 serial MOFs. (c) XRD patterns. (d) N<sub>2</sub> adsorption/desorption isotherms. The analogous isotherms confirm the similar porous structure of the MIL-100 serial MOFs. There is a large non-negligible N<sub>2</sub> adsorption at relative high pressure for MIL-100-Cr, which corresponds to large interparticular porosity and is expected to be eliminated during preparation of electrolyte pellet. (e) FT-IR spectra. The FT-IR spectra together with the XRD patterns confirm the successful synthesis of isostructural MIL-100 materials. SEM images of (f) MIL-100-Al, (g) MIL-100-Cr, and (h) MIL-100-Fe.



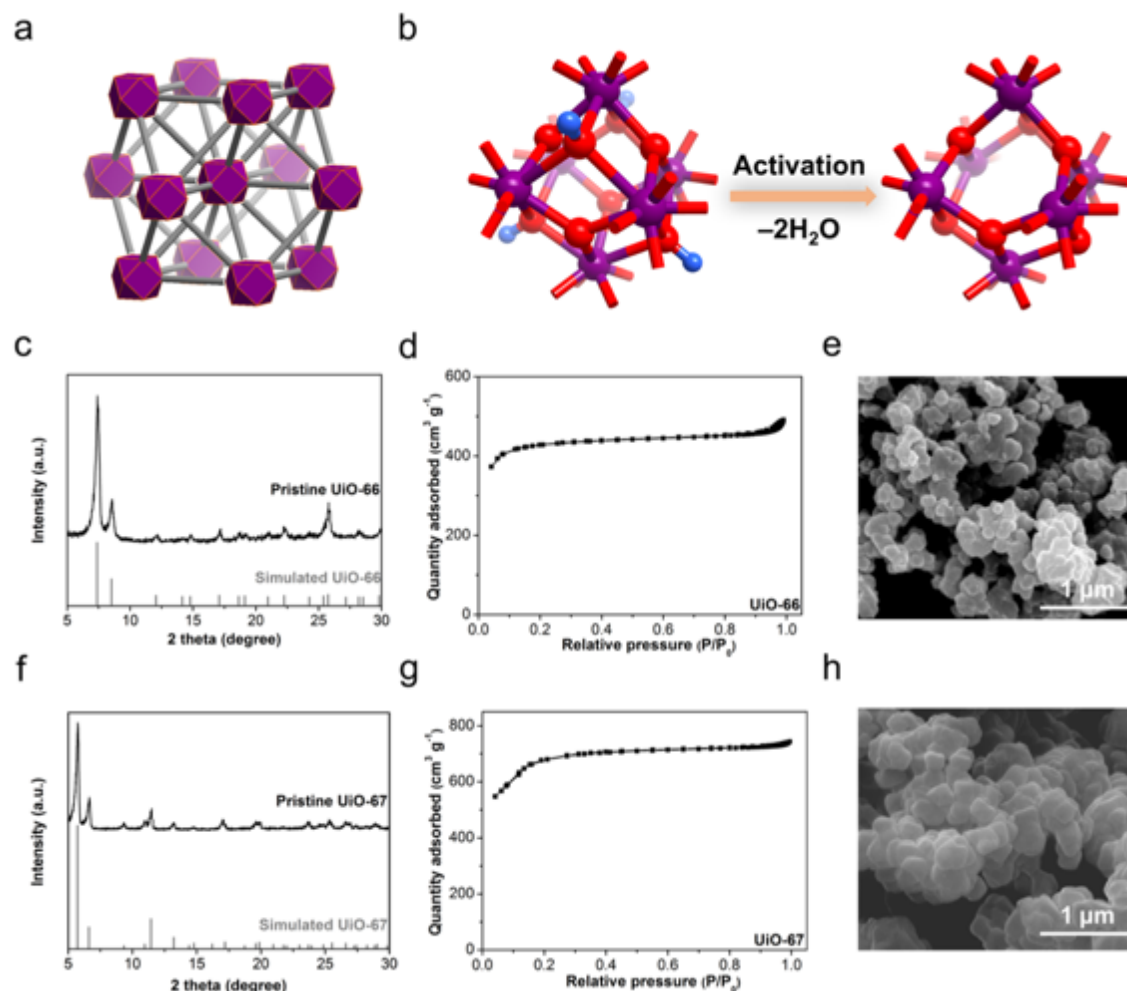


**Figure 2-9** Structures and characterizations of UiO-(66/67) serial MOFs: (a) Topology structure of UiO-(66/67) serial MOFs, the purple polyhedra represent inorganic  $Zr_6O_4(OH)_4$  clusters, the grey sticks manifest organic linkers (BDC and BPDC for UiO-66 and UiO-67, respectively). (b) Schematic illustration for activation of UiO-(66/67) serial MOFs (purple: Zr, red: O, blue: H). OMSs are created by dehydration of  $Zr_6O_4(OH)_4$  units. Characterizations of synthesized (c-e) UiO-66 and (f-h) UiO-67. (c, f) XRD patterns. Insets show the crystal structures of the corresponding MOFs. (d, g)  $N_2$  adsorption/desorption measurements. The curve of UiO-66 exhibit a typical microporous isotherm with a BET surface area of  $1376 \text{ cm}^2 \text{ g}^{-1}$  and a microporous volume of  $0.55 \text{ cm}^3 \text{ g}^{-1}$ . The isotherm of UiO-67 show an adsorption/desorption step at ca.  $0.1 P/P_0$  due to presence

of two types of pores (see supplementary Table 1). The calculated BET surface area is 2000 cm<sup>2</sup> g<sup>-1</sup> and microporous volume is 0.7 cm<sup>3</sup> g<sup>-1</sup>. (e, h) SEM images.

**Table 2-2** Ambient conductivities and activation energies of various LPC@MOF electrolytes.

| LPC@MOF electrolyte | Conductivity (mS cm <sup>-1</sup> ) | Activation energy (eV) |
|---------------------|-------------------------------------|------------------------|
| LPC@MIL-100-Al      | 1.22                                | 0.21                   |
| LPC@MIL-100-Fe      | 0.9                                 | 0.18                   |
| LPC@UiO-67          | 0.65                                | 0.12                   |
| LPC@HKUST-1         | 0.38                                | 0.18                   |
| LPC@MIL-100-Cr      | 0.23                                | 0.18                   |
| LPC@UiO-66          | 0.18                                | 0.21                   |

To examine the effect of pore size on ionic conductivity, UiO-66 (Zr<sub>6</sub>O<sub>4</sub>(OH)<sub>4</sub>(BDC)<sub>6</sub>, BDC=1,4-dicarboxylate) and UiO-67 (Zr<sub>6</sub>O<sub>4</sub>(OH)<sub>4</sub>(BPDC)<sub>6</sub>, BPDC=biphenyl-4,4'-dicarboxylate) were used as a model system. As depicted in **Table 2-1** and **Figure 2-9**, both UiO-66 and UiO-67 are obtained by bridging the Zr<sub>6</sub>O<sub>4</sub>(OH)<sub>4</sub> cornerstones with BDC or BPDC linkers, possessing the same topology structure and OMS, but with different pore size. Upon activation, the Zr<sub>6</sub>O<sub>4</sub>(OH)<sub>4</sub> units (eight-coordinated Zr) undergo dehydration and the resulting Zr<sub>6</sub>O<sub>6</sub> clusters (seven-coordinated Zr) possess unsaturated open Zr<sup>4+</sup> sites. The UiO-66 exhibits bi-continuous porous channels with a pore diameter of 0.75 nm and 1.2 nm, respectively; while UiO-67 shows a similar porous structure with a larger pore diameter of 1.2 nm and 2.3 nm, respectively.<sup>36</sup> The EIS measurements show that LPC@UiO-67 exhibits a higher ionic conductivity (0.65 mS cm<sup>-1</sup> vs. 0.18 mS cm<sup>-1</sup>). We propose that the higher conductivity observed for UiO-67 is attributed to its larger pore channels that allow more effective solvation of the lithium ions, with less of a confinement effect (see **Figure 2-10** and **Table 2-3**).

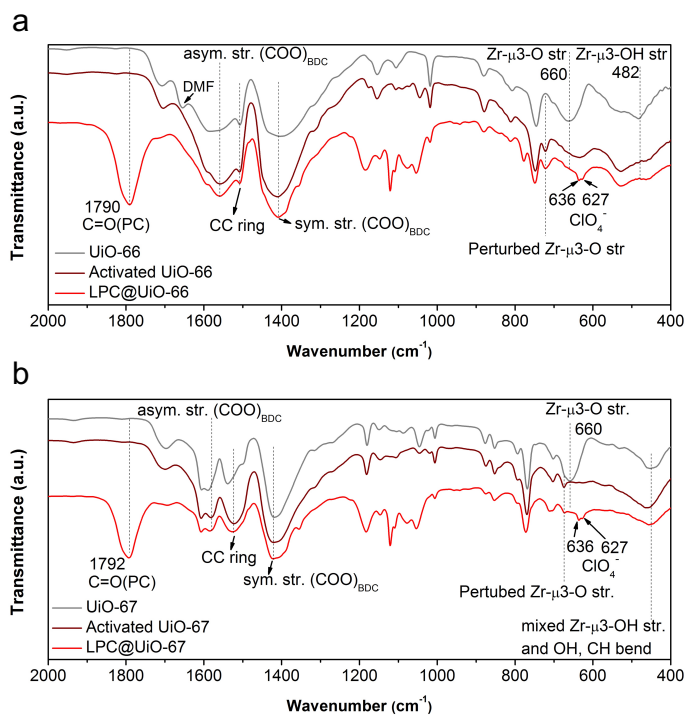


**Figure 2-10** FT-IR spectra of (a) pristine UiO-66, activated UiO-66 and LPC@UiO-66, (b) pristine UiO-67, activated UiO-67 and LPC@UiO-67.

**Table 2-3** Major peak assignments for pristine/activated UiO-(66/67) and LPC@UiO-(66/67) electrolytes.

|                  | Zr- $\mu_3$ -OH | Zr- $\mu_3$ -O | Asym. str. of<br>(COO) <sub>BDC</sub> | CC ring | (C=O) <sub>PC</sub> | ClO <sub>4</sub> <sup>-</sup> |
|------------------|-----------------|----------------|---------------------------------------|---------|---------------------|-------------------------------|
| Pristine UiO-66  | 482             | 660            | 1576(b)                               | 1506    | -                   | -                             |
| Activated UiO-66 | -               | 720            | 1557                                  | 1506    | -                   | -                             |
| LPC@UiO-66       | -               | 720(b)         | 1559                                  | 1506    | 1790                | 627, 636                      |
| Pristine UiO-67  | 457(*)          | 660            | 1589                                  | 1540    | -                   | -                             |
| Activated UiO-67 | -               | 675            | 1581                                  | 1522    | -                   | -                             |
| LPC@UiO-67       | -               | 673            | 1584                                  | 1525    | 1792                | 627, 636                      |

(\*) Zr- $\mu_3$ -OH (457) assigned to UiO-67 is obscured by mixed -OH and -CH bend in the same range.

(b) broadened peaks involving multi-components.

## Notes:

UiO-66 and UiO-67 show similar trends in following aspects. 1) Owing to the removal of capping hydroxides at Zr metal centers after activation, those vibrations associated with Zr- $\mu_3$ -OH are eliminated, coupled with blue shifts of peaks pertaining to Zr- $\mu_3$ -O due to distorted local symmetry of Zr<sub>6</sub> clusters.<sup>36,37</sup> After complexing with LPC, Zr- $\mu_3$ -O vibrations are either broadened or red shifted, signifying the symmetry recovery of Zr clusters due to introduced guest molecules. 2) Activation causes the red shift of asymmetric components of (COO) in BDC linkers. After complexing with LPC, those shifts are partially recovered. 3) Aside from a typical peak at 627 cm<sup>-1</sup> for characteristic ClO<sub>4</sub><sup>-</sup> vibration in LPC, the ClO<sub>4</sub><sup>-</sup> at LPC@UiO-(66/67) electrolytes exhibits significant breakdown of its tetrahedral symmetry, as evidenced by the emergence of new peaks at 636 cm<sup>-1</sup>.

The carboxyl (C=O) stretching of PC is indicative of Li<sup>+</sup> solvation status by PC. The peak at 1792 cm<sup>-1</sup> for LPC@UiO-67 compared with 1790 cm<sup>-1</sup> for LPC@UiO-66 demonstrates weaker C=O (PC) interaction of Li<sup>+</sup> within UiO-67 pore channels. It is believed that the slightly expanded pore channels of UiO-67 allow incorporation of more PC to leverage Li<sup>+</sup> and ClO<sub>4</sub><sup>-</sup> under nano-confinement, therefore affording higher ionic conductivity.

The electrolytes exhibit temperature-dependent conductivities with typical Arrhenius-like behavior. Specifically, the activation energies measured are in the range of 0.12-0.21 eV (**Figure 2-2d**), which are slightly higher than that of LPC liquid electrolyte (0.10 eV, see **Figure 2-11**). The activation energy for conduction in LPC@UiO-67 is consistently lower than that of LPC@UiO-66 (0.12 eV vs. 0.21 eV) which could be due to its larger pore size (**Table 2-3**). The activation energies for these MOFs electrolytes are in the same range or lower compared to the activation energies reported for solid electrolytes, including the well-established ceramic

electrolytes (e.g.,  $\text{Li}_{10}\text{GeP}_2\text{S}_{12}$  (0.25 eV),<sup>11</sup> glassy  $\text{Li}_2\text{S-P}_2\text{S}_5$  (0.19 eV),<sup>38</sup> and garnet  $\text{Li}_7\text{La}_3\text{Zr}_2\text{O}_{12}$  (0.3–0.4 eV)<sup>39</sup>).

**Figure 2-2e** further compares the ionic conductivity of  $\text{LPC@UiO-67}$ ,  $\text{LPC@MIL-100-Al}$ , and  $\text{LPC@MIL-100-Fe}$  with other solid-state electrolytes that have been well studied. The conductivity at room temperature of these MOF-ion channel electrolytes surpasses most polymeric electrolytes (e.g.,  $\text{LiClO}_4/\text{PEO}$  with  $\text{TiO}_2$  additive and PEO-based single ion polymer<sup>40</sup>), ceramic electrolytes (e.g., garnet  $\text{Li}_7\text{La}_3\text{Zr}_2\text{O}_{12}$ <sup>39</sup>, and  $\text{LiPON Li}_{3.5}\text{PO}_3\text{N}_{0.5}$ <sup>41</sup>), and other MOF-based systems (e.g., Li alkoxide@MOFs<sup>21</sup>, Li halide-PC@MOFs,<sup>23</sup> and ionic liquid@MOFs<sup>29</sup>). With a conductivity higher than  $10^{-4} \text{ S cm}^{-1}$  and an activation energy below 0.21 eV, such  $\text{LPC@MOFs}$  electrolytes represent an exciting family of fast ion conductors.<sup>42</sup>

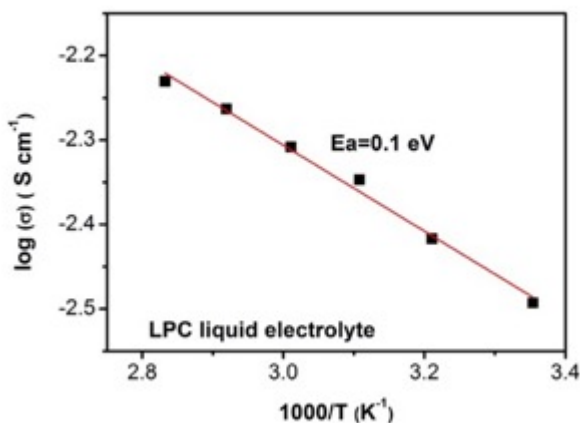


**Figure 2-11** Arrhenius plot of LPC liquid electrolyte and calculated activation energy for ionic conduction.

## 2.2.2 Spectroscopic Studies of Activated and Modified Ionic Channels

Raman spectroscopy was used to characterize the nature of the molecular features that lead to LPC@MOFs with high ionic conductivity. **Figure 2-12a** shows the Raman spectra of PC, LPC, HKUST-1 soaked with PC (denoted as PC@HKUST-1), and LPC@HKUST-1. Both PC@HKUST-1 and LPC@HKUST-1 show the featured peaks of HKUST-1 associated with the BTC ligands at 746, 832 and 1010  $\text{cm}^{-1}$ , which agree well with the literature (see detailed assignments in **Table 2-4**).<sup>43, 44</sup> Upon infiltrating HKUST-1 with LPC, the peak ascribed the Cu–O (carboxylate oxygen atom from the ligands) vibration shifts from 496  $\text{cm}^{-1}$  to 499  $\text{cm}^{-1}$ . These observations are consistent with the shortening/strengthening of the Cu–O bonds.<sup>44</sup>

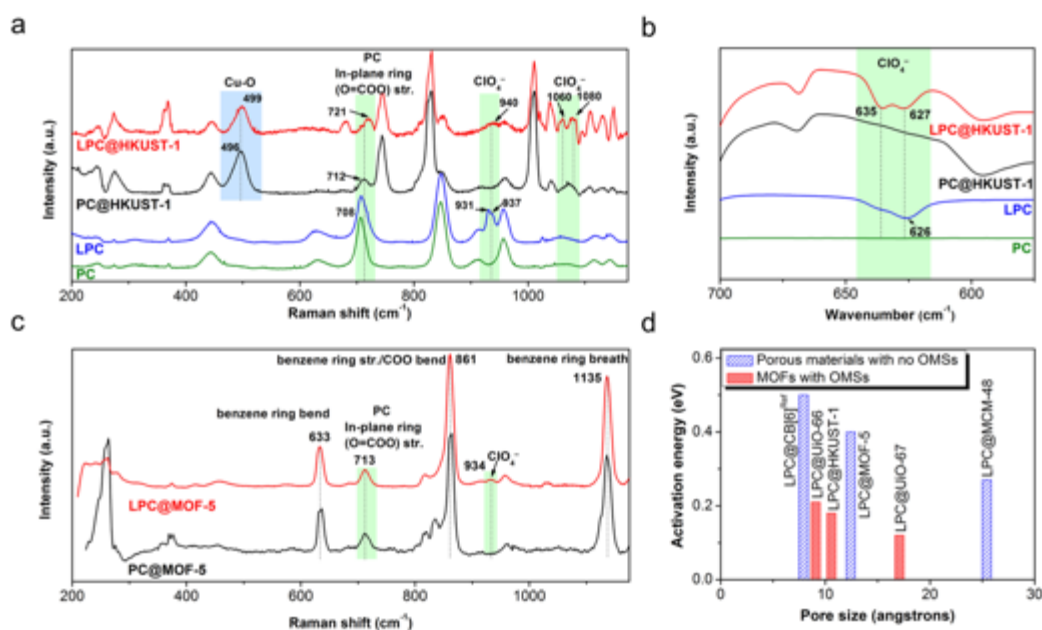


**Figure 2-12** Spectroscopic investigation of LPC@MOFs electrolytes. (a) Raman spectra of PC, LPC, PC@HKUST-1, and LPC@HKUST-1. (b) FT-IR spectra of PC, LPC, PC@HKUST-1, and LPC@HKUST-1. (c) Raman spectra of PC@MOF-5 and LPC@MOF-5. (d) Comparison of the activation energies of four LPC@MOFs electrolytes (LPC@HKUST-1, LPC@UiO-66, LPC@UiO-67, and LPC@MOF-5) and two liquid-in-solid conductors ((LPC@CB[6])<sup>28</sup> and

LPC@MCM-48) vs. their pore sizes, indicating the effect of pore size and OMS on their activation energy. The pore size of LPC@UiO-66 and LPC@UiO-67 are averaged based the pore diameter of their bi-continuous pore channels.

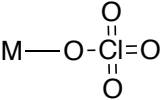
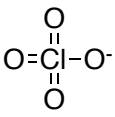
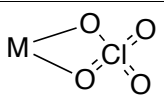
**Table 2-4** Detailed peak assignments for Raman spectra of PC, LPC, activated HKUST-1,<sup>44</sup> PC@HKUST-1, and LPC@HKUST-1.<sup>a</sup>

| PC                 | LPC                | HKUST-1 | PC@HKUST-1                | LPC@HKUST-1               | Assignments   |
|--------------------|--------------------|---------|---------------------------|---------------------------|---|
| -                  | -                  | 276     | 276                       | 274                       | Cu-Cu ( <b>HKUST-1</b> )  |
| 444                | 446                | 449     | 444                       | 446                       | O=COO ( <b>PC</b> )<br>bending + Cu-O<br>( <b>HKUST-1</b> )   |
| -                  | -                  | 505     | 496                       | 499                       | Cu-O ( <b>HKUST-1</b> )   |
| 708                | 708                | 722     | 712                       | 721                       | O=COO ( <b>PC</b> ) in-<br>plane stretching + C-<br>H out-of-plane<br>bending of ring<br>( <b>HKUST-1</b> ) |
| -                  | -                  | 746     | 746                       | 746                       | C-H out-of-plane<br>bending of ring<br>( <b>HKUST-1</b> )   |
| -                  | -                  | 828     | 832                       | 832                       | C-H out-of-plane<br>bending of ring<br>( <b>HKUST-1</b> )   |
| 850                | 850                | -       | 850                       | 850                       | Symmetric stretching<br>of <b>PC</b> ring   |
| -                  | 931, 937           | -       | -                         | 940                       | $\nu_1$ vibration mode of<br><b>ClO<sub>4</sub><sup>-</sup></b>   |
| 959                | 959                | -       | 960                       | 960                       | In-plane <b>PC</b> ring<br>stretching   |
| -                  | -                  | 1008    | 1010                      | 1010                      | Symmetric stretching<br>(C=C) of benzene<br>ring ( <b>HKUST-1</b> )   |
| -                  | -                  | -       | -                         | 1060, 1080                | $\nu_3$ vibration mode of<br><b>ClO<sub>4</sub><sup>-</sup></b>   |
| 1058,1116,<br>1144 | 1058,1116,<br>1144 | -       | 1070, 1109,<br>1131, 1150 | 1070, 1109,<br>1131, 1150 | O=COO ( <b>PC</b> ) in-<br>plane stretching   |

<sup>a</sup>Peaks at 1041 cm<sup>-1</sup> are tentatively assigned to signals of ligands in HKUST-1.

The Raman spectra related to PC provide further insights into the interactions between the MOFs and LPC. PC exhibits a well-resolved peak at 708 cm<sup>-1</sup>, originating from the characteristic PC in-plane carbonyl (O=COO) stretching.<sup>45</sup> Upon addition of LiClO<sub>4</sub>, LPC shows a broadened carbonyl stretching peak at 708 cm<sup>-1</sup> due to its solvation with Li<sup>+</sup> ions.<sup>45, 46</sup> The emerging peaks at 931 and 937 cm<sup>-1</sup> represent the  $\nu_1$  symmetric vibrational stretch of ClO<sub>4</sub><sup>-</sup> and ClO<sub>4</sub><sup>-</sup> paired with Li<sup>+</sup>, respectively.<sup>47</sup> Since the carbonyl stretching is sensitive to the surrounding environment, the Raman shift increases from 708 cm<sup>-1</sup> for PC to 712 cm<sup>-1</sup> for PC@HKUST-1, indicating their interaction with the MOF scaffold. The frequency of the carbonyl stretching further increases to 721 cm<sup>-1</sup> for LPC@HKUST-1, implying stronger solvation of Li<sup>+</sup> ions within the channels.<sup>46</sup> In addition, carbonyl stretching of “free” PC as in LPC is barely observed in LPC@HKUST-1, further confirming the presence of PC and LiClO<sub>4</sub> within the pore channels of MOF.

**Table 2-5** Vibration of ClO<sub>4</sub> group as a function of symmetry.<sup>48, 49a</sup>

| State of ClO <sub>4</sub>   | Symmetry        | Coordination state | Vibration mode                          |  |   |  |
|---|-----------------|--------------------|---|--|---|--|
|  | C <sub>3v</sub> | monodentate        | A <sub>1</sub>                          | E  | A <sub>1</sub> +E                                     | A <sub>1</sub> +E                                    |
|  | T <sub>d</sub>  | uncoordinated      | $\nu_1$<br>A<br>(931 cm <sup>-1</sup> ) | $\nu_2$<br>E <sup>b</sup><br>(460 cm <sup>-1</sup> ) | $\nu_3$<br>F <sub>2</sub><br>(1100 cm <sup>-1</sup> ) | $\nu_4$<br>F <sub>2</sub><br>(626 cm <sup>-1</sup> ) |
|  | C <sub>2v</sub> | bidentate          | A <sub>1</sub>                          | A <sub>1</sub> +A <sub>2</sub> <sup>b</sup>          | A <sub>1</sub> +B <sub>1</sub> +B <sub>2</sub>        | A <sub>1</sub> +B <sub>1</sub> +B <sub>2</sub>       |

<sup>a</sup>A and B, non-degenerate; E, doubly degenerate; F, triply degenerate. <sup>b</sup>Infrared disallowed.



The perchlorate group has a built-in spectroscopic handle that enables determination of the complexation state when coordinated to the Cu metal centers. As perchlorate becomes coordinated to the OMS, the original  $T_d$  symmetry of perchlorate is reduced to  $C_{3v}$  and then  $C_{2v}$  for monodentate and bidentate perchlorate, respectively (see **Table 2-5**). Consistent with the enhanced  $\text{Li}^+$  solvation, the peaks associated with free  $\text{ClO}_4^-$  at  $931\text{ cm}^{-1}$  and  $\text{Li}^+-\text{ClO}_4^-$  ion-pairs at  $937\text{ cm}^{-1}$  disappear in  $\text{LPC@HKUST-1}$ , and a new peak appearing at  $940\text{ cm}^{-1}$  indicates the coordination of  $\text{ClO}_4^-$  to the OMS.<sup>45, 47, 50-53</sup> For  $\text{PC@HKUST-1}$ , the peaks at  $1070$ ,  $1109$ ,  $1131$ , and  $1150\text{ cm}^{-1}$  pertain to the stretching and bending of the PC molecules. In  $\text{LPC@HKUST-1}$ , an emergence of two well-resolved peaks at  $1060$  and  $1080\text{ cm}^{-1}$  is attributed to the breakdown of  $\text{ClO}_4^-$  symmetry, which is regarded as evidence for the coordination of  $\text{ClO}_4^-$  to  $\text{Cu}^{\text{II}}$  complex according to reported literature.<sup>48, 49, 54-56</sup>

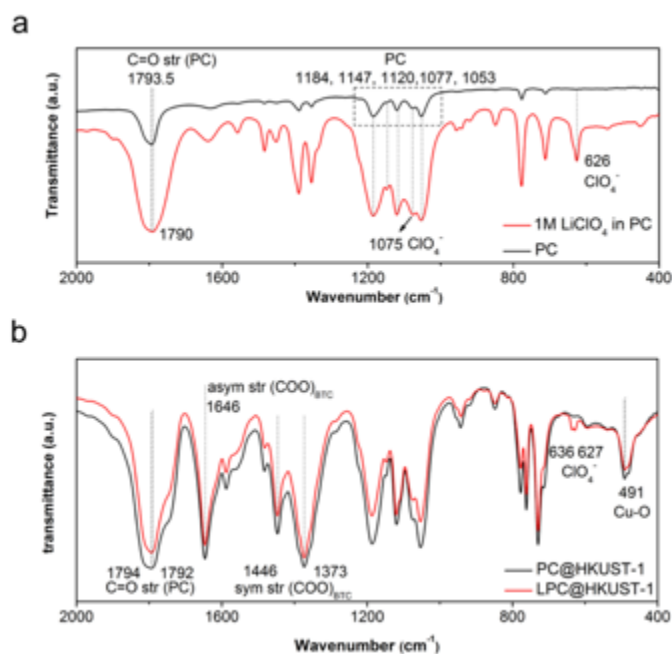


**Figure 2-13** FT-IR spectra of (a) PC and 1M LPC, (b)  $\text{PC@HKUST-1}$  and  $\text{LPC@HKUST-1}$ .

The complexation of  $\text{ClO}_4^-$  with OMS is further confirmed by FT-IR. **Figure 2-12b** shows the FT-IR spectra for PC, LPC, PC@HKUST-1, and LPC@HKUST-1 (see full spectra in **Figure 2-13**). LPC shows a sharp peak at  $626\text{ cm}^{-1}$ , which arises from the symmetric vibration of the  $\text{ClO}_4^-$  ions. LPC@HKUST-1 exhibits two distinct  $\text{ClO}_4^-$  peaks at  $635$  and  $627\text{ cm}^{-1}$  due to its interaction with the OMS. To confirm this observation, copper (II) perchlorate hexahydrate ( $\text{Cu}(\text{ClO}_4)_2 \cdot 6\text{H}_2\text{O}$ ) was heated to remove crystalline water, resulting in complexation of  $\text{ClO}_4^-$  to the copper centers. As compared in **Figure 2-14**, the FT-IR spectrum of  $\text{Cu}(\text{ClO}_4)_2 \cdot 6\text{H}_2\text{O}$  shows the  $\text{ClO}_4^-$  peak at  $627\text{ cm}^{-1}$ . During the dehydration process,  $\text{ClO}_4^-$  coordinates to the Cu(II) sites, creating an additional peak at  $635\text{ cm}^{-1}$ . This analogous scenario constitutes strong evidence that the peak at  $635\text{ cm}^{-1}$  in LPC@HKUST-1 is associated with the breakdown of the symmetric structure of free  $\text{ClO}_4^-$  and its coordination to OMS.<sup>55, 57, 58</sup>

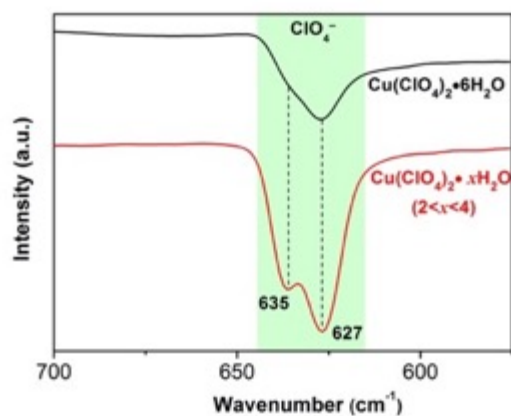


**Figure 2-14** FT-IR spectra of  $\text{Cu}(\text{ClO}_4)_2 \cdot 6\text{H}_2\text{O}$  and  $\text{Cu}(\text{ClO}_4)_2 \cdot x\text{H}_2\text{O}$ , where  $2 < x < 4$ .

The spectroscopic studies clearly suggest that OMSs do play essential roles in ionic conduction. To experimentally verify this finding, an electrolyte analogue was prepared using MOF-5 ( $\text{Zn}_4\text{O}(\text{BDC})_3$ ), which possesses a similar pore diameter (1.2 nm) to that of HKUST-1 (1.1 nm) but contains no OMS (**Figure 2-15**). Compared with LPC@HKUST-1, LPC@MOF-5 shows

inferior room temperature ionic conductivity of  $0.13 \text{ mS cm}^{-1}$  higher activation energy of  $0.4 \text{ eV}$  (Figure 2-15). Figure 2-12c further compares the Raman spectra of PC@MOF-5 and LPC@MOF-5, where the stretching at  $934 \text{ cm}^{-1}$  in LPC@MOF-5 indicates ion pairing between  $\text{ClO}_4^-$  and  $\text{Li}^+$ . This observation confirms the essential role of OMSs, which coordinate with anions to form negatively charged ionic-channel analogs.

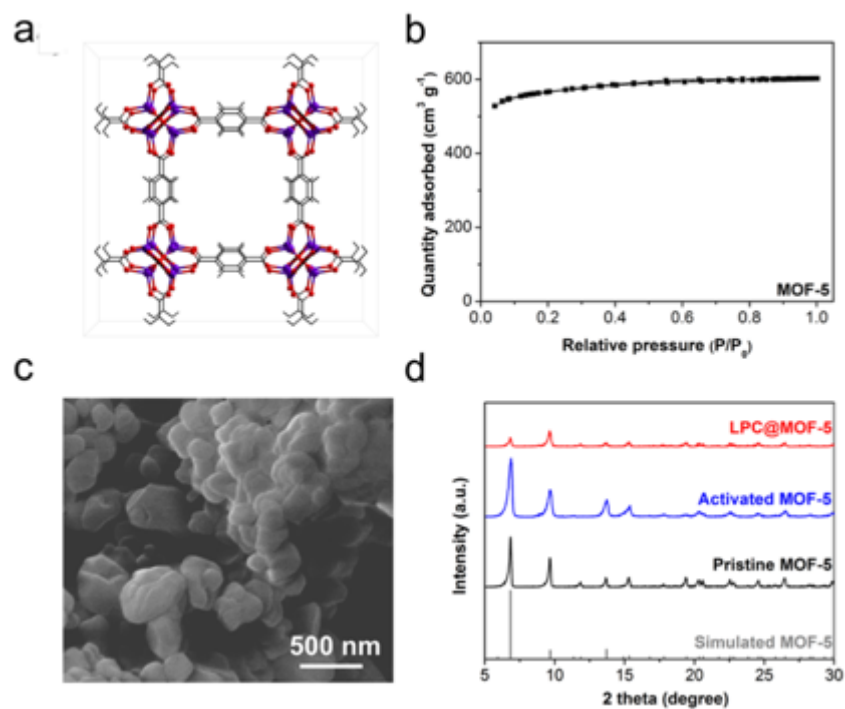


**Figure 2-15** (a) Cubic structure of MOF-5 ( $\text{Zn}_4\text{O}(\text{BDC})_3$ ) in a ball-and-stick model (purple: Zn, red: oxygen, black: carbon), in which oxo-centered ( $\mu_4\text{-O}$ )  $\text{Zn}_4$  tetrahedra are interconnected through BDC to yield a highly porous framework with pore aperture of  $8 \text{ \AA}$  and pore diameter of  $12 \text{ \AA}$ .<sup>59, 60</sup> (b)  $\text{N}_2$  adsorption/desorption isotherms of MOF-5. The pristine MOF-5 exhibits higher BET surface area of  $1810 \text{ m}^2 \text{ g}^{-1}$  and pore volume of  $0.75 \text{ cm}^3 \text{ g}^{-1}$  compared with HKUST-1. (c) SEM image of MOF-5. (d) XRD patterns of simulated, pristine, activated, and LPC infiltrated MOF-5. The major crystal structure is unaltered, except for the change of a few peak intensities due to the presence of guest molecules.<sup>61</sup>

**Figure 2-12d** summarizes and compares the activation energies of four LPC@MOFs electrolytes with two porous materials infiltrated with LPC. The pore sizes of LPC@CB[6], LPC@UiO-66, LPC@HKUST-1, and LPC@MOF-5 are in a similar range; nevertheless, those with OMSs show significantly lower activation energy. For example, LPC@MOF-5 (pore size of 1.2 nm) and LPC@CB[6]<sup>28</sup> (pore size of 0.75 nm) show an activation energy of 0.4 eV and 0.5 eV, respectively, which is more than twice that of LPC@HKUST-1 (pore size of 1.1 nm) and LPC@UiO-66 with an average pore size of 1 nm (**Figure 2-16**). A similar phenomenon is found between LPC@UiO-67 (pore size of 2.3 nm with OMSs) and mesoporous silica LPC@MCM-48 (pore size of 2.5 nm without OMS, **Figure 2-17**). The LPC@MCM-48 exhibits a notably higher activation energy (~ 0.27 eV) than LPC@UiO-67 (~ 0.12 eV). It is important to note that the activation energy for both MOFs with OMSs and MOFs without OMS seem to decrease with increasing pore size as perhaps confinement and tortuosity effects are reduced with larger pores.

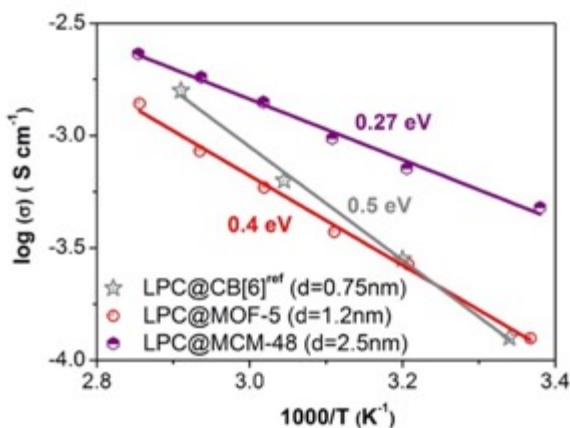


**Figure 2-16** Arrhenius plots of LPC@CB[6]<sup>28</sup>, LPC@MOF-5, and LPC@MCM-48. The plot of LPC@CB[6] is linearly fitted based on conductivity data reported in the reference, resulting in an activation energy different from the reported value.

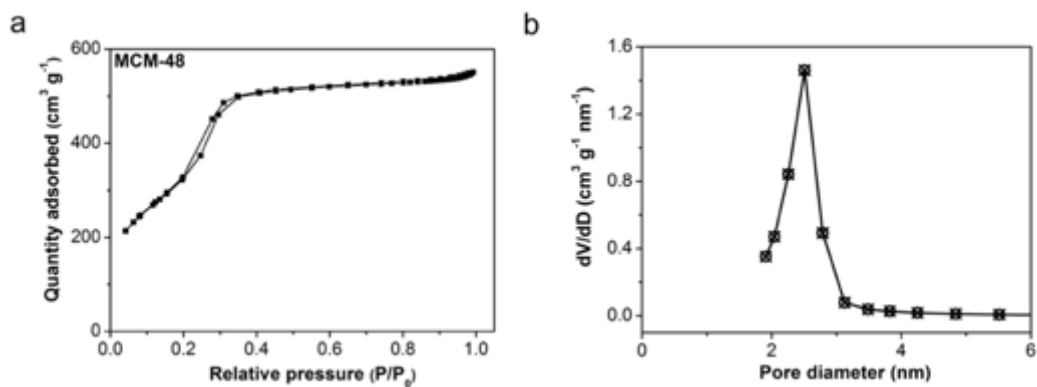


**Figure 2-17** Synthesized MCM-48 mesoporous silica (a) N<sub>2</sub> adsorption/desorption isotherms (BET surface area: 1301 cm<sup>2</sup> g<sup>-1</sup>, total pore volume: 0.85 cm<sup>3</sup> g<sup>-1</sup>). (b) BJH pore size distribution. MCM-48 was prepared according to a method reported in the literature.<sup>62</sup>

### 2.2.3 Electrochemical Performance of the Electrolytes

In short, we have achieved lithium ion conduction in MOF channels by complexing electrolyte anions to the OMSs within channels filled with solvent molecules. Such complexing weakens the interactions between  $\text{Li}^+$  cations and the anions, enabling fast conduction of  $\text{Li}^+$  ions through the channels. Stronger interactions between the OMSs and the anions, and larger pore sizes lead to electrolytes with higher ionic conductivity and lower activation energy. A series of experiments were then designed to characterize some of the electrochemical properties, one of the MOF electrolytes,  $\text{LPC@UiO-67}$ , in view of its high ionic conductivity and high stability. **Figure 2-18a** shows the cyclic voltammetry (CV) of a cell, which contains a lithium metal counter electrode, an  $\text{LPC@UiO-67}$  electrolyte pellet, and a stainless steel (SS) working electrode ( $\text{Li}|\text{LPC@UiO-67}|\text{SS}$ ). The cell was tested using a scan rate of  $0.5 \text{ mV s}^{-1}$  at a potential range from  $-0.2$  to  $5 \text{ V vs. Li/Li}^+$ . Liquid LPC and PP separator were used to assemble the reference cells. During the cathodic sweep below  $1 \text{ V vs. Li/Li}^+$ , the current associated with the irreversible reduction of  $\text{ClO}_4^-$  and PC is less pronounced in  $\text{LPC@UiO-67}$  in comparison with that of LPC.<sup>62</sup> During the anodic sweep, the onset of the oxidation current peak upshifts by  $0.2 \text{ V}$  for  $\text{LPC@UiO-67}$  in comparison with that of LPC, demonstrating improved anodic stability of  $\text{LPC@UiO-67}$ . In addition, the anodic stability of  $\text{LPC@HKUST-1}$  is inferior to that of  $\text{LPC@UiO-67}$ . Compared with the CVs of  $\text{LPC@HKUST-1}$ ,  $\text{LPC@UiO-66}$  and  $\text{LPC@MIL-100}$  serial MOF (**Figure 2-19**), we confirm a working voltage window of  $\text{LPC@UiO-67}$  from  $-0.2$  to  $4.5 \text{ V}$ . For instance,  $\text{LPC@HKUST-1}$  shows much significant cathodic current below  $2 \text{ V vs. Li/Li}^+$ , which is related to the reduction of  $\text{Cu}^{\text{II}}$ . The redox peaks around  $0 \text{ V}$  associated with lithium plating/stripping is less reversible compared with  $\text{LPC@UiO-67}$ .

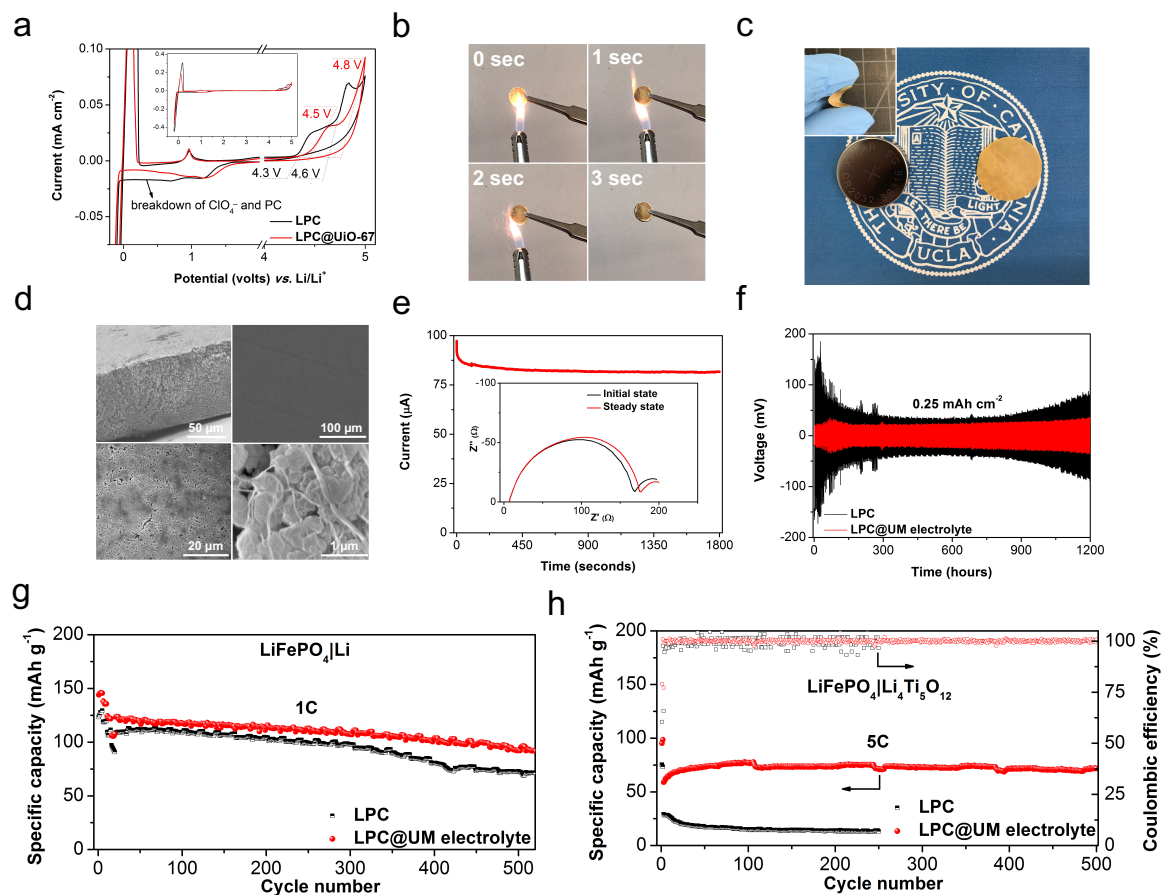


**Figure 2-18** Electrochemical performance of LPC@MOF electrolyte and prototype lithium-based batteries. (a) Cyclic voltammetry (CV) comparison between LPC@UiO-67 pellet and LPC electrolytes. (b) Flammability test of a LPC@UiO-67 electrolyte pellet. (c) Photograph of a LPC@UiO-67/PTFE membrane (LPC@UM) next to a coin cell (inset shows a bent LPC@UM). (d) SEM images of LPC@UM (top-left: cross-sectional view). (e) Current-time profile for Li|LPC@UM|Li cell at 20 mV of polarization (inset: impedance spectra at initial and steady states). (f) Li symmetric cell test comparison between LPC@UM and LPC at a current density of 0.125 mA cm<sup>-2</sup> (0.25 mAh cm<sup>-2</sup>). (g) Galvanostatic long-cycle stability tests at 1 C (1 C=170 mA g<sup>-1</sup>, initially cycled at 0.2, 0.5, 1, and 2 C for five cycles each) of prototype LiFePO<sub>4</sub>|Li batteries with LPC@UM electrolyte and LPC liquid electrolyte. (h) Long-term cycling stability of prototype LiFePO<sub>4</sub>|Li<sub>4</sub>Ti<sub>5</sub>O<sub>12</sub> batteries with LPC@UM electrolyte and LPC liquid electrolyte at 5 C (first

two cycles at 1 C).

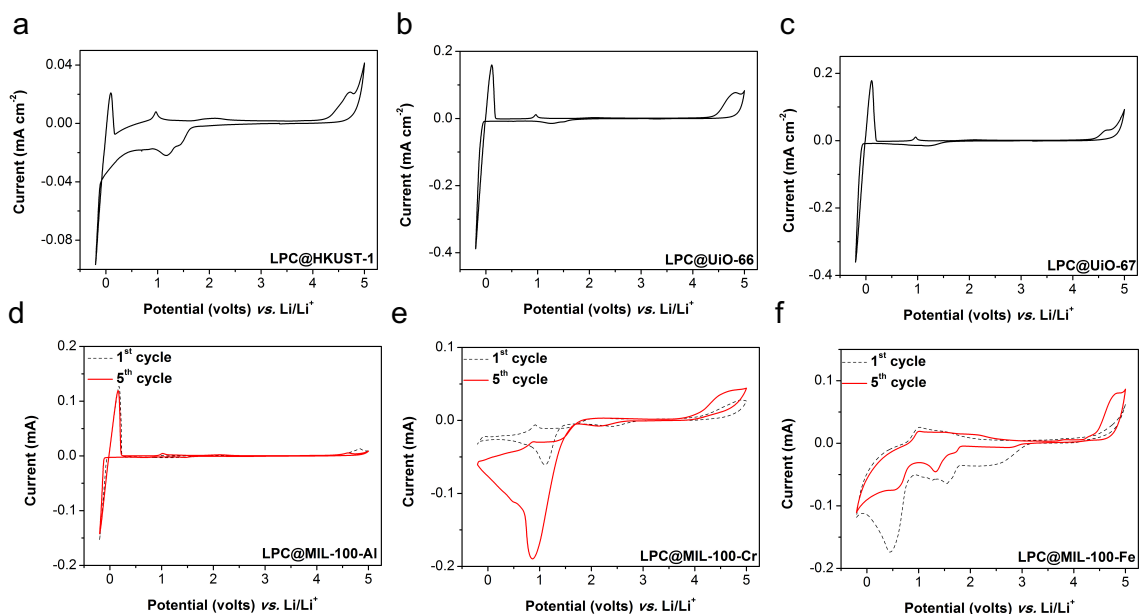


**Figure 2-19** Cyclic voltammetry of stainless steel|electrolyte|Li with (a) LPC@HKUST-1, (b) LPC@UiO-66, (c) LPC@UiO-67, (d) LPC@MIL-100-Al, (e) LPC@MIL-100-Cr and (f) LPC@MIL-100-Fe at  $0.5 \text{ mV s}^{-1}$  between  $-0.2$  to  $5 \text{ V vs. Li/Li}^+$

Since the incorporated LPC component is firmly confined within the MOF scaffolds, substantially improved safety is achieved compared with that of conventional liquid electrolytes with high flammability. A combustion test of a LPC@UiO-67 electrolyte pellet and a LPC-saturated polypropylene (PP) membrane (Celgard 3401) is shown in **Figure 2-18b** and **Figure 2-20** for comparison. Upon direct contact with a flame for 2 s, the LPC@UiO-67 electrolyte did not burn and only exhibits minor surface decomposition, in sharp contrast to the immediate combustion of the PP membrane soaked with liquid LPC.

For practical purposes, we fabricated the MOF electrolyte into a flexible membrane by mixing it with 10 wt.% of polytetrafluoroethylene (PTFE) as a binder (**Figure 2-18c**). This



membrane format is compatible with the electrochemical experiments and is the most likely form for it to be integrated into battery devices. In the paragraphs below we refer to the LPC@UiO-67/PTFE electrolyte membrane as LPC@UM. SEM images (**Figure 2-18d**) of the 70-100  $\mu\text{m}$  thick membrane show that PTFE polymer fibers tightly thread the MOF particles into a robust and dense structure.

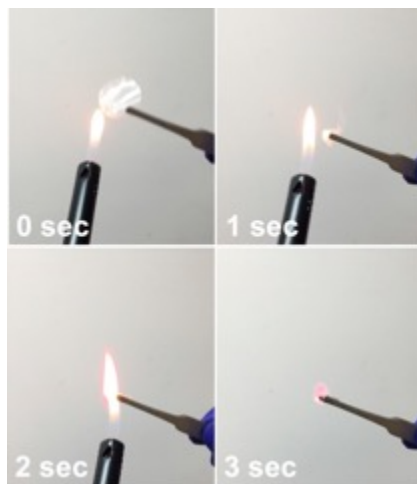


**Figure 2-20** Flammability test for PP separator saturated with LPC.

We also evaluated the lithium-ion transference number,  $t_{\text{Li}^+}$ , of the LPC@UM membrane using the potentiostatic polarization method<sup>63</sup> (**Figure 2-18e**, see Experimental Section for details). In liquid LPC electrolyte, the typical value for  $t_{\text{Li}^+}$  is 0.2-0.4<sup>64</sup> as  $\text{Li}^+$  are solvated in conventional liquid carbonate electrolytes, resulting in relatively free anions and ion-pairs. Here, we obtained a much higher value of 0.65 which is consistent with having the  $\text{ClO}_4^-$  effectively immobilized at the OMSs, enabling the  $\text{Li}^+$  to dominate the transport properties. A similar value was reported by Park et. al.<sup>23</sup> using a different strategy for synthesizing a MOF solid electrolyte.

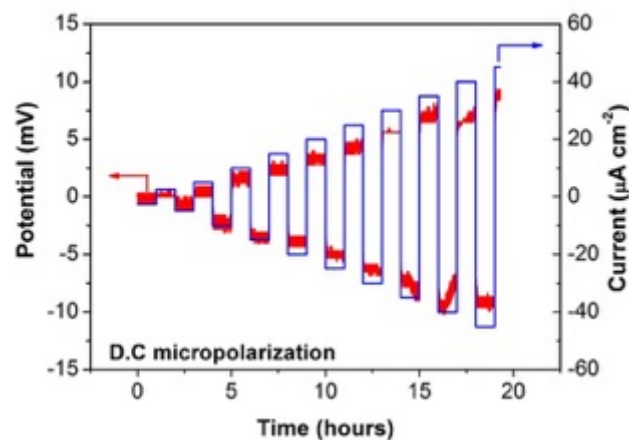


**Figure 2-21** DC micropolarization of Li|LPC@UM|Li cell from 2.5 to 50  $\mu\text{A cm}^{-2}$ .

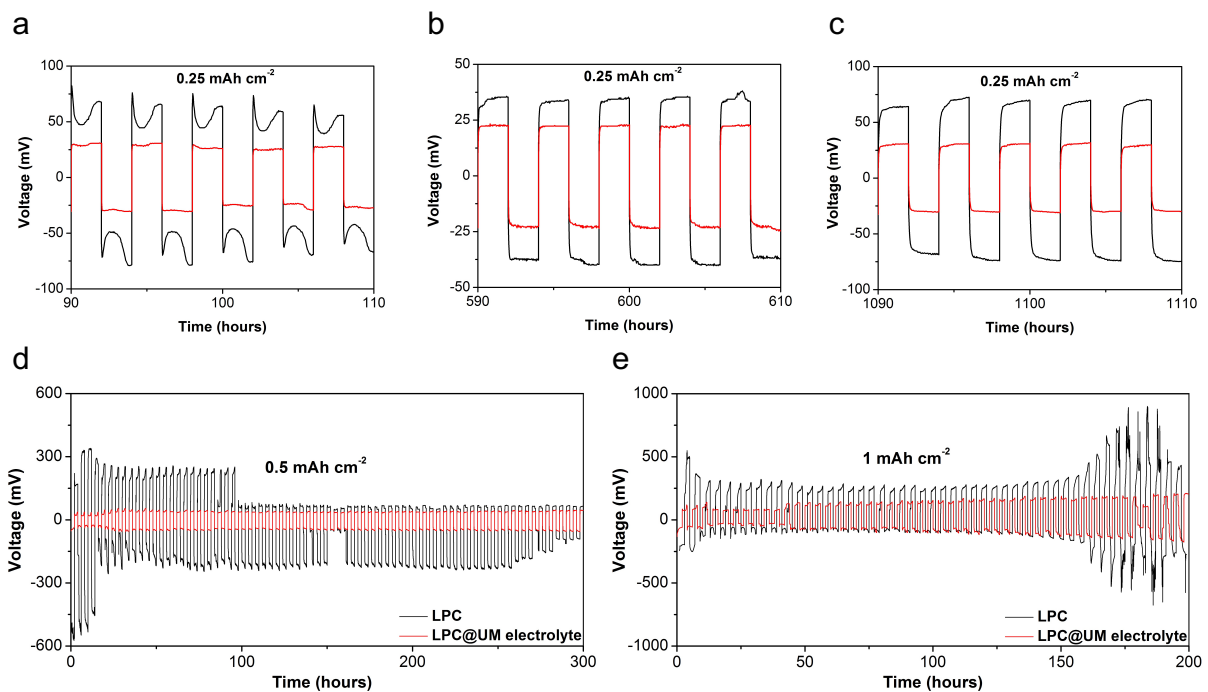


**Figure 2-22** Li symmetric cell using LPC@UM electrolyte at (a-c) 0.25  $\text{mAh cm}^{-2}$  (0.125  $\text{mA cm}^{-2}$ ), (d) 0.5  $\text{mAh cm}^{-2}$  (0.25  $\text{mA cm}^{-2}$ ) and (e) 1  $\text{mAh cm}^{-2}$  (0.5  $\text{mA cm}^{-2}$ )

A second important experiment involved using the LPC@UM as a membrane for the plating and stripping of lithium. These experiments were carried out in Li|LPC@UM|Li

symmetric cells that were cycled at current densities up to  $0.25 \text{ mA cm}^{-2}$ . At low current density, we assume a linear relationship between potential and current according to Tafel equation at low value of polarization. **Figure 2-21** shows the DC (direct current) stepped current cycling from  $2.5$  to  $50 \text{ uA cm}^{-2}$ , the potential increased linearly with current, the corresponding resistance ( $\sim 175\text{-}200 \text{ } \Omega \text{ cm}^2$ ) based on Ohm's law is in good agreement with ac impedance. Even at higher current density ( $0.125, 0.25$  and  $0.5 \text{ mA cm}^{-2}$  in 2 hour segments) (**Figure 2-18f** and **Figure 2-22**), the potentials at early stage are consistent with values predicted by dc micropolarization as well as ac impedance. The voltage profile of prolonged cycling of  $0.125 \text{ mA cm}^{-2}$  is depicted at **Figure 2-18f** and **Figure 2-22(a-c)** the cell delivers a stable voltage plateau at  $\sim 20 \text{ mV}$  up to 600 h operation despite it gradually accumulates minor overpotential of  $10 \text{ mV}$  by the end of the cycling (1200 h). In comparison, the cell with a commercial separator and liquid LPC electrolyte shows higher overpotential fluctuating from  $50 \text{ mV}$  up to  $180 \text{ mV}$  and irregular curves (see zoom-in curves in **Figure 2-22(a-c)**), which could be ascribed to high interfacial resistance and unstable SEI formation.

Finally, we assembled prototype Li-metal batteries with  $\text{LiFePO}_4$  cathodes and Li anodes ( $\text{LiFePO}_4|\text{Li}$ ) with LPC and LPC@UM electrolyte. As shown in **Figure 2-18g** and **Figure 2-23**, these  $\text{LiFePO}_4|\text{Li}$  batteries were evaluated at rates from  $0.2$  to  $2 \text{ C}$ . At  $0.2 \text{ C}$ , the cell with LPC@UM electrolyte exhibits a good specific capacity of  $146 \text{ mAh g}^{-1}$ , while that at  $2 \text{ C}$  has a capacity of  $106 \text{ mAh g}^{-1}$ . By comparison, the cell based on liquid electrolyte could only afford  $90 \text{ mAh g}^{-1}$  at  $2 \text{ C}$ . We also carried out extended cycling at  $1 \text{ C}$  and observed that 75% of the initial capacity was retained after 500 cycles. These results show that while the LPC@UM effectively functions as a  $\text{Li}^+$  conducting electrolyte for Li-metal batteries, future study is required in order to

achieve long term stability.

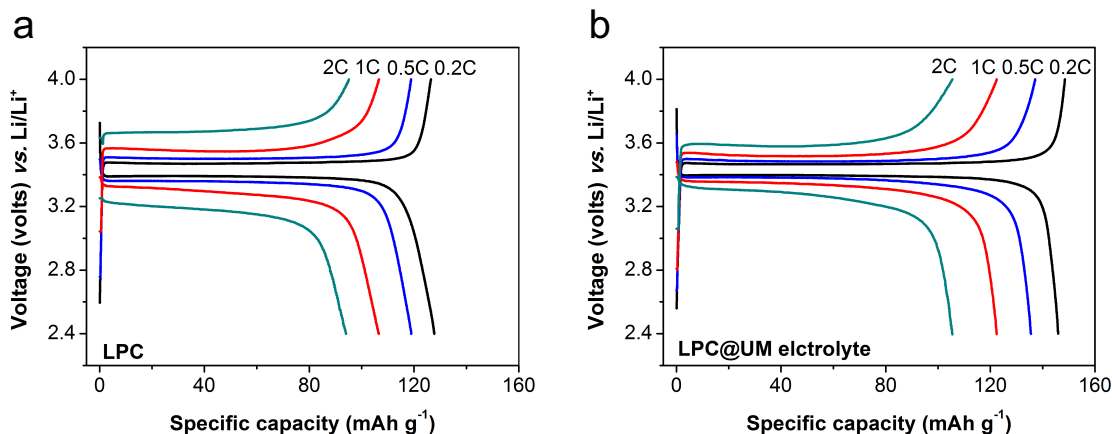


**Figure 2-23** Typical voltage-capacity curves of LPC@UM electrolyte in LiFePO<sub>4</sub>|Li cells at various rates.

To further illustrate lithium-shuttling efficiency at higher current density, we assembled prototype Li-ion batteries using LiFePO<sub>4</sub> cathodes and Li<sub>4</sub>Ti<sub>5</sub>O<sub>12</sub> anodes, where an excess Li source is not available. The cells were cycled at a rate of 5 C, and no significant capacity loss is observed in the cell with LPC@UM electrolyte even after 500 cycles with an average Coulombic efficiency (CE) of 99.99% (**Figure 2-18f**). As a reference, the cell based on liquid electrolyte shows drastic capacity decay, with only 25% capacity retention at 250 cycles and a low average CE of 99.67%. To the best of our knowledge, this is the first demonstration of successfully cycled Li full cells using solid-state electrolytes based on MOFs.

## 2.3 Conclusion

We have demonstrated a design and synthesis of MOFs-based electrolytes with biomimetic ionic channels for fast and effective transport of lithium ions. Our approach results in six new superionic conductors, the best of which exhibits an ambient conductivity surpassing  $10^{-3} \text{ S cm}^{-1}$ , activation energies below 0.21 eV and enhanced  $\text{Li}^+$  transference number. These features endow Li-based batteries with superior rate performance and cycling stability. These advantages over conventional LPC liquid electrolytes derive from their unique  $\text{Li}^+$  conduction mechanism, where the anions in LPC@MOFs electrolytes are immobilized to the OMS whereas the  $\text{ClO}_4^-$  anions in LPC are either free or pairing with  $\text{Li}^+$ . We believe that our findings could open a new avenue of exploring MOFs as new solid-state electrolytes for next-generation battery devices.

## 2.4 Experimental Section

**Synthesis of HKUST-1.** HKUST-1 was synthesized according to a modified microwave-assisted method.<sup>65</sup> In a typical synthesis, 0.42 g of benzene-1,3,5-tricarboxylic acid (BTC) and 0.88 g of copper (II) nitrate trihydrate were dissolved in 24 mL solution of ethanol and water (volume ratio of 1:1). After continuous stirring for 20 min, the sample was transferred to a microwave reactor (Ultrawave, Milestone Inc.). The solution was heated at 800 W under nitrogen with a ramp rate of 10 °C per min before being held at 140 °C for 1h. The product was collected by centrifugation and washed for further use.

**Synthesis of MIL-100-(Al/Cr/Fe).** Isostructural MIL-100-(Al, Cr, Fe) MOFs were synthesized according to a modified microwave-assisted method.<sup>66</sup> For MIL-100-Al, 1.43 g of aluminum nitrate nonahydrate and 1.21 g of trimethyl trimesate were dispersed in 20 mL of water, followed by the addition of 4 mL of nitric acid (4 M). The mixture was transferred to the microwave reactor, heated at 1500 W to 240 °C in 6 min, and held for 1 min. For MIL-100-Cr, 2.4 g of chromium nitrate nonahydrate and 0.84 g of BTC were dispersed in 30 mL of water, followed by the addition of 5 mL of nitric acid (4 M). The mixture was heated in the microwave reactor at 1500 W to 200 °C in 10 min, and held for 5 min. For MIL-100-Fe, 2.43 g of iron (III) nitrate nonahydrate and 0.84 g of BTC were dispersed in 30 mL of water. The mixture was heated in the microwave reactor at 1500 W to 130 °C in 2 min 30 s, and held for 5 min. After the reactions, all of the samples were collected by centrifugation and washed several times for further use.

**Synthesis of UiO-(66/67).** UiO-66 and UiO-67 were prepared according to a reported method.<sup>67</sup> In a typical synthesis of UiO-66 MOF, 1.23 g of BDC ligand and 1.25 g of ZrCl<sub>4</sub> were dissolved in 100 mL of N,N-dimethylformamide (DMF) and 50/10 mL of DMF/hydrochloric acid (37 wt% HCl, concentrated) mixture, respectively. These two fully dissolved solutions were combined and

magnetically stirred for an additional 30 min. The resulting transparent precursor solution was loaded in a tightly sealed glass vial and heated at 150 °C for 20 h. Afterwards, the precipitate was separated from solvents by centrifugation and first washed by DMF three times (3×40 mL). Methanol exchange was performed on the DMF-washed sample over a period of 3 d. The sample was replenished with fresh methanol twice a day (each for 40 mL). Eventually the sample was dried at 80 °C for 1 d prior to further characterization. UiO-67 was prepared in a similar procedure with different reagents, in which 1.35 g of BPDC ligand and 1 g of ZrCl<sub>4</sub> were dissolved in 150 mL of DMF and 75/7.5 mL of DMF/HCl (37 wt% HCl, concentrated) mixture, respectively.

**Synthesis of MOF-5.** MOF-5 was prepared by a room temperature synthesis.<sup>68</sup> In a typical synthesis, 17 g of zinc acetate dihydrate (Zn(OAc)<sub>2</sub>•H<sub>2</sub>O) and 5.1 g of BDC were dissolved in 500 mL of DMF and 400/8.5 mL of DMF/triethylamine mixture, respectively. Upon addition of the metal salt solution into the ligand solution, white precipitate forms immediately. After continuous stirring for 2.5 h, the precipitate was centrifuged and washed by DMF. Solvent change was carried out by immersing DMF- washed samples in chloroform (CHCl<sub>3</sub>) and renewing the solvent once a day for one week. The resulting product was evacuated overnight and stored in a moisture-free environment for further use.

**Synthesis of LPC@MOFs solid-state electrolytes.** MOFs, including HKUST-1, UiO-(66/67), MIL-100-(Al/Cr/Fe), and MOF-5 were synthesized according to the reported literature and characterized by various techniques (see synthetic method and materials characterization in Supporting Information). The MOF samples were activated under vacuum at 200 °C (350 °C for MIL-100-Al and UiO-(66/67)) overnight, subsequently soaked in the LPC electrolyte, collected by vacuum filtration, and pressed into pellets with a diameter of 13 mm at 300 MPa. The surface of the pellets was wiped with tissue paper prior to further electrochemical tests.

**Preparation of LPC@MOFs electrolyte membranes.** UiO-67 powders were homogeneously dispersed in ethanol, and 10 wt% polytetrafluoroethylene (PTFE) aqueous solution was added to the mixture. After continuous stirring and evaporation of the solvent, the mixture was rolled into flexible MOFs/PTFE composite membranes. The membranes were cut into a desirable size and subjected to the activation process and the soaking process. LPC@UiO-67/PTFE membrane electrolytes (LPC@UM) were pressed at 200 MPa to extrude any excessive liquid electrolyte and wiped with tissue paper.

**Materials characterizations and structural analysis.** Crystalline structures of the MOFs and LPC@MOFs electrolytes were determined with a Panalytical X'Pert Pro or a Rigaku powder X-ray diffractometer (XRD) using  $K\alpha$  radiation ( $\lambda = 1.54 \text{ \AA}$ ). Surface morphology and particle size were determined by scanning electron microscopy (Nova 230 Nano SEM). (UV-VIS) Raman spectra were collected by a triple monochromator and detected with a charge coupled device (CCD). Pellets of samples were excited by an argon ion laser at a wavelength 457.9 nm at a laser power of 100 mW. The liquid samples were infused into capillary tubes for characterization. Infrared spectra experiments were performed in a transmission mode on a Jasco 420 Fourier transform infrared (FT-IR) spectrophotometer. Thermogravimetric analysis (TGA) was carried out in air atmosphere by a ramping rate of  $5 \text{ }^\circ\text{C min}^{-1}$ . Copper and lithium ratio was determined by inductively coupled plasma atomic emission spectrometer (ICP-AES, Shimadzu, ICPE-2000) using standard copper and lithium solutions from Sigma-Aldrich. Calibration and quantitative analysis were carried out by a series of standard Cu/Li (5, 10, 20, 40 ppm) and 40 ppm LPC@HKUST-1 in 2 wt%  $\text{HNO}_3$  solution.

**Electrochemical studies.** Ionic conductivity was measured using electrochemical impedance spectroscopy (EIS) after placing the pellets between two stainless steel blocking contacts in a



2032-type coin cell. The conductivity of LPC liquid electrolyte was collected by saturating a glass fiber membrane (Whatman, GF-C) with LPC. The frequency range was from  $10^6$  to 1 Hz, and alternating-current (AC) amplitude was 100 mV. Ionic conductivity ( $\kappa$ ,  $S\text{ cm}^{-1}$ ) was determined by using the end point of the semi-circle as the ionic resistivity ( $R$ , ohm), thickness ( $L$ , cm), and area of the pellet ( $A$ ,  $\text{cm}^2$ ) based on  $\kappa = L/(R \times S)$ . To measure the activation energies, conductivity was measured at different temperatures and calculated based on the Arrhenius relation with a linear fitting coefficient over 0.99.

For cyclic voltammetry (CV) tests, lithium foils were utilized as reference/counter electrodes and stainless-steel plates were used as the working electrodes. The CV of LPC@MOFs pellets were performed between  $-0.2$  and  $5$  V (vs.  $\text{Li}/\text{Li}^+$ ) at  $0.5\text{ mV s}^{-1}$ . All voltammetry and impedance measurements were conducted on a Solartron1860/1287 electrochemical interface.

Lithium symmetric cells were assembled by sandwiching LPC@UM electrolyte between two pieces of lithium foil in a coin-cell; a single drop ( $\sim 6$  ul) of electrolyte was delivered to the electrolyte/electrode interface. The Li stripping/plating tests were performed using the symmetric cells by charging and discharging for a periodic 2 h each at current densities of  $0.125$  and  $0.25\text{ mA cm}^{-2}$ .

Lithium ion transference number ( $t_{\text{Li}^+}$ ) was measured by combining an AC impedance measurement and a potentiostatic polarization measurement using Li/electrolyte/Li cells. First, an AC impedance test ( $10^6$  to 1 Hz, 20 mV amplitude) was performed to obtain the initial bulk resistance ( $R_b^0$ ) and the interfacial resistance ( $R_{\text{int}}^0$ ). The symmetric cell was then subjected to a constant DC voltage ( $V$ , 20 mV), during which the initial current ( $I_0$ ) was monitored until reaching the steady-state current ( $I_{\text{ss}}$ ). Another AC impedance test was then conducted to obtain the steady state bulk resistance ( $R_b^{\text{ss}}$ ) and the steady state interfacial resistance ( $R_{\text{int}}^{\text{ss}}$ ).  $t_{\text{Li}^+}$  was then calculated

by the formula:  $t_{Li^+} = I_{ss}R_b^{ss}(V - I_0R_{int}^0)/(I_0R_b^0(V - I_{ss}R_{int}^{ss}))$ .

Prototype lithium metal batteries were fabricated by assembling a conventional LiFePO<sub>4</sub> cathode and a Li chip into a CR2032 coin cell. The cathode electrodes were prepared by homogenously blending LiFePO<sub>4</sub>, acetylene black, and PVdF with a ratio of 7:2:1 in NMP. The resulting slurry was uniformly coated on a conductive carbon-coated Al foil and dried in a vacuum oven at 70 °C for 24 h. The cathodes and as-prepared LPC@UM electrolyte were pressed together at 200 Mpa to minimize interface resistance, and one drop (~ 6 uL) of electrolyte was added to ensure permeation into the electrode matrix. The specific capacity is calculated based on the active materials in the cathode, which corresponds to an areal loading of approximately 2 mg cm<sup>-2</sup>. 1 C charge/discharge rate here is defined as 170 mA g<sup>-1</sup>. The cycling tests were carried out at 0.2, 0.5, 1, and 2 C for five cycles each and at 1 C for subsequent cycles at ambient temperature (electrochemical window: 2.4-4 V vs. Li/Li<sup>+</sup>). All the electrochemical tests were carried out at ambient temperature at ~ 25 °C unless specified.

## 2.5 References

1. Tarascon, J.M. & Armand, M. Issues and challenges facing rechargeable lithium batteries. *Nature* **414**, 359-367 (2001).
2. Xu, K. Electrolytes and interphases in Li-ion batteries and beyond. *Chem. Rev.* **114**, 11503-11618 (2014).
3. Armand, M. & Tarascon, J.M. Building better batteries. *Nature* **451**, 652-657 (2008).
4. Chazalviel, J.N. Electrochemical aspects of the generation of ramified metallic electrodeposits. *Phys. Rev. A* **42**, 7355-7367 (1990).
5. Bachman, J.C. et al. Inorganic Solid-State Electrolytes for Lithium Batteries: Mechanisms and Properties Governing Ion Conduction. *Chem. Rev.* **116**, 140-162 (2016).
6. Manthiram, A., Yu, X. & Wang, S. Lithium battery chemistries enabled by solid-state electrolytes. *Nature Rev. Mat.* **2**, 16103 (2017).
7. Kamaya, N. et al. A lithium superionic conductor. *Nat. Mater.* **10**, 682-686 (2011).
8. Wenzel, S. et al. Direct observation of the interfacial instability of the fast ionic conductor  $\text{Li}_{10}\text{GeP}_2\text{S}_{12}$  at the lithium metal anode. *Chem. Mater.* **28**, 2400-2407 (2016).
9. Kato, Y. et al. High-power all-solid-state batteries using sulfide superionic conductors. *Nat. Energy* **1**, 16030 (2016).
10. Hartmann, P. et al. Degradation of NASICON-type materials in contact with lithium metal: Formation of mixed conducting interphases (MCI) on solid electrolytes. *J. Phys. Chem. C* **117**, 21064-21074 (2013).
11. Oh, D.Y. et al. Excellent compatibility of solvate ionic liquids with sulfide solid electrolytes: Toward favorable ionic contacts in bulk-type all-solid-state lithium-ion batteries. *Adv. Energy Mater.* **5**, 1500865 (2015).

12. Han, X. et al. Negating interfacial impedance in garnet-based solid-state Li metal batteries. *Nat. Mater.* **16**, 572-579 (2017).
13. Meyer, W.H. Polymer Electrolytes for Lithium-Ion Batteries. *Adv. Mater.* **10**, 439-448 (1998).
14. Song, J.Y., Wang, Y.Y. & Wan, C.C. Review of gel-type polymer electrolytes for lithium-ion batteries. *J. Power Sources* **77**, 183-197 (1999).
15. Croce, F., Appetecchi, G.B., Persi, L. & Scrosati, B. Nanocomposite polymer electrolytes for lithium batteries. *Nature* **394**, 456-458 (1998).
16. Lemoine, D. et al. Ligand-gated ion channels: New insights into neurological disorders and ligand recognition. *Chem. Rev.* **112**, 6285-6318 (2012).
17. Dawson, R.J.P. et al. Structure of the acid-sensing ion channel 1 in complex with the gating modifier Psalmotoxin 1. *Nat. Commun.* **3**, 936 (2012).
18. Chui, S.S.Y., Lo, S.M.F., Charmant, J.P.H., Orpen, A.G. & Williams, I.D. Chemically functionalizable nanoporous material  $[\text{Cu}_3(\text{TMA})_2(\text{H}_2\text{O})_3]_n$ . *Science* **283**, 1148 (1999).
19. Furukawa, H., Cordova, K.E., O’Keeffe, M. & Yaghi, O.M. The Chemistry and Applications of Metal–organic Frameworks. *Science* **341** (2013).
20. Ramaswamy, P., Wong, N.E. & Shimizu, G.K.H. MOFs as proton conductors - challenges and opportunities. *Chem. Soc. Rev.* **43**, 5913-5932 (2014).
21. Wiers, B.M., Foo, M.-L., Balsara, N.P. & Long, J.R. A solid lithium electrolyte via addition of lithium isopropoxide to a metal–organic framework with open metal sites. *J. Am. Chem. Soc.* **133**, 14522-14525 (2011).

22. Ameloot, R. et al. Ionic Conductivity in the Metal–Organic Framework UiO-66 by Dehydration and Insertion of Lithium tert-Butoxide. *Chemistry – A European Journal* **19**, 5533-5536 (2013).
23. Park, S.S., Tulchinsky, Y. & Dincă, M. Single-Ion Li<sup>+</sup>, Na<sup>+</sup>, and Mg<sup>2+</sup> Solid Electrolytes Supported by a Mesoporous Anionic Cu–Azolate Metal–Organic Framework. *Journal of the American Chemical Society* **139**, 13260-13263 (2017).
24. Lee, J.-h., Im, S.-j. & Park, S.-H., Vol. U.S. Patent No. 9,105,940. (2015).
25. Gerbaldi, C. et al. Innovative high performing metal organic framework (MOF)-laden nanocomposite polymer electrolytes for all-solid-state lithium batteries. *J. Mater. Chem. A* **2**, 9948-9954 (2014).
26. Yuan, C. et al. Enhanced electrochemical performance of poly(ethylene oxide) based composite polymer electrolyte by incorporation of nano-sized metal–organic framework. *J. Power Sources* **240**, 653-658 (2013).
27. Zhang, J. et al. Superior Conductive Solid-like Electrolytes: Nanoconfining Liquids within the Hollow Structures. *Nano Lett.* **15**, 3398-3402 (2015).
28. Park, J.H. et al. Solid lithium electrolytes based on an organic molecular porous solid. *Chem. Commun.* **51**, 9313-9316 (2015).
29. Fujie, K., Ikeda, R., Otsubo, K., Yamada, T. & Kitagawa, H. Lithium Ion Diffusion in a Metal–Organic Framework Mediated by an Ionic Liquid. *Chem. Mater.* **27**, 7355-7361 (2015).
30. Talin, A.A. et al. Tunable electrical conductivity in metal–organic framework thin-film devices. *Science* **343**, 66 (2014).

31. Skarmoutsos, I., Ponnuchamy, V., Vetere, V. & Mossa, S. Li<sup>+</sup> solvation in pure, binary, and ternary mixtures of organic carbonate electrolytes. *J. Phys. Chem. C* **119**, 4502-4515 (2015).
32. Wang, Q., Sun, J., Yao, X. & Chen, C. Micro calorimeter study on the thermal stability of lithium-ion battery electrolytes. *J. Loss Prev. Process Ind.* **19**, 561-569 (2006).
33. Llewellyn, P.L. et al. High Uptakes of CO<sub>2</sub> and CH<sub>4</sub> in Mesoporous Metal—Organic Frameworks MIL-100 and MIL-101. *Langmuir* **24**, 7245-7250 (2008).
34. Song, J.Y., Wang, Y.Y. & Wan, C.C. Conductivity study of porous plasticized polymer electrolytes based on poly(vinylidene fluoride): A comparison with polypropylene separators. *J. Electrochem. Soc.* **147**, 3219-3225 (2000).
35. Volkringer, C. et al. Infrared Spectroscopy Investigation of the Acid Sites in the Metal—Organic Framework Aluminum Trimesate MIL-100(Al). *J. Phys. Chem. C* **116**, 5710-5719 (2012).
36. Chavan, S. et al. H<sub>2</sub> storage in isostructural UiO-67 and UiO-66 MOFs. *Phys. Chem. Chem. Phys.* **14**, 1614-1626 (2012).
37. Valenzano, L. et al. Disclosing the Complex Structure of UiO-66 Metal Organic Framework: A Synergic Combination of Experiment and Theory. *Chem. Mater.* **23**, 1700-1718 (2011).
38. Mizuno, F., Hayashi, A., Tadanaga, K. & Tatsumisago, M. New, highly ion-conductive crystals precipitated from Li<sub>2</sub>S–P<sub>2</sub>S<sub>5</sub> glasses. *Adv. Mater.* **17**, 918-921 (2005).
39. Murugan, R., Thangadurai, V. & Weppner, W. Fast lithium ion conduction in garnet-type Li<sub>7</sub>La<sub>3</sub>Zr<sub>2</sub>O<sub>12</sub>. *Angew. Chem. Int. Ed.* **46**, 7778-7781 (2007).

40. Bouchet, R. et al. Single-ion BAB triblock copolymers as highly efficient electrolytes for lithium-metal batteries. *Nat. Mater.* **12**, 452-457 (2013).
41. Yu, X., Bates, J.B., Jellison, G.E.J. & Hartb, F.X. A Stable Thin-Film Lithium Electrolyte: Lithium Phosphorus Oxynitride. *J. Electrochem. Soc.* **144**, 524-532 (1997).
42. Colomban, P. & Novak, A. Proton transfer and superionic conductivity in solids and gels. *J. Mol. Struct.* **177**, 277-308 (1988).
43. Prestipino, C. et al. Local structure of framework Cu(II) in HKUST-1 metallorganic framework: Spectroscopic characterization upon activation and interaction with adsorbates. *Chem. Mater.* **18**, 1337-1346 (2006).
44. Dhumal, N.R., Singh, M.P., Anderson, J.A., Kiefer, J. & Kim, H.J. Molecular interactions of a Cu-based metal–organic framework with a confined imidazolium-based ionic liquid: A combined density functional theory and experimental vibrational spectroscopy study. *J. Phys. Chem. C* **120**, 3295-3304 (2016).
45. Sagane, F., Abe, T. & Ogumi, Z. Li<sup>+</sup>-ion transfer through the interface between Li<sup>+</sup>-ion conductive ceramic electrolyte and Li<sup>+</sup>-ion-concentrated propylene carbonate solution. *J. Phys. Chem. C* **113**, 20135-20138 (2009).
46. Xuan, X., Wang, J., Tang, J., Qu, G. & Lu, J. Vibrational spectroscopic studies on ion solvation of lithium perchlorate in propylene carbonate+N,N-dimethylformamide mixtures. *Spectrochim. Acta Mol. Biomol. Spectrosc.* **56**, 2131-2139 (2000).
47. Battisti, D., Nazri, G.A., Klassen, B. & Aroca, R. Vibrational studies of lithium perchlorate in propylene carbonate solutions. *J. Phys. Chem. A* **97**, 5826-5830 (1993).
48. Lewis, D.L., Estes, E.D. & Hodgson, D.J. The infrared spectra of coordinated perchlorates. *J Cryst. Mol. Struct.* **5**, 67-74 (1975).

49. Hathaway, B.J. & Underhill, A.E. The infrared spectra of some transition-metal perchlorates. *J. Chem. Soc.* **592**, 3091-3096 (1961).
50. Cazzanelli, E., Croce, F., Appetecchi, G.B., Benevelli, F. & Mustarelli, P. Li<sup>+</sup> solvation in ethylene carbonate–propylene carbonate concentrated solutions: A comprehensive model. *J. Chem. Phys* **107**, 5740-5747 (1997).
51. Klassen, B., Aroca, R., Nazri, M. & Nazri, G.A. Raman spectra and transport properties of lithium perchlorate in ethylene carbonate based binary solvent systems for lithium batteries. *J. Phys. Chem. B* **102**, 4795-4801 (1998).
52. Klassen, B., Aroca, R. & Nazri, G.A. Lithium perchlorate: Ab initio study of the structural and spectral changes associated with ion pairing. *J. Phys. Chem. A* **100**, 9334-9338 (1996).
53. Grondin, J. et al. Raman study of tetraglyme-LiClO<sub>4</sub> solvate structures. *Phys. Chem. Chem. Phys.* **6**, 4260-4267 (2004).
54. Wickenden, A.E. & Krause, R.A. Complexes of nickel(II) with acetonitrile. Coordination of perchlorate. *Inorg. Chem.* **4**, 404-407 (1965).
55. Sant'Ana, A.C., Alves, W.A., Santos, R.H.A., Ferreira, A.M.D. & Temperini, M.L.A. The adsorption of 2,2':6',2''-terpyridine, 4'-(5-mercaptopentyl)-2,2':6',2''-terpyridinyl, and perchlorate on silver and copper surfaces monitored by SERS. *Polyhedron* **22**, 1673-1682 (2003).
56. Pereira, D.C., Faria, D.L.A.d. & Constantino, V.R.L. Cu(II) hydroxy salts: Characterization of layered compounds by vibrational spectroscopy. *J. Braz. Chem. Soc.* **17**, 1651-1657 (2006).



57. Wang, Z., Huang, B., Xue, R., Chen, L. & Huang, X. Ion association and solvation studies of LiClO<sub>4</sub>/ethylene carbonate electrolyte by Raman and infrared spectroscopy. *Journal of Electrochemistry Society* **145**, 3346-3350 (1998).
58. Brooksby, P.A. & Fawcett, W.R. Infrared (attenuated total reflection) study of propylene carbonate solutions containing lithium and sodium perchlorate. *Spectrochim. Acta Mol. Biomol. Spectrosc.* **64**, 372-382 (2006).
59. Rowsell, J.L.C., Spencer, E.C., Eckert, J., Howard, J.A.K. & Yaghi, O.M. Gas Adsorption Sites in a Large-Pore Metal–organic Framework. *Science* **309**, 1350 (2005).
60. Li, H., Eddaoudi, M., O'Keeffe, M. & Yaghi, O.M. Design and synthesis of an exceptionally stable and highly porous metal–organic framework. *Nature* **402**, 276-279 (1999).
61. Perez, E.V., Balkus Jr, K.J., Ferraris, J.P. & Musselman, I.H. Mixed-matrix membranes containing MOF-5 for gas separations. *Journal of Membrane Science* **328**, 165-173 (2009).
62. Kim, T.-W., Chung, P.-W. & Lin, V.S.Y. Facile Synthesis of Monodisperse Spherical MCM-48 Mesoporous Silica Nanoparticles with Controlled Particle Size. *Chem. Mater.* **22**, 5093-5104 (2010).
63. Evans, J., Vincent, C.A. & Bruce, P.G. Electrochemical measurement of transference numbers in polymer electrolytes. *Polymer* **28**, 2324-2328 (1987).
64. Georén, P. & Lindbergh, G. Characterisation and modelling of the transport properties in lithium battery gel electrolytes: Part I. The binary electrolyte PC/LiClO<sub>4</sub>. *Electrochim. Acta* **49**, 3497-3505 (2004).

65. Seo, Y.-K. et al. Microwave synthesis of hybrid inorganic–organic materials including porous  $\text{Cu}_3(\text{BTC})_2$  from Cu(II)-trimesate mixture. *Micropor. Mesopor. Mat.* **119**, 331-337 (2009).
66. García Márquez, A. et al. Green Microwave Synthesis of MIL-100(Al, Cr, Fe) Nanoparticles for Thin-Film Elaboration. *Eur. J. Inorg. Chem.* **2012**, 5165-5174 (2012).
67. Katz, M.J. et al. A facile synthesis of UiO-66, UiO-67 and their derivatives. *Chem. Commun.* **49**, 9449-9451 (2013).
68. Tranchemontagne, D.J., Hunt, J.R. & Yaghi, O.M. Room temperature synthesis of metal–organic frameworks: MOF-5, MOF-74, MOF-177, MOF-199, and IRMOF-0. *Tetrahedron* **64**, 8553-8557 (2008).

## **Chapter 3 Metal–organic Frameworks Enabled Tethered Anion Separator for Durable Lithium Rechargeable Batteries**

Progress towards next-generation batteries with high energy density and power capability have encountered stunning challenges due to the poor mass transport in electrochemical devices especially under high current operation. The dilemma originates from the relatively small fraction of total conductivity contributing effective  $\text{Li}^+$  conductivity, or in other words, the low  $\text{Li}^+$  transference number of conventional liquid electrolyte. To address the issues, we propose integrating metal–organic frameworks (MOF) into separator for tethering anion movement and improving the  $\text{Li}^+$  transport, affording doubled value compared with liquid electrolyte (from 0.34 to 0.67). The MOF porous scaffolds with Lewis acidic sites are capable of capturing and anchoring the anions. We demonstrate that the MOF functionalized separators substantially improve the electrochemical performances of Li electrodes in areal capacity over  $2 \text{ mA h cm}^{-2}$  for each galvanostatic cycling. In addition, the presence of MOF enables durable full cell ( $\text{LiFePO}_4$  and  $\text{Li}_4\text{Ti}_5\text{O}_{12}$ ) delivering areal capacity of  $3 \text{ mA h cm}^{-2}$  for over 1000 cycles at  $4 \text{ mA cm}^{-2}$ . The absence of severe concentration polarizations in above systems evidently stems from enhanced transport efficiency of  $\text{Li}^+$  by introducing MOF and the findings open up new routes to functionalize battery separators for high energy and power systems.

### 3.1 Introduction

Electrification of automobiles seeking sustainable energy, powered by lithium rechargeable batteries, is a mainstream trend for transportation recently.<sup>1</sup> Yet the present lithium-ion battery packs could only afford a typical energy density of  $\sim 150 \text{ Wh kg}^{-1}$  and limited charge rate (normal charge at  $\sim 0.1\text{C}$ ).<sup>2</sup> The progressive market penetration of electric vehicles heavily relies on advancements of battery technologies including energy density and power capability targeting easing driving range anxieties.

The employment of metallic Li ( $3860 \text{ mA h g}^{-1}$ ,  $-3.04 \text{ V vs. SHE}$ ) as anode<sup>2, 3</sup> and increasing the areal loading of electrochemical active materials<sup>4, 5</sup> have been proposed as viable approaches towards high energy systems while they substantially compromise the power density due to growth of dangerous Li dendrites and severe concentration polarization during fast charging. The paradox roots from the poor transport efficiency during instant passage of massive charge carriers in electrochemical systems. Specifically, the low  $\text{Li}^+$  transference number ( $t_{\text{Li}^+}$ ) of commercial electrolytes ( $\sim 0.3$ ) due to bulky solvation sheath of  $\text{Li}^+$  over anions leads to inferior mobility of  $\text{Li}^+$  and build-up of concentration polarization, which limit the charge/discharge rates, add overpotential on operating voltages, deteriorate the cycle lifespan and restrict the thickness of electrodes that may be used.<sup>5-7</sup>

Functional layers regulating ion transports have been incorporated into cell configurations to improve  $t_{\text{Li}^+}$ . For instance, laminating nanoporous ceramic membrane<sup>8</sup> or single-ion conducting ionomer<sup>9</sup> parallel to separators were demonstrated with enhanced  $t_{\text{Li}^+}$  and reduced Li dendritic deposition. However, such designs either are incompatible with current battery manufacture or sacrifice the volumetric energy density. Alternatively, Yuan *et al.*<sup>10-12</sup> reported enhanced rate capability by direct modification of commercial polyolefin separators with ceramic nanoparticles

and polymers. Yet, an average of 40% improvement of  $t_{\text{Li}^+}$  compared with pristine separator in liquid electrolyte renders this approach inefficient.

In this study, we introduce a novel functional component, metal–organic frameworks (MOF), into glass fiber (GF) separator for effectively improving the  $\text{Li}^+$  transport efficiency. MOF is an emerging type of crystalline porous solids, which is constructed by periodically bridging of inorganic metal clusters using organic ligands.<sup>13</sup> Partial coordination sites on metal centers are removable upon thermal activation and the resulting open metal sites with Lewis acidity are capable of complexing the anions in liquid electrolyte, thereby promoting the transport of  $\text{Li}^+$ .<sup>14, 15</sup> Herein we exemplify our concept by a zirconium-based MOF, UiO-66- $\text{NH}_2$ , which consists of metal nodes ( $\text{Zr}_6\text{O}_4(\text{OH})_4$ ) interconnected by organic linkers (2-aminoterephthalic acid,  $\text{NH}_2$ -BDC).<sup>16</sup> The functional groups, like dangling  $-\text{COOH}$  and  $-\text{NH}_2$ , are utilized to facilitate the formation of composite separator with GF (borosilicate). The capped groups of  $\mu_3\text{-OH}$  undergo dehydration upon thermal activation (from  $\text{Zr}_6\text{O}_4(\text{OH})_4$  to  $\text{Zr}_6\text{O}_6$ ), yielding vacant sites for tethering anions (**Figure 3-1**).<sup>15</sup> Meanwhile, the microporous scaffolds of MOF spatially allow ion carriers accessing the unsaturated metal sites. The liquid electrolyte infiltrated MOF-GF separator (denoted as MOG) exhibit doubled  $t_{\text{Li}^+}$  without compromising  $\text{Li}^+$  conductivity. In device performances, metallic Li-based electrodes employing MOG separator show improved  $\text{Li}^+$  stripping/plating efficiency and dendrites blocking capability under high areal capacity over  $2 \text{ mA h cm}^{-2}$ . We also successfully demonstrated that the MOG separator alleviated polarization in full cell configuration by high active material loading of  $45 \text{ mg cm}^{-2}$ . Overall, different from conventional ceramics or polymers modified separators, we reveal that MOF could serve as electrolyte regulator tethering mobile anions and improving  $t_{\text{Li}^+}$  of liquid electrolyte. The

exceptional device performances provide a new design standpoint for functional separators by taking advantage of vast pool of MOF candidates.

### 3.2 Result and Discussion

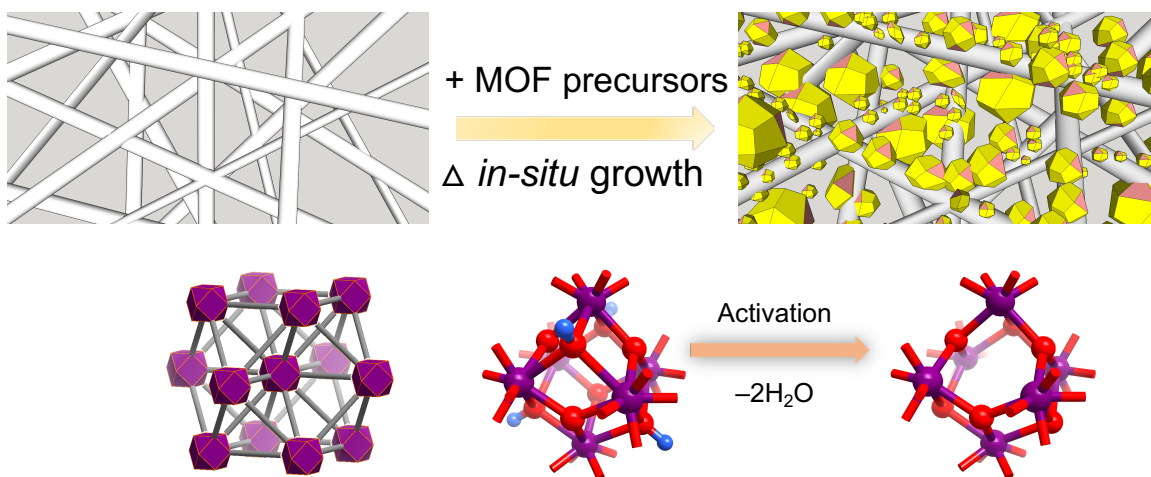


**Figure 3-1** Schematic drawing and photograph showing *in-situ* growth of MOF on bare glass fiber separator.

GF was selected as separator matrix due to its superior thermal stability ( $\sim 500$  °C), low cost and available hydroxyl groups on borosilicate backbones.<sup>17</sup> Facile *in-situ* growth of MOF within GF porous scaffold was achieved by infiltration of MOF precursors and subsequent heat treatment. We hypothesized that MOF would preferably grow on GF owing to affinity between abundant  $-OH$  from GF and functional groups from MOF, which was examined by scanning electron microscopy (SEM). **Figure 3-2a** and **3-2b** show the SEM images of GF and MOG, respectively. The GF membrane is composed by entanglement of fibers with micro-sized diameter. After *in-situ* growth of MOF, the fibrous structure is retained, and the surface of fibers are decorated with numerous nodes. The crystal structure of nodes was determined by powder X-ray diffraction (XRD). **Figure 3-2c** shows the XRD patterns of GF, MOG and MOF, where the MOF represents the products from MOF precursors without the presence of GF. All collected peaks of MOG and MOF are indexable to the simulated pattern of UiO-66 parent material (at the bottom of

**Figure 3-2c).** Hence, the nodes on fibers are ascribed to UiO-66-NH<sub>2</sub> on GF. The N<sub>2</sub> adsorption/desorption isotherms were collected to evaluate the pore structure. As a reference, the MOF exhibits surface area of 795 m<sup>2</sup> g<sup>-1</sup> and micropore size peaking at 9 Å (**Figure 3-3**). The MOF show reasonably decreased surface area of 453 m<sup>2</sup> g<sup>-1</sup> and expanded pore size of 13 Å considering the weight ratio of MOF in MOG is ~ 40%. Infrared spectroscopy (IR) was performed to shed insight to bond evolutions (**Figure 3-2d**). For spectrum of GF, a broad peak centering at 1064 cm<sup>-1</sup> accompanied by a pronounced shoulder at 972 cm<sup>-1</sup> are attributed to characteristic vibrations of Si–O–Si and Si–OH, respectively.<sup>18</sup> For the bare MOF, Zr–μ<sub>3</sub>–O (metal clusters) and O=C–O/N–H (ligands) are featured by sharp signals at 666 cm<sup>-1</sup> and 1570/1621 cm<sup>-1</sup>, respectively.<sup>19</sup> The composite MOG maintains major characteristic peaks of GF and MOF, though the intensity of Si–OH is decreased and redshifts of –COO/N–H are observed due to interaction between GF and MOF.



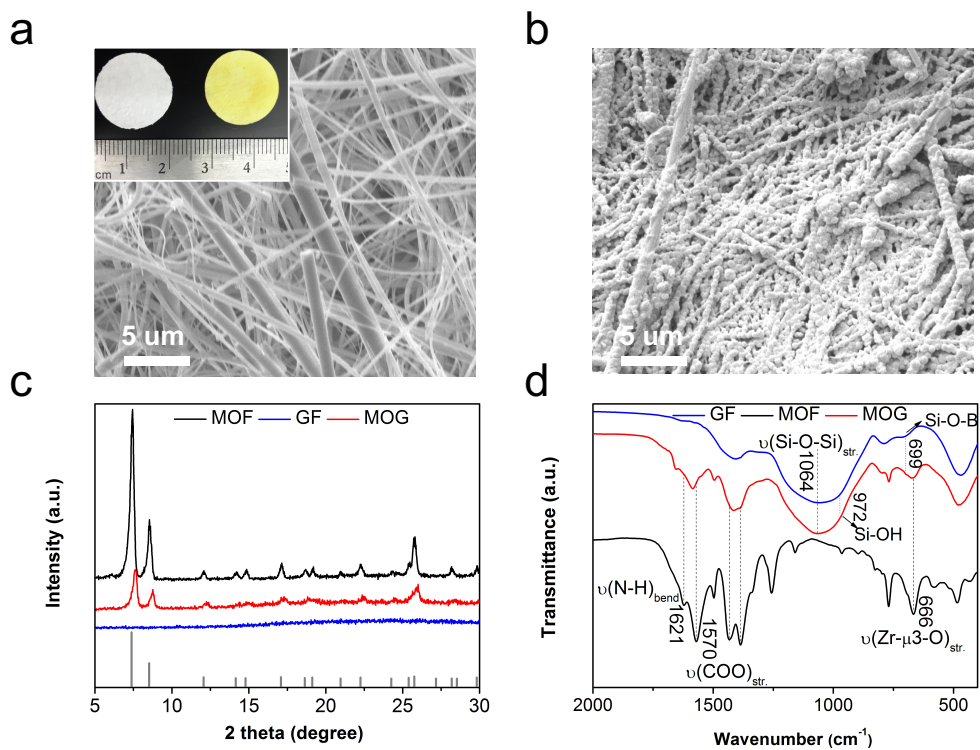


**Figure 3-2** SEM images of (a) glass fiber (GF, inset shows the pictures of white GF and yellowish MOF/GF) and (b) MOF/GF composite separator (MOG). (c) XRD patterns of MOF, GF and MOG (bottom of the figure: simulated pattern for MOF). (d) FT-IR spectra of MOF, GF and MOG.

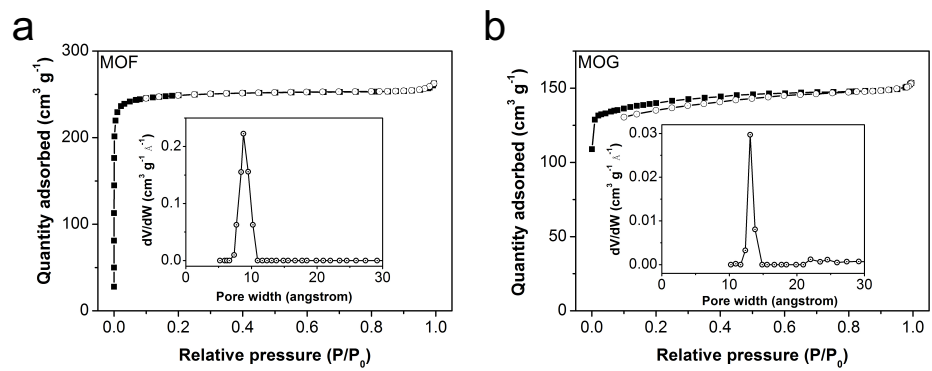


**Figure 3-3** N<sub>2</sub> adsorption/desorption isotherms (insets: pore size distribution curves) of (a) MOG and (b) GF.

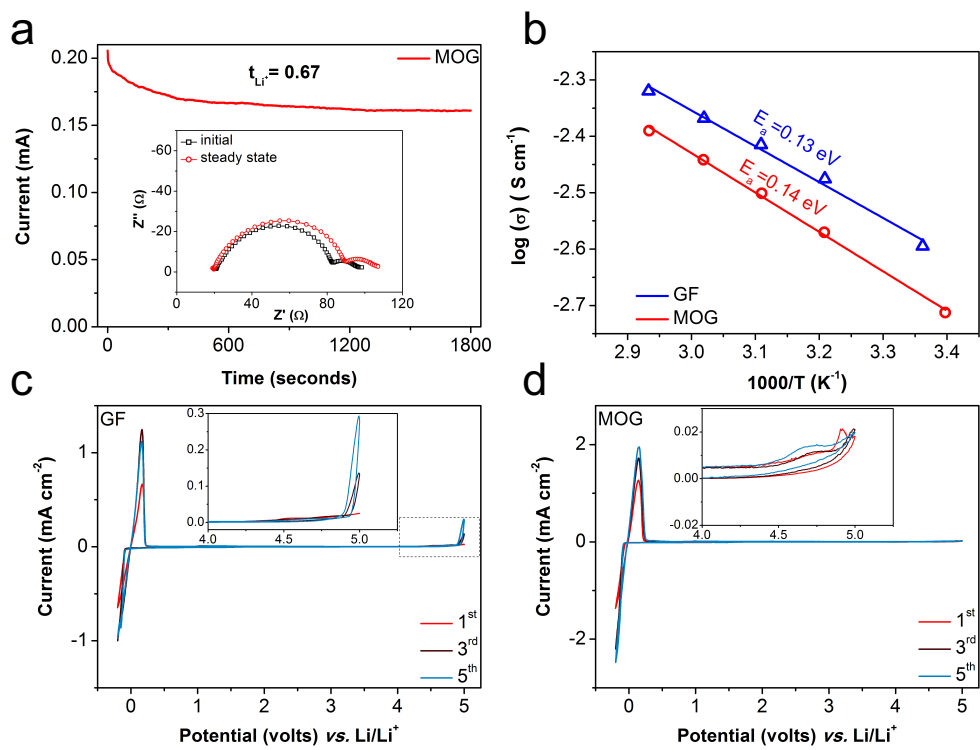


**Figure 3-4** Measurement of  $\text{Li}^+$  transference number by potentiostatic polarizations of Li|Li symmetric cells using GF and MOG, where the insets show the EIS before and after polarization. (b) Temperature dependent conductivities of electrolyte saturated GF and MOG, the activation energies were obtained from linear fittings of Arrhenius equation. CV curves of stainless steel|Li cells using (c) GF and (d) MOG. The tests were performed between  $-0.2$  to  $5$  V (vs.  $\text{Li}/\text{Li}^+$ ) at sweep rate of  $1 \text{ mV s}^{-1}$ .

The electrolyte properties in separators were characterized by conventional  $\text{LiClO}_4$  in propylene carbonate (1M). Separators including GF and MOG are subject to thermal activation for generating unsaturated metal sites before device assembly. **Figure 3-4a** show the measurements of  $t_{\text{Li}^+}$ , which are calculated from potentialstatic polarization and electrochemical impedance spectroscopy (EIS) in Li symmetric cell configuration (see details in Experimental Section).<sup>20</sup> The cell using MOG affords almost doubled  $t_{\text{Li}^+}$  of 0.67 compared with 0.34 from the cell using bare

GF (**Figure 3-5**). The results testify our hypothesis that anions are tethered in presence of MOF, facilitating the transport of  $\text{Li}^+$ . In addition, thermal activation energy was obtained from Arrhenius equation by linear fitting conductivities of electrolytes at various temperature (see Experimental Section for details). The devices were fabricated by sandwiching electrolyte saturated separators between two identical stainless-steel plates. As shown in **Figure 3-4b** the conductivity of the cell using MOG at room temperature decrease 20% compared with the one using GF, meanwhile, the activation energy is slightly changed, both of which suggest that MOF impose obstruction on anion transport and such interaction enhance the  $\text{Li}^+$  conductivity.

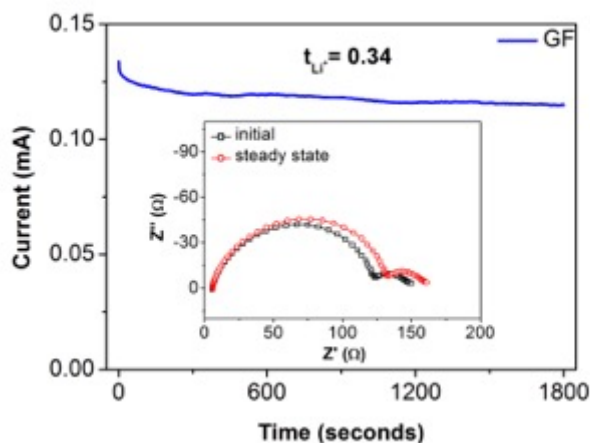


**Figure 3-5**  $\text{Li}^+$  transference number of liquid electrolyte in GF separator

The sub-conclusions are further evidenced by the results from cyclic voltammetry (CV). The CV tests were carried out by asymmetric cell configuration where stainless-steel plates were used as working electrode and Li as counter/reference electrodes. As shown in **Figure 3-4c** and **3-4d**, redox peaks near 0 V (vs.  $\text{Li}/\text{Li}^+$ ) arise from the  $\text{Li}^+$  stripping and plating processes on working electrodes. The corresponding peak current from the cell using MOG is 100% higher than the cell using GF, resulting from higher  $\text{Li}^+$  diffusion coefficient in MOG as indicated by Randles-Sevcik equation.<sup>21</sup> Moreover, we found out that the MOF alleviate the oxidation of electrolyte. The anodic

stability was evaluated by prolonged CV cycling. After five cycles, the cell using GF exhibits progressive increasing peak current above 4.4 V (vs. Li/Li<sup>+</sup>), instead the cell using MOG maintains substantial smaller (10X) peak current associating with oxidation of electrolyte components.<sup>22</sup>

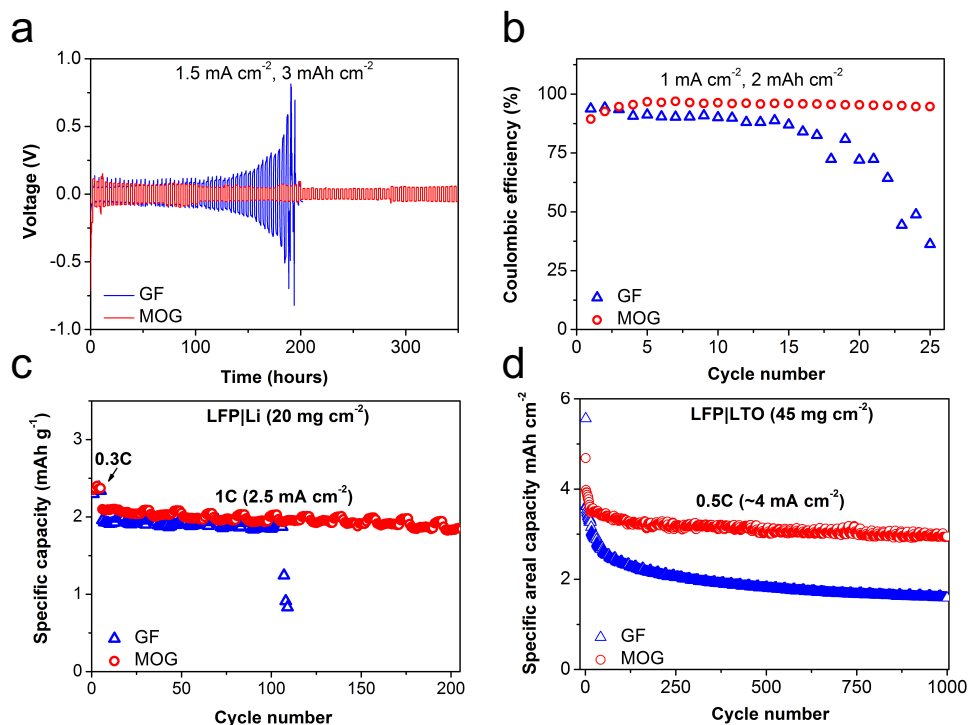


**Figure 3-6** (a) Polarization characterization of Li stripping and plating tests in Li|Li cells using GF and MOG (3 mA h cm<sup>-2</sup> for each cycle at 1.5 mA cm<sup>-2</sup>). (b) Coulombic efficiency evaluation of Li stripping and plating process in Cu|Li cells (2 mA h cm<sup>-2</sup> for each discharge at 1 mA cm<sup>-2</sup>). (c) Galvanostatic cycling of LiFePO<sub>4</sub>|Li cells using GF and MOG at current density of 1C (2.5 mA cm<sup>-2</sup>). (d) Long-term cycling of LiFePO<sub>4</sub>|Li<sub>4</sub>Ti<sub>5</sub>O<sub>12</sub> full cells using GF and MOG at current density of 0.5C (4 mA cm<sup>-2</sup>)

The long-term stability against Li was evaluated by Li symmetric cells (Li|Li cells). The galvanostatic tests were performed under 1.5 mA cm<sup>-2</sup> by amount of 3 mA h cm<sup>-2</sup> for each cycle.

As displayed in **Figure 3-6a**, the cell using GF suffers from escalating polarization as indicated by increasing overpotential along with the cycles. After 200 h operation, the cell voltage drastically increases from 50 mV to 800 mV and the curve exhibit zigzag profile afterwards, which are typical signs of proliferating formation of Li dendrites.<sup>23</sup> In sharp contrast, the cell using of MOG manifests a steady and smooth curve up to 350 h (55 mV), demonstrating MOF's role in blocking Li dendrites and ameliorating interfacial resistance with Li. **Figure 3-6b** depicts the Coulombic efficiency of Li<sup>+</sup> plating and stripping on Cu with areal capacity of 2 mA h cm<sup>-2</sup> at 1 mA cm<sup>-2</sup>. The cell using MOF steadily delivers an average Coulombic efficiency of 95%, compared with 80% for the cell using bare GF.

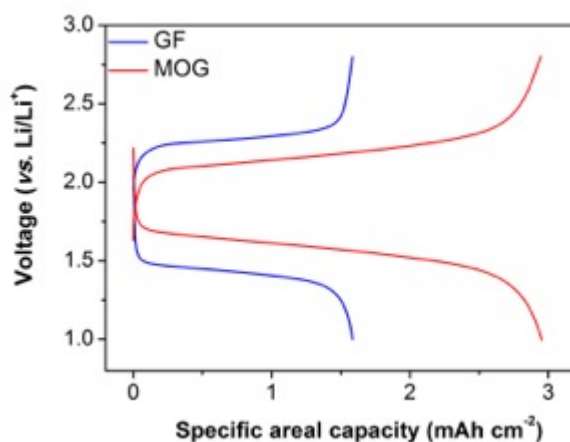


**Figure 3-7** Typical voltage-capacity plots of LiFePO<sub>4</sub>|Li<sub>4</sub>Ti<sub>5</sub>O<sub>12</sub> full cells using GF and MOG at 0.5C (4 mA cm<sup>-2</sup>)

In lithium metal batteries employing LiFePO<sub>4</sub> as cathode (LiFePO<sub>4</sub>|Li, **Figure 6c**), the cell using MOG delivers a specific capacity of 2 mA h cm<sup>-2</sup> at 205<sup>th</sup> cycle under current density of 2.5 mA cm<sup>-2</sup> (first 5 cycles at 0.75 mA cm<sup>-2</sup>), which corresponds to capacity retention of 80%. In comparison, the cell using GF suffers from abrupt capacity decline to 1.5 mA h cm<sup>-2</sup> starting from 106<sup>th</sup> cycle. Based on space charge theory, the mechanism of dendrite formation could be

interpreted by the ion concentration gradient across the cell upon polarization at high current density.<sup>24</sup> Due to inferior mobility of  $\text{Li}^+$  than anions (low  $t_{\text{Li}^+}$ ), the depletion of  $\text{Li}^+$  near electrode surface leads to local space charge, decomposition of anions and dendritic growth. MOF functionalized separator (MOG) transform the electrolyte by tethering anions and improve the  $t_{\text{Li}^+}$  and hence concentration polarization is mitigated. Consequently, MOG as separators endow Li-based devices with smaller overpotential, higher Coulombic efficiency and improved dendrites blocking ability. We further demonstrated exceptional cycling stability in full cell configuration using MOG as separator. **Figure 6d** shows the galvanostatic cycling of  $\text{LiFePO}_4|\text{Li}_4\text{Ti}_5\text{O}_{12}$  cells using MOG and GF. At high active material loading ( $\text{LiFePO}_4$ ) of  $45 \text{ mg cm}^{-2}$  and current density of  $\sim 4 \text{ mA cm}^{-2}$ , areal capacity of  $3 \text{ mA h cm}^{-2}$  could be achieved at 1000<sup>th</sup> cycle corresponding to 74% capacity retention. In sharp contrast, the cell using GF suffers from aggressive capacity fading to  $1.6 \text{ mA h cm}^{-2}$  with only 44 % capacity retained. Moreover, the smaller voltage hysteresis at 1000<sup>th</sup> cycle for the cell using MOG also support the notion that MOG as separator considerably alleviate the concentration polarization in thick electrodes (see **Figure 3-7**).<sup>5, 6</sup>

### 3.3 Conclusion

In this study, separators were functionalized by MOF to tackle the intrinsic limitation of liquid electrolyte. By taking advantage of unsaturated metal sites in MOF, the  $\text{Li}^+$  transference number was improved from 0.34 for pristine separator to 0.67 for MOF functionalized separator. On top of that, the issues of  $\text{Li}^+$  stripping and plating processes in terms of huge overpotential, low Coulombic efficiency and dendrites penetration were mitigated even under high current density. Moreover, remarkable cycling performance of full cell using thick electrode ( $45 \text{ mg cm}^{-2}$ ) and MOF functionalized separator was demonstrated, which allows areal capacity of  $3 \text{ mA h cm}^{-2}$  reversibly cycling for over 1000 times under  $4 \text{ mA cm}^{-2}$ . Overall, this work proposes a composite separator employing MOF to improve the  $\text{Li}^+$  transference number, electrochemical performances of Li electrodes and conventional lithium ion batteries with thick electrodes. We also envision that the present composite strategy could be readily extended to other integration approaches like coating or laminating a MOF functional layer on separators.

### 3.4 Experimental Section

**Preparation of UiO-66-NH<sub>2</sub>-glass fiber (MOF-GF) separators.** The MOF precursors were prepared by dissolving 2-aminoterephthalic acid (NH<sub>2</sub>-BDC) and ZrCl<sub>4</sub> in mixture of dimethylformamide (DMF) and H<sub>2</sub>O. Glass fiber (Whatman, GF/C) disks with tailored diameter of 18 mm were soaked in MOF precursors. After sonicating for 30 min and aging for overnight, the *in-situ* growth of MOF on GF was carried out in a microwave reactor (900 W) at °C for min. After reaction, the yellowish separators were repeatedly rinsed by DMF and Methanol, followed by drying at vacuum oven at 80 °C.

**Physical characterization.** The morphology was examined by SEM using Nova Nano 230 (FEI). Thin layer of gold was coated on samples by plasma sputtering before analysis. Crystalline structure was determined by Rigaku powder XRD using K $\alpha$  radiation ( $\lambda = 1.54 \text{ \AA}$ ) run at 30 kV and 15 mA. A Jasco 420 FT-IR spectrophotometer was used to collect infrared spectra in transmission mode. The N<sub>2</sub> adsorption/desorption curves were acquired by ASAP 2020 plus (Micrometrics) at 77 K. The surface area was calculated based on the Brunauer-Emmett-Teller (BET) equation from the adsorption branch. The pore size distribution was derived from Density Function Theory (DFT) models. All samples before tests were degassed at 80 °C for 24 h.

**Electrochemical characterization.** The separators were thermally activated at 200 °C under dynamic vacuum to remove residual solvents and generate unsaturated metal sites. 1 M LiClO<sub>4</sub> in propylene carbonate with fluoroethylene carbonate additive (5 volume %) was used as liquid electrolyte. All characterizations were performed in coin cell (CR2032) configuration and volume of electrolyte was ~ 100 ul. The Li<sup>+</sup> transference number was evaluated by conventional Bruce-Vincent method in lithium symmetric cell. The cells were polarized by a small constant potential (V, 20 mV) for 30 mins, the corresponding polarization currents including the initial current (I<sub>0</sub>)



and final steady-state current ( $I_{ss}$ ) were recorded. Meanwhile, the interfacial resistance before ( $R_{int}^0$ ) and after ( $R_{int}^{ss}$ ) potentiostatic polarization were derived from EIS (Solartron) by alternating current amplitude of 20 mV from 100 kHz to 1 Hz. The  $Li^+$  transference number was calculated as following equation:  $t_{Li^+} = I_{ss}(V - I_0 R_{int}^0) / (I_0(V - I_{ss} R_{int}^{ss}))$ . The ionic conductivity was measured by sandwiching electrolyte saturated separators by two blocking electrodes (stainless steel plates), which is approximated by equation:  $\sigma = 4L / \pi R D^2$ , where  $\sigma$  is conductivity; L and D are thickness and diameter of separator, respectively; R is resistance value from EIS. Activation energy ( $E_a$ ) from Arrhenius behavior of conductivity ( $\sigma = \sigma_0 \exp(-E_a/RT)$ ) was derived by linear fitting between  $\log(\sigma)$  and  $1000/T$ . The measurements were conducted in convection oven (VWR) by equilibrating the cells at various temperatures. The electrochemical stability window was determined by CV using lithium foils as reference/counter electrodes and stainless-steel plates (SS) as the working electrodes. The cells were tested between  $-0.2$  and  $5$  V at  $1 \text{ mV s}^{-1}$  (Biologic).

The polarization of  $Li^+$  plating and stripping in Li|Li cells were carried out at  $1.5 \text{ mA cm}^{-2}$  for a periodic 2 h. The Coulombic efficiency in Cu|Li cells were obtained by plating at  $1.5 \text{ mA cm}^{-2}$  for 2 h and stripping to voltage cutoff at  $1.2 \text{ V}$  (vs. Li/Li<sup>+</sup>). LiFePO<sub>4</sub> electrodes were fabricated by mixing LiFePO<sub>4</sub>, poly(vinylidene difluoride) and carbon nanotube in mass ratio of 85:10:5 at N-methyl-2-pyrrolidone. The blends were casted on carbon-coated aluminum and dried at  $80 \text{ }^\circ\text{C}$  under vacuum. The thickness or loading of electrodes were controlled by tuning the slurry viscosity and height of doctor blade. Li<sub>4</sub>Ti<sub>5</sub>O<sub>12</sub> electrodes were prepared in the same manner and the weight ratio between LiFePO<sub>4</sub> and Li<sub>4</sub>Ti<sub>5</sub>O<sub>12</sub> in full cells is 1:1.

### 3.5 References

1. Hannan, M.A., Lipu, M.S.H., Hussain, A. & Mohamed, A. A review of lithium-ion battery state of charge estimation and management system in electric vehicle applications: Challenges and recommendations. *Renewable and Sustainable Energy Reviews* **78**, 834-854 (2017).
2. Albertus, P., Babinec, S., Litzelman, S. & Newman, A. Status and challenges in enabling the lithium metal electrode for high-energy and low-cost rechargeable batteries. *Nature Energy* **3**, 16-21 (2018).
3. Lin, D., Liu, Y. & Cui, Y. Reviving the lithium metal anode for high-energy batteries. *Nature Nanotechnology* **12**, 194 (2017).
4. Wu, B. et al. Interfacial behaviours between lithium ion conductors and electrode materials in various battery systems. *Journal of Materials Chemistry A* **4**, 15266-15280 (2016).
5. Du, Z., Wood, D.L., Daniel, C., Kalnaus, S. & Li, J. Understanding limiting factors in thick electrode performance as applied to high energy density Li-ion batteries. *Journal of Applied Electrochemistry* **47**, 405-415 (2017).
6. Diederichsen, K.M., McShane, E.J. & McCloskey, B.D. Promising Routes to a High Li<sup>+</sup> Transference Number Electrolyte for Lithium Ion Batteries. *ACS Energy Letters* **2**, 2563-2575 (2017).
7. Jiang, F. & Peng, P. Elucidating the Performance Limitations of Lithium-ion Batteries due to Species and Charge Transport through Five Characteristic Parameters. *Scientific Reports* **6**, 32639 (2016).
8. Tu, Z. et al. Nanoporous Hybrid Electrolytes for High-Energy Batteries Based on Reactive Metal Anodes. *Advanced Energy Materials* **7**, 1602367-n/a (2017).

9. Tu, Z. et al. Designing Artificial Solid-Electrolyte Interphases for Single-Ion and High-Efficiency Transport in Batteries. *Joule* **1**, 394-406 (2017).
10. Chi, M. et al. Excellent rate capability and cycle life of Li metal batteries with ZrO<sub>2</sub>/POSS multilayer-assembled PE separators. *Nano Energy* **28**, 1-11 (2016).
11. Wang, Z. et al. Self-Assembly of PEI/SiO<sub>2</sub> on Polyethylene Separators for Li-Ion Batteries with Enhanced Rate Capability. *ACS Applied Materials & Interfaces* **7**, 3314-3322 (2015).
12. Mao, X. et al. Polyethylene separator activated by hybrid coating improving Li<sup>+</sup> ion transference number and ionic conductivity for Li-metal battery. *Journal of Power Sources* **342**, 816-824 (2017).
13. Horike, S., Umeyama, D. & Kitagawa, S. Ion Conductivity and Transport by Porous Coordination Polymers and Metal–Organic Frameworks. *Accounts of Chemical Research* **46**, 2376-2384 (2013).
14. Park, S.S., Tulchinsky, Y. & Dincă, M. Single-Ion Li<sup>+</sup>, Na<sup>+</sup>, and Mg<sup>2+</sup> Solid Electrolytes Supported by a Mesoporous Anionic Cu–Azolate Metal–Organic Framework. *Journal of the American Chemical Society* **139**, 13260-13263 (2017).
15. Ameloot, R. et al. Ionic Conductivity in the Metal–Organic Framework UiO-66 by Dehydration and Insertion of Lithium tert-Butoxide. *Chemistry – A European Journal* **19**, 5533-5536 (2013).
16. Kandiah, M. et al. Synthesis and Stability of Tagged UiO-66 Zr-MOFs. *Chemistry of Materials* **22**, 6632-6640 (2010).
17. Zhang, B. et al. A superior thermostable and nonflammable composite membrane towards high power battery separator. *Nano Energy* **10**, 277-287 (2014).

18. Thomas, B.J.C., Shaffer, M.S.P. & Boccaccini, A.R. Sol-gel route to carbon nanotube borosilicate glass composites. *Composites Part A: Applied Science and Manufacturing* **40**, 837-845 (2009).
19. Valenzano, L. et al. Disclosing the Complex Structure of UiO-66 Metal Organic Framework: A Synergic Combination of Experiment and Theory. *Chemistry of Materials* **23**, 1700-1718 (2011).
20. Doyle, M., Fuller, T.F. & Newman, J. The importance of the lithium ion transference number in lithium/polymer cells. *Electrochimica Acta* **39**, 2073-2081 (1994).
21. Mukherjee, R., Krishnan, R., Lu, T.-M. & Koratkar, N. Nanostructured electrodes for high-power lithium ion batteries. *Nano Energy* **1**, 518-533 (2012).
22. Aurbach, D. et al. Design of electrolyte solutions for Li and Li-ion batteries: a review. *Electrochimica Acta* **50**, 247-254 (2004).
23. Lu, Y. et al. Stable Cycling of Lithium Metal Batteries Using High Transference Number Electrolytes. *Advanced Energy Materials* **5**, 1402073-n/a (2015).
24. Chazalviel, J.N. Electrochemical aspects of the generation of ramified metallic electrodeposits. *Physical Review A* **42**, 7355-7367 (1990).

## **Chapter 4 Improving $\text{Li}^+$ Transference Number of Liquid Electrolyte by Metal–organic Frameworks**

Lithium batteries capable of cycling under high current density is a pivotal aspect for next-generation battery technologies. However, such operations generally induce huge concentration polarization and fast capacity decay. To circumvent the issues, various electrolyte additive has been proposed to enhance the  $\text{Li}^+$  transport efficiency by improving  $\text{Li}^+$  transference number yet a cost-effective approach remains unexplored. We present a facile method to effectively modulate the ion transport of conventional liquid electrolyte by addition of metal–organic frameworks (MOF). The MOF herein serve as anion capturer to immobilize anions while the facilitate the transport of  $\text{Li}^+$ . The resulting hybrid electrolytes exhibit doubled  $\text{Li}^+$  transference number compared with respective liquid electrolyte, superior interfacial stability and compatibility towards metallic Li and cathodes.

## 4.1 Introduction

The widespread adoption of portable electronics and emerging market of electric vehicles (EVs) have spurred the interests on fast-charging technologies for lithium batteries. The improvements on battery performances including lifespan and power capability under high rate operation are of particular significance in relieving driving range anxiety for EVs. However, high current inevitably induces severe polarizations, especially concentration polarization for  $\text{Li}^+$  transport, which is a major reason for resulting poor performances.<sup>1</sup> The  $\text{Li}^+$  transference number (denoted as  $t_{\text{Li}^+}$ ), defined as ratio of  $\text{Li}^+$  conductivity to overall conductivity, is typically around 0.3.<sup>2</sup> The inefficient transport of  $\text{Li}^+$  would lead to depletion of  $\text{Li}^+$  and breakdown of anions in vicinity of electrodes, which is responsible for deteriorated performances during fast charging and discharging processes.<sup>3, 4</sup> Hence, improving the  $\text{Li}^+$  transport efficiency of liquid electrolytes serves as a promising route towards advancements of batteries operating under high rate.

The incorporation of inorganic additives has been demonstrated to improve the  $t_{\text{Li}^+}$  of liquid electrolyte. For instance, Pfaffenhuber *et. al.* reported that  $t_{\text{Li}^+}$  of 0.1M  $\text{LiClO}_4$  at tetrahydrofuran (THF) could be increased from 0.13 to 0.41 by adding 0.15 volume % silica.<sup>5</sup> In another example, 30 weight % additive of  $\text{Li}_2\text{SiO}_3$  improve the  $t_{\text{Li}^+}$  of 1M  $\text{LiPF}_6$  in carbonates to 0.42.<sup>6</sup> The mechanisms are generally interpreted as preferential adsorption of anions on the surface of inorganic species. Alternatively, covalent grafting positive segment of ionic liquid on oxide nanoparticles and dispersing the functionalized nanoparticle within respective liquid electrolyte yield composite electrolytes with increased  $t_{\text{Li}^+}$ .<sup>7, 8</sup> The ionic coupling between charged endpoint in oxides with counterions in liquid phase render anions relative immobile. In these previous studies, manipulating anion mobility improves  $t_{\text{Li}^+}$  to a certain extent ( $t_{\text{Li}^+} < 0.5$ ) while there is lack of cost-effective approach to transform the  $\text{Li}^+$  transport behaviors.

Herein we develop a straightforward technique to enhance  $t_{\text{Li}^+}$  of commercial liquid electrolyte by metal–organic frameworks (MOF). As exemplified in **Figure 4-1a** and **4-1b**, UiO-66-NH<sub>2</sub> is constructed by inorganic metal nodes ( $\text{Zr}_6\text{O}_4(\text{OH})_4$ ) periodically bridged by organic linkers (2-aminoterephthalic acid), forming cubic scaffold with small tetrahedral and large octahedral micropores.  $\mu_3$ -OH ligands in metal clusters ( $\text{Zr}_6\text{O}_4(\text{OH})_4$ ) are removable upon heating (thermal activation) and the dehydration generates unsaturated metal sites ( $\text{Zr}_6\text{O}_6$  units) with strong Lewis acidity. Blending activated MOF with liquid electrolyte yield well-dispersed hybrid electrolyte (**Figure 4-1c**). We propose that MOF nanocages would interact and immobilize anions *via* unsaturated metal sites, which simultaneously facilitates rapid transport of  $\text{Li}^+$ .

## 4.2 Results and Discussions

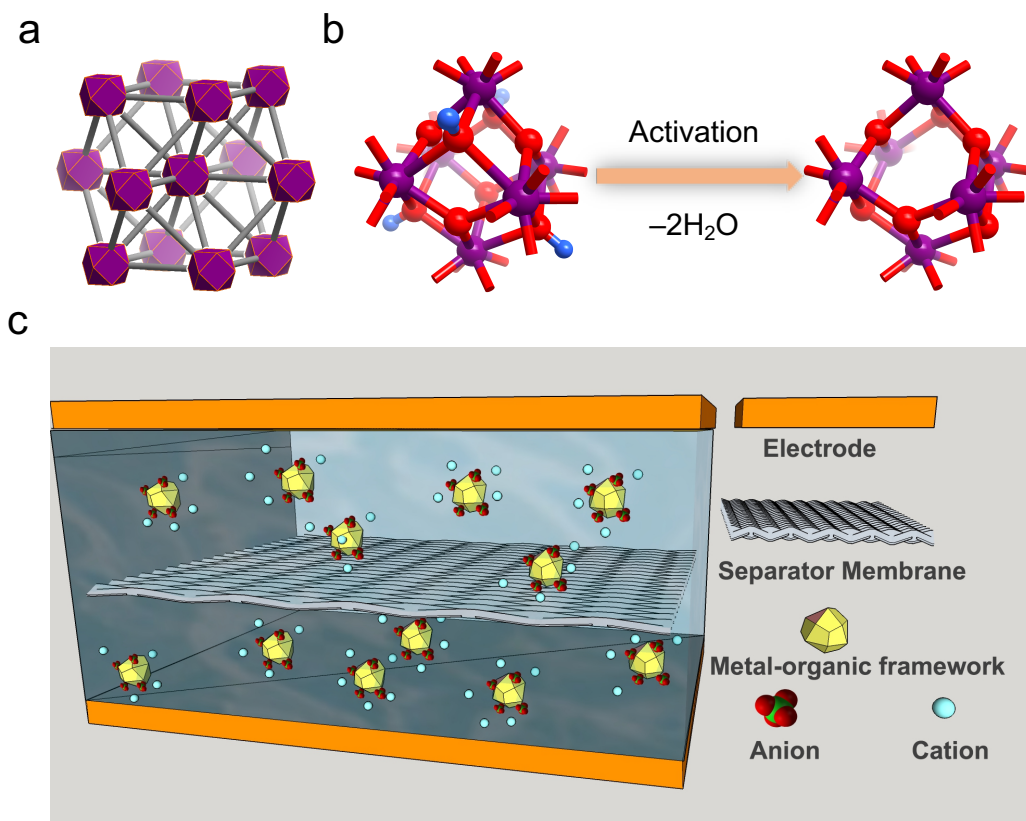


**Figure 4-1** (a) Representative topology structure of UiO-66-NH<sub>2</sub> (MOF) constructed from organic linkers (grey sticks) bridged metal clusters (purple polyhedron). (b) Illustration showing creation of unsaturated metal sites by dehydration (thermal activation) of capped hydroxyl on Zr<sup>4+</sup> centers. (c) Schematic drawing of hybrid electrolyte containing MOF and liquid electrolyte (LE) in electrochemical device.



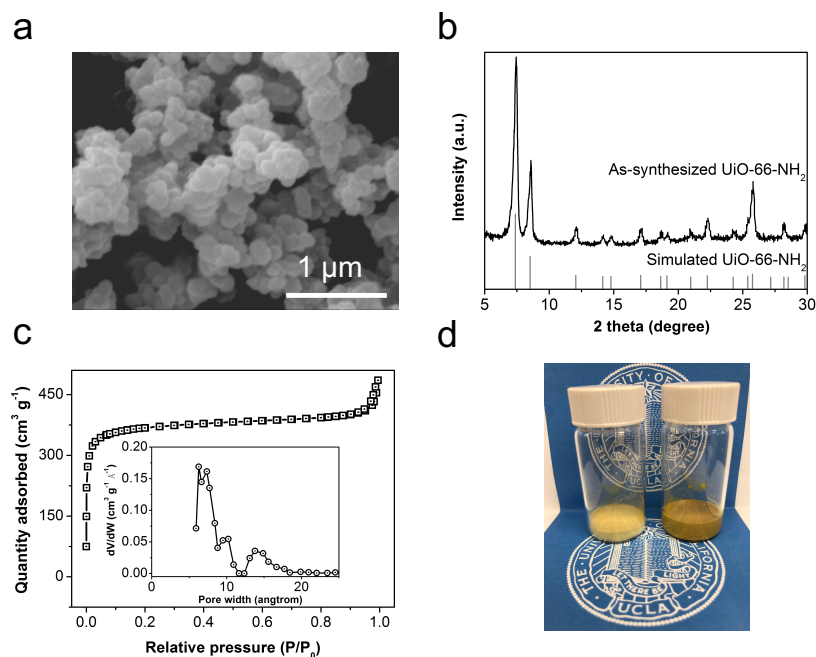


**Figure 4-2** (a) SEM image of as-synthesized MOF. (b) As-synthesized and simulated XRD patterns of MOF. (c) N<sub>2</sub> adsorption/desorption isotherms of MOF (inset: pore size distribution derived from DFT model). (d) Photograph: the vial in the left of is activated MOF, the vial in the right is 0.2MOF@LE prepared by blending MOF with LE.

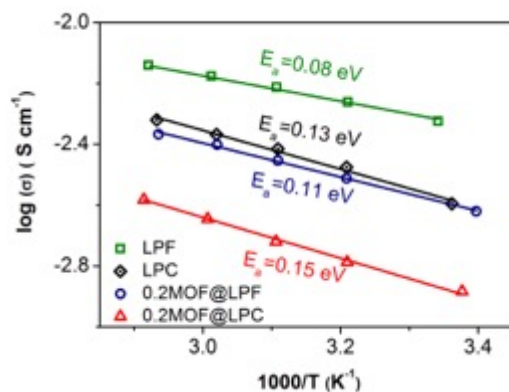


**Figure 4-3** Temperature dependent conductivities of LE (LPC and LPF) and 0.2MOF@LE (0.2MOF@LPC and 0.2MOF@LPF)

The morphology and crystal structure of as-synthesized MOF were characterized by scanning electron microscopy (SEM) and powder X-ray diffraction (XRD), respectively. As shown in **Figure 4-2a**, the MOF show intergrown crystal with average primary particle size of ~200 nm. The diffraction pattern as displayed in **Figure 4-2b** is indexable to the simulated pattern of its analogue UiO-66. The Brunauer-Emmett-Teller (BET) surface area of 1215 m<sup>2</sup> g<sup>-1</sup> and micropore diameter peaking at 8 Å are quantified by N<sub>2</sub> adsorption/desorption isotherms (**Figure 4-2c**), which are in line with literature reported.<sup>9</sup> The pore aperture allows the access of common electrolyte species (ionic diameter: ClO<sub>4</sub><sup>-</sup>: 4.74 Å, PF<sub>6</sub><sup>-</sup>: 5.08 Å).<sup>10</sup> Before introduction of liquid electrolyte, MOF was activated under dynamic vacuum at elevated temperature for generating open metal sites (OMSs) through elimination of guest molecule and capped hydroxide. Afterwards, every 0.2 mg activated MOF powders were homogeneously blended with 1 ul LE to produce 0.2MOF@LE (**Figure 4-2d**). The LE exemplified here are 1M LiClO<sub>4</sub> in PC (propylene carbonate, denoted as LPC) and 1M LiPF<sub>6</sub> in EC/DEC (ethylene carbonate/diethyl carbonate, denoted as LPF), which are denoted as 0.2MOF@LPC and 0.2MOF@LPF, respectively.

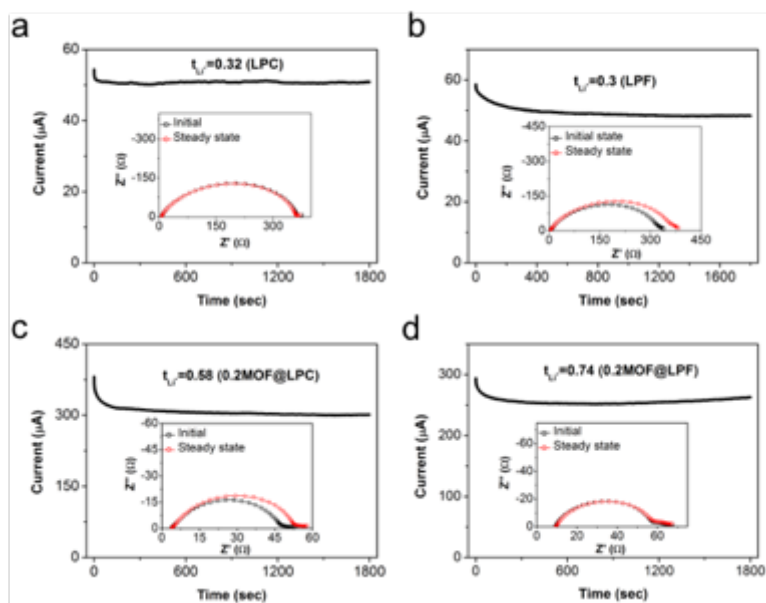


**Figure 4-4** Measurements on  $\text{Li}^+$  transference number of LE and 0.2MOF@LE using potentiostatic polarization (insets: EIS curves of Li symmetric cells before and after polarization)

The ionic conductivity and thermal activation energy of electrolytes were characterized by electrochemical impedance spectroscopy (EIS). The ionic conductivities were evaluated by sandwiching electrolyte-saturated glass fibers between two stainless steel plates. As shown in **Figure 4-3**, the ambient conductivity (25 °C) of 0.2MOF@LE account for ~ 50 % of their LE counterparts. Despite higher conductivity of LE, one critical drawback of LE is their low  $\text{Li}^+$  transference number ( $t_{\text{Li}^+} = \sim 0.3$ ) due to inferior  $\text{Li}^+$  mobility than anions (see **Figure 4-4**).<sup>2</sup> The  $t_{\text{Li}^+}$  of 0.2MOF@LE were obtained by classical potentiostatic polarization approach (see details in Experimental Section).<sup>11, 12</sup> As shown in **Figure 4-4**, 0.2MOF@LPC and 0.2MOF@LPF give values of 0.58 and 0.74, which are 93% and 150% higher than respective LE. Given the conductivity and transference number, the conductivities for cation and anion are separated and summarized in **Figure 4-5a**, where anion conductivity for 0.2MOF@LPF is substantially decreased while overall  $\text{Li}^+$  conductivity is instead improved. This phenomenon is in good

agreement with our proposed concept that the UMS in activated MOF serve as anchoring points for anions and the resulting anion-decorated ionic channels could promote the transport of  $\text{Li}^+$ . Based on Arrhenius equation, by linearly fitting plots of temperature dependent conductivity, the derived activation energy of 0.2MOF@LE is similar to LE, signifying analogous diffusion barrier. The electrochemical stability window of electrolytes was determined by cyclic voltammetry (CV) using stainless steels (SS) as working electrodes and Li as counter/reference electrodes (SS|electrolyte|Li). As shown in **Figure 4-5b** and **4-5c**, the reaction currents for lithium plating/stripping ( $\sim 0$  V vs.  $\text{Li}/\text{Li}^+$ ) in 0.2MOF@LE are considerably higher than LE benchmarks, which is in accordance with results that  $\text{Li}^+$  conductivities are improved by virtue of MOF.<sup>13</sup> Moreover, anodic stability of 0.2MOF@LE up to 5 V vs.  $\text{Li}/\text{Li}^+$  further confirms the robustness of MOF structures.

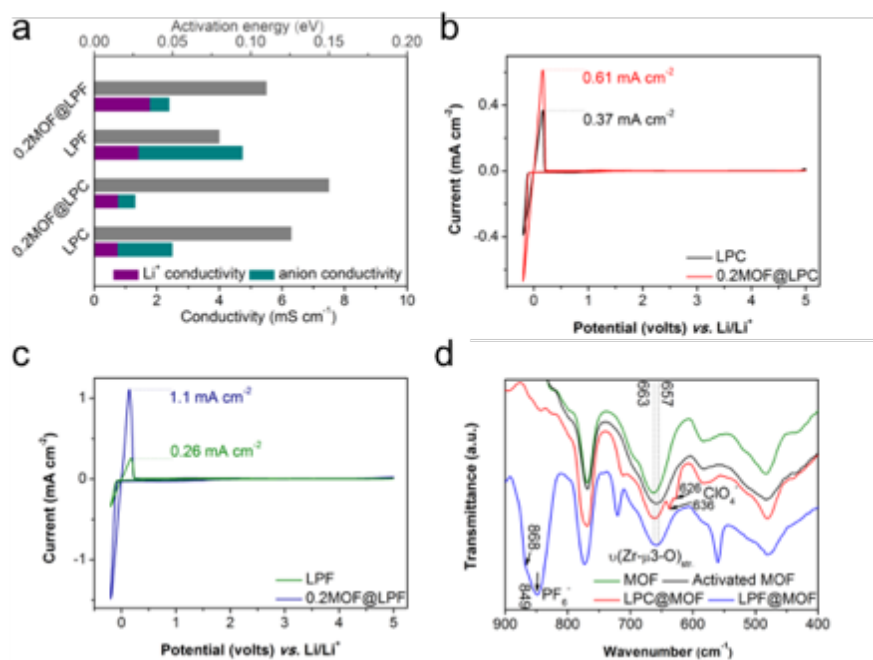
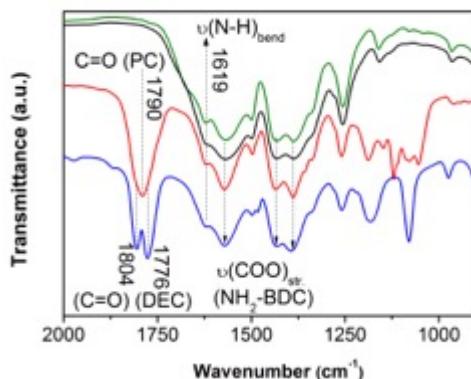


Figure 4-5 (a)  $\text{Li}^+$  transference number, ionic conductivity and thermal activation energy of LE and 0.2MOF@LE. Comparison of CV curves at sweep rate of  $1 \text{ mV s}^{-1}$  between  $-0.2$  to 5 V vs.

Li/Li<sup>+</sup>: (b) LPC and 0.2MOF@LPC, (c) LPF and 0.2MOF@LPF. (d) FT-IR spectra of as-synthesized MOF, activated MOF, LPC@MOF and LPF@MOF.



**Figure 4-6** FT-IR spectra of as-synthesized MOF, activated MOF, LPC@MOF and LPF@MOF in wavenumber between 900 to 2000 cm<sup>-1</sup>

To elucidate the interaction between confined LE and MOF scaffold, Infrared spectroscopy (IR) was performed on flow-free LE@MOF, which were collected by filtering out LE from 0.2MOF@LE. **Figure 4-5d** and **Figure 4-6** show the FT-IR (Fourier-transform-IR) spectra of as-synthesized MOF, activated MOF, LPC@MOF and LPF@MOF, characteristic peaks of MOF ligands (2-aminoterephthalic acid) locate at 1389/1434/1570 and 1619 cm<sup>-1</sup>, which are attributed to stretching vibrations of carboxylic group (COO) and bend vibration of amine group (N-H), respectively.<sup>14, 15</sup> Signal at 1790 cm<sup>-1</sup> (LPC@MOF) and 1776/1804 cm<sup>-1</sup> (LPF@MOF) represent Li<sup>+</sup>-coordinating carbonyl groups (C=O) from respective solvents.<sup>16, 17</sup> Dehydration of Zr<sub>6</sub>O<sub>4</sub>(OH)<sub>4</sub> inorganic moieties results in Zr<sub>6</sub>O<sub>6</sub> with exposed metal sites, the vibration pertaining to Zr-μ<sub>3</sub>-O shows a consequent redshift from 663 to 657 cm<sup>-1</sup>.<sup>18, 19</sup> After complexing of LE, vibrations of Zr-μ<sub>3</sub>-O exhibit recovered blueshift, which accompanied with the emergence of anion asymmetric

vibrations ( $636$  and  $868\text{ cm}^{-1}$  for  $\text{ClO}_4^-$  and  $\text{PF}_6^-$ , respectively).<sup>20, 21</sup> These observations are coincident with the notion that the symmetry structures of anions are perturbed due to tethering of anions on  $\text{Zr}^{4+}$  unsaturated sites.<sup>22</sup>

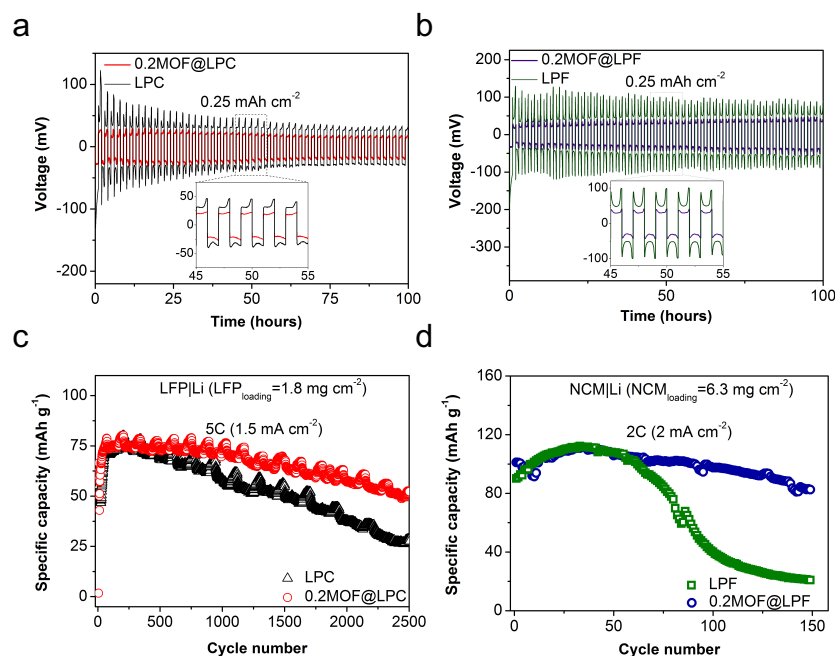


**Figure 4-7** Li|Li symmetric cells in (a) LPC and 0.2MOF@LPC, and (b) LPF and 0.2MOF@LPF for Li stripping and plating tests at  $0.25\text{ mA cm}^{-2}$  (time interval: 1 h). (c) LFP|Li cells using LPC and 0.2MOF@LPC at current density of 5C ( $1.5\text{ mA cm}^{-2}$ ). (d) NCM|Li cells using LPF and 0.2MOF@LPF at current density of 2C ( $2\text{ mA cm}^{-2}$ )

The stability of electrolyte against metallic Li was evaluated in Li symmetric cell configuration. As shown in **Figure 4-7a** and **4-7b**, the galvanostatic cycling was conducted under  $0.25\text{ mA cm}^{-2}$  with amount of  $0.25\text{ mAh cm}^{-2}$  for each cycle, the cells in 0.2MOF@LE show more stable voltage profile and substantial reduced overpotential than the cells in LE. The cell using 0.2MOF@LPF, for instance, the potential variation from 29 to 40 mV is only 38%, in sharp contrast with the difference of 104% (between 48 to 98 mV) from the cell using LPF (see insets

of **Figure 4-7a** and **4-7b**). Moreover, overpotential growth of the cell in LPF is escalating to 190 mV by 300 h (see elongated cycle at **Figure 4-8**), in contrast, the cell in 0.2MOF@LPF delivers stable potential of 60 mV which demonstrates that MOF is able to mitigate deteriorated interface of electrolyte towards Li. These phenomena root from the superiority of the ionic channels constructed by MOF in two aspects. Firstly, entrapment of anions within MOF nanocages boosts the transport of  $\text{Li}^+$ , which leads to low interfacial resistivity and ameliorated overpotential as a consequence. Second, the introduction of MOF to LE assists smooth transition of local ion distribution, thereby producing more stable solid-electrolyte interphases (SEI).<sup>23-25</sup> The low  $\text{Li}^+$  transference number of LE is generally responsible for large concentration polarization and insufficient  $\text{Li}^+$  supply under high current operation, which induce the breakdown of anions in vicinity of electrodes and consequently initialize the growth of Li dendrites, the corresponding SEI evolution is indicative by uneven voltage profiles of  $\text{Li}^+$  stripping and plating in LE.<sup>3,26</sup>

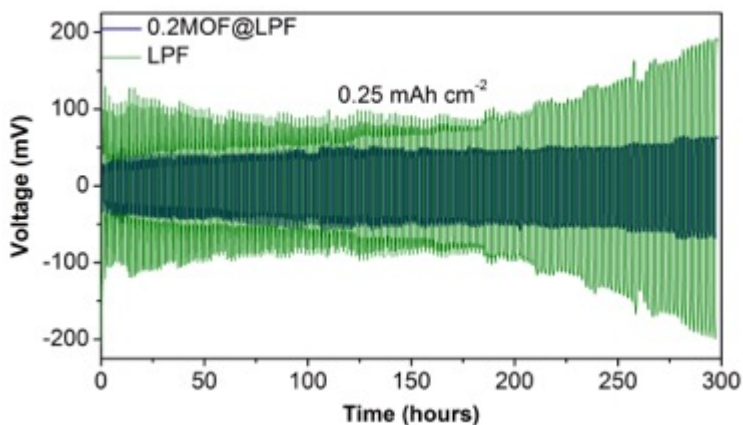


**Figure 4-8** Long term Li stripping and plating tests under  $0.25 \text{ mA cm}^{-2}$  using LPF and 0.2MOF@LPF

Considering the inferior anodic stability of LPC than LPF, prototype  $\text{LiFePO}_4(\text{LFP})|\text{Li}$  cells operating  $\sim 3.3$  V (vs.  $\text{Li}/\text{Li}^+$ ) were fabricated using LPC and  $0.2\text{MOF}@LPC$ .  $\text{LiNi}_{0.33}\text{Co}_{0.33}\text{Mn}_{0.33}\text{O}_2(\text{NCM})|\text{Li}$  cells operating at  $\sim 3.7$  V employ LPF and  $0.2\text{MOF}@LPF$ . High current densities were applied for galvanostatic cycling as comparisons on corresponding capacity decay are of particular interest to highlight the difference of  $\text{Li}^+$  transference number between LE and  $0.2\text{MOF}@LE$ . Long-term cycling of  $\text{LFP}|\text{Li}$  cells were performed at 5C ( $1.5 \text{ mA cm}^{-2}$ ), as shown in **Figure 4-7c**, specific capacity of the cells was initially stabilized at  $\sim 75 \text{ mAh g}^{-1}$ , the cell using  $0.2\text{MOF}@LPC$  affords capacity retention of 70% after prolonged 2500 cycles, which corresponds to passage of total 115 coulombs and average 0.012 % fading per cycle. In comparison, the cell using LPC exhibit rapid 0.028% decay per cycle, suggesting faster build-up of polarization under high rate operation. In another example, we increased the cathode loading of NCM to exaggerate the difference. The  $\text{NCM}|\text{Li}$  cell using  $0.2\text{MOF}@LPF$  maintains 80% capacity after 150 cycles at 2C ( $2 \text{ mA cm}^{-2}$ ) while the cell using LPF exhibit drastic capacity decay to  $20 \text{ mAh g}^{-1}$  by 150<sup>th</sup> cycle. The result is consistent with the evolution of voltage profile for Li stripping and plating test, where the  $\text{Li}|\text{Li}$  cell using LPF shows accelerating overpotential increase due to low  $\text{Li}^+$  transference number, large polarization and unstable SEI.



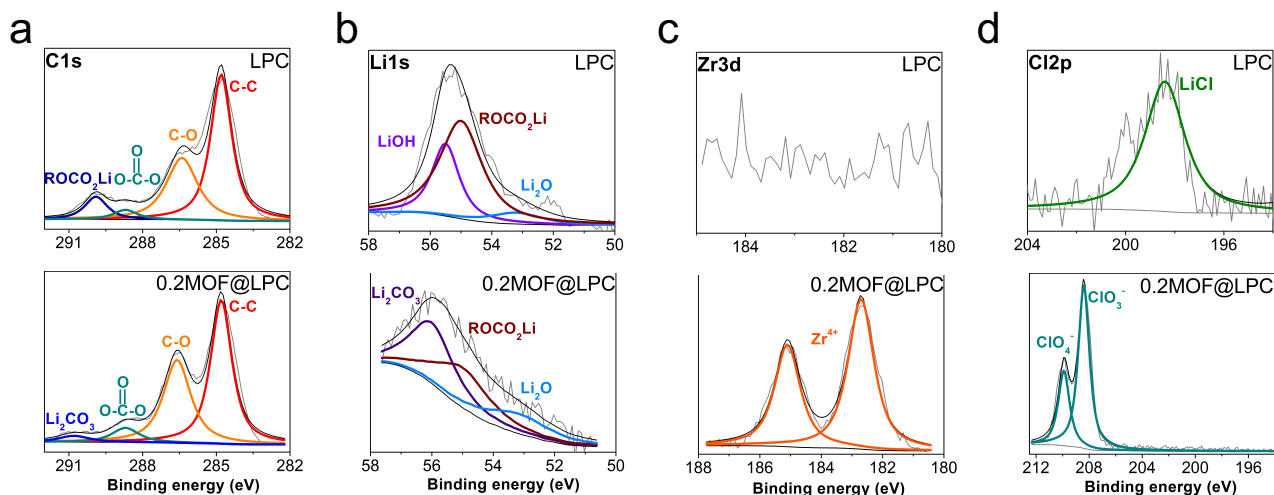


**Figure 4-9** XPS analysis of Li collected from Li|Li cells after cycling at 0.25 mA cm<sup>-2</sup> for 100 h.

(a) C1s, (b) Li1s, (c) Zr3d, (d) Cl2p

X-ray photoelectron spectroscopy (XPS) was carried out on Li surfaces harvested from cycled Li|Li cells. As exemplified by deconvolutions of Li 1s and C 1s spectra from cycled Li in LPC and 0.2MOF@LPC (**Figure 4-9a** and **4-9b**), the content ratio of Li<sub>2</sub>CO<sub>3</sub> over ROCO<sub>2</sub>Li is higher at Li cycled in 0.2MOF@LPC than the one in LPC, resulting more stable SEI in 0.2MOF@LPC could be which could be interpreted by lower solubility of Li<sub>2</sub>CO<sub>3</sub> as compared with ROCO<sub>2</sub>Li.<sup>27</sup> Moreover, the binding energy of Zr 3d (185.1, 182.8 eV) indicates that Zr is tetravalent, suggesting Zr<sup>4+</sup> is not reduced upon contacting with metal Li (**Figure 4-9c**).<sup>28</sup> More importantly, Cl 2p as displayed in **Figure 4-9d** proves that ClO<sub>4</sub><sup>-</sup> is reduced to covalent bonded LiCl in LPC, while major Cl species of 0.2MOF@LPC remain as ionic form without byproduct of LiCl.<sup>29, 30</sup>

### 4.3 Conclusion

Our findings provide a novel pathway towards hybrid electrolytes in which  $\text{Li}^+$  transference number of liquid electrolyte could be readily improved by metal–organic frameworks (MOF). We illustrate the approach using activated MOF with unsaturated metal sites that could tether anions and promote the transport of  $\text{Li}^+$ . The resulting hybrid electrolytes exhibit enhanced transference number (up to 0.74), stable interfacial resistance against metallic Li and superior compatibility towards various cathode materials (up to 5 V vs.  $\text{Li}/\text{Li}^+$ ). The cathode|Li cells employing hybrid electrolytes show substantial improvement on cycle lifespan especially under high rate operation, benefiting from meliorated  $\text{Li}^+$  transport efficiency and mitigated concentration polarization. By taking advantage of vast library of MOF, the proposed strategy opens up a new vista for improving the transport efficiency of  $\text{Li}^+$  of conventional liquid electrolyte.

## 4.4 Experimental Section

**Synthesis of UiO-66-NH<sub>2</sub>.** The MOF (UiO-66-NH<sub>2</sub>) were synthesized based on a facile hydrothermal method according to a reported literature. Typically, 5 mmol 2-aminoterephthalic acid (NH<sub>2</sub>-BDC), 3 mmol ZrCl<sub>4</sub> and 22.4 mmol HCl (35 wt%) were added into 150 mL dimethylformamide (DMF) for 30 minutes continuously stirring. The excessive ligands ratio over metal salt and addition of concentrated HCl were intended for modulating the growth Zr cluster nodes as well as obtaining highly crystalline products, especially for UiO-66-NH<sub>2</sub>. The transparent mixture after fully dissolution were transferred into a 250 mL glass bottle at pre-heated 120 °C for 21 hours. The pale-yellow precipitates were collected *via* centrifugation and thoroughly washed by DMF (3 times) and methanol (3 times).

**Materials structure and characterization.** SEM images were acquired using...The XRD patterns were collected by Rigaku powder X-ray diffractometer (XRD), operating at 30 kV/15 mA with K $\alpha$  radiation ( $\lambda = 1.54 \text{ \AA}$ ). N<sub>2</sub> adsorption and desorption isotherms were obtained by ASAP 2020 plus (Micrometrics) at 77 K, the corresponding pore size distribution was derived from Density Function Theory (DFT) models. Before each isotherm, the samples were subject to degas at 150 °C overnight to remove guest molecules condensed in the pores. Infrared spectra were performed on a Fourier transform infrared (FT-IR) spectrophotometer (Jasco 420) using transmission mode. For XPS studies, the cycled Li|Li cells were disassembled in glovebox, the harvested Li electrodes were then sealed in a transporter and immediately transferred to high-vacuum chamber of XPS (AXIS Ultra DLD). The obtained spectra were calibrated by C 1s peak at 284.8 eV and fitted to Gaussian-Lorentzian functions for peak deconvolutions.

**Preparation and characterization of electrolytes with MOF additives.** 1 M LiClO<sub>4</sub> in PC (LPC) liquid electrolytes were homemade by dissolving LiClO<sub>4</sub> (Sigma, 99.99%) in PC (Sigma) with 5

volume percentage additives of fluoroethylene carbonate (FEC). Before preparation, drying of LiClO<sub>4</sub> salts in vacuum oven (150 °C) overnight was conducted to remove trace amount of moisture. 1 M LiPF<sub>6</sub> in EC/DEC (weight ratio of 1:1) is commercially available and used as received (BASF). The dehydration of MOF was carried out by thermal activation at 200 °C under dynamic vacuum. 0.2MOF@LE were prepared by combining every 0.2 mg activated MOF with 1ul LE. The well-dispersion of MOF in LE was achieved by rigorous magnetic stirring of the mixture. For FT-IR studies on LE confined within MOF, flow-free powders (LE@MOF) were collected by vacuum filtration of 0.2MOF@LE.

The ionic conductivity of 0.2MOF@LE and LE were measured by sandwiching electrolyte saturated glass fibers (Whatman, GF/C) between two stainless steel electrodes in coin cell configuration. The glass fiber separators were tailored into disks with identical diameter (D) and varying thickness (L) between 180 to 210 um. The resistances (R) of electrolyte were obtained by EIS (Solartron) and respective conductivity ( $\sigma$ ) is approximated by calculating  $(4L/\pi RD^2)$ . The temperature dependent conductivities were collected by equilibrating coin cells in a convection oven (VWR) at various temperature. The results were linearly fitted into Arrhenius equation  $\sigma = \sigma_0 \exp(-E_a/RT)$  and activation energies ( $E_a$ ) were derived from the sloping of lines (coefficient of determination  $r^2 > 0.99$ ).

Li<sup>+</sup> transference number was evaluated by a potentiostatic polarization method coupled with EIS technique in Li|Li cells. Typically, the cells were subject to a micropotential (V, 20 mV) polarization in period of 30 minutes, yielding the initial current ( $I_0$ ) and steady-state current ( $I_{ss}$ ). To exclude the impact of interfacial evolution, the interfacial resistance before ( $R_{int}^0$ ) and after ( $R_{int}^{ss}$ ) polarization were determined by EIS. The  $t_{Li^+}$  could thereby be calculated by the formula:  $t_{Li^+} = I_{ss}(V - I_0 R_{int}^0) / (I_0(V - I_{ss} R_{int}^{ss}))$ .

CV tests were performed in a two-electrode configuration using coin type cells (CR2032), where lithium disks were utilized as reference/counter electrodes and stainless-steel plates (SS) were used as the working electrodes. Electrolyte saturated PP separators (MTI) were sandwiched between two electrodes were tested between  $-0.2$  and  $5$  V (vs. Li/Li<sup>+</sup>) at  $1$  mV s<sup>-1</sup> (Biologic).

### **Electrochemical device studies.**

Li stripping and plating tests were conducted by Li|Li symmetric cells, where LE and 0.2MOF@LE with equivalent amount of 30 ul were used as electrolytes. The cells were tested under  $0.25$  mA cm<sup>-2</sup> by time interval of 1 h. To evaluate the feasibility of electrolytes with cathodes. LiFePO<sub>4</sub>, LiNi<sub>1/3</sub>Co<sub>1/3</sub>Mn<sub>1/3</sub>O<sub>2</sub> and LiMn<sub>1.5</sub>Ni<sub>0.5</sub>O<sub>2</sub> with different upper voltage cutoffs were utilized as cathode materials. LiFePO<sub>4</sub> and LiNi<sub>1/3</sub>Co<sub>1/3</sub>Mn<sub>1/3</sub>O<sub>2</sub> electrode slurries were prepared by homogeneously mixing cathode materials, carbon black (CB), and polyvinylidene fluoride (PVdF) with a weight ratio of 7:2:1 in N-methyl-2-pyrrolidone (NMP). The slurries were coated on aluminum foil and dried in vacuum oven at  $80$  °C. The loading of active LiFePO<sub>4</sub> is  $\sim 1.8$  mg cm<sup>-2</sup> and LiNi<sub>1/3</sub>Co<sub>1/3</sub>Mn<sub>1/3</sub>O<sub>2</sub> is  $\sim 6.3$  mg cm<sup>-2</sup>. Cathode|Li cells were assembled in glove box (O<sub>2</sub><0.5ppm) using 30 ul electrolytes and PP as separators. The upper cutoffs for LiFePO<sub>4</sub> (1C=170 mA g<sup>-1</sup>) and LiNi<sub>1/3</sub>Co<sub>1/3</sub>Mn<sub>1/3</sub>O<sub>2</sub> (1C=160 mA g<sup>-1</sup>) are set at  $4$  V and  $4.3$  V, respectively. The cycling tests were carried out in ambient environment and the temperature fluctuation is  $\pm 3$  °C.

## 4.5 References

1. Park, M., Zhang, X., Chung, M., Less, G.B. & Sastry, A.M. A review of conduction phenomena in Li-ion batteries. *Journal of Power Sources* **195**, 7904-7929 (2010).
2. Zugmann, S. et al. Measurement of transference numbers for lithium ion electrolytes via four different methods, a comparative study. *Electrochimica Acta* **56**, 3926-3933 (2011).
3. Bai, P., Li, J., Brushett, F.R. & Bazant, M.Z. Transition of lithium growth mechanisms in liquid electrolytes. *Energy & Environmental Science* **9**, 3221-3229 (2016).
4. Tikekar, M.D., Archer, L.A. & Koch, D.L. Stabilizing electrodeposition in elastic solid electrolytes containing immobilized anions. *Science Advances* **2** (2016).
5. Pfaffhuber, C. & Maier, J. Quantitative estimate of the conductivity of a soggy sand electrolyte: example of (LiClO<sub>4</sub>, THF):SiO<sub>2</sub>. *Physical Chemistry Chemical Physics* **15**, 2050-2054 (2013).
6. Ren, Y., Mu, D., Wu, F. & Wu, B. Novel Slurry Electrolyte Containing Lithium Metasilicate for High Electrochemical Performance of a 5 V Cathode. *ACS Applied Materials & Interfaces* **7**, 22898-22906 (2015).
7. Moganty, S.S., Jayaprakash, N., Nugent, J.L., Shen, J. & Archer, L.A. Ionic-Liquid-Tethered Nanoparticles: Hybrid Electrolytes. *Angewandte Chemie International Edition* **49**, 9158-9161 (2010).
8. Lu, Y., Moganty, S.S., Schaefer, J.L. & Archer, L.A. Ionic liquid-nanoparticle hybrid electrolytes. *Journal of Materials Chemistry* **22**, 4066-4072 (2012).
9. Katz, M.J. et al. A facile synthesis of UiO-66, UiO-67 and their derivatives. *Chemical Communications* **49**, 9449-9451 (2013).

10. Ue, M. Mobility and Ionic Association of Lithium and Quaternary Ammonium Salts in Propylene Carbonate and  $\gamma$ -Butyrolactone. *Journal of Electrochemistry Society* **141**, 3336-3342 (1994).
11. Bruce, P.G., Evans, J. & Vincent, C.A. Conductivity and transference number measurements on polymer electrolytes. *Solid State Ionics* **28-30**, 918-922 (1988).
12. Evans, J., Vincent, C.A. & Bruce, P.G. Electrochemical measurement of transference numbers in polymer electrolytes. *Polymer* **28**, 2324-2328 (1987).
13. Laoire, C.O., Plichta, E., Hendrickson, M., Mukerjee, S. & Abraham, K.M. Electrochemical studies of ferrocene in a lithium ion conducting organic carbonate electrolyte. *Electrochimica Acta* **54**, 6560-6564 (2009).
14. Yang, J. et al. Metal-organic frameworks with inherent recognition sites for selective phosphate sensing through their coordination-induced fluorescence enhancement effect. *Journal of Materials Chemistry A* **3**, 7445-7452 (2015).
15. Kandiah, M. et al. Synthesis and Stability of Tagged UiO-66 Zr-MOFs. *Chemistry of Materials* **22**, 6632-6640 (2010).
16. Seo, D.M. et al. Role of Mixed Solvation and Ion Pairing in the Solution Structure of Lithium Ion Battery Electrolytes. *The Journal of Physical Chemistry C* **119**, 14038-14046 (2015).
17. Battisti, D., Nazri, G.A., Klassen, B. & Aroca, R. Vibrational studies of lithium perchlorate in propylene carbonate solutions. *The Journal of Physical Chemistry* **97**, 5826-5830 (1993).
18. Chavan, S. et al. H<sub>2</sub> storage in isostructural UiO-67 and UiO-66 MOFs. *Physical Chemistry Chemical Physics* **14**, 1614-1626 (2012).

19. Valenzano, L. et al. Disclosing the Complex Structure of UiO-66 Metal Organic Framework: A Synergic Combination of Experiment and Theory. *Chemistry of Materials* **23**, 1700-1718 (2011).
20. Cresce, A.V. et al. Solvation behavior of carbonate-based electrolytes in sodium ion batteries. *Physical Chemistry Chemical Physics* **19**, 574-586 (2017).
21. Lewis, D.L., Estes, E.D. & Hodgson, D.J. The infrared spectra of coordinated perchlorates. *Journal of Crystal and Molecular Structure* **5**, 67-74 (1975).
22. Ameloot, R. et al. Ionic Conductivity in the Metal–Organic Framework UiO-66 by Dehydration and Insertion of Lithium tert-Butoxide. *Chemistry – A European Journal* **19**, 5533-5536 (2013).
23. Lu, Y., Das, S.K., Moganty, S.S. & Archer, L.A. Ionic Liquid-Nanoparticle Hybrid Electrolytes and their Application in Secondary Lithium-Metal Batteries. *Advanced Materials* **24**, 4430-4435 (2012).
24. Tu, Z. et al. Designing Artificial Solid-Electrolyte Interphases for Single-Ion and High-Efficiency Transport in Batteries. *Joule* **1**, 394-406 (2017).
25. Lu, Y. et al. Stable Cycling of Lithium Metal Batteries Using High Transference Number Electrolytes. *Advanced Energy Materials* **5**, 1402073-n/a (2015).
26. Jiang, F. & Peng, P. Elucidating the Performance Limitations of Lithium-ion Batteries due to Species and Charge Transport through Five Characteristic Parameters. *Scientific Reports* **6**, 32639 (2016).
27. Verma, P., Maire, P. & Novák, P. A review of the features and analyses of the solid electrolyte interphase in Li-ion batteries. *Electrochimica Acta* **55**, 6332-6341 (2010).



28. Wang, D. et al. Improved high voltage electrochemical performance of  $\text{Li}_2\text{ZrO}_3$ -coated  $\text{LiNi}_{0.5}\text{Co}_{0.2}\text{Mn}_{0.3}\text{O}_2$  cathode material. *Journal of Alloys and Compounds* **647**, 612-619 (2015).
29. Atanasoska, L., Naoi, K. & Smyrl, W.H. XPS studies on conducting polymers: polypyrrole films doped with perchlorate and polymeric anions. *Chemistry of Materials* **4**, 988-994 (1992).
30. Nazri, G. & Muller, R.H. Composition of Surface Layers on Li Electrodes in PC,  $\text{LiClO}_4$  of Very Low Water Content. *Journal of Electrochemistry Society* **132**, 2050-2054 (1985).

**Chapter 5 Nanofluidic Electrolyte with Versatile Electrolyte Modulator for  
High-Performance Lithium Batteries**

## 5.1 Introduction

The developments of high-power lithium-ion batteries (LIBs) are acute needs for widespread adoptions of electric vehicles and booming market of portable electronics. Whereas high-rate operation of LIBs generally induces severe polarization and side reactions, resulting in rapid deterioration of the cycling life and thermal runaway. Developing low-cost yet effective techniques that enable LIBs with fast-charging capability and high-rate performance, in this context, represents a key direction of research and development.

LIBs are operated based on separation of electrons and ions in the electrodes, and their subsequent respective translocation through the external circuits and the electrolytes. To improve the electric conductivity, various conductive components were incorporated within the electrodes. To improve the ionic conduction, current strategies are focused on shortening the ionic diffusion length of active materials, as well as developing electrolytes with higher ionic conductivity. In liquid electrolytes, the mobility of lithium ions ( $\text{Li}^+$ ) is generally inferior than that of anions. The ratio of conductivity carried out by  $\text{Li}^+$  vs. by  $\text{Li}^+$  and the counter anions is generally defined as lithium-ion transference number,  $t_{\text{Li}^+}$ . The current commercial electrolytes may provide an overall ionic conductivity at an order of  $\sim 10^{-3} \text{ mS cm}^{-1}$  but with a low  $t_{\text{Li}^+}$  that is typically less than 0.3.<sup>1</sup> Since the anions do not participate the normal electrode reactions, unavoidably resulting in concentration polarization of the anions in the vicinity of electrolyte-electrode interphase, particularly, during a fast charging or discharging process.<sup>2</sup> The resulted polarization inevitably reduces the power output and energy efficiency; furthermore, it may further cause side reactions and Joule heating, leading to shortened cycling life.<sup>3,4</sup>

Much efforts have been devoted to improving  $t_{\text{Li}^+}$  of liquid electrolytes, focusing on reducing the mobility of anions in electrolytes. For example, silica particles were added to liquid

electrolyte, where preferential adsorption of the anions on the particles increases  $t_{\text{Li}^+}$  from 0.13 to 0.41 for 0.1 M LiClO<sub>4</sub> in THF upon addition of 0.15 vol % silica.<sup>5</sup> Similarly, covalently attaching the anions of an ionic liquid to inorganic particles also increases the  $t_{\text{Li}^+}$  of the ionic-liquid electrolyte (e.g., from 0.05 to 0.35 upon addition of 16 wt % ZrO<sub>2</sub>).<sup>6,7</sup> As an alternate approach, high  $t_{\text{Li}^+}$  exceeding 0.5 could be achieved in superconcentrated electrolytes of lithium bis(trifluoromethanesulfonyl)imide (LiTFSI) in acetonitrile and ether-based solvents, where mobility of the anions is retarded by the charge couplings between the anions and the cations.<sup>8,9</sup> However, this effect does not be applied for other electrolytes, for instance, LiPF<sub>6</sub><sup>-</sup>-based electrolyte systems.<sup>10</sup> In these previous arts, manipulating anion mobility improves  $t_{\text{Li}^+}$  to a certain extent, yet general approaches towards more efficient transport of Li<sup>+</sup> ( $t_{\text{Li}^+} > 0.5$ ) in liquid electrolyte and respective electrochemical behaviors have been scarcely explored.

Herein, we report novel electrolyte additive based on anion-adsorbent metal organic framework (MOF) as an anion sponge for modulating the transport behavior of commercial LE (LP40, 1M LiPF<sub>6</sub> in EC/DEC). The MOF is a class of hybrid organic–inorganic crystalline porous materials with a variety of architectures and tunable properties.<sup>11</sup> As exemplified by MIL-100(Al) in **Figure 5-1a**, MIL-100(Al) (Al<sub>3</sub>O(BTC)<sub>2</sub>OH·(H<sub>2</sub>O)<sub>2</sub>) is a cubic-zeotype mesoporous material which is built up from Al<sup>3+</sup> inorganic trimers sharing a common  $\mu_3$ -O and benzene-1,3,5-tricarboxylate (BTC) anions.<sup>12</sup> Their linkage theoretically generates two types of mesoporous cages (25 and 29 Å) that are accessible through microporous windows (6 and 9 Å). In this compound, the aluminum atom is octahedrally coordinated with four carboxyl oxygen atoms from BTC, one  $\mu_3$ -O atom and one terminal water or hydroxide group. As illustrated in **Figure 5-1b**, the terminal species could be eliminated upon heating (thermal activation) and resulting Al<sup>3+</sup> open metal sites (OMS) are coordinatively unsaturated sites with strong Lewis acidity.<sup>13,14</sup> In addition

of LE (**Figure 5-1b**), the counter ions ( $\text{PF}_6^-$  anions) spontaneously interact with those unsaturated OMS in nanocages. The resulting nanofluidic electrolyte (colloid-like) exhibits enhanced  $\text{Li}^+$  transference number without sacrificing  $\text{Li}^+$  conductivity. As a consequence, the fabricated prototype lithium-based batteries show substantial improvements in terms of cycle life and power capability. Moreover, the MOF modulate the electrochemical window by exhibiting higher stability against metallic Li and oxidative cathode (4.8V vs.  $\text{Li}/\text{Li}^+$ ), which is of particular significance for boosting overall energy density of Li metal batteries.

## 5.2 Results and Discussions

### 5.2.1 MOF Structure and Electrolyte Properties of Nanofluidic Electrolyte

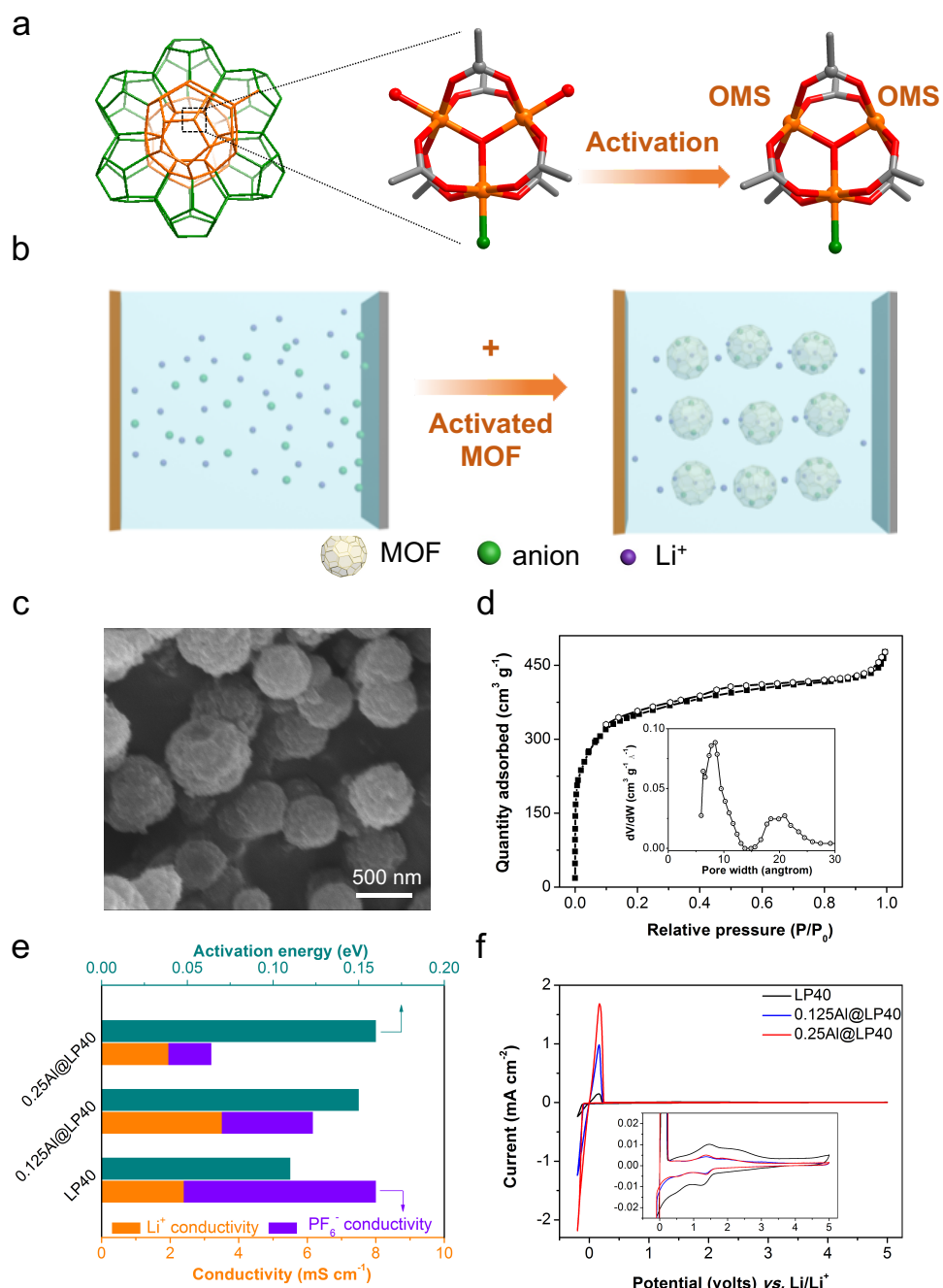


**Figure 5-1** (a) Structure representation of two types of mesoporous cages in MIL-100(Al) and Illustration of OMS evolution in a metal trimer unit of MIL-100(Al) serial MOFs (orange atoms

Al, red atoms O, grey atoms C, green atoms anionic ligands). (b) Schematic showing ion distribution in bare liquid electrolyte and in liquid electrolyte with MOF. (c) SEM image of as-synthesized MOF. (d) N<sub>2</sub> adsorption/desorption isotherms (inset: pore size distribution diagram). (e) Basic electrolyte properties (conductivity and activation energy) of baseline electrolyte and nanofluidic electrolyte. (f) Two-electrode CV tests comparing the Li<sup>+</sup> stripping/plating kinetics

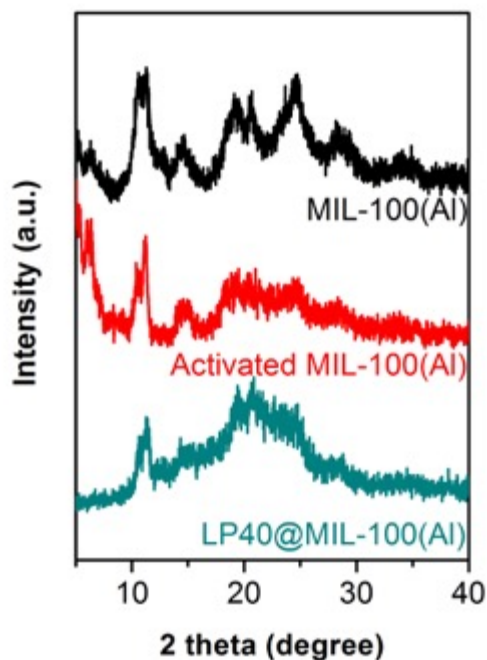


**Figure 5-2** XRD pattern of as-synthesized, activated and LP40 complexed MIL-100(Al)

**Figure 5-1c** depicts a representative scanning electron microscope (SEM) image of the as-synthesized MIL-100(Al), which shows uniformly distributed nanoparticles with diameter of a few hundreds of nanometers. **Figure 5-1d** shows the N<sub>2</sub> adsorption/desorption isotherms of MIL-100(Al), which indicates characteristic microporous solids with a Brunauer–Emmett–Teller (BET) surface area of 1190 cm<sup>3</sup> g<sup>-1</sup> and pore size peaking at 9 Å and 20 Å (DFT model) in line with the

reported pore window and mesoporous cage of MOF.<sup>15</sup> Powder x-ray diffraction (XRD) were performed to examine the crystalline structure of MIL-100(Al). Except for minor intensity change, major peaks of MIL-100(Al) are retained and consistent with literature reported after activation and complexation with LP40 (**Figure 5-2**).<sup>16</sup>

Several fundamental properties of electrolyte including ionic conductivity, transference number and activation energy were studied by two combination ratios between LE and MOF: 0.125 mg ul<sup>-1</sup> and 0.25 mg ul<sup>-1</sup> signify that every 1 ul LP40 0.125 mg (0.125Al@LP40) and 0.25 mg (0.25Al@LP40) activated MIL-100(Al) were added, respectively. And they are denoted as nanofluidic electrolyte (NE) for convenience. The ambient ionic conductivity was measured using an electrolyte cell by two identical platinum electrodes with fixed cell parameters. As summarized in **Figure 5-1e**, 0.125Al@LP40 and 0.25Al@LP40 maintain 77% and 40% conductivity of LP40, respectively. The thermal activation energy was obtained from the temperature dependent conductivity (see Arrhenius plots in **Figure 5-3**), 0.125Al@LP40 and 0.25Al@LP40 show comparable activation energy of ~0.15 eV relative to 0.11 eV for LP40. Li<sup>+</sup> transference number measurements were carried out by classic Bruce-Vincent method (**Figure 5-4** and **Figure 5-5**). 0.125Al@LP40 and 0.25Al@LP40 afford one-fold higher transference number of ~0.6 than 0.3 for LP40. Compared with LP40, 0.125Al@LP40 shows 45% higher Li<sup>+</sup> conductivity and 54% lower PF<sub>6</sub><sup>-</sup> conductivity, 0.25Al@LP40 exhibit similar Li<sup>+</sup> conductivity while 78% lower PF<sub>6</sub><sup>-</sup> conductivity. Therefore, we reveal that MOF with OMS could modulate the ion transport behavior by immobilizing PF<sub>6</sub><sup>-</sup> anions as well as promoting the transport of Li<sup>+</sup> cations.



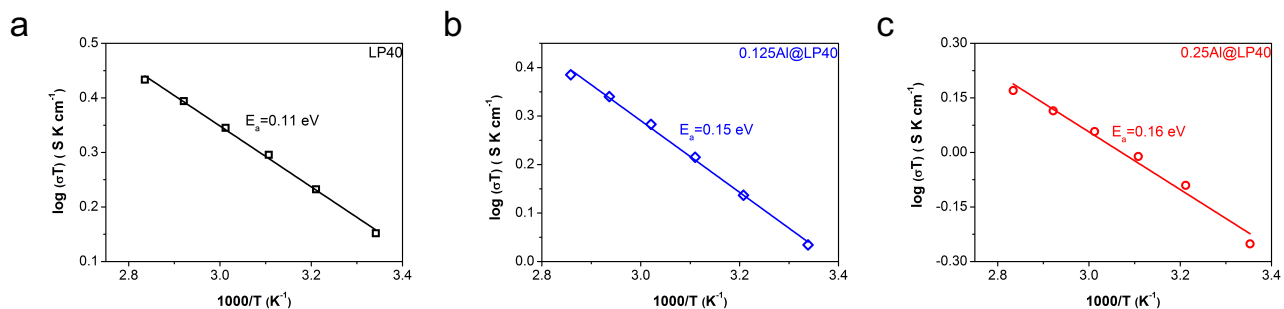


**Figure 5-3** Arrhenius plots (temperature dependent conductivity) of LP40 and nanofluidic electrolyte

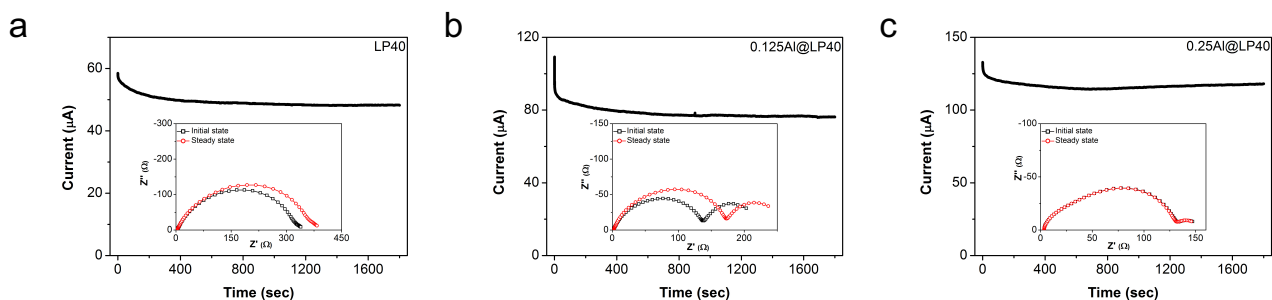


**Figure 5-4** Potentiostatic polarizations of LP40 and nanofluidic electrolyte in symmetric Li-Li cell configuration (insets: EIS measurements before and after polarizations)

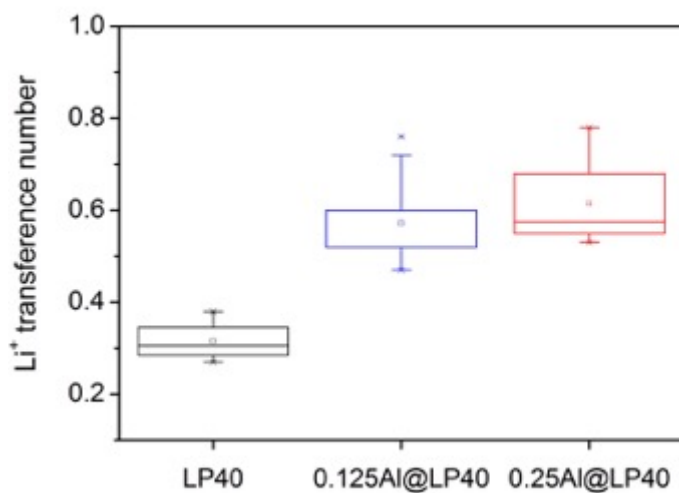


**Figure 5-5**  $\text{Li}^+$  transference number of LP40 and nanofluidic electrolyte

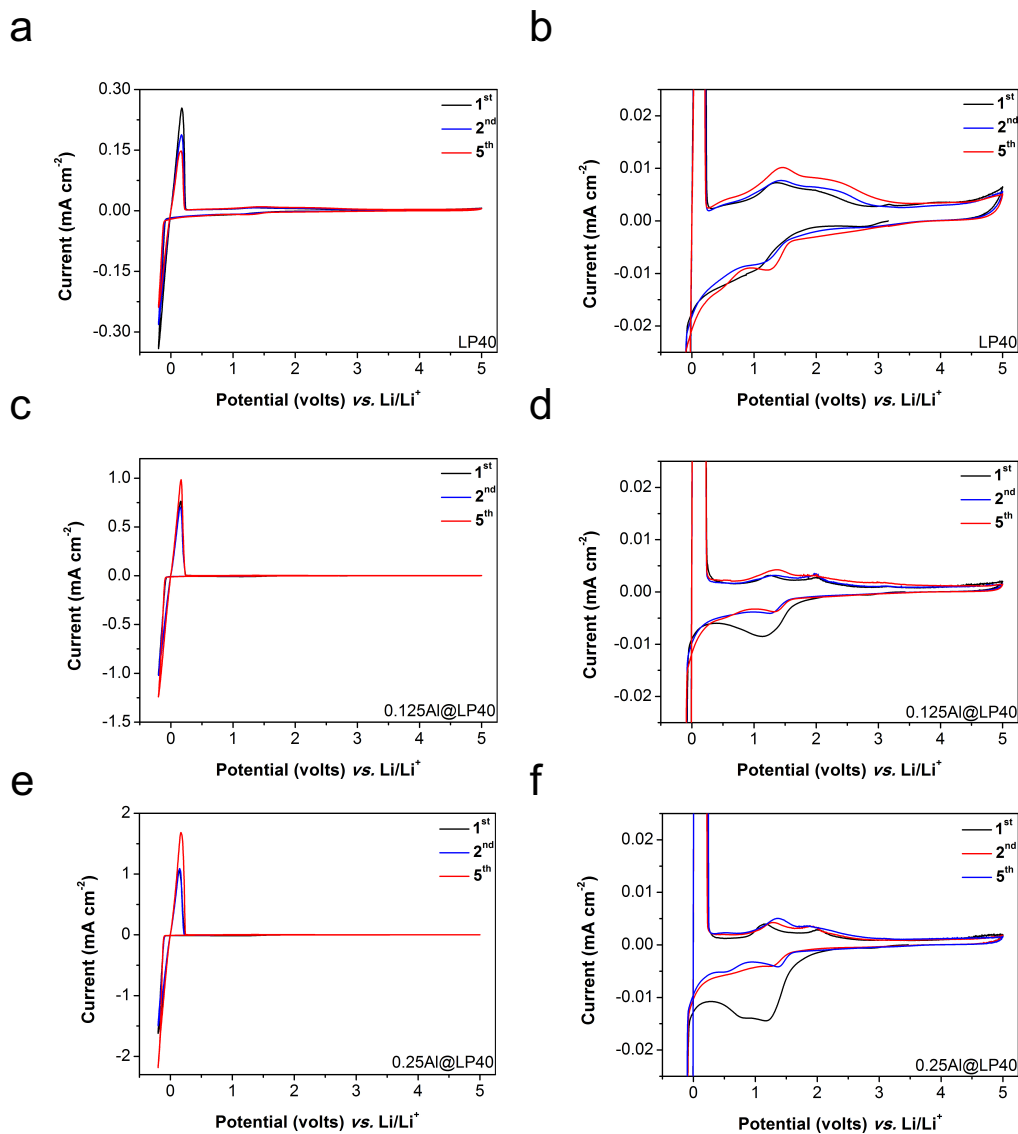


**Figure 5-6** Two-electrode CV evolutions of first 5 cycles for (a, b) LP40, (c, d) 0.125Al@LP40, (e, f) 0.25Al@LP40.

As depicted in **Figure 5-1f** electrochemical stability window was evaluated by cyclic voltammetry (CV) in coin cell configuration at a potential ranging from  $-0.2$  to  $5$  V vs.  $\text{Li/Li}^+$ , where Li were used as counter/reference electrode and stainless steel is working electrode. The notable redox peaks from  $-0.2$  to  $0.3$  V are ascribed to the  $\text{Li/Li}^+$  stripping and plating peaks ( $\text{Li} \leftrightarrow$

$\text{Li}^+ + e^-$ ). As shown in **Figure 5-6**, the higher peak current density of NE compared with LP40 suggest faster redox kinetics in vicinity of electrolyte-electrode interface, and this result is further confirmed by three-electrode cells (**Figure 5-7**). Moreover, the peaks associated with electrolyte decomposition ( $< 1.5 \text{ V}$  and  $> 4.3\text{V}$ ) are less pronounced for NE compared with LP40, suggesting improved electrochemical stability upon addition of MOF.

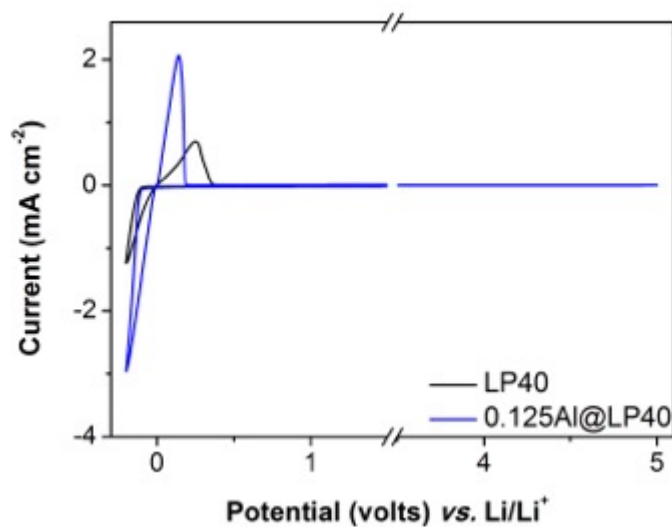


**Figure 5-7** Three-electrode CV comparison between LP40 and 0.125Al@LP40

## 5.2.2 Ion Dynamic Behavior Confined within MOF

To shed light on the anion transport behavior within MOF, excessive LP40 were filtered out to yield LP40@MOF (LP40 confined within MOF), which composition formula was estimated by coupled plasma atomic emission spectroscopy (ICP-AES) and thermogravimetric analysis (TGA). The ICP-AES gives Al/Li ratio of 1.3, which is slightly below the theoretical value of 2 due to excessive LE presence within MOF. TGA results indicate that solvent contents decrease from 81.4% to ~30% for 0.125Al@LP40 and LP40@MOF, respectively. As shown in **Figure 5-8** and **Table 5-1**, for each LiPF<sub>6</sub>, 15 equivalent molar EC/DEC solvent molecules are present in the 0.125Al@LP40, while for LP40@MOF the ratio between solvents and LiPF<sub>6</sub> decreases to ~4, implying highly concentrated mobile ions within MOF.

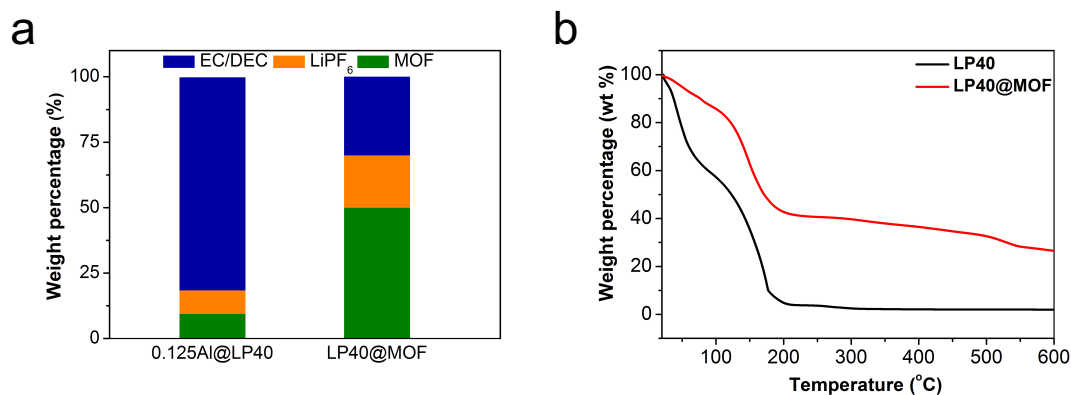


**Figure 5-8** (a) Weight percentages of MOF, LiPF<sub>6</sub> and solvents (EC/DEC) for nanofluidic electrolyte (0.125Al@LP40) and LP40@MOF. (b) TGA curves of LP40 and LP40@MOF.

Table 5-1 Summary of weight contribution and estimated formula for nanofluidic electrolyte (0.125Al@LP40) and LP40@MOF.

|              | Wt% (MOF) | Wt% (LiPF <sub>6</sub> ) | Wt% (EC/DEC) | Formula (molar ratio)                    |
|--------------|-----------|--------------------------|--------------|--|
| 0.125Al@LP40 | 9.4       | 9                        | 81.6         | (0.003)MOF•LiPF <sub>6</sub> •15(EC/DEC) |
| LP40@MOF     | ~50       | ~20                      | ~30          | (0.4)MOF•LiPF <sub>6</sub> •4(EC/DEC)    |

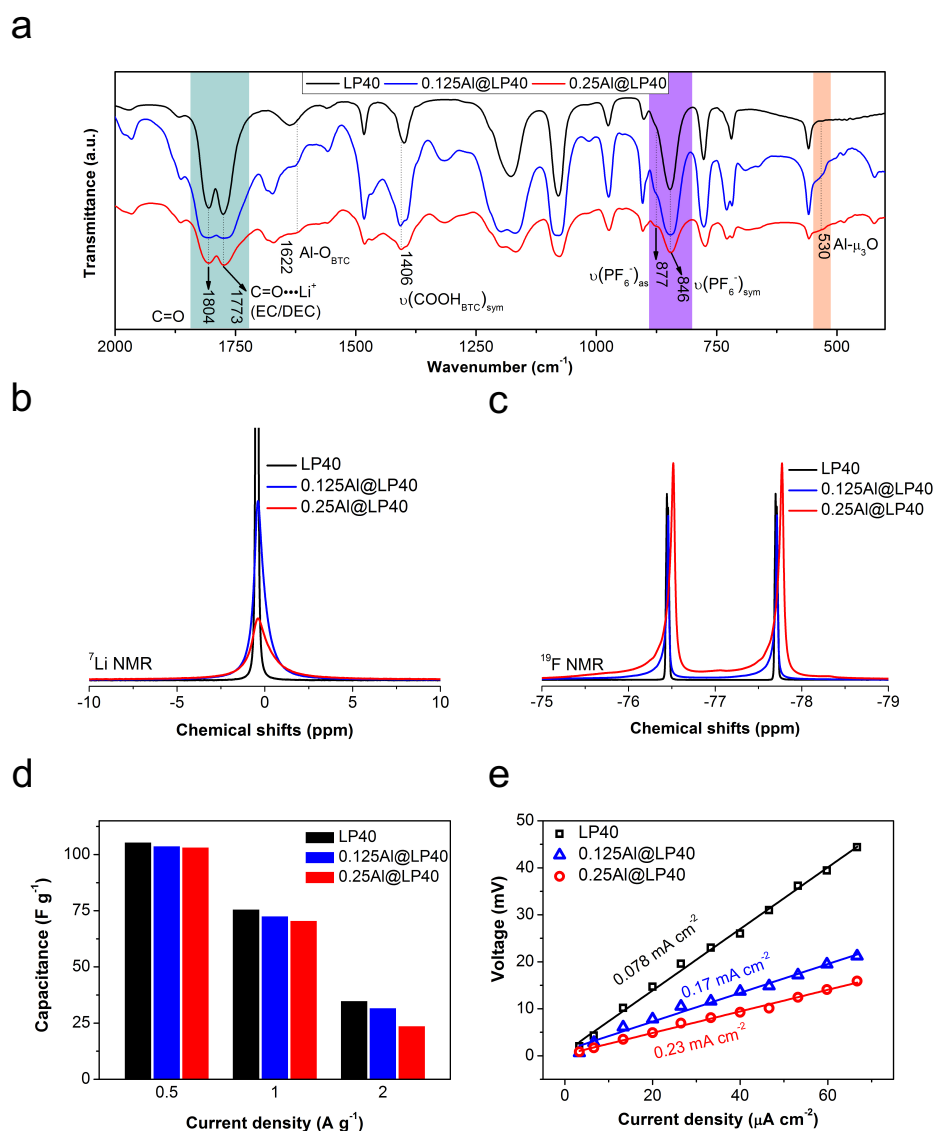


**Figure 5-9** LP40 and NE comparison in (a) FT-IR. (b) Static <sup>7</sup>Li and (c) <sup>19</sup>F NMR spectra. (d) Evaluation of diffusion polarization by rate performance of double layer capacitors. (e) Evaluation

of reaction kinetics by exchange current density derived from stepped D.C. micropolarization (Li-Li symmetric cells).

The interaction between liquid electrolyte and MOF was studied by Infrared spectroscopy, as shown in **Figure 5-9a**, the peaks for NE locating at 1406 and 1622  $\text{cm}^{-1}$  are characteristic vibrations from MOF backbones, which could be ascribed to symmetric vibration of  $-\text{COOH}$  from benzene-1,3,5-carboxylic acid (BTC) and coordination bonds between deprotonated  $-\text{COOH}$  and  $\text{Al}^{3+}$  ( $\text{Al-O}_{\text{BTC}}$ ), respectively.<sup>17</sup> The broad shoulder peaks at 530  $\text{cm}^{-1}$  are signals from  $\text{Al}-\mu_3\text{O}$  metal trimers, which deviates from 545  $\text{cm}^{-1}$  for MIL-100(Al) (see **Figure 5-10**) due to coordinated guest molecules.<sup>18</sup> Meanwhile, the peaks at 846 and 877  $\text{cm}^{-1}$  are attributed to the symmetric and asymmetric vibrations of  $\text{PF}_6^-$  anion.<sup>19</sup> Compared with neat LP40, the emergence of the new asymmetric vibration for NE serves as evidence that symmetry of  $\text{PF}_6^-$  degrades upon encapsulation of LP40 in MOF. This phenomenon is coincident with the change of  $\text{Al}-\mu_3\text{O}$ , demonstrating the interaction of anions on open  $\text{Al}^{3+}$  sites. Moreover, the carbonyl groups from solvents (EC/DEC) exhibit two characteristic peaks at 1773 and 1804  $\text{cm}^{-1}$ . The latter one is generally an indication of uncoordinated carbonyl (free) and the former one signifies those carbonyl groups interacting with the  $\text{Li}^+$ .<sup>19,20</sup> Therefore, the relative intensity of peak at 1773 over 1804  $\text{cm}^{-1}$  (denoted as  $I_0$ ) roughly reflects the coordination status of  $\text{Li}^+$ . The disparity regarding  $I_0$  between LP40 and NE suggest distinct solvation state of  $\text{Li}^+$ . Judged by 4 solvents per  $\text{Li}^+$  within MOF, we speculate that the  $\text{Li}^+$  solvation sheath within MOF has more compact structure due to less solvation number.

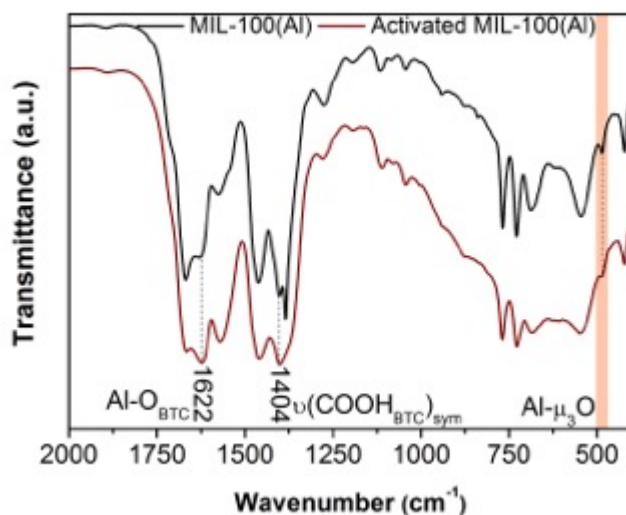


**Figure 5-10** FT-IR spectra of pristine and activated MIL-100(Al)

To understand the local chemical environment and dynamic behavior of mobile species, both static and field-pulsed NMR were performed. As shown in **Figure 5-9b** and **5-9c**,  $^7\text{Li}$  and  $^{19}\text{F}$  spectra for LE display sharpened line width which arise from the isotropic diffusion of  $\text{Li}^+$  and  $\text{PF}_6^-$ . Upon increasing the loading of MOF in NE, the chemical shift occurs for  $^{19}\text{F}$  spectra while  $^7\text{Li}$  spectra merely exhibits broadened peak feature, signifying anions' interaction towards MOF scaffolds. The diffusion ordered spectroscopy (DOSY) was performed to compare the relative ion diffusivities. The results as summarized in **table 5-2** indicate that  $\text{PF}_6^-$  diffusion coefficient of NE decrease much significantly than  $\text{Li}^+$  relative to LE, further testifying the interaction of  $\text{PF}_6^-$  with MOF besides nanoconfinement effect.

To study the dynamic behavior of NE, we assembled the double layer capacitors (DLC) using symmetric activated carbon electrodes for evaluating concentration polarization where no Faradic reactions are involved. We speculate that the reduced anion mobility in NE due to presence of MOF modulators could encumber the formation of double layer (Helmholz layer), therefore

decreasing the capacitance especially at high current density. As expected, the rate performance of DLC decreases as increasing the loading of MOF in NE (**Figure 5-9d** and **Figure 5-11**), this result is in good agreement to the decreased anion conductivity as shown in **Figure 5-1e**. Li-Li symmetric cells using LP40 and NE were fabricated to investigate the effect of MOF modulator on electrochemical reaction kinetics. By performing stepped D.C. (direct current) micropolarization to minimize the diffusion polarization, the relationship between voltage (V) and current (I) were plotted in **Figure 5-12**, where the cell using LP40 exhibit much higher and unstable overpotential compared with the cells using NE at same current density. The aforementioned V-I relationships were linearly fitted in **Figure 5-9e**, the exchange current density  $i_0$  could be derived by Tafel equation (see Experimental Section for details).<sup>21</sup> Compared with LP40, the  $i_0$  is doubled and tripled for 0.125Al@LP40 and 0.25Al@LP40, respectively.

**Table 5-2** Diffusion coefficients of electrolyte components from NMR DOSY

| Samples      | Diffusion coefficient ( $\text{e}^{-10} \text{ m}^2 \text{ s}^{-1}$ ) |               |      | $t_{\text{Li}^+} = (D_{\text{Li}^+} / (D_{\text{Li}^+} + D_{\text{PF}_6^-}))$ |
|--------------|---|---------------|------|---|
|              | $\text{PF}_6^-$   | $\text{Li}^+$ | DEC  |   |
| LP40         | 3.88  | 1.41          | 3.06 | 0.27  |
| 0.125Al@LP40 | 2.57  | 1.26          | 2.90 | 0.33  |
| 0.25Al@LP40  | 1.98  | 1.26          | 2.95 | 0.39  |



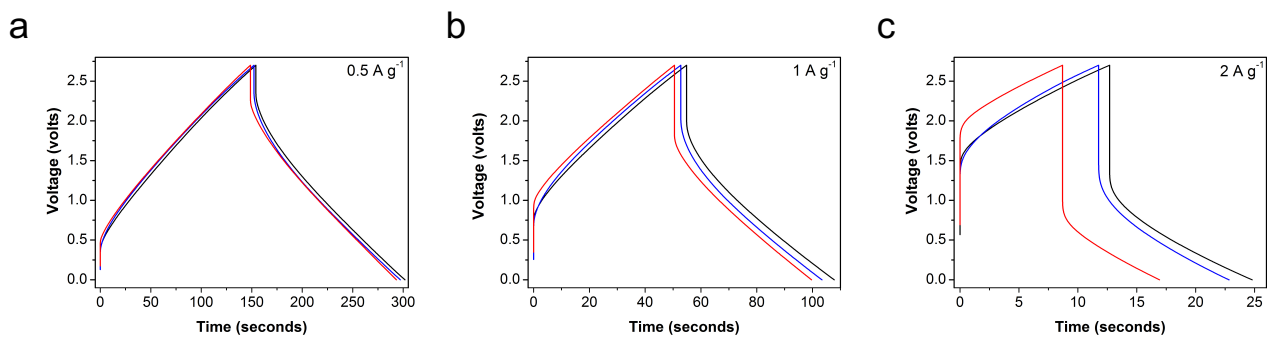


**Figure 5-11** Voltage-time curves of double layer capacitors using LP40 and nanofluidic electrolyte at different rates.

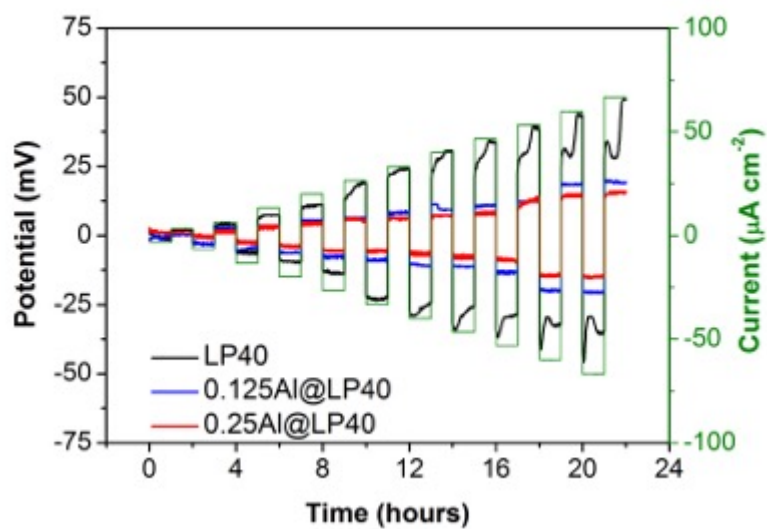


**Figure 5-12** Stepped D.C. micropolarization of Li-Li symmetric cells using LP40 and nanofluidic electrolyte.

## 5.2.3 Electrochemical Performance of the Electrolytes

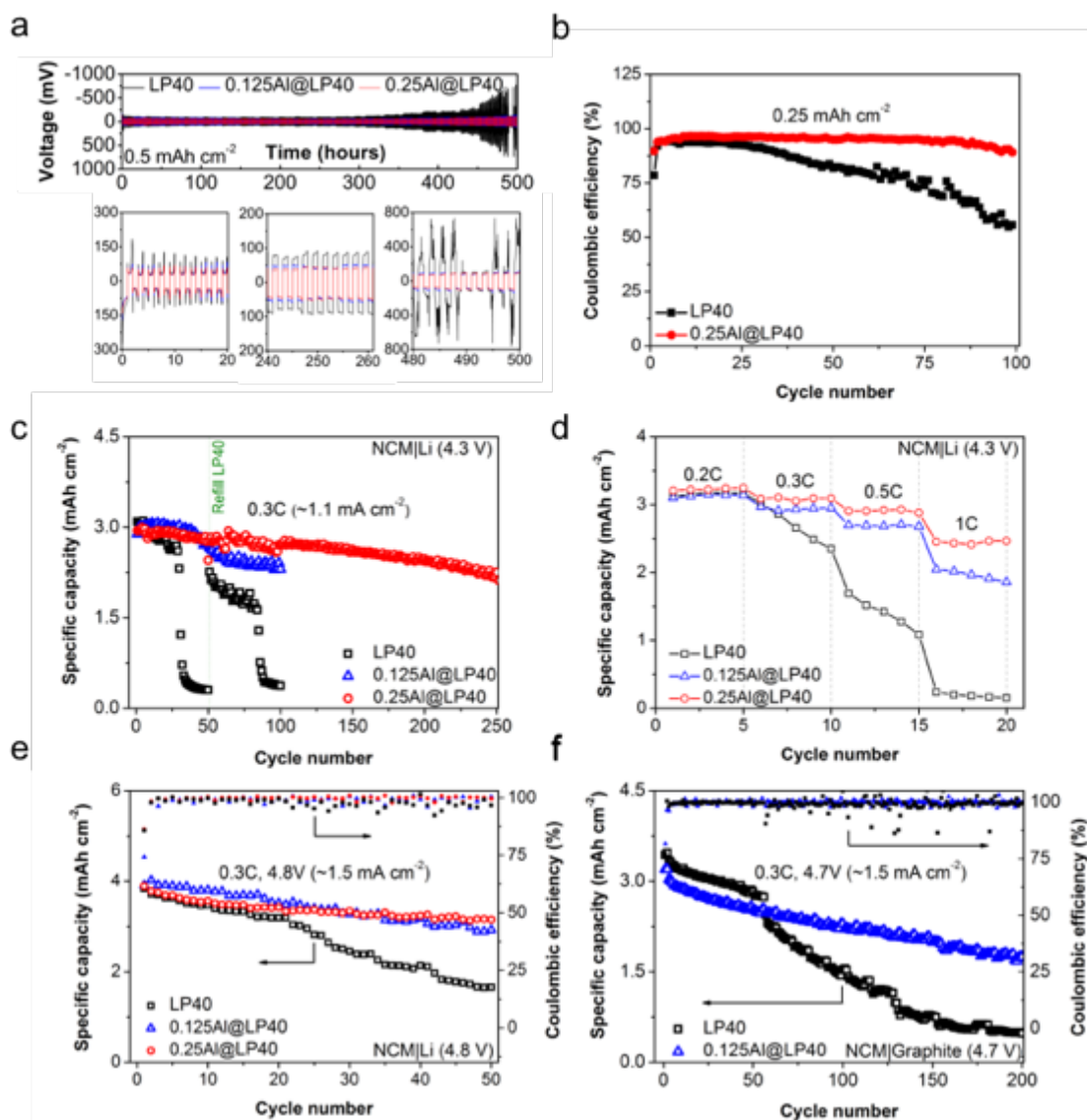


**Figure 5-13** LP40 and NE device performances in (a) Li|Li symmetric cells at 0.5 mAh cm<sup>-2</sup>. (b) Li|Cu asymmetric cells at 0.25 mAh cm<sup>-2</sup>. (c) NCM|Li cells at 0.3C (1C=160 mA g<sup>-1</sup>) with upper voltage of 4.3V. (d) Rate performance of NCM|Li cells (4.3 V). (e) NCM|Li cells at 0.3C (1C=250 mA g<sup>-1</sup>) with upper voltage of 4.8V. (f) NCM|graphite full cells at 0.3C with upper voltage of 4.7 V.

As shown in **Figure 5-13a**, the long-term interfacial stability between electrolyte and Li metal was studied by Li strip-plate tests at  $0.5 \text{ mA cm}^{-2}$  (2 h for each cycle segment). At initial stage, the potential for cells using LP40 and NE are 26 and 35 mV, respectively. Due to buildup of resistive interface, they gradually stabilized at 40 and 80 mV, respectively. After 400 hours' operation, the cell using LP40 started suffering from escalating overpotential and the zigzag curve is a typical sign of proliferating Li dendrites. Remarkably, the cells using NE still could afford flat plateau at  $\sim 80 \text{ mV}$ , suggesting their much more stable electrolyte-Li interfaces. Thus, the electrolyte with MOF modulators alleviate the interfacial resistance and restrain the growth of dendritic Li. As shown in **Figure 5-13b**, Asymmetric Li-Cu cells were fabricated to evaluate the Li strip-plate efficiency, the cell using NE (0.25Al@LP40) maintains 88% Coulombic efficiency at 100<sup>th</sup> cycle in contrast with only 55% for bare LP40. The higher average Coulombic efficiency of Li-Cu cell using NE further testify its stable and less resistive interface.

To study the compatibility of NE with high energy cathode, we assembled prototype NCM|Li cells with NCM loading of  $\sim 20 \text{ mg cm}^{-2}$ . For galvanostatic cycling at 0.3C ( $1.1 \text{ mA cm}^{-2}$ ) and normal voltage cutoff at 4.3V (**Figure 5-13c**), NCM|Li cells using NE show minor capacity decay. In contrast, the cell using LP40 only retains 85% of its original capacity at 27<sup>th</sup> cycle and starts drastic deterioration to  $\sim 0 \text{ mAh g}^{-1}$  at 50<sup>th</sup> cycle. This disparity could be majorly ascribed to the distinct Li cycling stability. We speculate that in free  $\text{PF}_6^-$  and relative low mobility of  $\text{Li}^+$  in LP40 would induce large polarization and severe electrolyte breakdown, therefore aggressive formation of solid electrolyte interface (SEI) and detachment of non-electroactive Li initiated, as illustrated in schematic **Figure 5-13d**.<sup>22</sup> Instead, NE with high  $\text{Li}^+$  transference number offer higher  $\text{Li}^+$  mobility, lower polarization and thereby less resistive SEI. The rate performances were evaluated for both 4.3V (**Figure 5-13f** and **Figure 5-14(a-b)**) and 4.8V (**Figure 5-14(c-d)**), the cell

with 0.25Al@LP40 exhibit the best rate performance. At 1C rate the cells using 0.25Al@LP40 deliver 650% and 250% higher capacity than the cells using LP40 at 4.3V and 4.8V, respectively. As shown in **Figure 5-13e**, the advantage of MOF is further testified under high voltage (4.8V), NCM|Li cell with 0.25Al@LP40 exhibit 550% energy density improvement compared with the cell with LP40 (Fig. SX), which implies the effectiveness of NE under high voltage operation. Galvanostatic cycling of NCM|graphite full cells at 0.3C (4.7) show that the cell with 0.125Al@LP40 maintain 1.7 mAh cm<sup>-2</sup> at 200<sup>th</sup> cycle relative to ~ 0 mAh cm<sup>-2</sup> for cell using LP40, confirming the compatibility of NE with high voltage cathode in high energy density full cells.

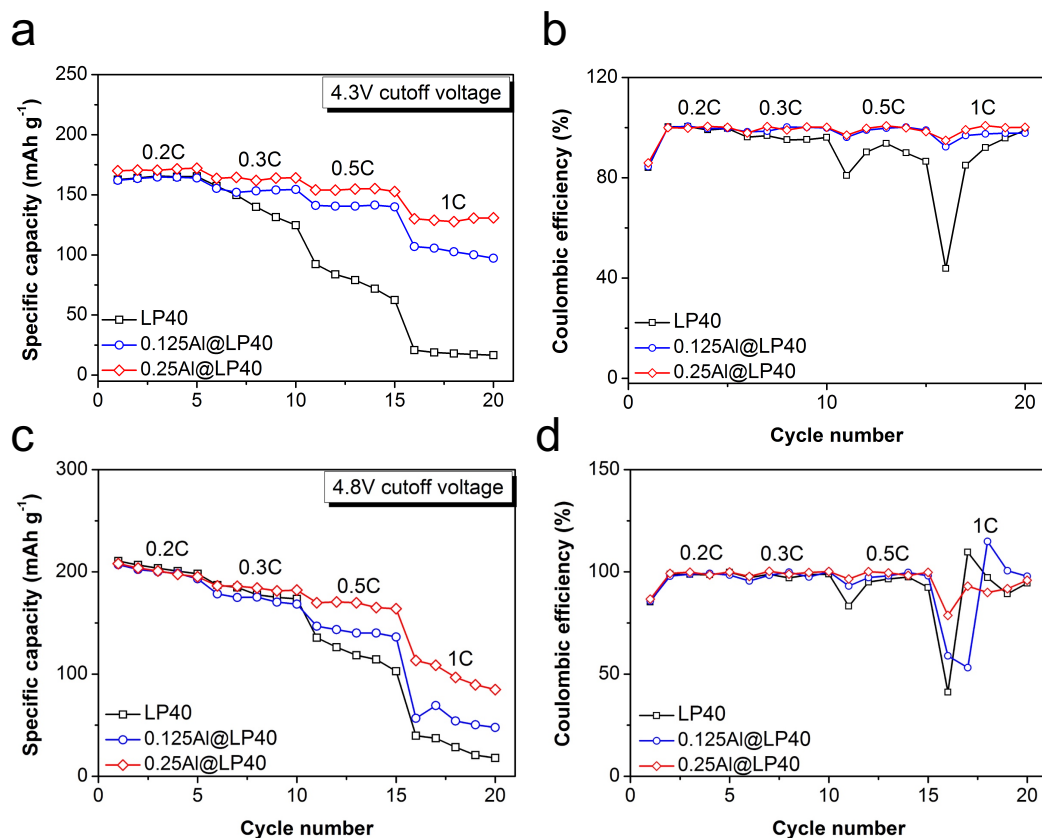


**Figure 5-14** Rate performances of NCM-Li cells using LP40 and nanofluidic electrolyte at upper voltage of (a, b) 4.3V and (c, d) 4.8V

As judged by the NCM|Li cell using LP40, we speculate that the poor cycle performances originate from the accumulative buildup of resistive SEI accompanied by rapid consumption of liquid electrolyte particularly at high current density and areal capacity.<sup>23</sup> In other words, the capacity fading rate is mainly a function of SEI resistivity and available liquid electrolyte. To distinguish the SEI properties in LP40 and NE, we regenerated the cells after 50 cycles by replenishing liquid electrolyte yet kept cycled Li. Thereafter the discrepancy on cycle performance is only dependent on SEI properties. The cycling performances are shown in **Figure 5-13c** and the fading rates (% fading per cycle) at different segments are summarized at **table 5-3**, where LP40 shows much higher capacity fading than NE at early stage, implying much resistive SEI accumulated on Li moieties. Afterwards accelerating decay took place due to deteriorated reaction and diffusion kinetics. After refilling electrolyte, LP40 recovered partial capacity benefiting from alleviated diffusion polarization and cell repacking, while it continued aggressive fading after a few cycles. This is consistent with our hypothesis that progressive growth of resistive SEI would resume once sufficient electrolyte was provided. In sharp contrast, the NE (0.125Al@LP40) reversed the fading trend from the minor capacity dimple, which demonstrates that the cell with NE could sustain prolonged cycling once ion transport is guaranteed. The cell with 0.25Al@LP40 exhibits superior cycling performance with capacity fading rate of 0.1% per cycle throughout 250 cycles.

**Table 5-3** Evolution of capacity fading rate for NCM-Li cells using LP40 and nanofluidic electrolyte, liquid electrolyte was replenished for all cells after 50 cycles at 0.3C.

| <b>Electrolyte</b>  | <b>Evolution of capacity fading rate</b> |   |   |  |  |
|---------------------|--|---|---|--|--|
| <b>LP40</b>         | segment<br>fading                        | 1 <sup>st</sup> →29 <sup>th</sup><br>0.6% | 30 <sup>th</sup> →50 <sup>th</sup><br>4.1%  | 51 <sup>st</sup> →83 <sup>rd</sup><br>1.4%   | 84 <sup>th</sup> →100 <sup>th</sup><br>4.0%  |
| <b>0.125Al@LP40</b> | segment<br>fading                        | 1 <sup>st</sup> →40 <sup>th</sup><br>~0%  | 41 <sup>st</sup> →50 <sup>th</sup><br>0.9%  | 51 <sup>st</sup> →60 <sup>th</sup><br>0.8%   | 61 <sup>st</sup> →100 <sup>th</sup><br>0.2%  |
| <b>0.25Al@LP40</b>  | segment<br>fading                        | 1 <sup>st</sup> →50 <sup>th</sup><br>0.1% | 51 <sup>st</sup> →100 <sup>th</sup><br>0.1% | 101 <sup>st</sup> →200 <sup>th</sup><br>0.3% | 201 <sup>st</sup> →250 <sup>th</sup><br>0.3% |

## 5.2.4 Mechanism Insights on Interface between Nanofluidic Electrolyte and Electrodes

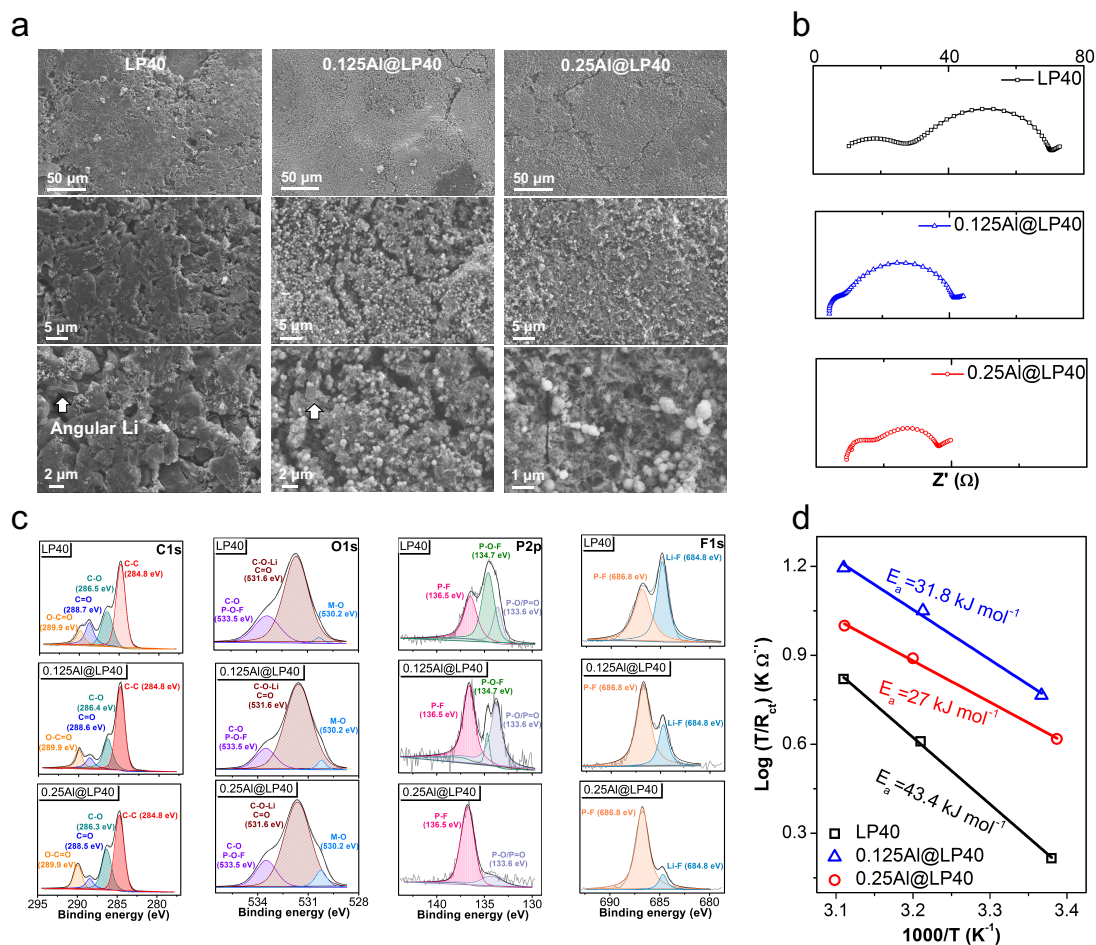


**Figure 5-15** Post-cycle evaluations of Li-Li cells using LP40 and NE after 300 hours' operation at 0.5 mAh cm<sup>-2</sup>: (a) SEM images, (b) Electrochemical impedance spectroscopy of cycled cells, and (c) XPS analysis of cycled Li. (d) Activation energy of charge transfer resistance derived from NCM-Li cells employing LE and NE

To probe the origin of superiority for cells using NE, the morphology of cycled Li from Li|Li cells (150 cycles at 0.5 mAh cm<sup>-2</sup>) were examined by SEM in **Figure 5-15a**. The Li using

neat LP40 shows angular and porous morphology (left column in **Figure 5-15a**, which is associated with the infinite volume change of Li and sluggish kinetics of electrochemical deposition. For comparison, the cells using NE (0.125Al@LP40, middle column) display uniform coverages of spheroidal MOF on surface of cycled Li (determined by low contrast under electron beam). With increased amount of MOF in NE (0.25Al@LP40 in right column), diminishment of angular shaped Li was observed, which demonstrates that MOF as electrolyte modulator could effectively tune the property of SEI and respective morphology of Li moieties. Analogous trend was observed for Li harvested from cycled NCM|Li porotype cells (see **Figure 5-16**).

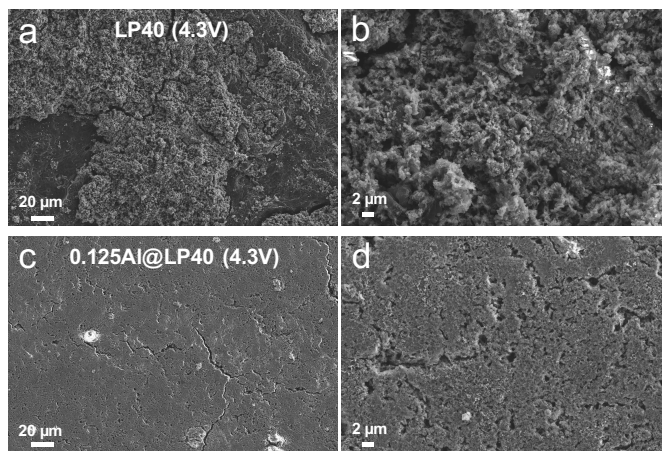


**Figure 5-16** SEM images of Li harvested from NCM-Li cells using (a, b) LP40 and (c, d) nanofluidic electrolyte (0.125Al@LP40) after 50 cycles at 0.3C and 4.3V



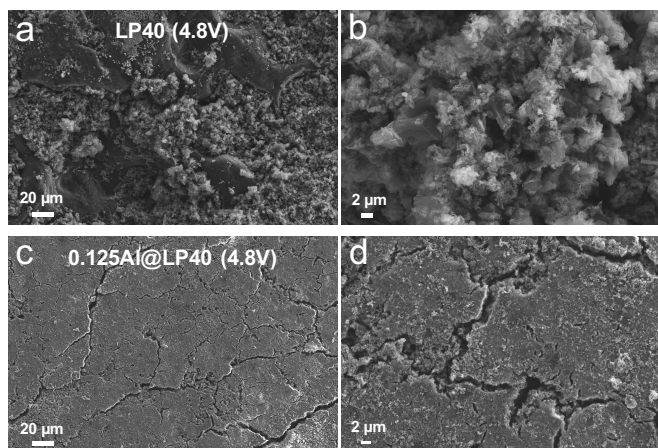


**Figure 5-17** SEM images of Li harvested from NCM-Li cells using (a, b) LP40 and (c, d) nanofluidic electrolyte (0.125Al@LP40) after 50 cycles at 0.3C and 4.8V

To quantitatively determine the resistivity evolution of interfacial layers, the resistances of Li|Li symmetric cells before and after 150 cycles were evaluated by electrochemical impedance spectroscopy (EIS). As plotted in **Figure 5-15b**, the Nyquist plots shows either one depressed semicircle (before cycle) or two serial semicircles (after cycle) accompanied with a tail line. The intercepts of semicircle at high frequency represent Ohmic resistance of the cells, those semicircles signify SEI or charge transfer resistance and the last tails indicate diffusion process. As summarized in the **Table 5-4**, the cell using 0.25Al@LP40 shows highest Ohmic resistance, which is in good agreement with aforementioned ionic conductivity. Meanwhile, the cell with 0.25Al@LP40 shows the lowest charge transfer resistance ( $R_{ct}$ ), this observation is consistent with earlier measurements on exchange current density ( $i_0$ ), reflecting the disproportional relationship between  $R_{ct}$  and  $i_0$ . After 300 h galvanostatic cycling at 0.5 mAh cm<sup>-2</sup> (2 h for each cycle), the trend still well maintained.

**Table 5-4** Ohmic resistance and interfacial resistance (SEI resistance plus charge transfer resistance) of Li-Li fresh cells and cycled cells using LP40 and nanofluidic electrolyte.

|            | Fresh cells ( $\Omega \text{ cm}^{-2}$ ) |                          | Cycled cells ( $\Omega \text{ cm}^{-2}$ ) |                          |
|------------|--|--------------------------|---|--------------------------|
|            | $R_e$                                    | $R_{\text{interfacial}}$ | $R_e$                                     | $R_{\text{interfacial}}$ |
| LP40       | 5  | 711                      | 11.5                                      | 124                      |
| 0.125@LP40 | 5.3                                      | 285                      | 8.7                                       | 71.5                     |
| 0.25@LP40  | 5.7                                      | 258                      | 18  | 52                       |

The compositions of SEI species on Li from cycled Li|Li cells (150 cycles) were analyzed by X-ray photoelectron spectroscopy (XPS). As shown in **Figure 5-15c**, Signals from C=O (288.7 eV at C1s) and M-O (520.2 eV at O1s) increase along with increasing amount of MOF in NE, which corresponds to the -COOH carboxylic acid (ligands) and Al- $\mu_3$ O-Al bond (metal clusters) of MIL-100(Al), respectively. The second distinction lies on signals from P2p and F1s, where P-F bond ( $\sim$ 136.6 eV for P2p and  $\sim$ 686.8 eV for F1s) from  $\text{PF}_6^-$  anions at NE shows relatively stronger intensities than bare LP40. In addition, the decomposition products of  $\text{PF}_6^-$  as indicated by P-O-F (134.7 eV), P-O/P=O ( $\sim$ 133.6 eV) and Li-F (684.8 eV) shows considerably weaker intensities at NE in comparison with LP40, demonstrating the notion that MOF could suppress the breakdown of anions by immobilizing anions *via* open metal sites. The relative integrity of  $\text{PF}_6^-$  in NE after cycling is in accordance with enhanced stability against Li from CV.

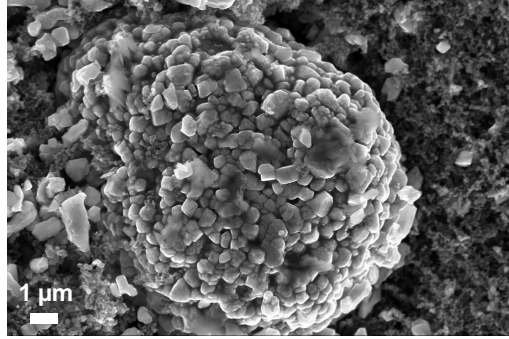


**Figure 5-18** SEM of pristine NCM electrode.

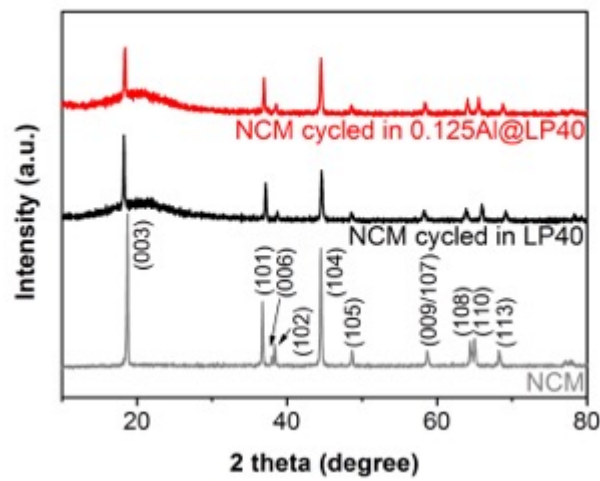


**Figure 5-19** XRD patterns of pristine NCM electrode and NCM electrodes harvested from cycled NCM-Li cells using LP40 and nanofluidic electrolyte (50 cycles at 0.3C and 4.3V).

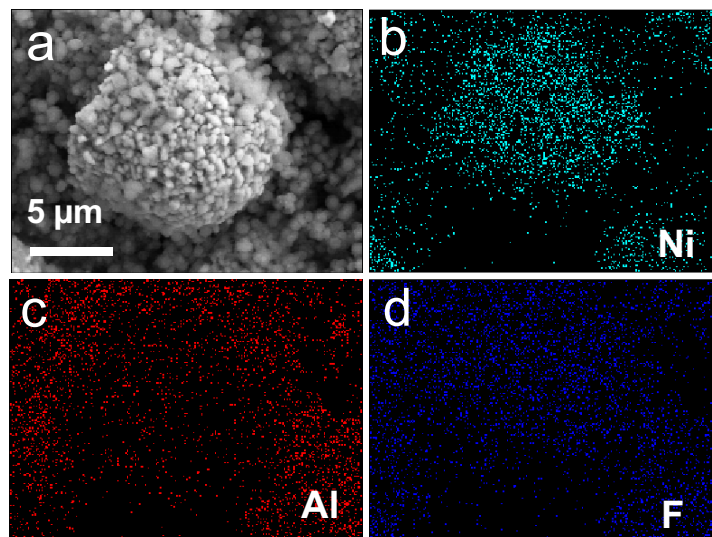


**Figure 5-20** (a) SEM and (b-d) EDS mappings of NCM electrode collected from NCM-Li cell using nanofluidic electrolyte. MOF distribution was confirmed by SEM equipped with EDS. Microspherical NCM composed by secondary nanoparticles could be identified by Ni mapping. Moreover, MIL-100(Al) spreading on NCM is confirmed by Al signals.

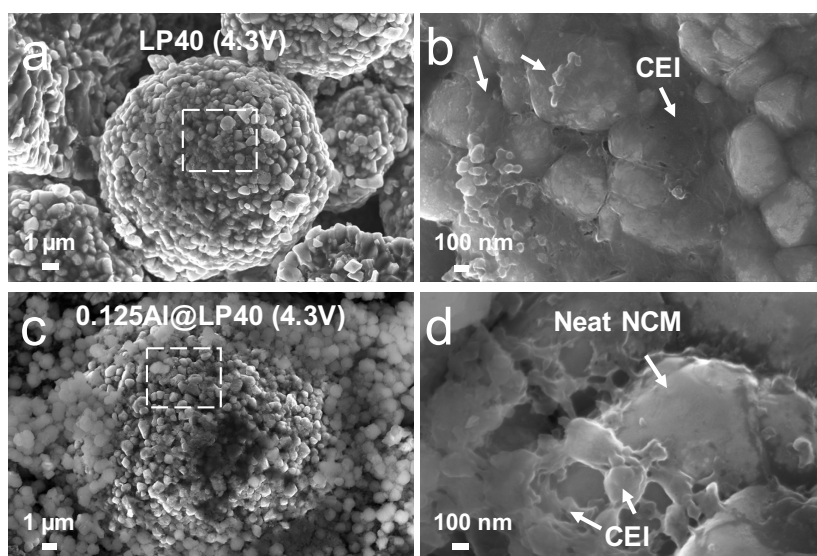


**Figure 5-21** SEM images of NCM cathode electrodes collected from NCM-Li cells using (a, b) LP40 and (c, d) 0.125Al@LP40 after 50 cycles at 0.3C and 4.3V. MOF containing organic component could be recognized by low contrast under electron beam irradiation under vacuum.

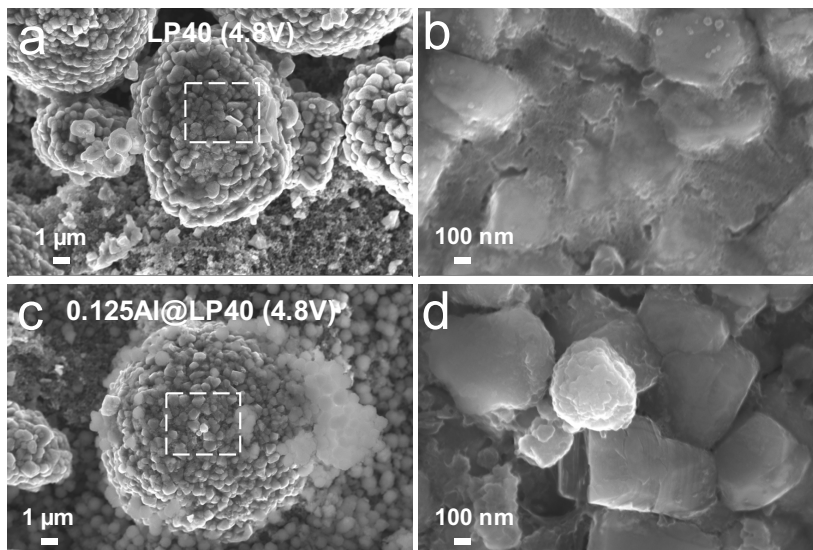


**Figure 5-22** SEM images of NCM cathode electrodes collected from NCM-Li cells using (a, b) LP40 and (c, d) 0.125Al@LP40 after 50 cycles at 0.3C and 4.3V.

The cathode-electrolyte interphase (CEI) were characterized by NCM electrodes collected from NCM|Li cells after 50 cycles at 0.3C. Compared with pristine spheroidal NCM composed by polyhedral primary particles (see SEM image in **Figure 5-18**), cycled NCM in bare LP40 shows substantial decomposition products from electrolyte side reactions, as indicated by the indiscernible boundaries between aculeated NCM primary particles. The accumulation of this interphase (CEI) over cycling is regarded as major reason for deteriorating kinetics of cathode. In sharp contrast, for cathodes cycled in NE (0.125Al@LP40 at 4.3V and 4.8V), the MOF-covered NCM is confirmed by XRD (**Figure 5-19**) and energy-dispersive X-ray spectroscopy (**Figure 5-20**), where considerably less side product is observed in that partial exposure of neat NCM particles (**Figure 5-21** and **Figure 5-22**). The thickness of CEI was further examined by high resolution transmission electron microscopy (HRTEM) and selected area electron diffraction (SAED) as shown in **Figure 5-23**. The CEI was identified by certain transitional regions from amorphous

interphase to bulk crystalline NCM phases and the thickness of CEI was reduced from ~20 nm for NCM in LP40 to ~5 nm for NCM in NE. The integrity of  $\text{PF}_6^-$  anions in CEI is characterized by XPS (**Figure 5-24(a-b)**). Less breakdown of anions occurs for NCM cycled in NE as illustrated by domination content ratio of P-F bond in F species. Moreover, the reversibility of NCM is revealed by oxidation state of Ni.<sup>24</sup> From deconvoluted  $\text{Ni}^{3+}$  and  $\text{Ni}^{2+}$  peaks from Ni2p spectra (**Figure 5-24(c-d)**), the ratio of electroactive  $\text{Ni}^{2+}$  for NCM cycled in NE is higher than in LP40 at high voltage (4.8V). Therefore, the improved cycling performance of NCM-Li cells using NE benefits from both SEI on Li and CEI on NCM.

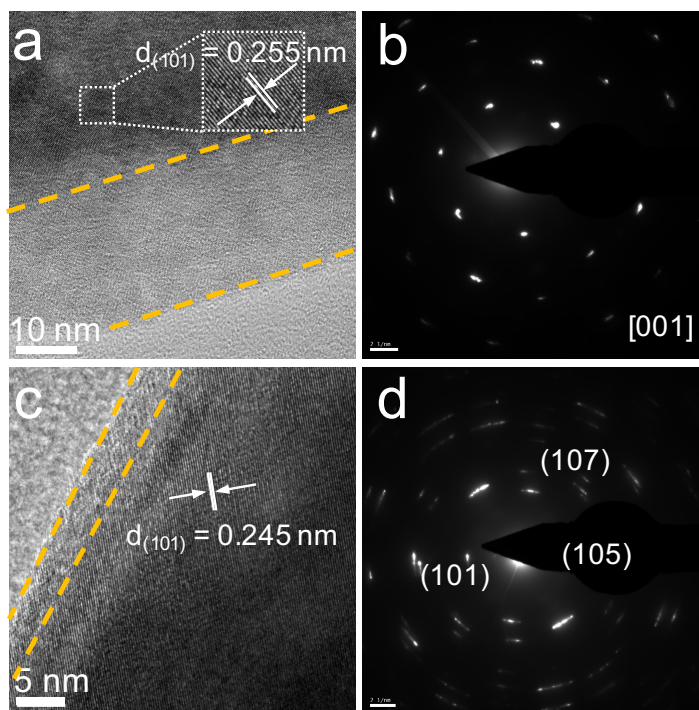


**Figure 5-23** HRTEM and SEAD images of NCM electrodes harvested from cycled NCM-Li cells using (a, b) LP40 and (c, d) nanofluidic electrolyte (50 cycles at 0.3C and 4.3V)

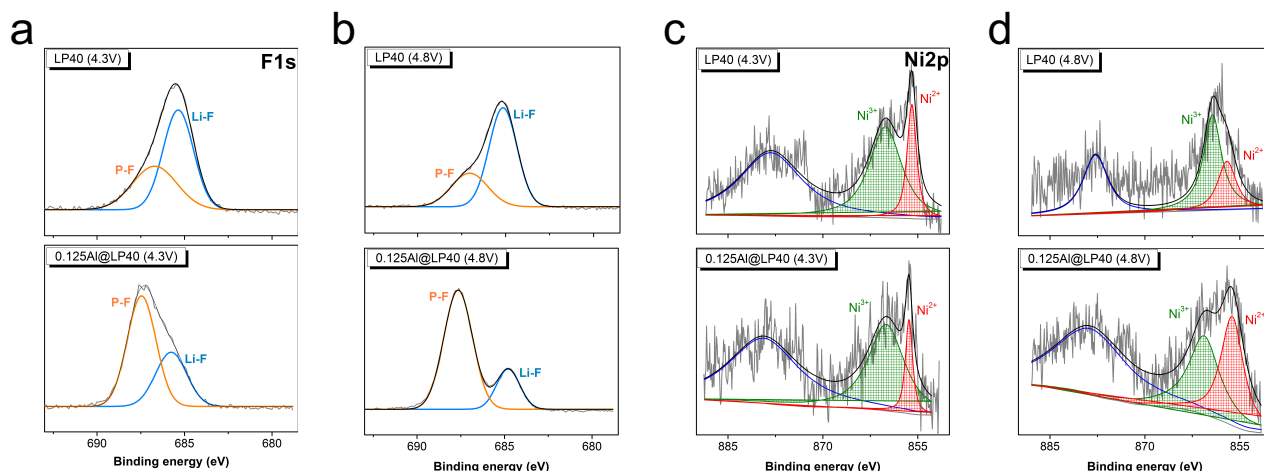


**Figure 5-24** XPS signals from cycled NCM electrodes (50 cycles at 0.3C) harvested from NCM-Li cells using LP40 and nanofluidic electrolyte (0.125Al@LP40): F1s at (a) 4.3V, (b) 4.8V; Ni2p at (c) 4.3V, (d) 4.8V.

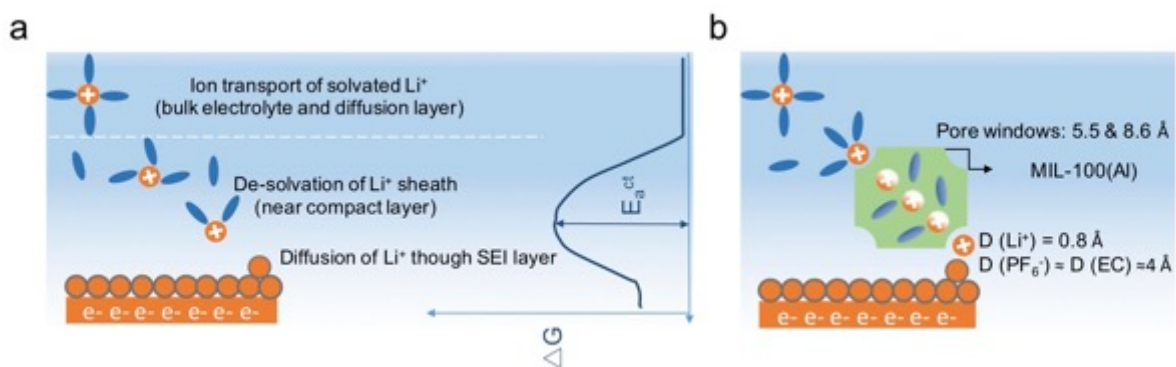


**Figure 5-25** Schematic drawings depicting solvated  $\text{Li}^+$  travel from bulk electrolyte to electrode at (a) liquid electrolyte (LE), and (b) nanofluidic electrolyte (NE).

In short, the mechanisms of presented NE could be elucidated in two aspects. First, electrode-electrolyte interface is a pivotal region governing redox reactions. The corresponding charge transfer resistance usually constitute the highest resistance in lithium batteries at low temperature and high rate.<sup>25</sup> Our findings show a significant enhancement of exchange current

density (**Figure 5-9e**) as well as reduction of associated charge transfer resistance (**Figure 5-15b**). As illustrated in **Figure 25** for typical charge transfer processes, besides the ion transport of solvated  $\text{Li}^+$ , the de-solvation of  $\text{Li}^+$  sheath and subsequent diffusion through SEI layer are two crucial steps towards redox reactions.<sup>26, 27</sup> Particularly for stripping of  $\text{Li}^+$  sheath, which is an energy-consuming process due to strong binding between  $\text{Li}^+$  and polar solvents.<sup>28, 29</sup> We simplified this step as a thermally activated process and corresponding activation energy could be calculated based on **Equation 5-3** (see Experimental Section for details).<sup>30</sup> The interaction between solvents and  $\text{Li}^+$  in presence of activated MOF is weakened as indicated by FT-IR results, which facilitate the breakdown of  $\text{Li}^+$  solvation sheath and the resulting activation energy of charge transfer is reduced by ~40% as shown in **Figure 5-15d** and **Figure 5-26**. We envision that the transport of  $\text{Li}^+$  within MOF mimics the ligand-gated ionic channel existing in biological system, the efficient and selective transport of ions is simultaneously mediated by functional groups and ingenious channel structure, where the negatively charged membrane interior serves as a selectivity filter and solvent-filled larger cavity leverages the permeation of ions with low activation energy of around 20-30  $\text{kJ mol}^{-1}$ .<sup>31</sup>

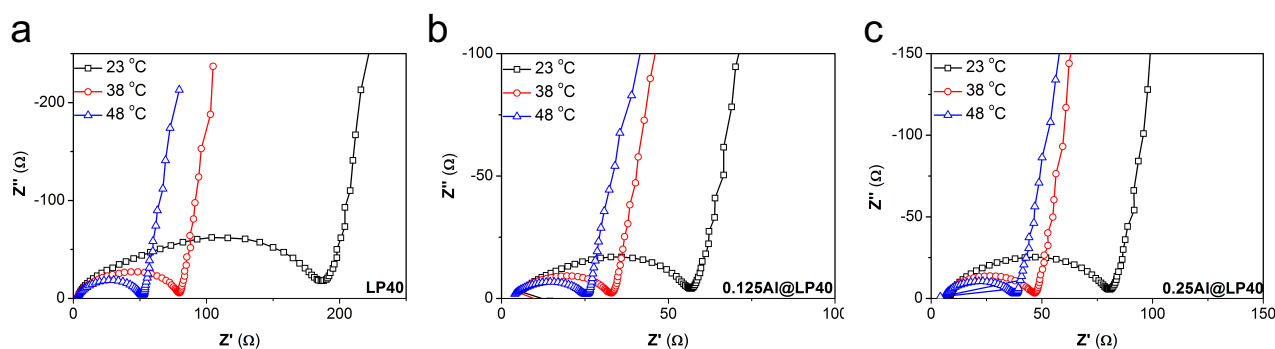


**Figure 5-26** Temperature dependent EIS curves of NCM-Li cells using LP40 and nanofluidic electrolyte.



$$\text{Critical current density: } J^* = \frac{2eC_0D_c}{t_aL} \quad (5-4-1)$$

$$\text{Sand's time: } \tau = \pi D \left( \frac{z_c C_c^0}{2J t_a} \right)^2 \quad (5-4-2)$$

Space charge model (chapter 1) suggests two key parameters: the cation transference number and its diffusion coefficient. With depletion of electrolyte upon cycling, the critical current density and Sand's time (**Equation 5-4-1 and 5-4-2**) could be used to determine the time when surface  $\text{Li}^+$  concentration goes zero to at anode, the progressive anion decomposition occurs thereafter for charge balance.<sup>2</sup> Benefitting from immobilized anion and fast transport of cation, the NE with higher diffusion coefficient and especially lower anion transference number imply prolonged Sand's time, hence the alleviated concentration polarization explains the enhanced rate capability and superior cycling performance.

### 5.3 Conclusions

In this chapter, built upon commercial liquid electrolyte, we reveal that a new type of nanofluidic electrolyte comprising metal–organic frameworks (MOF) shows distinctly enhanced  $\text{Li}^+$  transference number and  $\text{Li}^+$  transport efficiency, where the introduced MOF fundamentally serve as electrolyte modulators for commercial liquid electrolyte. The ubiquitous unsaturated metal sites in nanocages of MOF hinder the mobility of anions and allow the efficient passages of  $\text{Li}^+$ , alleviating the concentration polarization and improving the electrochemical kinetics. Such design provides a new angle of tackling intrinsic issue concerning the insufficient  $\text{Li}^+$  transport efficiency of commercial electrolyte, the proposed approach is readily applicable to battery systems with higher energy density and rate capability in a cost-effective manner.

## 5.4 Experimental Section

**Synthesis of MIL-100(Al).** MIL-100 (Al) was synthesized according to a reported microwave approach. Typically, 1.43 g of aluminum nitrate nonahydrate and 1.21 g of trimethyl trimesate were dissolved in 20 mL of water, 4 mL of nitric acid (4 M) was added to the solution dropwise. The mixture was loaded to a quartz tube and sealed in a microwave oven. The reactor was heated to 240 °C for 1 min by ramping rate of  $\sim 35$  °C min<sup>-1</sup> in the microwave power of 1500 W. After the reactions, all of the samples were washed by water/ methanol and collected by centrifugation for further use.

**Materials structure and characterization.** Crystalline structures of the MOF materials and NCM cathode were analyzed by Rigaku powder X-ray diffractometer (XRD) using K $\alpha$  radiation ( $\lambda = 1.54$  Å) run at 30 kV and 15 mA. Observation of morphology and particle size were performed by scanning electron microscopy (Zeiss). An affiliated energy-dispersive X-ray spectroscopy (EDS) was used to map the element distributions. N<sub>2</sub> adsorption and desorption isotherms were measured on ASAP 2020 plus (Micrometrics) at 77 K. Before analysis, samples were subject to degas at 150 °C for 24 h. The pore size distribution is determined by Density Function Theory model (slit pore, 77 K kernel). Infrared spectra were collected in a transmission mode using KBr pellets on a Jasco 420 Fourier transform infrared (FT-IR) spectrophotometer. Aluminum and lithium ratio was determined by inductively coupled plasma atomic emission spectrometer (ICP-AES, Shimadzu, ICPE-2000) using standard aluminum and lithium solutions (Sigma-Aldrich). Thermogravimetric analysis (TGA) were performed in argon atmosphere using a ramping rate of 10 °C min<sup>-1</sup>. The diffusion coefficients from diffusion ordered spectroscopy (DOSY) NMR is based on the principle of pulse-gradient spin echo NMR:

$$In(E) = In\left(\frac{S}{S_{g=0}}\right) = \gamma^2 \cdot g^2 \cdot D \cdot \delta^2 \cdot \left(\Delta - \frac{\delta}{3}\right) (5 - 1)$$

Where  $\gamma$ : gyromagnetic ratio ( $S^{-1} G^{-1}$ ),  $g$ : gradient strength,  $\delta$ : decays, diffusion gradient length,  $D$ : diffusion coefficient,  $\Delta$ : diffusion time.

For XPS studies, the cycled cells were disassembled in glovebox, the harvested electrodes were then sealed in a transporter and immediately transferred to high-vacuum chamber of XPS (AXIS Ultra DLD). The obtained spectra were calibrated by C 1s peak at 284.8 eV and fitted to Gaussian–Lorentzian functions for peak deconvolutions.

**Preparation of nanofluidic electrolyte.** The synthesized MIL-100 (Al) were thermally activated under dynamic vacuum at 350 °C, nanofluidic electrolyte (NE) were prepared by combining activated MIL-100 (Al) and liquid electrolyte (LP40, 1M LiPF<sub>6</sub> in EC/DEC, BASF) in weight (mg) vs. volume (ul) ratio of 0.125 (0.125Al@LP40) and 0.25 (0.25Al@LP40). The resulting mixtures were rigorously stirred to achieve homogeneity. For studies on properties of liquid electrolyte confined within MOF (LP40@MOF), flow-free powders were collected by vacuum filtration of nanofluidic electrolyte.

**Fundamental electrolyte properties.** Ionic conductivity was measured by electrochemical impedance spectroscopy (EIS) in an electrolyte flow cell using two identical platinum electrodes where the cell parameter ( $L/S$ ,  $L$  is thickness in cm and  $S$  is area in cm<sup>2</sup>) was determined by reference conductivity of LP40 (8 mS cm<sup>-1</sup> at 25 °C). The technique was carried out by applying a.c. magnitude of 100 mV in a frequency range 10<sup>6</sup>–1 Hz. The ionic resistivity ( $R$ , ohm) was identified by the end point of the semi-circle from resulting Nyquist plots and ionic conductivity ( $\kappa$ , S cm<sup>-1</sup>) was calculated based on  $\kappa = L/(R \times S)$ .

The temperature dependent conductivity was collected by coin cell configuration at various

temperature, where electrolyte saturated glass fiber separators (Whatman) were sandwiched between two stainless steel electrodes. The activation energy ( $E_a$ ) of electrolyte was derived from Arrhenius relation:

$$\sigma = Ae^{(-E_a/RT)} \quad (5-2)$$

The charge transfer resistivity ( $R_{ct}$ ) was obtained from Nyquist plots NCM|electrolyte|Li cells using polyethylene based separator (Celgard, 25  $\mu$ m), which exhibit a semicircle followed by a Warburg tail.  $R_{ct}$  is approximately equivalent to the fitted diameter of the semicircle. The activation energy of charge transfer originates from the thermodynamic aspect of charge transfer resistance:

$$R_{ct} = \frac{RT}{nFSi_0} \quad (5-3-1)$$

$$i_0 = nFk^0(C_{ED}^*)^{1-\alpha}(C_{EL}^*)^\alpha \quad (5-3-2)$$

$k^0$ : standard reaction constant

$C_{ED}^*, C_{EL}^*$ : Li concentration in electrode and electrolyte

$\alpha$ : transfer coefficient

$$k^0 = Be^{(-E_a/RT)} \quad (5-3-3)$$

B: frequency factor

$E_a$  : activation energy

$$\frac{T}{R_{ct}} = \frac{(nF)^2BS}{R}(C_{ED}^*)^{1-\alpha}(C_{EL}^*)^\alpha e^{(-E_a/RT)} = Ae^{(-E_a/RT)} \quad (5-3-4)$$

A potentiostatic polarization combined with EIS technique was used to evaluate  $\text{Li}^+$  transference number ( $t_{\text{Li}^+}$ ) in Li|electrolyte|Li cell. The symmetric cell was polarized by a constant d.c. potential (V, 20 mV) for 30 minutes, the initial current ( $I_0$ ) and final steady-state current ( $I_{\text{ss}}$ ) were recorded and the interfacial resistance was determined by EIS before ( $R_{\text{int}}^0$ ) and after ( $R_{\text{int}}^{\text{ss}}$ ) potentiostatic polarization. The  $t_{\text{Li}^+}$  could thereby be calculated by the formula:  $t_{\text{Li}^+} = I_{\text{ss}}(V - I_0 R_{\text{int}}^0) / (I_0(V - I_{\text{ss}} R_{\text{int}}^{\text{ss}}))$ .

For cyclic voltammetry (CV) tests in two-electrode configuration using coin cells, lithium foils were utilized as reference/counter electrodes and stainless-steel plates (SS) were used as the working electrodes. The CV of Li|electrolyte|SS was carried out between  $-0.2$  and  $5$  V at  $1 \text{ mV s}^{-1}$  (Biologic). For three-electrode configuration using flow cell, platinum electrode was used as reference electrode.

### **Electrochemical device studies.**

The electrodes of symmetric activated carbon (AC) capacitors (AC|electrolyte|AC) were prepared by homogeneously mixing AC, carbon black (CB), and polyvinylidene fluoride (PVdF) with a weight ratio of 8:1:1 in N-methyl-2-pyrrolidone (NMP). The resulting slurry was uniformly coated on a conductive carbon-coated Al foil and dried in a vacuum oven at  $70$  °C for 24 h. The electrodes with AC loading of  $5 \text{ mg cm}^{-2}$  were assembled into coin cells in glove box ( $\text{O}_2 < 0.5$  ppm) using polyethylene based separator (Celgard, 25  $\mu\text{m}$ ) and 100  $\mu\text{l}$  electrolyte. The galvanostatic cycling was carried out between 0 to 2.7 V at various current densities.

The exchange current density ( $i_0$ ) signifying reaction kinetics was calculated from two-electrode (Li|electrolyte|Li) galvanostatic polarization. By applying stepped small current (I) ranging from 3.3 to 66.7  $\mu\text{A cm}^{-2}$ , the  $i_0$  could be extracted from linear relationship from Tafel equation:  $i_0 = (I/V) \times (2RT/F)$  (here V is average overpotential,  $RT/F = 0.0256$  V). Li strip/plate

tests were performed using Li symmetric cells at  $0.5 \text{ mA cm}^{-2}$  for a periodic 1h. The Coulombic efficiency of Li plating and stripping on Cu (Cu|electrolyte|Li cells) was evaluated at  $0.25 \text{ mAh cm}^{-2}$  and upper voltage cutoff of 1.5V.

The NCM electrodes were prepared in a similar manner to AC electrodes. The active NCM loading is  $20 \text{ mg cm}^{-2}$  and weight ratio between NCM, CB and PVdF is 9:0.5:0.5. Li disks with areal capacity of  $93 \text{ mAh cm}^{-2}$  is commercially available (MTI). Normal voltage (4.3 V) and high voltage (4.8 V) upper cutoffs were controlled for prototype NCM|electrolyte|Li cells,  $160 \text{ mA g}^{-1}$  and  $250 \text{ mA g}^{-1}$  represent 1C for 4.3 V and 4.8 V, respectively. The replenishment of liquid electrolyte for NCM|Li cells at 50<sup>th</sup> cycle (0.3 C, 4.3 V) was carried out in glove box by disassembling, refilling and reassembling cycled cells

## 5.5 References

1. Zugmann, S. et al. Measurement of transference numbers for lithium ion electrolytes via four different methods, a comparative study. *Electrochimica Acta* **56**, 3926-3933 (2011).
2. Jiang, F. & Peng, P. Elucidating the Performance Limitations of Lithium-ion Batteries due to Species and Charge Transport through Five Characteristic Parameters. *Scientific Reports* **6**, 32639 (2016).
3. Bai, P., Li, J., Brushett, F.R. & Bazant, M.Z. Transition of lithium growth mechanisms in liquid electrolytes. *Energy & Environmental Science* **9**, 3221-3229 (2016).
4. Tikekar, M.D., Archer, L.A. & Koch, D.L. Stabilizing electrodeposition in elastic solid electrolytes containing immobilized anions. *Science Advances* **2** (2016).
5. Pfaffenhuber, C. & Maier, J. Quantitative estimate of the conductivity of a soggy sand electrolyte: example of (LiClO<sub>4</sub>, THF):SiO<sub>2</sub>. *Physical Chemistry Chemical Physics* **15**, 2050-2054 (2013).
6. Moganty, S.S., Jayaprakash, N., Nugent, J.L., Shen, J. & Archer, L.A. Ionic-Liquid-Tethered Nanoparticles: Hybrid Electrolytes. *Angewandte Chemie International Edition* **49**, 9158-9161 (2010).
7. Lu, Y., Moganty, S.S., Schaefer, J.L. & Archer, L.A. Ionic liquid-nanoparticle hybrid electrolytes. *Journal of Materials Chemistry* **22**, 4066-4072 (2012).
8. Borodin, O. et al. Liquid Structure with Nano-Heterogeneity Promotes Cationic Transport in Concentrated Electrolytes. *ACS Nano* **11**, 10462-10471 (2017).
9. Suo, L., Hu, Y.-S., Li, H., Armand, M. & Chen, L. A new class of Solvent-in-Salt electrolyte for high-energy rechargeable metallic lithium batteries. *Nature Communications* **4**, 1481 (2013).



10. Takeuchi, M. et al. Ion–ion interactions of LiPF<sub>6</sub> and LiBF<sub>4</sub> in propylene carbonate solutions. *Journal of Molecular Liquids* **148**, 99-108 (2009).
11. Horike, S., Umeyama, D. & Kitagawa, S. Ion Conductivity and Transport by Porous Coordination Polymers and Metal–Organic Frameworks. *Accounts of Chemical Research* **46**, 2376-2384 (2013).
12. Llewellyn, P.L. et al. High Uptakes of CO<sub>2</sub> and CH<sub>4</sub> in Mesoporous Metal–Organic Frameworks MIL-100 and MIL-101. *Langmuir* **24**, 7245-7250 (2008).
13. Yoon, J.W. et al. Controlled Reducibility of a Metal–Organic Framework with Coordinatively Unsaturated Sites for Preferential Gas Sorption. *Angewandte Chemie International Edition* **49**, 5949-5952 (2010).
14. Hwang, Y.K. et al. Amine Grafting on Coordinatively Unsaturated Metal Centers of MOFs: Consequences for Catalysis and Metal Encapsulation. *Angewandte Chemie International Edition* **47**, 4144-4148 (2008).
15. Yang, J.-C. & Yin, X.-B. CoFe<sub>2</sub>O<sub>4</sub>@MIL-100(Fe) hybrid magnetic nanoparticles exhibit fast and selective adsorption of arsenic with high adsorption capacity. *Scientific Reports* **7**, 40955 (2017).
16. García Márquez, A. et al. Green Microwave Synthesis of MIL-100(Al, Cr, Fe) Nanoparticles for Thin-Film Elaboration. *European Journal of Inorganic Chemistry* **2012**, 5165-5174 (2012).
17. Volkringer, C. et al. Infrared Spectroscopy Investigation of the Acid Sites in the Metal–Organic Framework Aluminum Trimesate MIL-100(Al). *The Journal of Physical Chemistry C* **116**, 5710-5719 (2012).

18. Leclerc, H. et al. Infrared study of the influence of reducible iron(iii) metal sites on the adsorption of CO, CO<sub>2</sub>, propane, propene and propyne in the mesoporous metal–organic framework MIL-100. *Physical Chemistry Chemical Physics* **13**, 11748-11756 (2011).
19. Cresce, A.V. et al. Solvation behavior of carbonate-based electrolytes in sodium ion batteries. *Physical Chemistry Chemical Physics* **19**, 574-586 (2017).
20. Seo, D.M. et al. Role of Mixed Solvation and Ion Pairing in the Solution Structure of Lithium Ion Battery Electrolytes. *The Journal of Physical Chemistry C* **119**, 14038-14046 (2015).
21. Lin, D. et al. Conformal Lithium Fluoride Protection Layer on Three-Dimensional Lithium by Nonhazardous Gaseous Reagent Freon. *Nano Letters* **17**, 3731-3737 (2017).
22. Cheng, X.-B. et al. A Review of Solid Electrolyte Interphases on Lithium Metal Anode. *Advanced Science* **3**, 1500213-n/a (2016).
23. Xie, J. et al. Stitching h-BN by atomic layer deposition of LiF as a stable interface for lithium metal anode. *Science Advances* **3** (2017).
24. Wang, D. et al. Role of zirconium dopant on the structure and high voltage electrochemical performances of LiNi<sub>0.5</sub>Co<sub>0.2</sub>Mn<sub>0.3</sub>O<sub>2</sub> cathode materials for lithium ion batteries. *Electrochimica Acta* **188**, 48-56 (2016).
25. Xu, K. & von Wald Cresce, A. Li<sup>+</sup>-solvation/desolvation dictates interphasial processes on graphitic anode in Li ion cells. *Journal of Materials Research* **27**, 2327-2341 (2012).
26. Xu, K. “Charge-Transfer” Process at Graphite/Electrolyte Interface and the Solvation Sheath Structure of Li<sup>+</sup> in Nonaqueous Electrolytes. *J. Electrochem. Soc.* **154**, A162-A167 (2007).

27. Xu, K., Lam, Y., Zhang, S.S., Jow, T.R. & Curtis, T.B. Solvation Sheath of Li<sup>+</sup> in Nonaqueous Electrolytes and Its Implication of Graphite/Electrolyte Interface Chemistry. *The Journal of Physical Chemistry C* **111**, 7411-7421 (2007).
28. von Wald Cresce, A., Borodin, O. & Xu, K. Correlating Li<sup>+</sup> Solvation Sheath Structure with Interphasial Chemistry on Graphite. *The Journal of Physical Chemistry C* **116**, 26111-26117 (2012).
29. Abe, T., Sagane, F., Ohtsuka, M., Iriyama, Y. & Ogumi, Z. Lithium-Ion Transfer at the Interface Between Lithium-Ion Conductive Ceramic Electrolyte and Liquid Electrolyte-A Key to Enhancing the Rate Capability of Lithium-Ion Batteries. *J. Electrochem. Soc.* **152**, A2151-A2154 (2005).
30. Dudney, N.J., West, W.C. & Nanda, J. Handbook of Solid State Batteries, Edn. 2nd. (World Scientific Series in Materials and Energy, 2016).
31. Åqvist, J. & Luzhkov, V. Ion permeation mechanism of the potassium channel. *Nature* **404**, 881 (2000).

## **Chapter 6 Metal–organic Frameworks as Electrode additives for High-Performance Lithium Ion Batteries**

We present a general type of porous coordination solids, metal–organic framework (MOF), as electrode additives to improve thermal stability, rate and cycle performances of batteries. The incorporation of MOF additives into electrodes is fully compatible with current battery manufacturing process. Activated MOF powders could serve as electrolyte modulator to enhance cationic transport and alleviate interfacial resistance by interacting liquid electrolyte with unsaturated open metal sites (OMS). Moreover, the flow-free liquid in solid configuration is realized by encapsulating liquid electrolyte into porous scaffold of MOF, which offers superior thermal stability.

## 6.1 Introduction

The popularity of portable electronics and commercialization of electric vehicles stimulates the extensive research and substantial growth of battery market. Though current state of the art lithium ion batteries could achieve energy density of  $\sim 250 \text{ W h kg}^{-1}$ , which corresponds to driving range of  $\sim 300$  miles. The long charging time, formidable cost and safety concern from intrinsic flammability of liquid electrolyte significantly retard the widespread adoption of electric vehicle and green energy technology. Therefore, researchers tackle those issue from several scientific aspects. For instance, nanosized electrode materials could reduce the diffusion length and therefore the diffusion kinetics within the solid electrode is enhanced. Despite evident improvement in rate performance, this strategy compromises the tap density of electrode materials and it is relatively difficult for scaled up production. Moreover, the safety issue of liquid electrolyte could be alleviated by using ceramic or polymer based solid electrolyte, while the insufficient ionic conductivity and challenging interfacial resistance fall short of commercial applications (**Figure 6-1**). So far seldom approach targeting industrial applications has been proposed to simultaneously resolve those key limitations existing in current batteries technologies. Hence a versatile yet readily applicable design in material or structure is of great significance in promoting the development for next-generation batteries and extensive utilization of renewable energy.

## 6.2 Result and Discussion

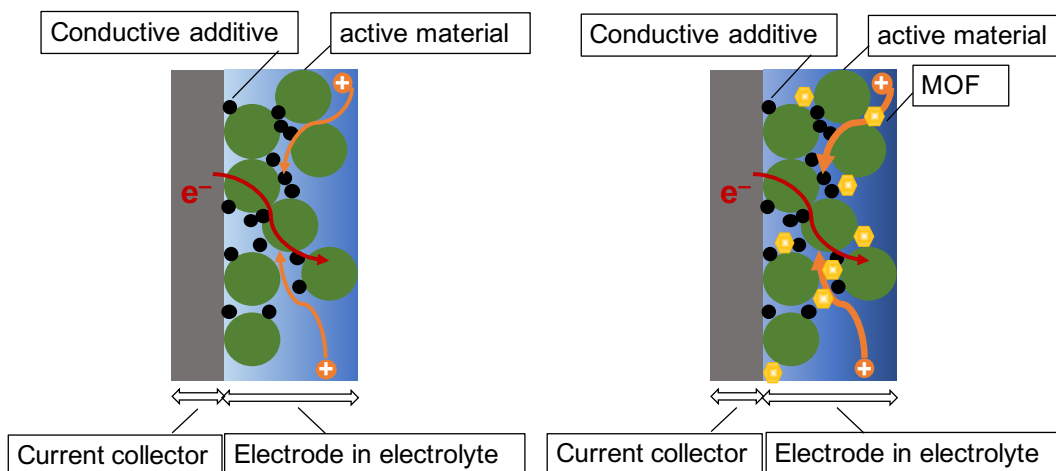


**Figure 6-1** Illustrative configuration of electrode structure and components.

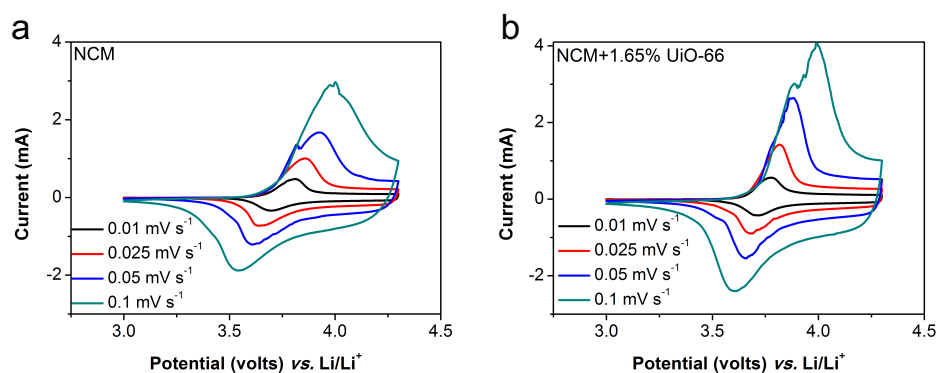


**Figure 6-2** The cyclic voltammetry of (a) NCM cathode ( $\text{LiNi}_{0.33}\text{Co}_{0.33}\text{Mn}_{0.33}\text{O}_2$ , reference electrode, denoted as REF) and (b) NCM cathode with MOF additive (high-performance electrode, abbreviated as HPE) at a variety of sweep rate, where metallic Li were used as both reference and counter electrodes.

MOF additive used here is exemplified while not restricted to UiO-66. The synthesized UiO-66 underwent a heat treatment ( $350\text{ }^\circ\text{C}$ ) under vacuum for thermal activation purposes. The activated UiO-66 were homogeneously mixed with  $\text{LiNi}_{0.33}\text{Co}_{0.33}\text{Mn}_{0.33}\text{O}_2$  (NCM), acetylene

black (CB), polyvinylidene fluoride (PVDF) by a weight ratio of 1.7 : 91.7 : 3.3 : 3.3 in N-Methyl-2-pyrrolidone (NMP), afterwards the resulting electrode slurry were coated on aluminum current collect using a doctor blade. The ratio between electrode components is for demonstration purpose and optimized ratio is subject to engineering process. After two step drying at 80 and 170 °C under vacuum. The baked electrodes were calendered to thickness of 60  $\mu\text{m}$  with NCM loading of 15  $\text{mg cm}^{-2}$ . For the reference electrodes without MOF, the NCM content is 93.3% instead while maintaining contents of CB and PVDF the same. Finally, the prepared electrodes were tailored into electrode disks with diameter of 14 cm for future use. For CR-2032 type coin cells, metallic lithium disks (15.6 cm diameter, MTI®) were used as both counter and reference electrodes, liquid electrolyte 1M  $\text{LiPF}_6$  in EC/DEC (ethylene carbonate/diethylene carbonate, w:w=1:1, BASF®) is commercially available, and the 25 $\mu\text{m}$  trilayer polypropylene-polyethylene-polypropylene membrane is purchased from Celgard®.

To distinguish the role of MOF additives within the electrodes, the diffusion coefficient of  $\text{Li}^+$  within the electrodes were characterized by cyclic voltammetry technique. We assembled the NCM-Li half cells both with (REF) and without MOF additives (HPE) and performed stepped CV sweeps a varied rate (from 0.01 to 0.1  $\text{mV s}^{-1}$ ). The redox peaks at 3.6 V and 4.0 V vs.  $\text{Li/Li}^+$  are ascribed to the de-intercalation and intercalation reactions of  $\text{Li}^+$ , respectively. As compared at same sweep rate in **Figure 6-2**, the HPE exhibits higher redox currents than REF, indicating enhanced reaction kinetics by incorporating 1.7 wt% MOF into bare electrodes. We speculated that the modulated  $\text{Li}^+$  transport by MOF within the electrodes facilitate the charge transfer process of electrochemical reactions.

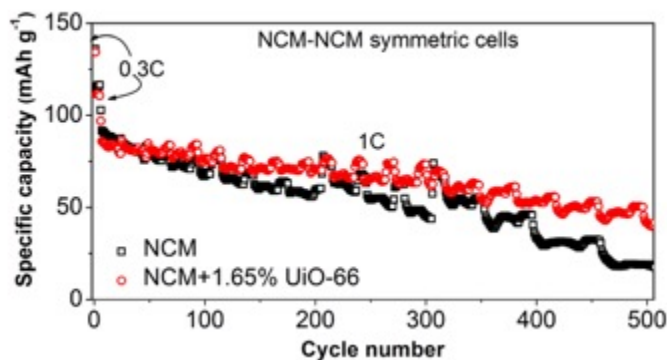


**Figure 6-3** Long-term cycling performance comparison between REF and HPE using NCM-NCM symmetric cell configurations.

The long-term cycling performance of NCM electrodes were evaluated by symmetric cell configuration to eliminate the impact of interface between Li with electrolyte. Firstly, we extract partial xLi in  $\text{Li}_{1-x}\text{Ni}_{0.33}\text{Co}_{0.33}\text{Mn}_{0.33}\text{O}_2$  by charging NCM-Li half-cells to 4.3V at 0.1C (1C=16 mA  $\text{g}^{-1}$ ), thereafter we harvested the charged NCM electrodes and paired with fresh NCM electrodes. As for NCM with MOF additives, we add 1.65% UiO-66 into electrodes, which are denoted as high-performance electrodes (HPE). As displayed in **Figure 6-3**, The fabricated NCM-NCM symmetric cells were subject to galvanostatic cycling under 0.3C for 5 cycles and 1C rate afterwards. The REF (NCM) exhibits 0.17% capacity fading per cycle, which is much higher than HPE (0.1%) over 500 cycles. Besides, the average Coulmobic efficiency of HPE is improved from 99.88% for REF to 99.94%. The superior cycling performance demonstrates that MOF additive is able to alleviate the parasitic reactions between positive electrodes and electrolyte.



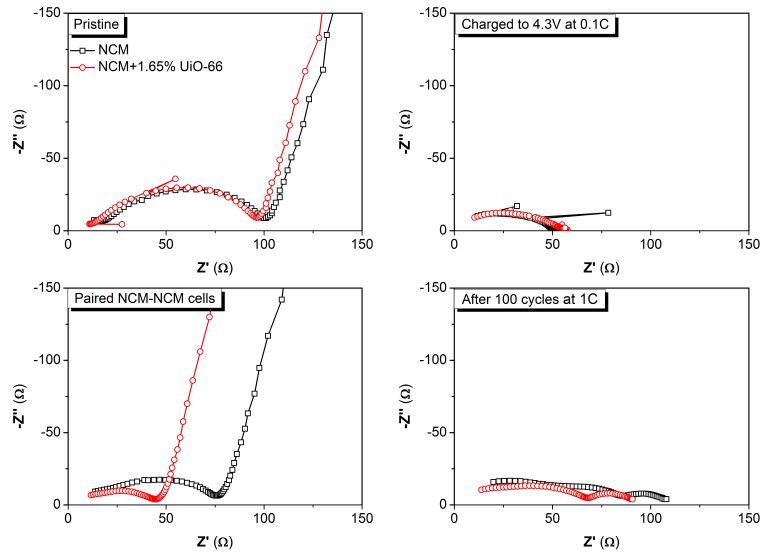


**Figure 6-4** Evolution comparison of electrochemical impedance spectroscopy (EIS) between REF and HPE.

To reveal the mechanism behind the improvements, a series of electrochemical impedance spectroscopy tests were performed. Firstly, as shown in **Figure 6-4**, the Nyquist plots of fresh NCM-Li half-cells show a semicircle accompanied with a sloping line, which could be ascribed to the interfacial resistances (NCM/Li with electrolyte, denoted as  $R_{ct}$ ) and diffusion process, respectively. After charging the NCM to 4.3V at 0.1C, we observe almost identical depressed semicircles for both REF and HPE. However, the paired NCM-NCM symmetric cells exhibit dramatic distinction in terms of  $R_{ct}$ , where HPE shows ~50% reduction of  $R_{ct}$  compared with REF. The difference is maintained even after 100 cycles at 1C. The comparisons of impedance evolution illustrate that MOF within the electrodes is able to alleviate the interfacial resistance, which is of importance especially for low-temperature application and high rate operation.

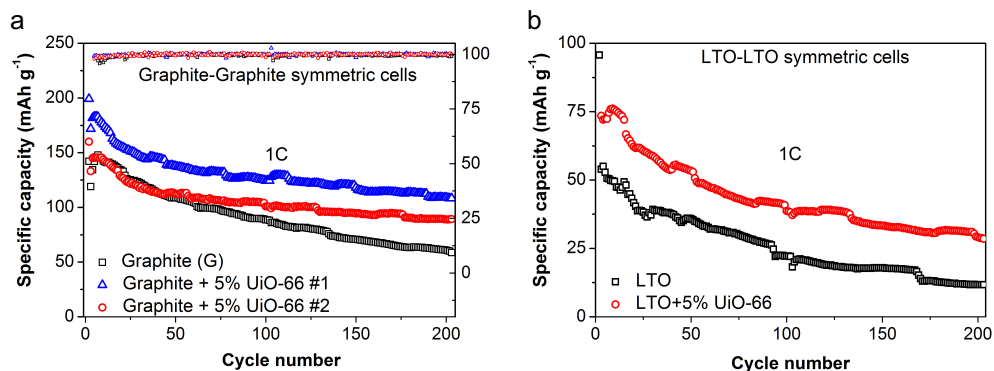


**Figure 6-5** (a) Cycling performance comparison between REF and HPE using graphite-graphite (C-C) symmetric cell configurations. (b) Cycling performance comparison between REF and HPE using Li<sub>4</sub>Ti<sub>5</sub>O<sub>12</sub>- Li<sub>4</sub>Ti<sub>5</sub>O<sub>12</sub> symmetric cell configurations.

Besides NCM cathode, performances of typical anodes including graphite (C) and lithium titanate (Li<sub>4</sub>Ti<sub>5</sub>O<sub>12</sub>, LTO) with MOF additives were also explored in **Figure 6-5**. MOF additive used here is exemplified while not restricted to UiO-66. The activated UiO-66 were homogeneously mixed with graphite/LTO, acetylene black (CB), polyvinylidene fluoride (PVDF) by a weight ratio of 5 : 87 : 5 : 2 in N-Methyl-2-pyrrolidone (NMP), afterwards the resulting electrode slurry were coated on copper current collect using a doctor blade. The ratio between electrode components is for demonstration purpose and optimized ratio is subject to engineering process. After two step drying at 80 and 170 °C under vacuum. The baked electrodes were calendered to thickness of 60 μm with anode loading of 7.5 mg cm<sup>-2</sup>. For the reference electrodes without MOF, the graphite/LTO content is 92% instead while maintaining contents of CB and PVDF the same. Finally, the prepared electrodes were tailored into electrode disks with diameter of 14 cm for future use. The performance improvements are summarized in table 3 (1C for graphite is 374 mA g<sup>-1</sup>, 1C for LTO is 170 mA g<sup>-1</sup>).

The EIS evolutions and Li<sup>+</sup> diffusion coefficient comparison of anodes (graphite and LTO) are shown from **Figure 6-6** to **Figure 6-10**, exhibiting similar trend to NCM cathode and hence demonstrating the versatility of MOF as high-performance electrodes.

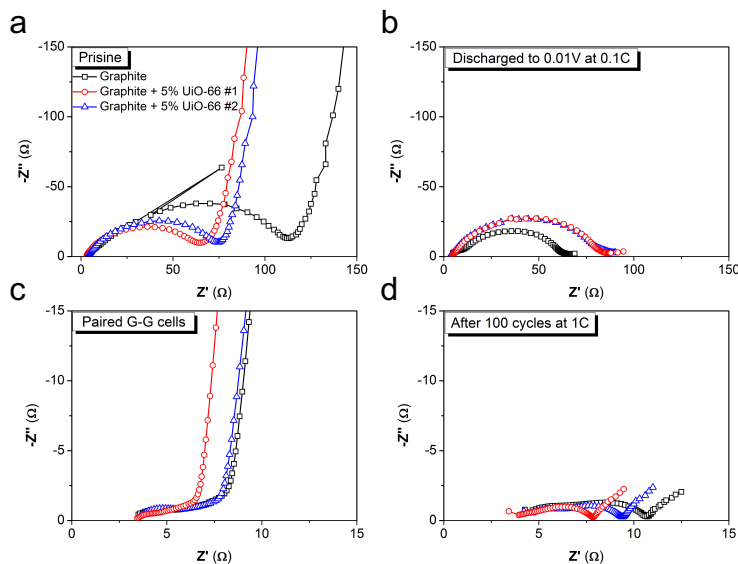


**Figure 6-6** Evolution comparison of electrochemical impedance spectroscopy (EIS) between REF and HPE for graphite anodes.

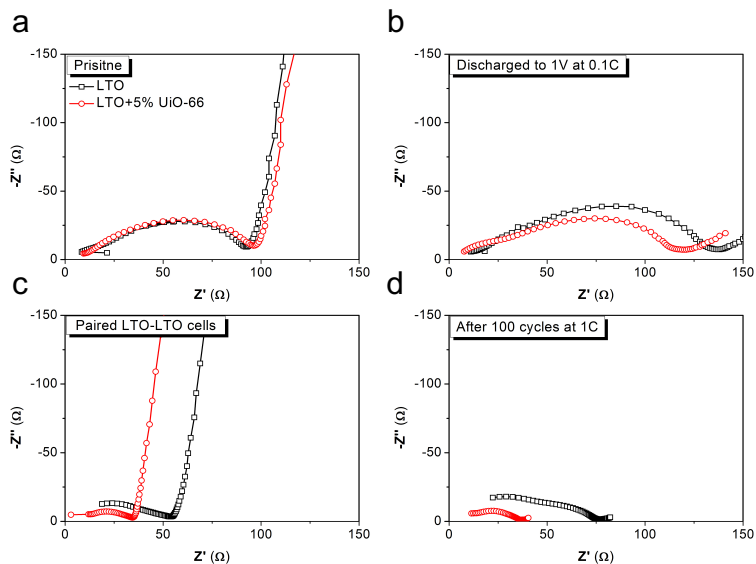


**Figure 6-7** Evolution comparison of electrochemical impedance spectroscopy (EIS) between REF and HPE for LTO anodes.

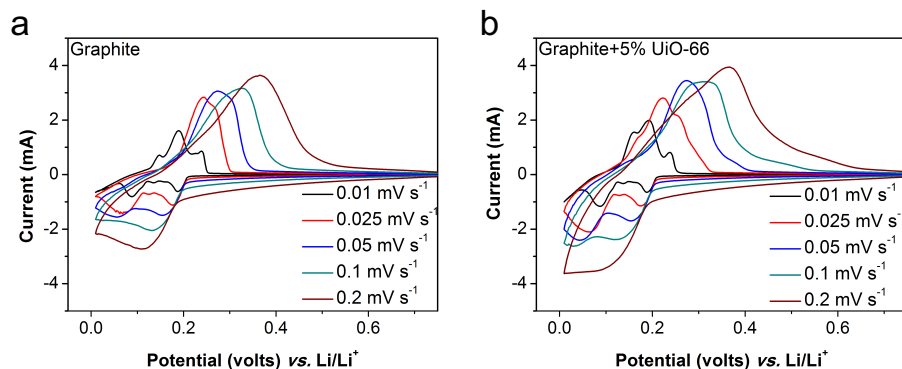


**Figure 6-8** The cyclic voltammetry of (a) graphite anode and (b) graphite anode with MOF additive at a variety of sweep rate, where metallic Li were used as both reference and counter electrodes.

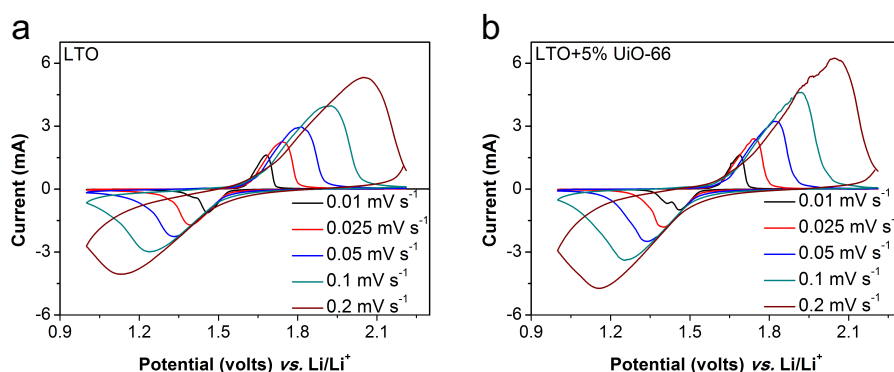


**Figure 6-9** The cyclic voltammetry of (a) LTO anode and (b) LTO anode with MOF additive at a variety of sweep rate, where metallic Li were used as both reference and counter electrodes.

**Table 6-1** Performance improvements of electrodes using MOF additives.

|                         |            | Graphite | LTO    | NCM    |
|-------------------------|------------|----------|--------|--------|
| <b>Added UiO-66 wt%</b> |            | 5        | 5      | 1.65   |
| <b>Fading per cycle</b> | <b>REF</b> | 0.3%     | 0.4%   | 0.17%  |
|                         | <b>HPE</b> | 0.2%     | 0.3%   | 0.1%   |
| <b>CE (200 cycles)</b>  | <b>REF</b> | 99.46%   | 99.50% | 99.91% |
|                         | <b>HPE</b> | 99.84%   | 99.80% | 99.95% |

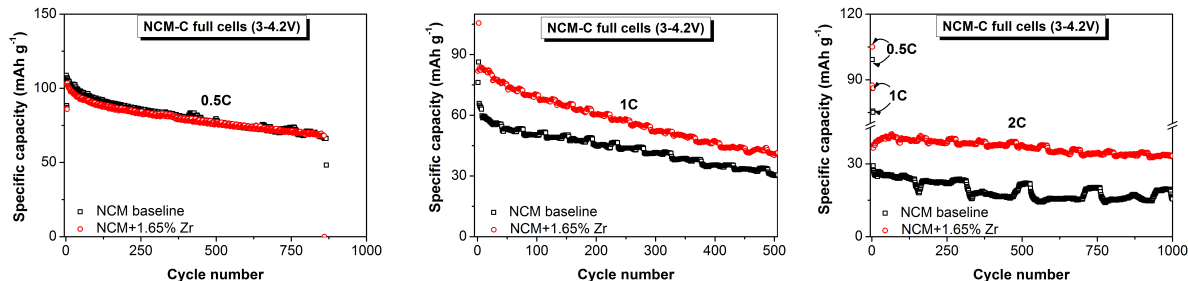


**Figure 6-10** Cycling performance comparisons between REF and HPE using NCM-C full cell configurations at different rates.

To illustrate the superiority of MOF additives in full cell configuration, NCM-C full cell (weight ratio between NCM and graphite is 15 : 7.5 mg cm<sup>-2</sup>) in coin cells were fabricated, where MOF additives were added to cathode side. The combination of NCM and graphite is for demonstrative purposes and any combination of aforementioned electrodes is applicable. The cells were tested under 0.1C, 1C and 2C between 2.5 to 4.2V for prolonged cycling. As shown in **Figure 6-10**, HPE (NCM-C) exhibit superior rate performance than REF, especially at 2C rate, the HPE could deliver almost one-fold higher specific capacity than REF. The cycling results from full cells suggest that the improvement in terms of rate capability is more evident in full cell configuration, where the electric field might influence the concentration polarization of anion.

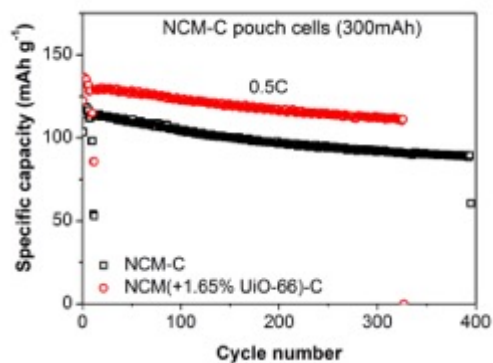


**Figure 6-11** Cycling performance comparisons between REF and HPE using NCM-C pouch cell.

As shown in **Figure 6-11** NCM-C full cells were further extended to pouch cells configuration for practical application purposes. The designed capacity for pouch cell is 300 mAh and corresponding mass loading of active material is identical to those electrodes used in coin cell. As shown in Fig. 8, reproducible results were obtained in pouch cells configuration in terms of rate and cycling performances. The advantages of MOF additives in electrodes of lithium-based battery are successfully demonstrated, while it is speculated that this is readily applicable to other alkali metal-based battery electrodes.

## Chapter 7: Summary and Perspectives

Ubiquitous portable electronics and emergence of electric vehicles require the next-generation batteries with higher energy density, faster charging capability and improved thermal safety. Nevertheless, little progress has been made on material chemistry of batteries since first commercialization of lithium-ion cells in 1991. Indeed, improvements on cell performances are majorly contributed by engineering and optimization processes. Under such circumstances, researchers shall have responsibility not only tackle the challenges from fundamental standpoints but also implement developed techniques in a cost-effective manner.

In this dissertation, we focus on realizing a more efficient transport of one important charge carrier in electrochemical systems, namely lithium ion, which is less investigated compared with electron. We believed that the electrochemical active species  $\text{Li}^+$  should earn higher ionic mobility compared with counterpart anions (electrochemical non-active). It is indeed the opposite case for commercial liquid electrolyte, the relative higher anion mobility due to bulky size of solvated  $\text{Li}^+$  give rise to huge concentration polarization and sluggish reaction kinetics, limiting power output, battery lifetime and energy density.

Inspired by ionic channel structures commonly existing in biological systems, our group approached this issue by exploring one emerging type of porous crystalline solids, metal–organic frameworks (MOF). Opened metal centers with unsaturated coordination sites could be generated *via* facile thermal activation. After infiltration of liquid electrolyte, anions are expected to complex the unsaturated metal sites, forming anion-decorated negatively charged pore channels and facilitating the transport of  $\text{Li}^+$ .

We first demonstrated that the ionic behaviors of liquid electrolyte in MOF is consistent with our hypothesis using a number of characterization techniques including spectroscopy. By

varying the availability of open metal centers, tortuosity of pore channels, spatial size of anions, aperture size of accessible MOF windows and metal centers with different Lewis acidity, we gained systematic comprehensions on how to design and improve the model of electrolytes built upon MOF and liquid electrolyte.

Based on the new class of MOF-based electrolytes, we investigated the respective electrochemical performances of rechargeable batteries. The integration approaches we employed but not restricted to are pseudo solid-state electrolytes, functional separators, electrolyte additives and electrode additives. As expected, the MOF function as electrolyte modulator, improving the  $\text{Li}^+$  transference number, reaction kinetics and mitigating concentration polarization. The enhanced cycle life under high current operation is of particular significance for high-rate battery applications.

The above works provide a new platform for design and improve the transport of  $\text{Li}^+$  in a cost-effective manner, the methodology we proposed are envisioned to be extended to other alkali ion-based electrolytes, potentially enabling numerous applications.